Exciton dynamics in organic semiconductors for efficient electroluminescent devices

Hwan-Hee Cho

Darwin College

Cavendish Laboratory, Department of Physics

University of Cambridge

This dissertation is submitted for the degree of

Doctor of Philosophy

May 2022

I would like to dedicate this thesis to my wife and family …

Declaration

This thesis is the result of my own work and includes nothing which is the outcome of work done in collaboration except as declared in the preface and specified in the text.

It is not substantially the same as any work that has already been submitted before for any degree or other qualification except as declared in the preface and specified in the text.

It does not exceed 60,000 words, including summary/abstract, tables, footnotes and appendices, but excluding table of contents, photographs, diagrams, figure captions, list of figures/diagrams, list of abbreviations/acronyms, bibliography and acknowledgements.

Hwan-Hee Cho

May, 2022

Abstract

Exciton dynamics in organic semiconductors for efficient electroluminescent devices

Hwan-Hee Cho

In this thesis, new approaches to realise efficient and stable visible and near-infrared (NIR) electroluminescence (EL) devices are explored by controlling exciton energy transfer and charge transport in organic semiconductors.

In the first part of the thesis, 'hyperfluorescence', which is the concept that thermally activated delayed fluorescence (TADF) materials are exploited as an exciton sensitiser to a fluorescent emitter, is investigated. Firstly, the possibility of excluding the host matrix is investigated based on the exploration of exciton energy transfer between donors and acceptors. Since a host matrix is removed, charge transport in TADF donors is studied in addition to energy transfer. Space-charge-limited current (SCLC) measurement based on single-carrier devices is employed. Secondly, encapsulated fluorophores are studied. To prevent aggregation and energy loss by Dexter energy transfer (DET), encapsulation of the molecules is used to increase intermolecular spacing so that the short-range energy transfer process can be effectively suppressed. Furthermore, newly designed deep blue multiple resonance emitters are explored. Using this concept, highly efficient deep blue hyperfluorescent organic light-emitting diodes (OLEDs) with ultra-narrow emission are demonstrated with the study of exciton dynamics on the basis of transient analysis. Additionally, they are also applied in conventional fluorescent OLEDs. With effective Förster resonance energy

transfer (FRET), efficient deep blue OLEDs showing ultra-narrow emission with 450 nm peak emission and $CIE_y \leq 0.05$ are demonstrated.

In the second part of the thesis, organic radicals are explored for efficient NIR EL devices. Recently, doublet fluorescent emission from organic radicals has emerged as a new route to more efficient light-emitting devices than those using established non-radical organic emitters. Charge recombination in radical-based devices results in doublet excitons with nanosecond emission and avoids the efficiency limit usually associated with singlets and triplets. Firstly, a novel NIR organic radical emitter with an 820 nm emission peak is used for efficient NIR EL devices. To improve charge transport and balance in an emitting layer (EML), mixed-host systems are utilised to improve the efficiency roll-off and operational lifetime. Secondly, a novel energy transfer mechanism between exciton donors and radical acceptors is devised to optimise device performance in devices. One of the anthracene derivatives is selected as an exciton donor to activate effective intersystem dual energy transfer, which means that singlet excitons are transferred to doublet excited states via FRET, and triplet excitons are transferred to doublet excited states via DET. Utilising this approach, highly efficient NIR EL devices are demonstrated based on the study of transient EL and magneto EL, as well as transient photophysical measurements.

Acknowledgements

First of all, I would like to show my great gratitude to my wife and family (parents and mother-in-law) for supporting my PhD in Cambridge. Without them, I would not have done my PhD successfully.

I would like to show my gratitude to Dr Dan Credgington for giving me an opportunity with initial supervision to pursue my PhD in the Cavendish Laboratory. Although he left the lab, I support his choice and hope for success in his career. I want to show my gratitude to Prof. Jang-Joo Kim and Dr Byungki Choi for their support of my PhD study at Cambridge. I would like to express my special thanks to the George and Lilian Schiff Foundation for the PhD studentship funding. I would like to acknowledge all of the former Credgington group members for helping me adapt myself to the new environment and learn how to use the lab equipment.

I would like to acknowledge Prof. Neil Greenham for his supervision from the second year of my PhD. Thanks to his support, I was able to develop my PhD projects continuously. I would like to give my special gratitude to Dr Emrys Evans for his advice and supervision on my PhD projects. I have been able to have an opportunity to do a new project on organic radicals and make excellent results with him learning new science. I am really thankful to Dr Dan Congrave for his superb support. Thanks to his active and enthusiastic support, I have made good progress on our collaboration work about a blue OLED. I would like to acknowledge Dr Alexander Romanov for the collaboration work on a new type of emitting materials, carbene-metal-amides, and active support on the project. I would like to acknowledge Sebastian Gorgon for his active support on transient photophysical measurement. I am so grateful to Prof. Sir Richard Friend for his supervision and words of encouragement on my PhD projects and for giving me a great opportunity to work with him after my PhD. I look forward

to researching more on new organic semiconductors and contributing to the development of this field.

I want to acknowledge the Kapitza hub administrators and all staff in the optoelectronics group and Cavendish Laboratory for helping postgraduate students and postdoc researchers focus on their studies and projects.

Table of Contents

List of Abbreviations

Aluminium ..... Al
Cyclic voltammetry CV
Current density-voltage ..... J-V
Conventional-type TADF ..... CT-TADF
Carbene metal amide ..... CMA
Conventional-type hyperfluorescence ..... CTHF
Commission Internationale de l'Éclairage ..... CIE
Dexter energy transfer ..... DET
Density functional theory ..... DFT
Electroluminesence ..... EL
External quantum efficiency ..... EQE
Electron injection layer ..... EIL
Electron transporting layer ..... ETL
Emitting layer ..... EML
Eelectron blocking layer ..... EBL
Electron-only device ..... EOD
Electron spin resonance ..... ESR
Förster resonance energy transfer ..... FRET
Full-width-half maximum ..... FWHM
Forward/reverse-DET ..... F-DET/R-DET
Ground state bleach ..... GSB
Hole blocking layer ..... HBL
Hole injection layer ..... HIL
Hole transporting layer ..... HTL
Highest occupied molecular orbital ..... HOMO
Hole-only device ..... HOD
Intensified charge-coupled device ..... ICCD

Intersystem crossing ..... ISC
Indium tin oxide ..... ITO
Internal quantum efficiency ..... IQE
Internal conversion IC
Luminance-voltage ..... L-V
Liquid crystal display ..... LCD
Lowest unoccupied molecular orbital ..... LUMO
Lithium fluoride ..... LiF
Multiple resonance ..... MR
Molecular orbital ..... MO
Microchannel plate photomultiplier tube ..... MCP-PMT
Magneto EL ..... MEL
Matrix-free hyperfluorescence ..... MFHF
Matrix-free TADF ..... MF-TADF
Non-colinear optical parametric amplifier ..... NOPA
Near-infrared ..... NIR
Organic light-emittind diode ..... OLED
Photoluminesence ..... PL
Power efficiency ..... PE
Reverse intersystem crossing ..... RISC
Space-charge-limited current ..... SCLC
Singly occupied molecular orbital ..... SOMO
Spin-orbit coupling ..... SOC
Thermally activated delayed fluorescence ..... TADF
Triplet-triplet annihilation ..... TTA
Triplet-triplet fusion ..... TTF
Time-correlated single-photon counting ..... TCSPC
Transient absorption ..... TA
Time-of-flight ..... TOF
Time-dependent density functional theory ..... TDDFT
Ultraviolet ..... UV
X-ray diffraction ..... XRD

Chapter 1 Introduction

In this chapter, the general context of lighting and display technologies is outlined for the research results in the thesis. This is followed by more details on the theoretical background (Chapter 2), experimental methods (Chapter 3), and the full results and discussion of the thesis (Chapter 4-7).

1.1 Organic light-emitting diodes (OLEDs) for displays

The demonstration of the first organic electroluminescent device in 1987 marked a new era in light-emitting technology.[1] From the late 2000s, organic light-emitting diodes (OLEDs) became a rival for liquid crystal displays (LCDs) due to superior efficiency, contrast, brightness, and ease of manufacture. OLEDs have now entered mass production and are widely applied in televisions, tablet personal computers, and smartphones, where they are increasingly replacing LCDs. The use of phosphorescent molecules to turn on emission from normally-dark triplet excited states was a key development, which significantly increased the performance of red and green OLED devices.[2–4] However, there are some critical issues that prevent the implementation of energy-efficient white lighting and cheap, ubiquitous display technology based on OLEDs. The main issue they face is “burn-in”, which is a consequence of the much lower operational lifetime and efficiency of blue fluorescent OLEDs compared to their

red and green counterparts.[5] The realisation of blue phosphorescent OLEDs with high stability remains a key challenge, with operational lifetimes still far from those required for OLED consumer products.[6–14] Moreover, current phosphorescent materials utilise one of the rarest elements on Earth - iridium, which may represent a barrier to cost-effective mass production in the long term. Both of these factors have driven the search for alternative approaches to efficient light emission.

In 2011, Adachi et al. demonstrated highly promising metal-free organic materials capable of harvesting singlet and triplet excitons via the concept of thermally activated delayed fluorescence (TADF).[15] In most efficient TADF materials, a small energy gap ($\leq$ 0.1 eV) between singlet and triplet states is achieved by separating electron and hole wavefunctions via a charge-transfer excitation between electron donating and accepting moieties. This is considered to enable a mechanism for up-conversion from nonradiative triplet excited states to radiative singlet excited states by reverse intersystem crossing (RISC). Using this approach, almost 100% electroluminescence (EL) internal quantum efficiency (IQE) has been demonstrated, with operating stability and colour purity becoming the next target.[16] Improved colour purity has recently been attained by developing multiple resonance (MR) TADF emitters, which do not rely on the formation of typical CT states, but these devices are generally limited by low stability that has not yet been fully solved.[17,18]

In terms of the technology for accomplishing high efficiency, stability, and colour purity in OLED devices, one of the most promising concepts in the field is to exploit TADF molecules as an exciton sensitiser,[19] which is the so-called 'hyperfluorescence'.[20] Here, the TADF molecule manages triplet up-conversion before energy transfer to a fluorescent component with a narrow emission profile. Förster resonance energy transfer (FRET) between those molecules must be as effective as

possible, while Dexter energy transfer (DET) must be prevented. Recently, using this concept with MR emitters, higher than 25% external quantum efficiency (EQE) and high stability with narrow emission spectra were achieved, showing the potential of satisfying the requirements for display applications.[21,22]

Research in this thesis: Chapter 4 explores hyperfluorescent OLEDs based on novel TADF materials, carbene-metal-amides (CMAs), with detailed studies of exciton energy transfer between donors and acceptors and charge transport in EL devices, showing the potential of excluding a wide gap host matrix in hyperfluorescent OLEDs. In chapter 5, encapsulated fluorescent molecules are studied to suppress aggregation and DET in the hyperfluorescent systems. Newly designed MR fluorescent dyes are investigated to realise highly efficient deep blue OLEDs with ultra-narrow emission, with optimised designs revealed from the transient analysis of films and devices.

1.2 Organic radicals for near-infrared electroluminescence

Whilst there are numerous demonstrations of visible-light emitters based on organic molecules for OLEDs, materials with efficient near-infrared (NIR) emission are less well-developed since multi-phonon emission reduces radiative luminescence quantum yields for lower gap organic semiconductors.[23–25] However, NIR OLEDs are of interest due to the wide range of technological applications in biosensing, optical imaging, photodynamic therapy, security in personal identification and surveillance, and communications. A variety of emission concepts, such as fluorescence,[26–28] phosphorescence,[29–32] TADF,[33–35] and sensitised fluorescence by TADF or phosphorescence[36–38] have been studied, but the EQE has not been satisfactory, typically under 5% for emission peak wavelengths of 800 nm and longer.

As a promising alternative, luminescent organic radical materials have been developed with doublet emission from 585 nm to 900 nm.[39–52] Organic radicals have unpaired electrons that give rise to doublet spin manifolds, for which efficient OLEDs with pure-red and mixed red/NIR EL from tris(2,4,6-trichlorophenyl)methyl (TTM) radical derivatives have been demonstrated.[50–52] The high efficiency was attributed to these devices using EL from doublet excitons rather than conventional singlet and triplet excitons that limit the efficiency in standard non-radical devices.

However, as radical emitters are typically dispersed at relatively low concentration in a wide-bandgap host matrix, exciton formation on the emitters occurs by sequential capture of electrons and holes (or vice versa) following injection and transport in the host. However, the lower energy orbitals of organic radicals compared to conventional fluorescent emitters causes severe electron trapping in devices, which results in significant efficiency roll-off, low radiance, and poor stability. Engineering of the transport and recombination of charges in an emitting layer (EML), therefore, provides opportunities to enhance device performance. A further strategy to facilitate control over the recombination zone is to arrange for electron-hole capture to occur primarily in the host followed by energy transfer to the emitter, thus decoupling the recombination process from charge trapping by the emitter.

Research in this thesis: Efficient NIR organic radical LEDs with around 820 nm peak emission are demonstrated in Chapter 6 based on the optimisation of direct charge recombination. Exciton formation and charge transport in radical doped films are investigated in different hosts, modifying charge transporting properties by mixing electron transporting and hole transporting layers. In Chapter 7, a newly designed energy transfer system is explored towards realising highly efficient NIR organic radical LEDs with longer than 800 nm peak emission. Energy transfer pathways and

exciton decay kinetics are revealed by time-resolved spectroscopy in addition to device characterisation with transient and magnetic field dependent EL.

Chapter 2 Theoretical background

This chapter will cover the theoretical background for physical mechanisms in organic semiconductors and electroluminescent devices. The physics of organic semiconductors is described to understand the photophysical characteristics, exciton dynamics, and exciton energy transfer in organic layers in devices, which are fundamental for the ideas explored in the thesis. Different emission mechanisms are described with their advantages and disadvantages in the context of the state of the art.

2.1 The physics of organic semiconductors

2.1.1 Exciton

A hole and electron bound by the electrostatic Coulomb force are defined as an exciton, which is electrically neutral, leading to the transportation of energy, not charge.[53–55] Figure 2-1(a) shows the schematic representation of the exciton. As an electron in the valence band is excited to the conduction band, the excited electron and hole (the positive charge in the valence band) are formed as an electron-hole pair, exciton, with stabilising energy provided by the repulsive Coulomb force from neighbouring electrons.[53–55] Thus, the exciton has slightly smaller energy than the single-particle energy gap. In general, excitons are generated by light absorption or electric field, as depicted in Figure 2-1(b). For organic semiconductors, as electrons are localised to each molecule occupying molecular orbitals, the valence and conduction bands in inorganic semiconductors correspond to the highest occupied molecular orbital

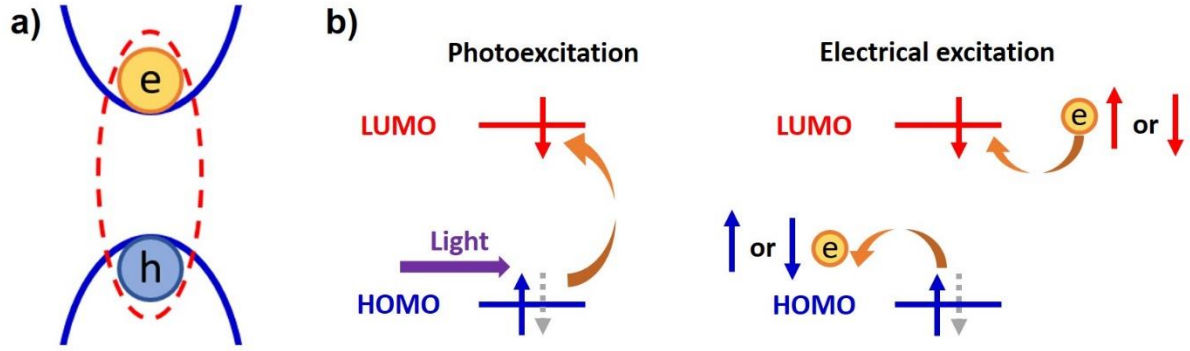

Figure 2-1. Schematic diagram of (a) the exciton in the two-band model and (b) Photoexcitation and electrical excitation to form excitons in organic semiconductors.

(HOMO) and lowest unoccupied molecular orbital (LUMO), respectively.

The concept of excitons was first introduced by Frenkel in 1931, which provides a good approximation for organic semiconductors having relatively small dielectric constant with van der Waals bonding, where excitons are well localised in one molecule.[56–58] The size of the exciton is therefore disposed to be small, and the interaction between hole and electron in a single organic molecule is relatively strong.[56–58] The typical binding energy of these Frenkel excitons is on the order of 0.1~1.0 eV.[58] However, excitons are not restricted to being located on one molecule. The hole and electron can be located on adjacent molecules to form excitons, termed charge-transfer excitons, which are also usually observed in organic molecules.[57] Also, the hole and electron may be located on the molecules away from each other, which is termed Wannier-Mott excitons.[54,57–59] This type of excitons is generally formed in inorganic semiconductors having large dielectric constants, such as silicon and gallium arsenide. The valance electrons are shared with a number of atoms as the interaction between neighbouring atoms is strong. Hence, the excited electron and hole are not localised in a single position, and the size of the electron-hole pair becomes quite larger with much less binding energy than Frenkel exciton, the order of 0.01 eV. The

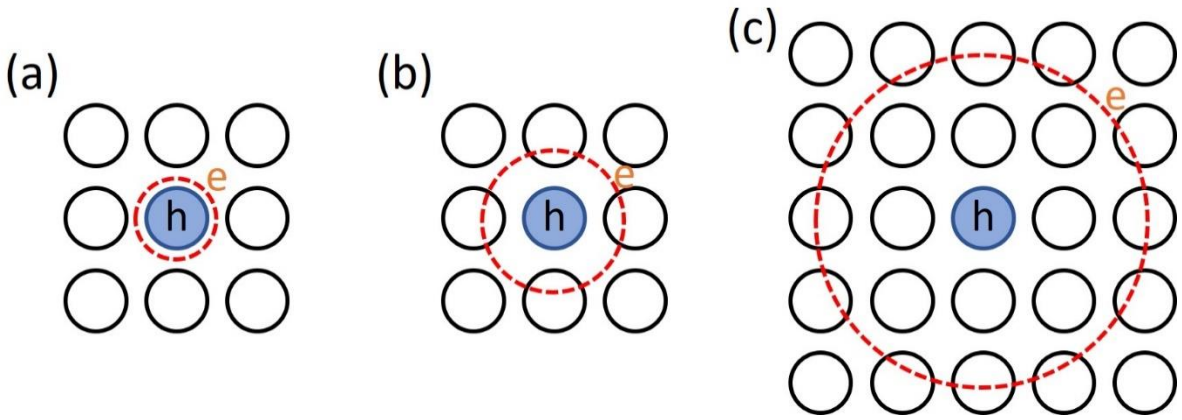

Figure 2-2. Schematic diagram of (a) Frenkel exciton, (b) Charge-transfer exciton, and (c) Wannier-Mott exciton.

schematic diagram of the three types of excitons is displayed in Figure 2-2.

As shown in Figure 2-1(b), there are two possible ways to form excitons in organic semiconductors, photoexcitation and electrical excitation. When excitons are formed by external light energy, one of the two electrons having different spin is excited from HOMO to LUMO. Hence, the photoexcited exciton can have only one kind of spin state, where the total spin angular momentum quantum number (S) is 0, as each electron on HOMO and LUMO has the opposite spin projection, which is termed 'singlet' as a state with paired electrons remains a single state.[60,61] On the other hand, as excitons are generated via electron transport under an external electric field, electrons on both LUMO and HOMO can have the s of either ½ (spin up ↑) or -½ (spin down ↓). Therefore, in addition to singlet ($S = 0$), the overall exciton spin states can be $S = 1$ with the spin projection quantum number (m_s) of -1, 0, 1, which is termed 'triplet' with three quantised states.[60,61]

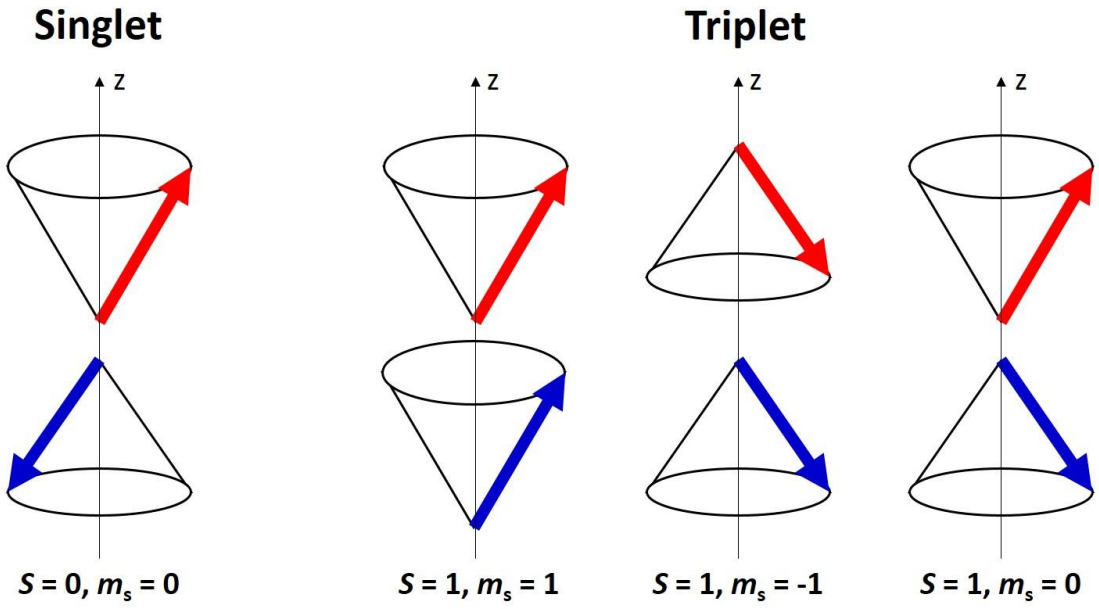

Figure 2-3. Schematic representation of singlet and triplet spin states in typical organic semiconductors.

Figure 2-3 shows the schematic illustration of one singlet and three triplet spin configurations. According to the Pauli exclusion principle,[62] no electrons can have the same spin state occupying the same orbital simultaneously. As described above, excitons formed in typical organic semiconductors have four different spin states as ↑↑, ↑↓, ↓↑, and ↓↓, where the first arrow and the second arrow present the spin direction of the first and second electron, respectively.[60,61] They are expressed by the spins and projections on the z-axis in a vector space with the form of $|s, m_s\rangle$. The triplet states at the overall $S = 1$ are expressed by,[60,61]

$$|1, 1\rangle = \uparrow\uparrow \tag{2-1}$$

$$|1, 0\rangle = \frac{1}{\sqrt{2}}(\uparrow\downarrow + \downarrow\uparrow) \tag{2-2}$$

$$|1, -1\rangle = \downarrow\downarrow \tag{2-3}$$

And, the singlet state at $S = 0$ is found to be,[60,61]

$$|0,0\rangle = \frac{1}{\sqrt{2}}(\uparrow\downarrow - \downarrow\uparrow) \tag{2-4}$$

In general, the S_1 (the first electronically excited singlet state) → S_0 (the ground electronic singlet state) transition is a spin-allowed process emitting light with energy corresponding to the energy gap of S_1 and S_0 (fluorescence) while T_1 (the first electronically excited triplet state) → S_0 transition is spin-forbidden due to the different spin states of T_1 and S_0 based on a selection rule.[60] However, the strong spin-orbit coupling (SOC) (coupling between the orbital magnetic moment and the spin magnetic moment) in phosphorescent emitters induced by heavy metal (especially iridium or platinum) enables the efficient triplet emission (phosphorescence).[4]

On the other hand, organic radicals, incorporating one unpaired electron on the outermost molecular orbital, show the doublet spin manifold, which is different from

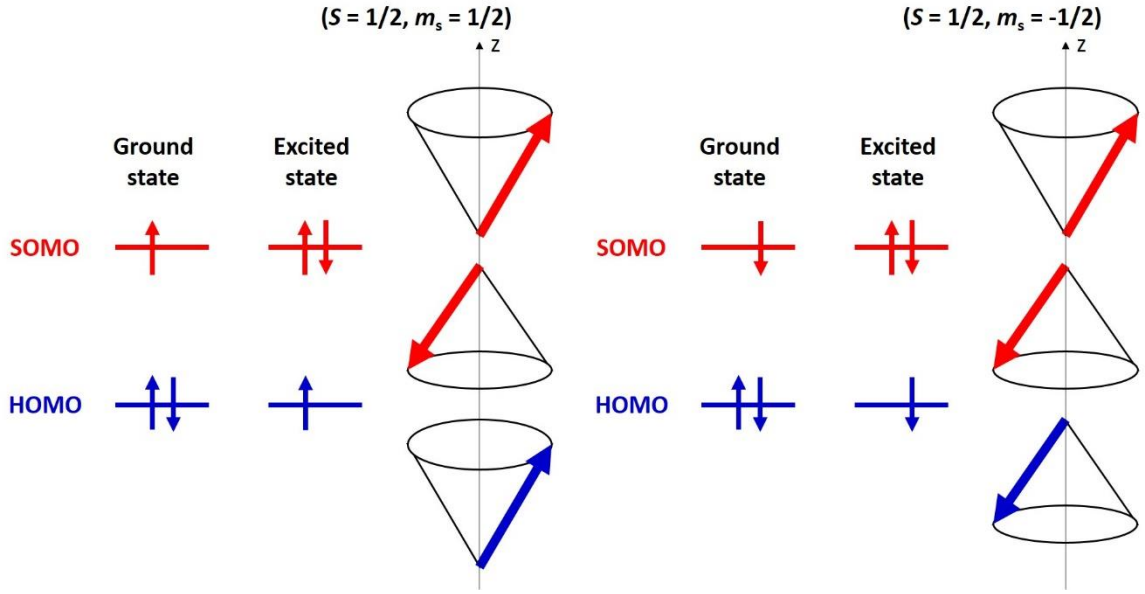

Figure 2-4. Schematic illustration of doublet spin states in organic radicals.

singlet and triplet spin states observed in typical organic semiconductors.[63,64] Figure 2-4 shows the schematic diagram of doublet spin states observed in organic radicals. In the ground state, one unpaired electron is located on the non-bonding singly occupied molecular orbital (SOMO), which is the intermediate of HOMO and LUMO, and this generates excitons that have one unpaired electron and total S = ½, which is termed 'doublet' as the spin degeneracy is two.[63,64] As the S of both the ground and excited states is maintained at the S = ½, D_1 (the first electronically excited doublet state) → D_0 (the ground electronic doublet state) transition is a spin-allowed process enabling efficient doublet fluorescence with nanosecond decay lifetime.

2.1.2 Photoluminescence and absorption

Photoluminescence (PL) is light emission from any form of matter after the absorption of photons in photoexcitation.[65] Photons are emitted from the lowest electronic excited state after the rapid relaxation processes of excitons (Kasha's rule).[66]

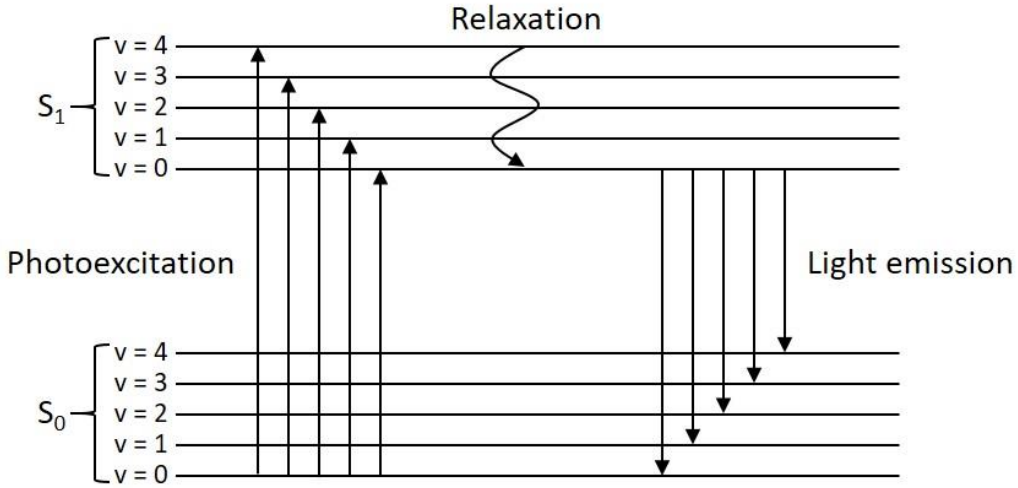

Figure 2-5. Schematic diagram of absorption and photoluminescence.

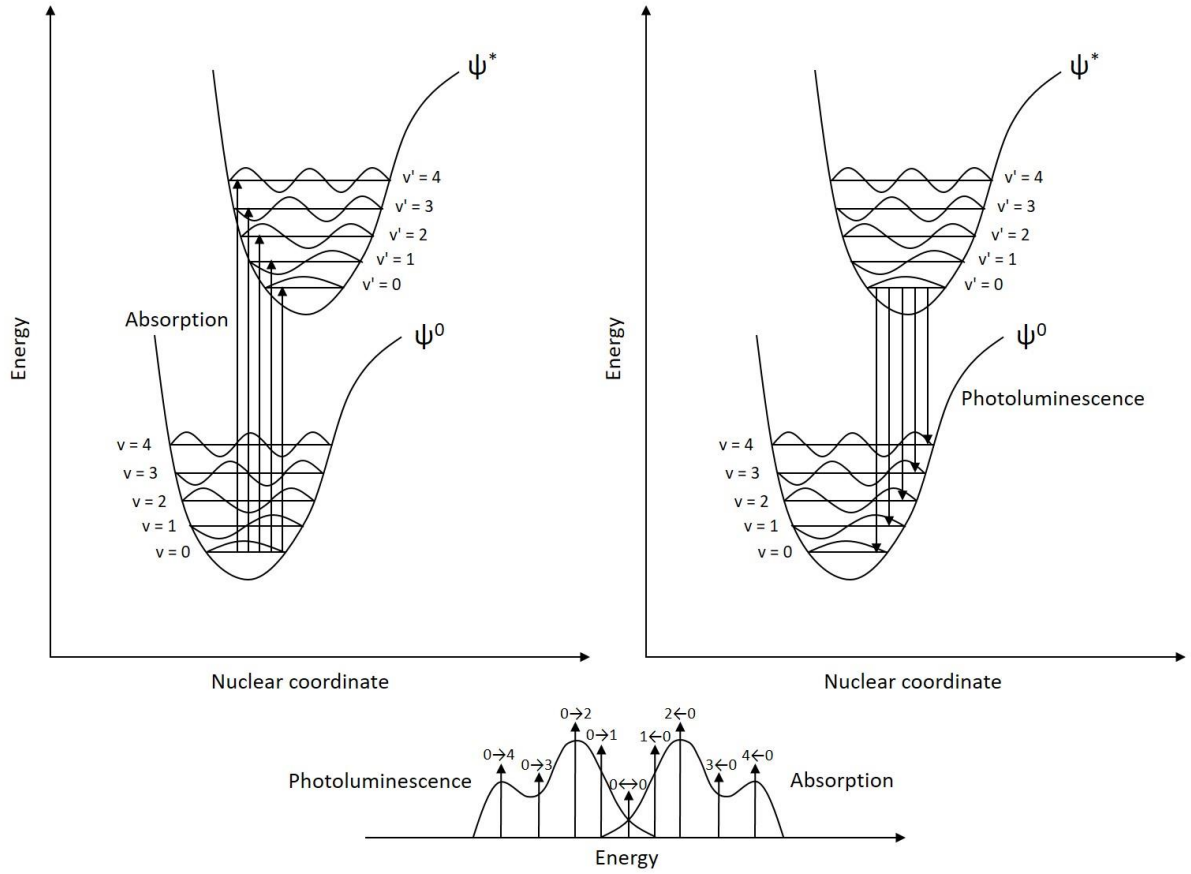

Figure 2-6. Schematic representation of absorption and photoluminescence with potential wells and vibrational wave functions.

The schematic illustration of PL and absorption is depicted in Figure 2-5. However, the spectra of both PL and absorption in organic semiconductors have fine structures with vibrational wavefunctions based on the Franck-Condon principle that governs the intensity of vibronic transitions.[67,68] The transition from the ground state to the excited state includes the changes in both electronic and vibrational energy levels, and the transition to a new vibrational energy level is compatible with the position and momentum of the nuclei in a molecule. Therefore, the excited state upon absorption of light results in the shift of the equilibrium position. Figure 2-6 displays the schematic

diagram of absorption and PL mechanisms to which the Franck-Condon principle is applied. According to the principle, the intensity of a vibronic transition in a molecule is proportional to the square of the overlap of the vibrational wavefunctions of the original and final state.[67,68]

In general, the absorbance of a material (A) is defined by

$$A = -\log_{10} T = \log_{10} \frac{I_s}{I_0} \tag{2-5}$$

where T is transmittance, I_0 and I_s are the intensity of the light before and after passing through the material,

For a non-scattering and uniform medium, the absorbance is linear to the optical path length (l), expressed as

$$A = \alpha l \tag{2-6}$$

where α is the absorption coefficient.

For a homogenous medium, such as a solution, the absorbance after propagating through the medium is proportional to the concentration of a solute and path length (Beer-Lambert law), expressed by

$$A = \varepsilon c l \tag{2-7}$$

where ε is the molar absorption coefficient, c is the molar concentration, and l is the optical path length.

2.1.3 Electroluminescence

Electroluminescence (EL) is the light emission from electrically formed excitons in semiconducting materials. Based on this mechanism, EL devices, that is, light-emitting diodes (LEDs), can be fabricated by utilising either inorganic or organic semiconductors. Here, EL devices exploiting organic semiconductors, which are termed organic light-emitting diodes (OLEDs), are explored.

The basic structure of the OLEDs is depicted in Figure 2-7. It generally consists of multiple layers, including an anode, a hole injection layer (HIL), a hole transporting layer (HTL), an emitting layer (EML), an electron transporting layer (ETL), an electron injection layer (EIL), and a cathode to optimise EL performance in devices. Given that the electric field is applied to the device, electrons and holes are transported from the cathode and the anode, respectively, to the EML. Afterwards, they recombine to form

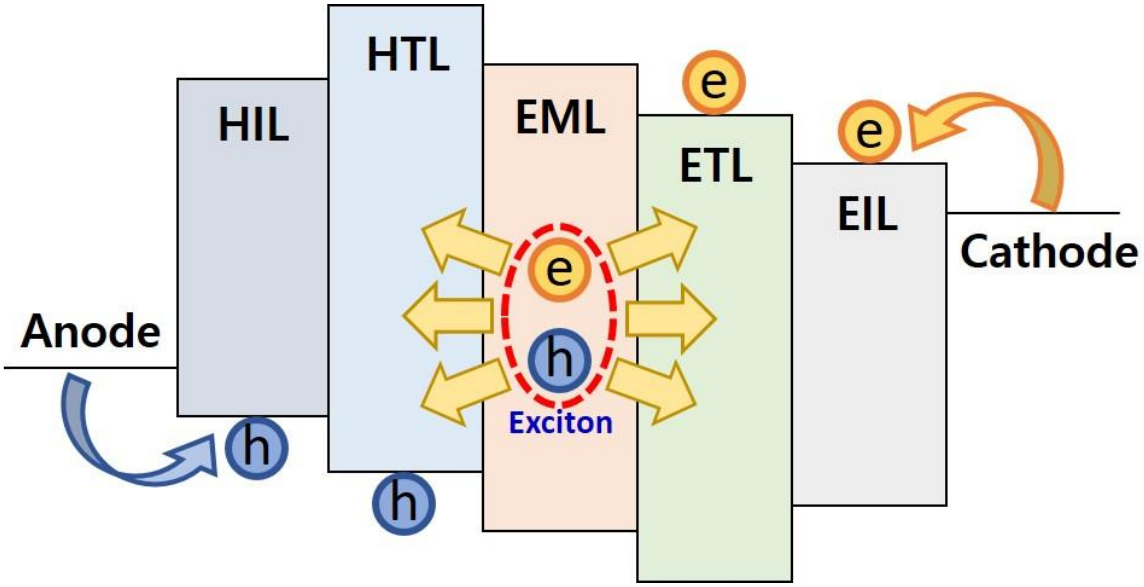

Figure 2-7. Schematic diagram of the OLED structure.

excitons and emit light.

Indium tin oxide (ITO) is commonly utilised as an anode since it provides a very low sheet resistance with high transmittance for visible light, and aluminium (Al) is typically used for the cathode. For better hole and electron injection, additional thin layers are applied between HTL and anode and ETL and cathode. Lithium fluoride (LIF) is generally used as an EIL with a thickness of ~1 nm to improve electron injection and protect organic layers from chemical reactions with the cathode.[4,69] One of the most commonly used HIL materials is 1,4,5,8,9,11-hexaazatri phenylene hexacarbonitrile (HATCN).[70,71] It was proved that the distinctively low energy levels of HATCN (LUMO: -5.5 eV and HOMO: -9.5 eV) provide effective hole injection for high device performance.[70–75] Furthermore, for the better hole and electron injection, p-doping and n-doping materials are applied to HIL and EIL layers, leading to substantially

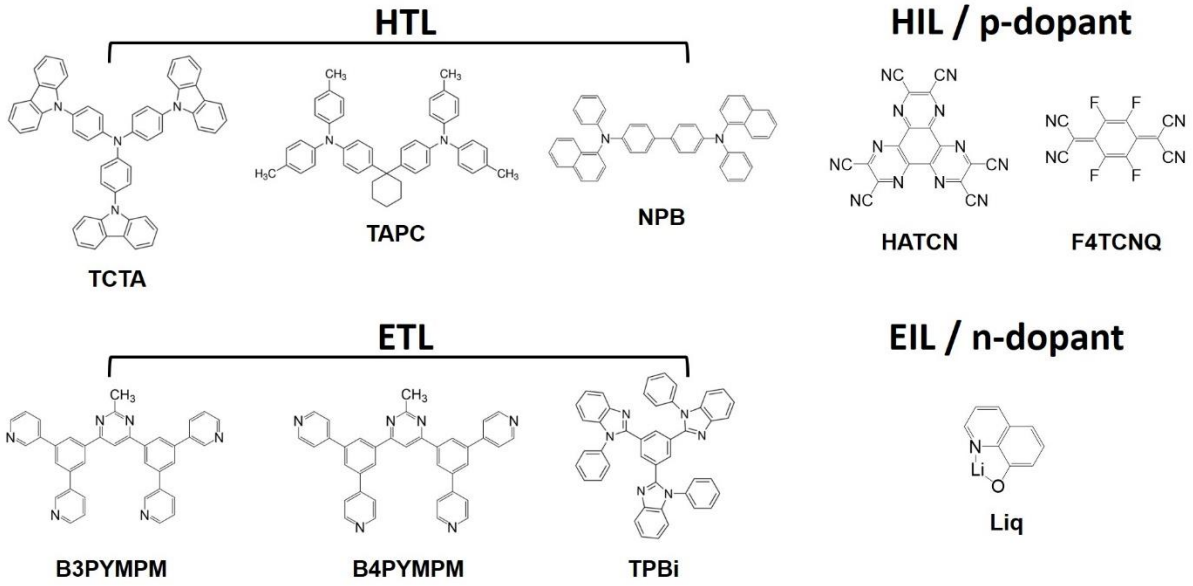

Figure 2-8. Chemical structures of the typical charge transporting materials widely utilised in OLEDs.

reduced turn-on and driving voltage of EL devices.[69,76] HTL materials include electron-donating moieties, such as amino groups, to provide sufficient hole injection from an anode, while ETL materials incorporate electron-withdrawing moieties, such as nitrile and heterocyclic ring, to promote electron injection from a cathode.[69,77] Also, additional layers between EML and ETL or/and HTL and EML are employed to block hole or/and electron leakage from EML to HTL or/and ETL to enhance efficiency further, and the layers are called hole and electron blocking layers (HBL and EBL), respectively.[4,69] However, they may cause charge accumulations leading to low device stability.[4,78,79]

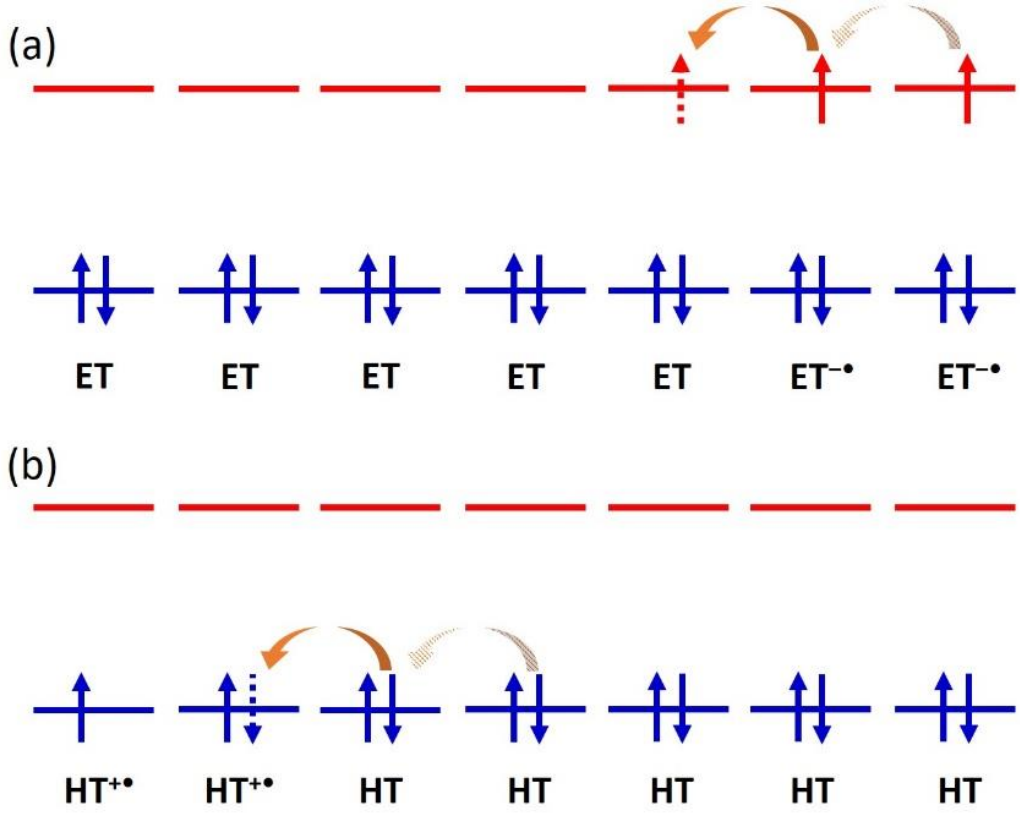

Figure 2-9. Schematic diagram of (a) electron and (b) hole transport based on the hopping model.

Figure 2-8 shows the chemical structures of the typical charge transporting materials commonly utilised in academia.[21,69,76,80]

The transport of charge carriers (electron and hole) in organic layers in OLEDs is interpreted based on the hopping model.[4,69,77] Figure 2-9 shows the schematic diagram of the charge transport process based on the hopping model. Radical anions and cations are generated from a cathode and an anode by chemical reduction and oxidation driven by an electric field.[69,77] Then, electrons hop to adjacent molecules with chemical oxidation and reduction as the anions and cations interact with neighbouring molecules. The consequent electron current in OLEDs results from these processes. Here, a hole is a model particle as a result of electron removal from the HOMO in neutral organic molecules.[4,69] As one electron in the HOMO is extracted and transported to an adjacent molecule by the hopping process, the empty electron position can be populated by another electron from the HOMO of a neighbouring molecule, and subsequently, this positive charge can move between molecules, called a hole.[4,69]

When the charge carriers arrive at an EML, they can recombine and form excitons for emitting light. The EML usually consists of host and dopant; more precisely, dopant molecules are dispersed in a host matrix, and host materials should have higher energy than dopant materials for effective energy transfer and charge recombination on dopant molecules. Excitons can be formed on host molecules and transferred to dopant molecules via energy transfer processes. Also, they can be directly formed on dopant molecules, typically when holes and electrons can be easily trapped on dopant sites due to the large HOMO and LUMO energy level difference between host and dopant. When they are located far away from each other, they act independently and are not bound. However, they can be bound when they are close enough within the critical distance (R_c), which can be extracted from the Coulomb potential energy (ΔE_{e-h}) expressed by[4]

$$\Delta \mathrm{E}_{e-h} = \frac{e^2}{4\pi\varepsilon_0\varepsilon R_c} = k_\mathrm{B}T \tag{2-8}$$

where e is the electron charge, ε_0 and ε are the dielectric constants of the vacuum and the host material, k_B is the Boltzmann constant (8.617×10^{-5} eV·K^{-1}), and T is the absolute temperature. Assuming $\varepsilon = 3$, R_c is ~18 nm at $300K$, meaning that they can be bound even though they are quite distant in the EML, but they can be easily separated by thermal energy at this distance.[4] From the weakly bound state, they become closer and meet at the same molecule (Frenkel exciton) or adjacent molecules (charge-transfer exciton) to form excitons by the Coulomb energy. They can have either singlet and triplet (typical organic semiconductors) or doublet spin states (organic radicals) in OLEDs, as studied in Section 2.1.1. They can have various emission mechanisms depending on the types of emitting materials. Section 2.2 will cover them more in detail.

2.1.4 Exciton energy transfer

In the donor-acceptor system, excitons formed on donor molecules can migrate to acceptor molecules via non-radiative energy transfer processes with intermolecular interaction between donor and acceptor.[60,61] FRET and DET are the two dominant mechanisms governing exciton energy transfer from donor to acceptor molecules in most organic materials.[60,61] Figure 2.10 exhibits the schematic diagram of FRET and DET. They can occur if the emission spectrum of the donor and the absorption spectrum of the acceptor are overlapped so that several vibronic transitions in the donor can correspond to those in the acceptor.[61] They have different interaction mechanisms: FRET is induced by near-field dipole-dipole interactions, and intermolecular orbital overlap enables DET.

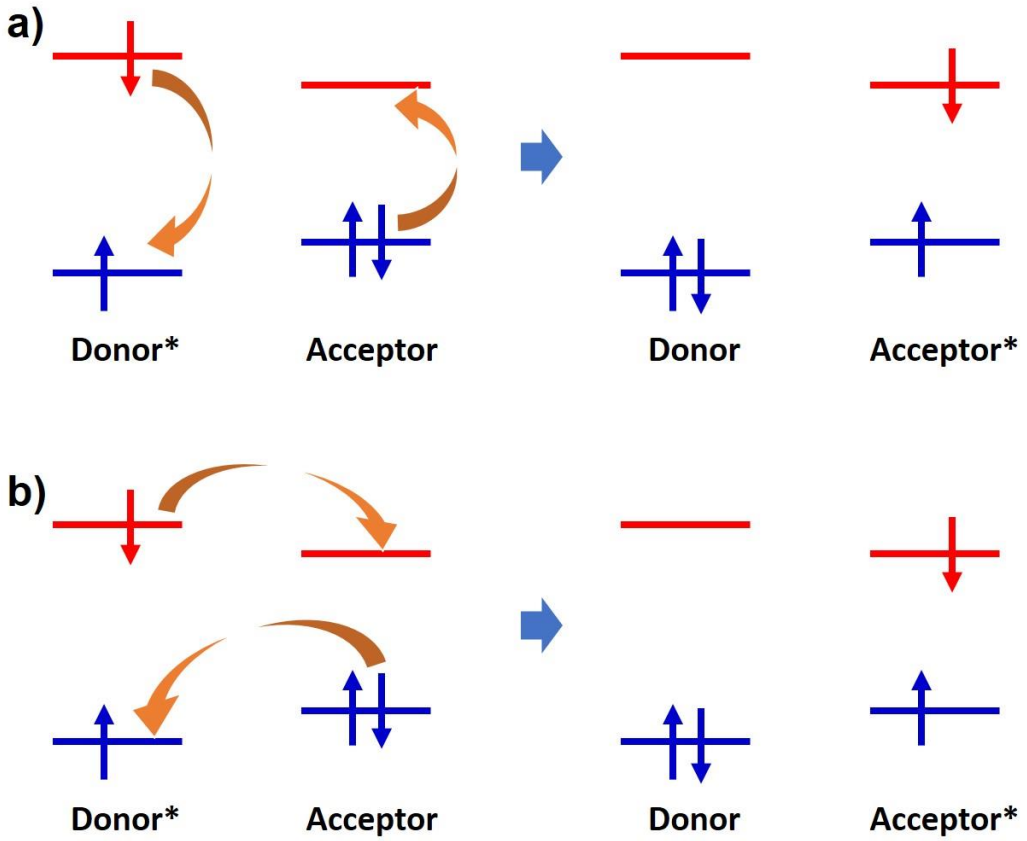

Figure 2-10. Schematic illustration of exciton energy transfer. (a) Förster resonance energy transfer (FRET). (b) Dexter energy transfer (DET).

As described above, FRET is on the basis of resonant dipole coupling, and singlet excitons are transferred by this mechanism. The rate of FRET (k_{FRET}) and the Förster radius (R_0) are expressed as[61,81–84]

$$k_{\mathrm{FRET}} = \frac{1}{\tau_{\mathrm{D}}}\left(\frac{R_0}{d}\right)^6 = k_{\mathrm{D}}\left(\frac{R_0}{d}\right)^6 \tag{2-9}$$

$$R_0^6 = \frac{9000 \ln 10 \eta_D \kappa^2}{128\pi^5 N_A n^4} \int \lambda^4 F_{\mathrm{D}}(\lambda)\epsilon_{\mathrm{A}}(\lambda)d\lambda \tag{2-10}$$

where N_{A} is Avogadro's number, n is the refractive index, η_{D} is the photoluminescence quantum efficiency (PLQE) of the donor, κ is the dipole orientation factor, λ is the

wavelength, F_D is the PL spectrum of the donor normalised to unity, ϵ_A is the molar decadic absorption coefficient of the acceptor, *d* is the intermolecular distance between the donor and acceptor, τ_D and k_D are the exciton lifetime and decay rate of the donor. From Equation 2-9, R_0 is the critical distance when $k_{FRET} = k_D$, and it is generally 3~7 nm if there is sufficient spectral overlap, which is much longer than the intermolecular distance, ~1 nm or less.[82–84]

The FRET efficiency (Φ_{FRET}) can be defined by[61]

$$\Phi_{FRET} = \frac{k_{FRET}}{k_D + k_{FRET}} \tag{2-11}$$

Using Equation 2-9, Equation 2-11 can be expressed by

$$\Phi_{FRET} = \frac{1}{\left(\frac{d}{R_0}\right)^6 + 1} \tag{2-12}$$

From Equation 2-12, Φ_{FRET} becomes 50% when d = R_0. Hence, it is described that R_0 is the distance that 50% of singlet excited states of donors can be transferred to those of acceptors via FRET.[61]

On the other hand, DET is based on the electron exchange mechanism by the donor-acceptor orbital overlap and occurs within the intermolecular distance (~1 nm). Thus, it is a shorter-range process compared to FRET. According to Dexter's theory, the rate of DET (k_{DET}) is defined as[61,82–85]

$$k_{DET} = KJ' \exp\left(\frac{-2d}{L}\right) \tag{2-13}$$

where *K* is related to the specific orbital interactions, J' is the normalised spectral overlap integral of the emission and absorption for the donor and acceptor ($J' = \int F_D(\lambda)\epsilon_A(\lambda)d\lambda$ where $\int F_D(\lambda)d\lambda = 1$ and $\int \epsilon_A(\lambda)d\lambda = 1$) and *L* is the van der

Waals radius of the donor and acceptor. As K is not related to any spectroscopic data, it is difficult to quantify k_{DET} experimentally.[61] The important point assumed in this equation is that the electronic distributions of the donor and acceptor molecules decrease exponentially in the radial direction, and k_{DET} is not dependent on the magnitude of the absorption coefficient of the acceptor.[82–85] Whereas singlet-singlet energy transfer is involved in both dipole-dipole interaction and orbital overlap, triplet-triplet energy transfer is due only to orbital overlap as it includes forbidden transitions ($T_1 \rightarrow S_0$ for the donor and $S_0 \rightarrow T_1$ for the acceptor).[61] To be specific, the Coulomb interaction is dominant even at short distances for spin-allowed transitions, whilst it is negligible for the forbidden transitions, stimulated only at around intermolecular spacing (~1 nm) due to the fact that the orbital overlap is necessary.[61] Therefore, as DET is the exchange of electrons between nearby molecules, this theory applies to triplet-triplet energy transfer.[60,61]

2.1.5 Intersystem crossing

Intersystem crossing (ISC) is a non-radiative transition between two isoenergetic vibronic levels belonging to electronic states of different spin multiplicities.[60,61] Thus, ISC is the transition between singlet and triplet spin states. For instance, excitons in the 0 vibronic level of the S_1 state can move to the isoenergetic vibronic level of the T_n state. Here, the $S_n \rightarrow T_n$ transition is generally called ISC, and reverse ISC (RISC) means the $T_n \rightarrow S_n$ transition. However, as described above, the transition between the different spin states is forbidden, but it is allowed with strong SOC.[4,60,61] For example, phosphorescent emitters incorporated with iridium or platinum enable ISC due to strong SOC induced by the heavy atom.[4] Thus, highly efficient triplet emission can be achieved, leading to a dramatic enhancement in OLED device performance.[2–4] The emission mechanism of phosphorescence is described in Section 2.2.2.

In general, most typical organic semiconductors based on aromatic hydrocarbons can not experience ISC (or RISC) due to the relatively large energy gap difference between S_1 and T_1. However, even without such heavy metal atoms, ISC can be activated in pure organic semiconductors when the energy level difference between S_1 and T_1 is pretty small, typically < 0.1 eV. Therefore, as non-radiative triplet excitons are converted to highly emissive singlet excitons via RISC, all excitons formed in EL devices can contribute to luminance. Accordingly, the IQE of 100% can be attained, and this mechanism is termed thermally activated delayed fluorescence (TADF) as the RISC process is endothermic and thermally activated.[15,16,60,61] The detailed mechanism of TADF is explored more in Section 2.2.3.

2.2 Emission mechanisms of OLEDs

2.2.1 Fluorescence

Fluorescence is the light emission from materials with the relaxation of excitons, which is normally induced by the absorption of light or electric field.[60,61] As studied in Section 2.1.1, fluorescence occurs between the same spin states (spin-allowed process), and as most organic semiconductors have a singlet ground state (S_0), it is generally considered as singlet emission from a singlet excited state (S_1). Figure 2-11 shows the schematic diagram of the fluorescence emission mechanism when excitons are generated under an electric field in OLEDs (Figure 2-7). Electrically generated excitons can have singlet and triplet spin states with the ratio of 1:3 based on the spin multiplicity and spin-statistics.[60,61,86,87] While singlet excitons are capable of emitting light, the radiative decay between T_1 and S_0 is spin-forbidden, limiting the IQE to only 25% in

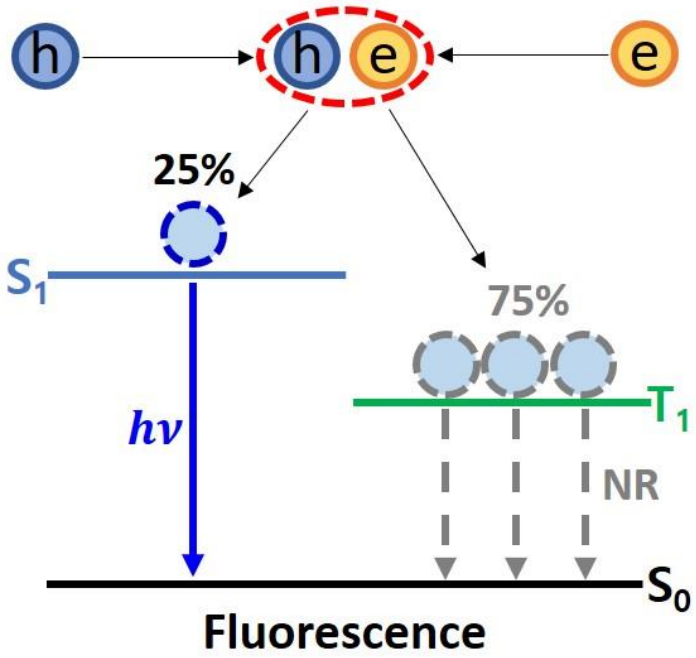

Figure 2-11. Schematic illustration of the fluorescence emission mechanism.

conventional fluorescent OLEDs.

One of the most important parameters in OLEDs is an EL EQE, which is a ratio of outcoupled photons to generated excitons, can be expressed as[88–90]

$$\mathrm{EQE} = \eta_{\mathrm{out}}\mathrm{IQE} = \eta_{\mathrm{out}}\eta_r\Phi_{\mathrm{PL}}\gamma \tag{2-14}$$

where η_{out} is the optical outcoupling efficiency, η_r is the fraction of the singlet exciton generation in charge recombination, Φ_{PL} is the value of PLQE, and γ is the charge balance factor. Even though Φ_{PL} and γ can be unity, assuming that the optical outcoupling efficiency (η_{out}) is 0.2~0.3, the EQE is limited to just 5~7.5 % in conventional fluorescent OLEDs as η_r is 0.25.

However, higher than 25% IQE with higher than 10% EQE in many fluorescent OLEDs has been reported based on additional singlet generation by utilising the

collision of two triplet excitons, termed triplet-triplet annihilation (TTA) (or triplet-triplet fusion (TTF)).[88–95] Figure 2-12(a) shows the schematic diagram of fluorescent OLEDs utilising the TTA process. In conventional fluorescent OLEDs, triplet densities are much higher than singlet densities due to the three times higher exciton generation as well as the much longer exciton lifetime of triplets (~microseconds) than singlets (~nanoseconds). As mentioned above, light is emitted only from the initially generated singlet excitons of 25% with nanosecond decay lifetime, and due to far slower radiative decay, non-radiative decay is dominant for triplets. However, if additional singlet excitons are generated by TTA, more excitons are able to participate in an emission process, leading to exceeding the IQE limit of 25%. This mechanism is usually examined by transient EL, as shown in Figure 2-12(b). With initial prompt emission by initially formed singlet excitons, delayed fluorescence is recorded with microsecond decay lifetime resulting from additionally generated singlet excitons by TTA.[88–94]

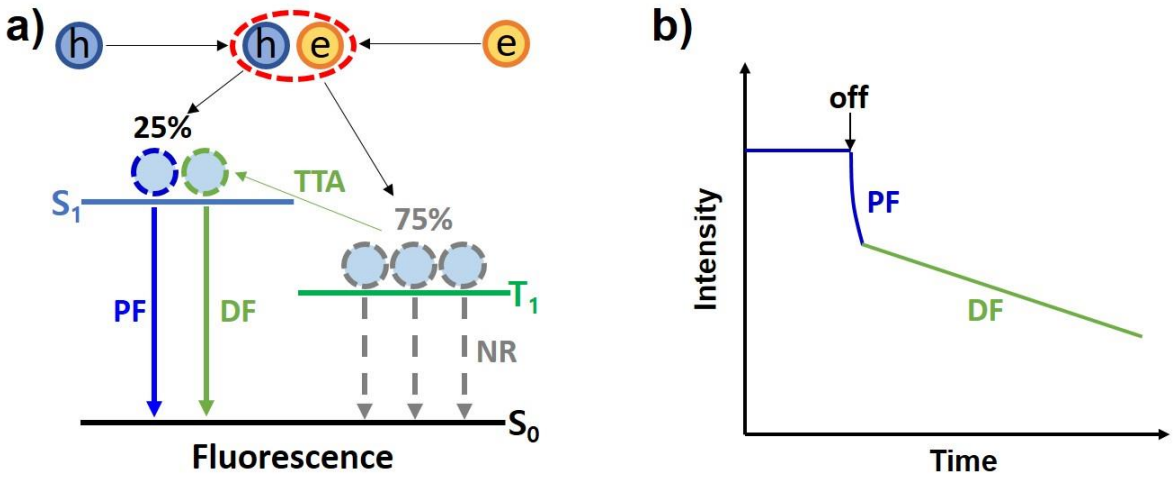

Figure 2-12. (a) Schematic illustration of the efficiency enhancement mechanism in fluorescence exploiting the TTA process. (b) Schematic representation of the typical transient EL profile observed in fluorescence OLEDs with the TTA process.

In principle, the collision of the two triplet excitons gives rise to nine configurations of the intermediate spin states, singlet ($S = 0$), triplet ($S = 1$), and quintet ($S = 2$), expressed as[88,90,96–98]

$$^3A^* + {}^3A^* \rightarrow 1/9\ {}^1(AA)^* \rightarrow {}^1A^* + {}^1A_0 \text{ (Singlet channel)} \quad (2\text{-}15)$$

$$^3A^* + {}^3A^* \rightarrow 3/9\ {}^3(AA)^* \rightarrow {}^3A^* + {}^1A_0 \text{ (Triplet channel)} \quad (2\text{-}16)$$

$$^3A^* + {}^3A^* \rightarrow 5/9\ {}^5(AA)^* \rightarrow {}^3A^* + {}^1A_0 \text{ or } {}^3A^* + {}^3A^* \text{ (Quintet channel)} \quad (2\text{-}17)$$

where $^1A_0$ is the ground singlet state, $^1A^*$ and $^3A^*$ are the excited singlet and triplet states, and $^1(AA)^*$, $^3(AA)^*$, and $^5(AA)^*$ are the intermediate states of singlet, triplet, and quintet exciton pairs.

In general, the energy of quintet states is expected to be higher than the two triplets, and with the condition of $E(S_1) \leq 2E(T_1) < E(T_2)$, the loss channel by the high lying triplet ($E(T_2)$) or quintet states can be excluded.[93,94] Thus, it is anticipated that the faction of singlet generation via one TTA event (f) is 25%. Then, the maximum fraction of the series of TTA processes (f_{TTA}) is given by[93,94]

$$f_{TTA} = \sum_{k=0}^{n=\infty} \left(\frac{1-f}{2}\right)^n = f\frac{1-f}{1+f} \quad (2\text{-}18)$$

Accordingly, f_{TTA} can be calculated to be 15%, and with the initial singlet generation proportion of 25%, the theoretical maximum IQE can be 40% in TTA-based fluorescent OLEDs. In this case, the fraction of delayed fluorescence is 37.5% (15% / (15% + 25%)). Furthermore, higher efficiency can be achieved if only singlet exciton generation is allowed by the TTA event when the energy level alignment is such that $E(S_1) \geq 2E(T_1)$.[93] In this case, f_{TTA} can be defined as[93,94]

$$f_{TTA} = \frac{1-f}{2} \quad (2\text{-}19)$$

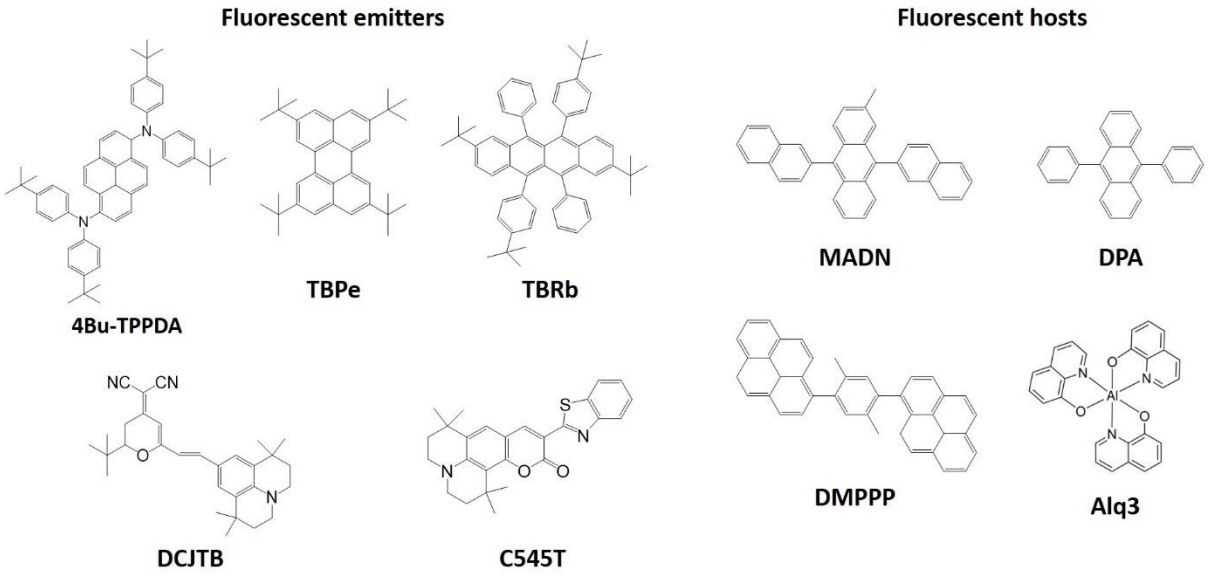

Figure 2-13. Typical fluorescent emitters and hosts commonly used in fluorescent OLEDs.

Hence, the maximum IQE of 62.5% could be obtained theoretically as the fraction of the additional singlet excitons by the TTA process is 37.5% based on Equation 2-19. Figure 2-13 shows typical fluorescent emitters and hosts commonly applied in fluorescent OLEDs.[69,99–102]

2.2.2 Phosphorescence

Phosphorescence is the form of light emission from materials by the radiative transition between different spin states, from excited triplet states to ground singlet states, unlike fluorescence which occurs by the relaxation between the same excited and ground spin states.[4,60] In general, the typical PL process (fluorescence) occurs on a nanosecond timescale as the spin states are conserved before and after light emission.

In contrast, as the transition between triplet and singlet states is spin-forbidden, the triplet emission is not generally observed from typical organic materials at room temperature. However, it was demonstrated that organo-transition metal complexes, especially incorporating iridium or platinum, can show very efficient phosphorescence with microsecond decay lifetimes.[2–4]

Figure 2-14 shows the schematic illustration for the emission mechanism of phosphorescence when excitons are electrically generated. The heavy metal complexes allow the singlet excited states of 25% to be converted to triplet excited states by fast ISC (order of 10^{12} to 10^{13}) due to a strong SOC effect, and the same SOC effect renders triplet excitons luminescent in such complexes.[4] Therefore, 100% of the excitons enable participation in the emission process exceeding the efficiency limit of fluorescence by a factor of four. Figure 2-15 shows typical iridium and platinum complexes showing high efficiency.[4,11,103,104]

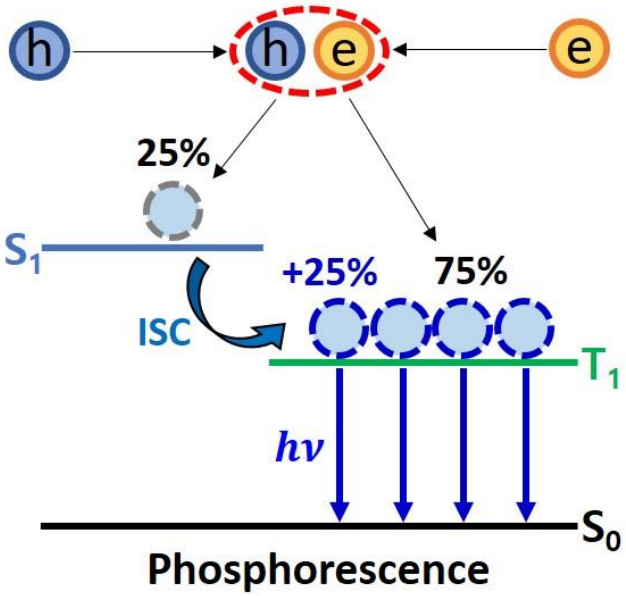

Figure 2-14. Schematic illustration of the phosphorescence emission mechanism.

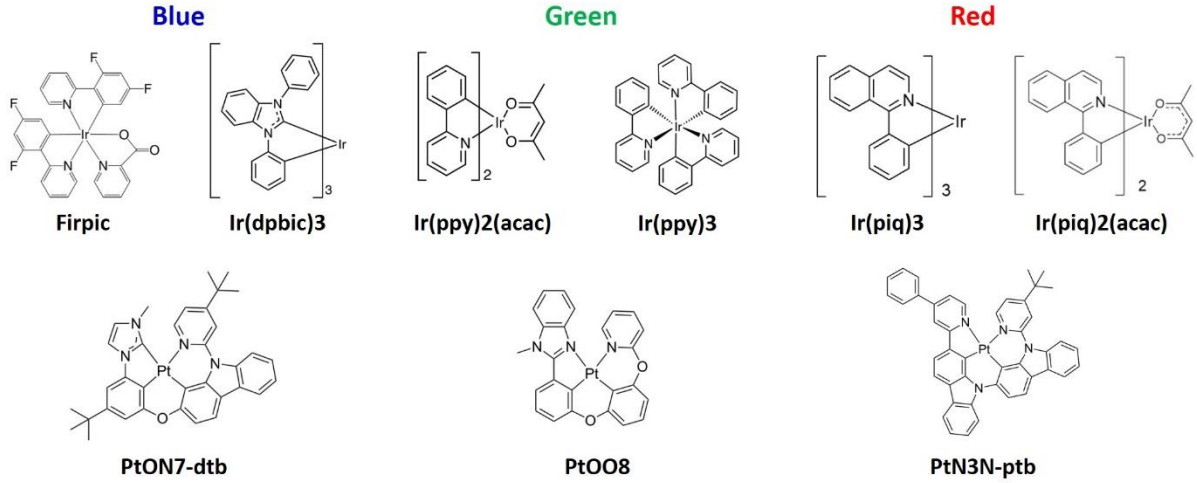

Figure 2-15. Examples of typical iridium- and platinum-based phosphorescent emitters.

2.2.3 Thermally activated delayed fluorescence

In 2011, TADF was proposed as a promising method to harvest triplet excitons from pure organic molecules.[15] Through TADF, a maximum EQE of around 20%, comparable to that of phosphorescence, was attained in 2012.[16] As illustrated in Figure 2-16, a small energy gap (≤ 0.1 eV) between singlet and triplet energy levels enables spin up-conversion from non-radiative triplet excited states to radiative singlet excited states by RISC.[16] Since then, a great deal of research on TADF has been carried out to enhance efficiency and stability by applying a diverse combination of donor and acceptor moieties to TADF emitters, achieving higher than 20% EQE.[105–115] Figure 2-17 shows the chemical structures of typical TADF materials showing high efficiency.[16,109,110,112–114] However, low stability due to unstable chemical structure and broad spectra resulting from large structural distortion between ground states and excited states are the issues necessary to be solved. In 2016, new types of boron-

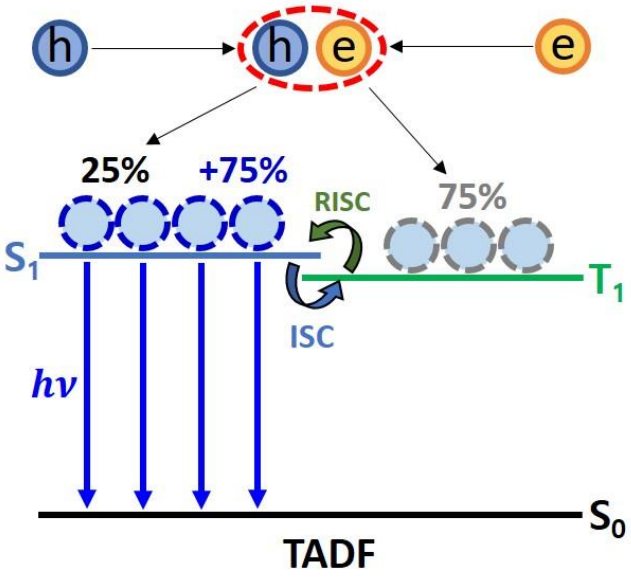

Figure 2-16. Schematic illustration of TADF emission mechanism.

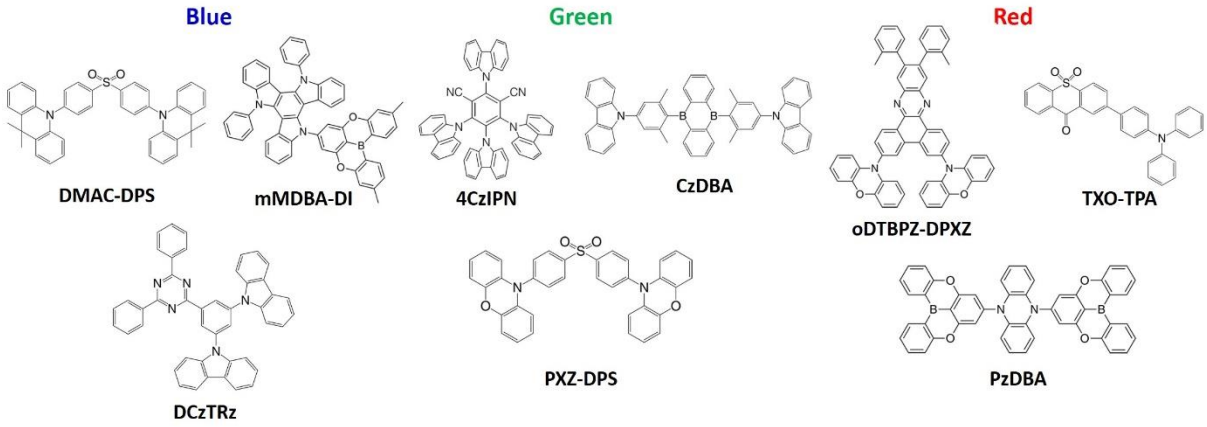

Figure 2-17. Chemical structures of typical efficient TADF materials showing high efficiency.

containing TADF materials were introduced to overcome the broad spectrum of TADF emission via minimising structural relaxation by MR effects (Figure 2-18).[17,18] However, the low device lifetime in TADF OLEDs has not been fully solved yet.

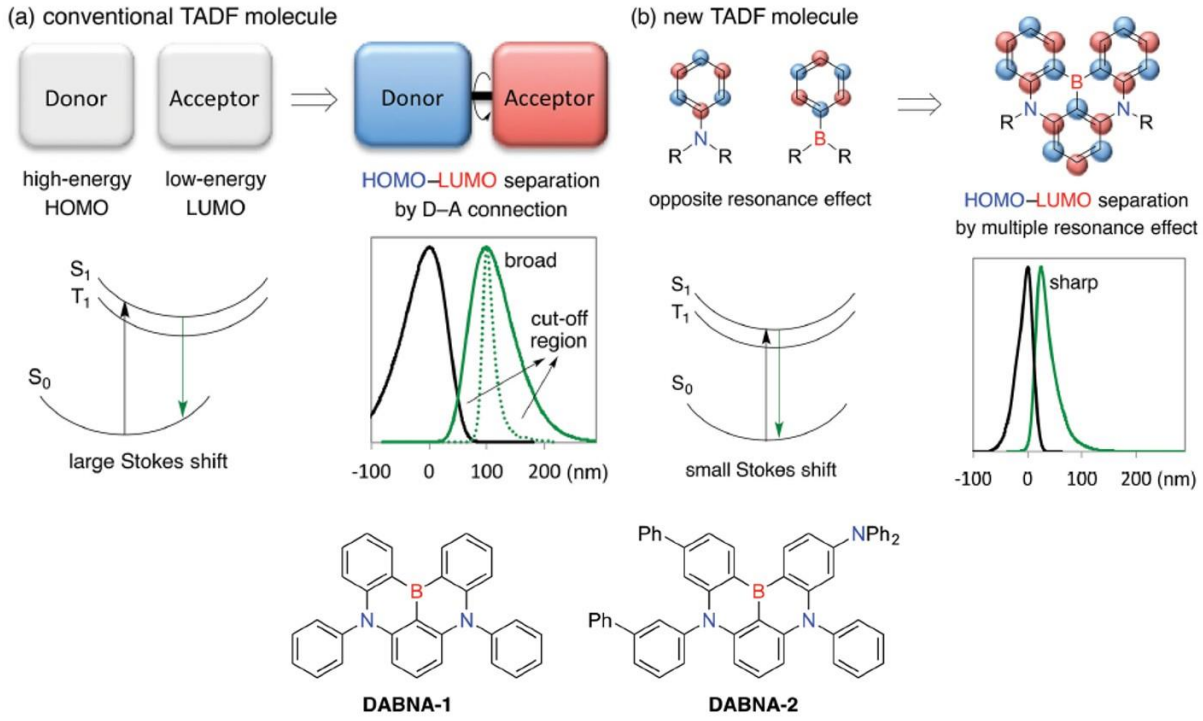

Figure 2-18. Multiple resonance (MR) effect in boron-containing TADF materials and their chemical structures. Reproduced with permission from the reference 17 (*Advanced Materials* **28**, 2777–2781 (2016). Copyright 2015 Wiley-VCH.

Theoretically, the singlet and triplet exciton densities (S and T) in TADF materials under photoexcitation are expressed by the following equations,[16,116–118]

$$\frac{dS}{dt} = -(k_{r,S} + k_{nr,S})S - k_{ISC}S + k_{RISC}T \tag{2-20}$$

$$\frac{dT}{dt} = -k_{nr,T}T - k_{RISC}T + k_{ISC}S \tag{2-21}$$

where $k_{r,S}$, $k_{nr,S}$, and $k_{nr,T}$ are the radiative and nonradiative rate constants of the singlet and the nonradiative rate constant of the triplet, and k_{ISC} and k_{RISC} are the rate constants of ISC and RISC, respectively. The solutions to Equation 2-20 and 21 can be expressed in the form of biexponential decays,

$$\mathrm{S,T} = A_1 \exp(-k_\mathrm{p} \mathrm{t}) + A_2 \exp(-k_\mathrm{d} \mathrm{t}) \tag{2-22}$$

where A_1 and A_2 are the fitting parameters of prompt and delayed components, k_p and k_d are the prompt and delayed emission decay rates, which can be described as[116–118]

$$k_\mathrm{p}, k_\mathrm{d} = \frac{k_{\mathrm{r,S}} + k_{\mathrm{nr,S}} + k_{\mathrm{ISC}} + k_{\mathrm{nr,T}} + k_{\mathrm{RISC}}}{2} \times$$

$$\left(1 \pm \sqrt{1 - \frac{4\left(k_{\mathrm{r,S}} + k_{\mathrm{nr,S}} + k_{\mathrm{ISC}}\right)\left(k_{\mathrm{nr,T}} + k_{\mathrm{RISC}}\right) - 4k_{\mathrm{ISC}}k_{\mathrm{RISC}}}{\left(k_{\mathrm{r,S}} + k_{\mathrm{nr,S}} + k_{\mathrm{ISC}} + k_{\mathrm{nr,T}} + k_{\mathrm{RISC}}\right)^2}}\right) \tag{2-23}$$

Assuming that $k_{\mathrm{r,S}}$, $k_{\mathrm{nr,S}}$, and $k_{\mathrm{ISC}} \gg k_{\mathrm{nr,T}}$ and k_{RISC}, k_p and k_d can be approximated by[116,117]

$$k_\mathrm{p} = k_{\mathrm{r,S}} + k_{\mathrm{nr,S}} + k_{\mathrm{ISC}} \tag{2-24}$$

$$k_\mathrm{d} = k_{\mathrm{nr,T}} + \left(1 - \frac{k_{\mathrm{r,S}}}{k_{\mathrm{r,S}} + k_{\mathrm{nr,S}} + k_{\mathrm{ISC}}}\right) k_{\mathrm{RISC}} \tag{2-25}$$

The PLQEs of the prompt and delayed emission (Φ_p and Φ_d) are given by

$$\Phi_\mathrm{p} = \frac{k_{\mathrm{r,S}}}{k_{\mathrm{r,S}} + k_{\mathrm{nr,S}} + k_{\mathrm{ISC}}} = \frac{k_{\mathrm{r,S}}}{k_\mathrm{p}} \tag{2-26}$$

$$\Phi_\mathrm{d} = \sum_{k=1}^{\infty} (\Phi_{\mathrm{ISC}} \Phi_{\mathrm{RISC}})^k \Phi_\mathrm{p} = \frac{\Phi_{\mathrm{ISC}} \Phi_{\mathrm{RISC}}}{1 - \Phi_{\mathrm{ISC}} \Phi_{\mathrm{RISC}}} \Phi_\mathrm{p} \tag{2-27}$$

where Φ_{ISC} and Φ_{RISC} are the efficiencies of ISC and RISC, described as

$$\Phi_{\mathrm{ISC}} = \frac{k_{\mathrm{ISC}}}{k_{\mathrm{r,S}} + k_{\mathrm{nr,S}} + k_{\mathrm{ISC}}} = \frac{k_{\mathrm{ISC}}}{k_\mathrm{p}} \tag{2-28}$$

$$\Phi_{\mathrm{RISC}} = \frac{k_{\mathrm{RISC}}}{k_{\mathrm{RISC}} + k_{\mathrm{nr,T}}} \tag{2-29}$$

Also, as the total PLQE (Φ_{total}) can be divided by Φ_p and Φ_d, Φ_{total}, Φ_p, and Φ_d are expressed by[119]

$$\Phi_{\text{total}} = \Phi_{\text{p}} + \Phi_{\text{d}} \tag{2-30}$$

$$\Phi_{\text{p}} = r_1 \Phi_{\text{total}} \tag{2-31}$$

$$\Phi_{\text{d}} = r_2 \Phi_{\text{total}} \tag{2-32}$$

$$r_1 = \frac{A_1 \tau_{\text{p}}}{A_1 \tau_{\text{p}} + A_2 \tau_{\text{d}}} \tag{2-33}$$

$$r_2 = \frac{A_2 \tau_{\text{d}}}{A_1 \tau_{\text{p}} + A_2 \tau_{\text{d}}} \tag{2-34}$$

where r_1 and r_2 are the intensity ratio of the prompt and delayed emission, τ_{p} and τ_{d} are the decay lifetime constants of the prompt and delayed emission, A_1 and A_2 are the fitting parameters of the biexponential fit ($A_1 e^{-t/\tau_{\text{p}}} + A_2 e^{-t/\tau_{\text{d}}}$) for the transient PL curve, respectively. These values are determined experimentally from the fitting of the transient PL profile. Accordingly, k_{p} and k_{d} are extracted by

$$k_{\text{p}} = \frac{\Phi_{\text{p}}}{\tau_{\text{p}}} \tag{2-35}$$

$$k_{\text{d}} = \frac{\Phi_{\text{d}}}{\tau_{\text{d}}} \tag{2-36}$$

In principle, k_{p} and k_{d} are highly affected by ISC, which is the non-radiative transition between different spin states. As $k_{\text{nr,T}}$ is significantly lower than k_{RISC} ($\Phi_{\text{RISC}} \approx 1$), k_{ISC} can be estimated by

$$k_{\text{ISC}} = \frac{\Phi_{\text{d}}}{\Phi_{\text{p}} + \Phi_{\text{d}}} k_{\text{p}} \tag{2-37}$$

Another key process in TADF is RISC. From Equation 2-24~29, k_{RISC} is given by

$$k_{\mathrm{RISC}} = \frac{k_{\mathrm{d}}\Phi_{\mathrm{RISC}}}{1-\Phi_{\mathrm{ISC}}\Phi_{\mathrm{RISC}}} = \frac{k_{\mathrm{p}}k_{\mathrm{d}}}{k_{\mathrm{ISC}}}\frac{\Phi_{\mathrm{d}}}{\Phi_{\mathrm{p}}} \quad (2\text{-}38)$$

Therefore, k_{ISC} and k_{RISC} can be extracted from Equation 2-37 and 38, respectively.

As RISC is thermally activated, delayed emission is highly suppressed at low temperature. The temperature dependence of k_{RISC} on the activation energy corresponding to a singlet-triplet energy gap (ΔE_{ST}) can be expressed by a Boltzmann distribution,[16,116]

$$k_{\mathrm{RISC}} \propto \exp\left(-\frac{\Delta E_{\mathrm{ST}}}{k_B T}\right) \quad (2\text{-}39)$$

where k_B is the Boltzmann constant (8.617×10^{-5} eV·K^{-1}), and T is the absolute temperature. Hence, k_{RISC} is increased at high temperature and small ΔE_{ST}.

2.2.4 TADF- or phosphor-sensitised fluorescence

In order to tackle the issues that TADF involves, as described in the previous section, a new way to harvest triplet excitons to attain 100% IQE was suggested in 2014,[19] which is the concept of using TADF molecules as exciton sensitisers for conventional fluorescent emitters, which is termed 'hyperfluorescence'.[20] As depicted in Figure 2-19, the triplet excited states of TADF emitters are up-converted to the singlet excited states by RISC, and they are transferred to the singlet excited states of fluorescent dyes by FRET to contribute to the fluorescent emission, so the IQE of 100% is theoretically possible while preserving the photophysical properties of a conventional fluorescent material.

Another way to harness triplet excitons for emitting light from fluorescent emitters is to utilise phosphorescent organometallic complexes as exciton sensitisers.

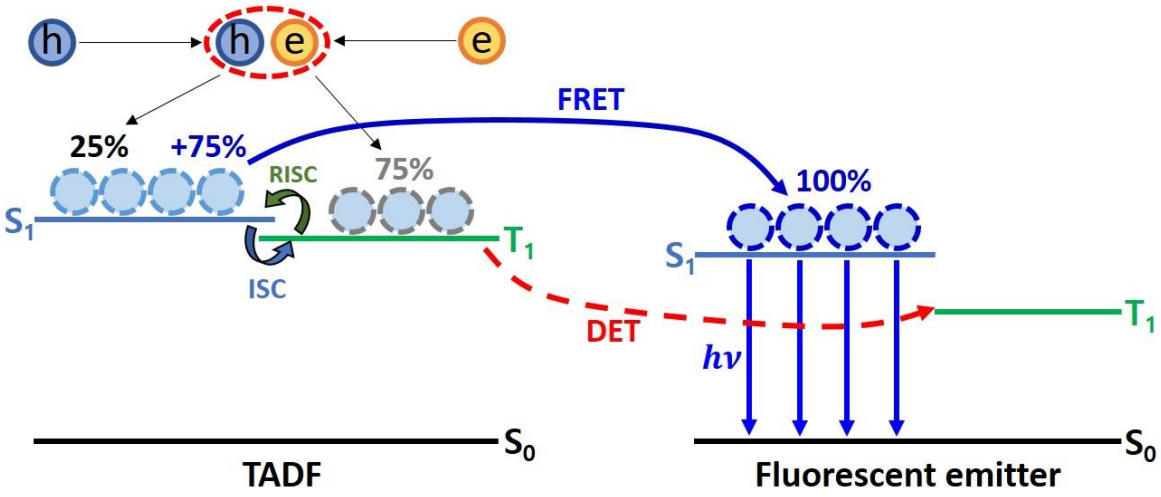

Figure 2-19. Schematic diagram for the emission mechanism of TADF-sensitised fluorescence.

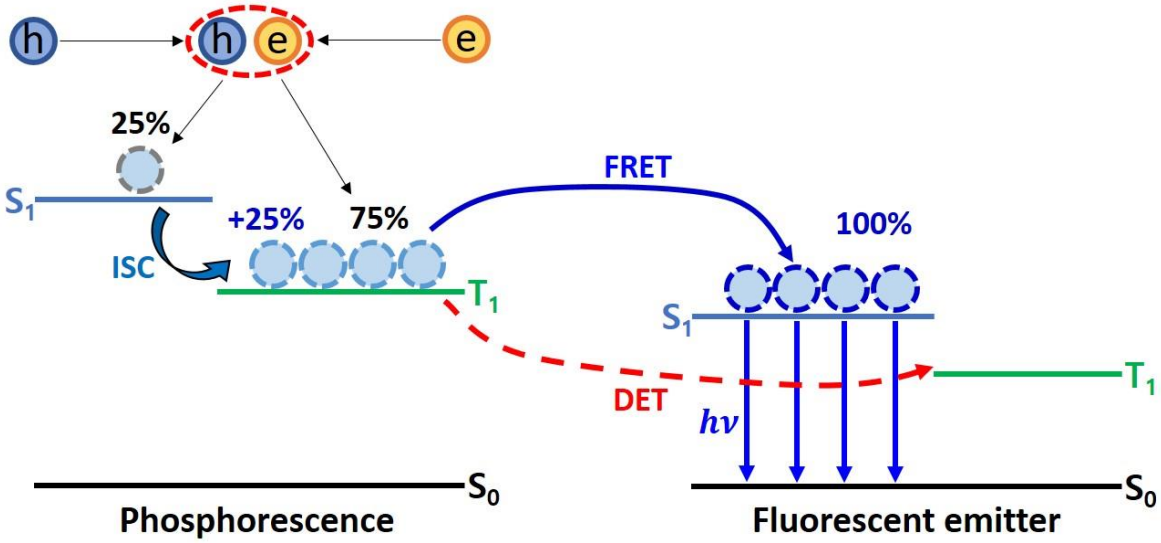

Figure 2-20. Schematic diagram for the emission mechanism of phosphor-sensitised fluorescence.

This so-called phosphor-sensitised fluorescence concept was initially suggested in 2000,[120] and recently, this has re-attracted much interest from academia since the substantial improvement of efficiency and lifetime was achieved.[100,102,121–123] Figure 2-20 is the schematic diagram of phosphor-sensitised fluorescence. FRET enables triplet excitons of phosphorescent emitters to be transferred to the singlet energy level of fluorescent dyes, leading to efficient fluorescence. There were some attempts to realise blue phosphor-sensitised fluorescence in 2018.[102,122] Even though the spectral overlap between the absorption of fluorescent dyes and the PL of phosphorescent dyes was not sufficient, higher than 10% EQE was obtained.

These types of fluorescence are up-and-coming because highly efficient fluorescent OLEDs with excellent colour purity and stability are achievable. However, some issues are preventing them from being applied to OLED products. Firstly, as well as the sensitiser donor and luminescent acceptor, wide-gap matrix molecules are typically included as a third EML component. The third component disperses donor molecules, which is typically necessary to prevent donor concentration quenching. Dilution into a host is also important for suppressing DET between donors and acceptors, which populates the non-emissive acceptor triplet state and constitutes a loss pathway. A considerable increase in driving voltage is also inevitable when a wide gap matrix is incorporated. Despite the fact that exciplex-forming hosts (mixed hosts of electron and hole transport materials) are capable of improving the driving voltage, this concept requires at least four components to be used in an EML, which adds further structural complexity to the device. Hence, hyperfluorescence has not yet been widely chosen for the mass production of OLEDs.[100,121,123] Also, the realisation of complete deep blue hyperfluorescence is reasonably limited. As sensitisers should have higher singlet and triplet energy levels than the singlet energy levels of deep blue fluorescent molecules to enable effective exciton energy transfer, the challenge becomes the design of stable and efficient sensitisers emitting deep blue or near-ultraviolet (UV) light.

However, higher than 25% EQE and high stability with narrow emission spectra were recently reported utilising this concept, showing the potential of realising efficient deep blue hyperfluorescent OLEDs.[21,22]

2.2.5 Doublet fluorescence

Another route to obtain the IQE of 100% in EL devices is to harness doublet emission. Doublet fluorescence from organic radicals has been recently much of interest due to its potential to achieve very high efficiency avoiding the efficiency limit usually related to singlet-triplet spin states in typical organic semiconductors.[39–52] One unpaired electron gives rise to a doublet spin manifold (Figure 2-4), and the ground and excited states are maintained in doublet spin states, leading to the efficient radiative $D_1 \rightarrow D_0$ transition with nanosecond exciton lifetime. Figure 2-21 shows the schematic diagram of doublet fluorescence in EL devices. All of the electrically generated doublet excitons

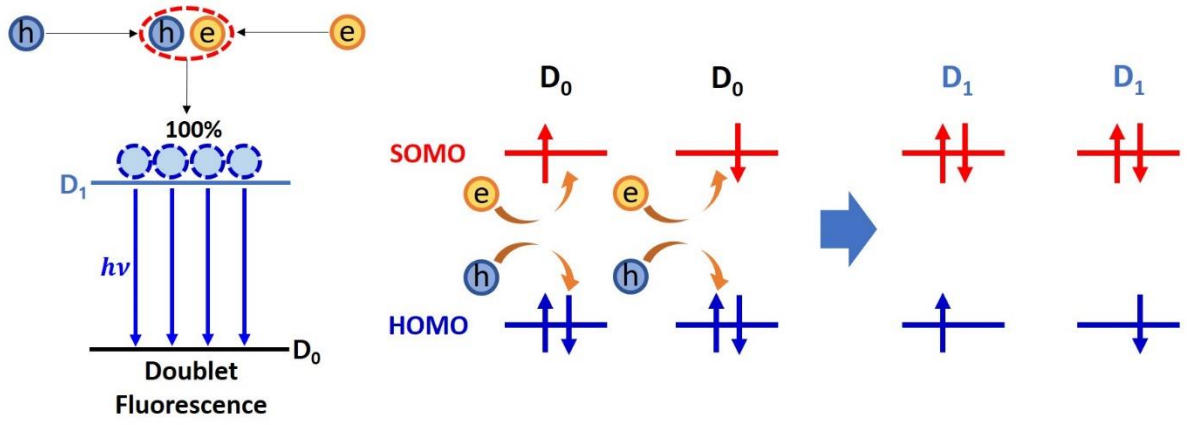

Figure 2-21. Schematic diagram for the emission mechanism of doublet fluorescence.

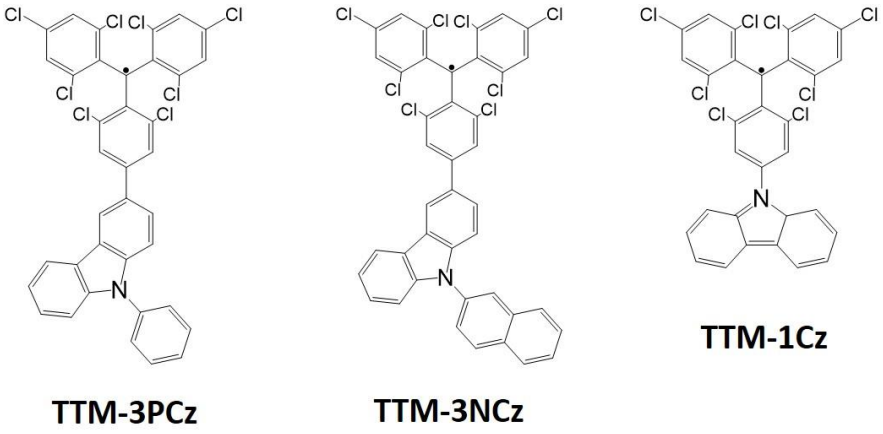

Figure 2-22. Chemical structures of TTM-based efficient organic radicals.

can be directly formed at radical sites in an EML. Therefore, a maximum IQE of 100% can be theoretically achieved. In general, as the organic radicals are dispersed in a wide bandgap host, direct charge recombination is the desired EL mechanism rather than energy transfer from the host.[50,63,64] Figure 2-22 shows some examples of efficient organic radicals based on tris-(2,4,6-trichlorophenyl)-methyl (TTM) radical.[50,51]

Chapter 3 Experimental methods

This chapter will describe various experimental methods utilised in this thesis for investigating photophysics for solutions and thin films and device physics for singlet-carrier and full devices.

3.1 Photophysics

3.1.1 Sample preparation

For making organic films, glass substrates were prepared, and they were cleaned with acetone and isopropyl alcohol with sonification for ten minutes before loading them into an evaporator (manufactured by Angstrom Engineering). Next, organic materials were loaded in alumina crucibles and were thermally evaporated on glass substrates to form amorphous films. The evaporation process was conducted in a vacuum chamber under ~10^{-7} Torr. As each organic material has different deposition properties, the evaporation process was calibrated based on the measurement of the film thickness. First, organic materials were deposited on silicon wafers, and their thickness was measured by ellipsometry (J. A. Woollam Co., Inc). Then, the new tooling factor was determined by multiplying the initial tooling factor by the ratio of the value measured by ellipsometry and the value recorded by the thickness monitor from the evaporator. For transient optical measurements, the films were encapsulated in a glove box to prevent degradation by air.

Regarding solutions, organic molecules were dissolved in solvents, such as toluene and tetrahydrofuran (THF), and quartz cuvettes with a 0.1 cm path length are used for the steady-state absorption and PL of the solutions. Micropipettes and micro scales are utilised to make solutions with accurate concentration.

3.1.2 Steady-state photoluminescence and absorption

Steady-state PL and absorption spectra provide the basic properties of organic materials to estimate how they work with other materials or in devices. Absorption spectra were measured by a Shimadzu UV-3600 Plus spectrophotometer. A blank glass substrate and a solvent-only cuvette were used for a film and a solution as a reference, respectively. Samples were scanned from 800 nm to 200 nm to obtain the absorption spectra from NIR to UV regions.

Luminescence spectra for solutions and films were obtained using an Edinburgh Instruments fluorescence spectrometer (FLS980) with a monochromated xenon arc lamp. The excitation wavelength was selected based on the absorption spectra of the testing films and solutions, and background noise was removed by subtracting the signal of the blank samples corresponding to a film and a solution mentioned above.

3.1.3 Photoluminescence quantum efficiency

Photoluminescence quantum efficiency (PLQE) is one of the most significant parameters to assess the performance of emitting materials. The PLQE (η) is formulated as[124,125]

$$\eta = \frac{number\ of\ photons\ emitted}{number\ of\ photons\ absorbed} \tag{3-1}$$

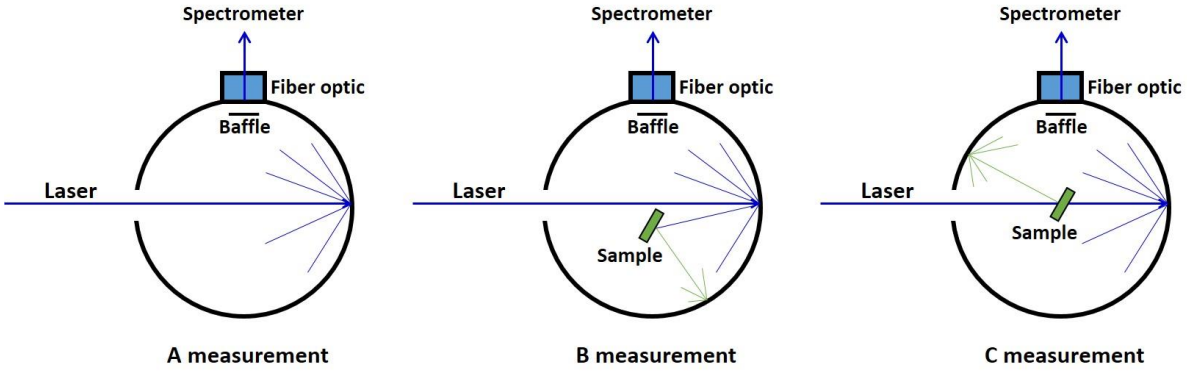

Figure 3-1. Schematic diagram of the three PLQE measurement configurations.

The most common way to measure PLQE is to utilise an integrating sphere.[124,125] There are three measurements necessary to calculate PLQE for the organic materials formed on glass or quartz substrates.[124] Figure 3-1 shows the schematic illustration of the three measurements. The laser is illuminated into the sphere without a sample in the first measurement, and the laser intensity is detected by the spectrometer.[124] For the second measurement, the sample is placed inside the sphere, and the laser is pointed onto the sphere wall, and then the third measurement is performed with the laser beam being directed onto the sample.[124] The absorption (A) and The PLQE (η) are formulated as[124]

$$A = \left(1 - \frac{L_c}{L_b}\right) \tag{3-2}$$

$$\eta = \frac{P_c - (1-A)P_b}{L_a A} \tag{3-3}$$

where L_a, L_b, and L_c are the laser intensity from the first, second, and third measurement, respectively, and P_b and P_c are the PL spectra from the second and third measurement, respectively.

PLQE measurements were conducted by the method described above using an integrating sphere with a nitrogen flow. PL spectra from a sample in an integrating sphere were recorded by an Andor spectrometer (Shamrock 303i) with an Andor iDus CCD array (Chapter 4) and an Edinburgh Instruments fluorescence spectrometer (FLS980) (Chapter 5~7). Two samples were made for each material, and their PLQE measurements were carried out twice. The PLQE values in this thesis are their average values.

3.1.4 Transient photoluminescence

Transient (or time-resolved) PL spectroscopy is a powerful method for investigating the kinetics of excitons in organic semiconductors.[126,127] Time-correlated single-photon counting (TCSPC) system (Chapter 4) and intensified charge-coupled device (ICCD) (Chapter 5~7) are the two technologies to measure transient PL employed in this thesis. TCSPC is based on the repetitive excitation of a sample by a

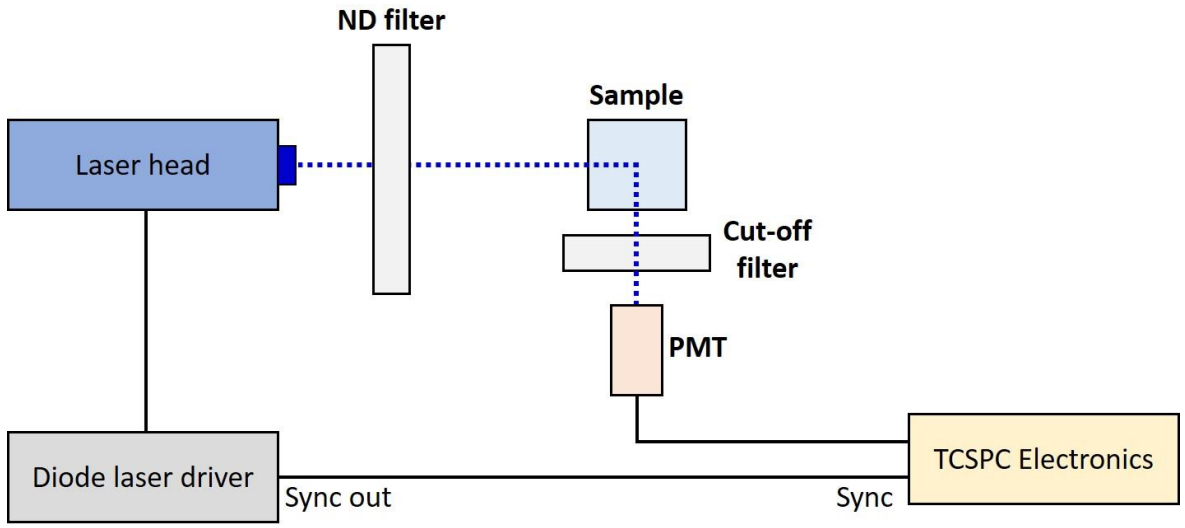

Figure 3-2. Schematic diagram of the TCSPC measurement setup.

laser pulse and the data collection over multiple cycles of excitation and emission.[128] Single photons are detected by a microchannel plate photomultiplier tube (MCP-PMT), and their arrival time and the time difference between the excitation pulse and the observed photons are recorded by TCSPC electronics (Figure 3-2).[128] They are stored in a histogram with the time (x-axis) and the number of photons is detected for the time (y-axis). In this thesis, samples were excited by a 375 nm laser (PicoQuant, LDH-P-C375B), and the signal was detected by an MCP-PMT (Hamamatsu, R3809U-50) and a TCSPC electronics (Edinburgh Instruments, Lifespec-ps and VTC900 PCI card).

On the other hand, CCD is a device that converts photons into electron charges to obtain an image, consisting of integrated electronic circuits (an array of

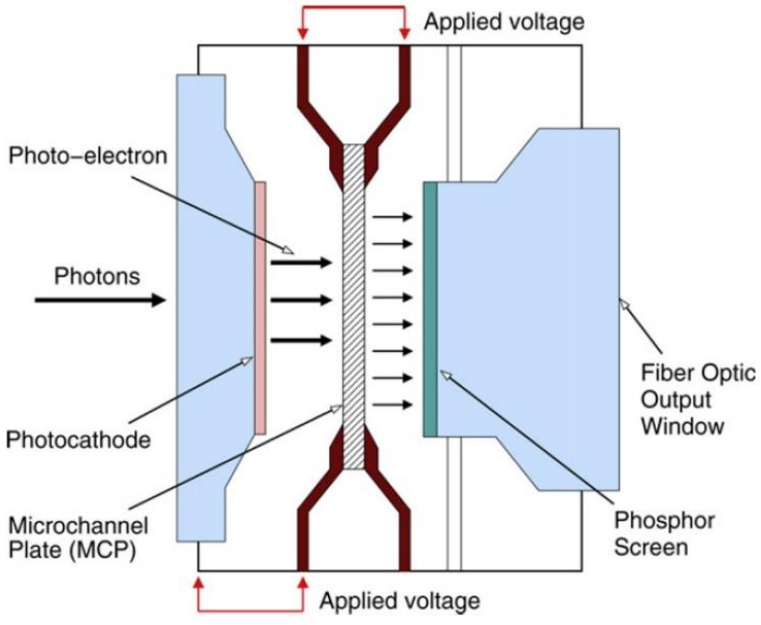

Figure 3-3. Schematic diagram of the intensifier in an ICCD camera. Reproduced with permission from the reference 131 (*Computer Methods in Applied Mechanics and Engineering* **213–216**, 383–398 (2012)). Copyright © 2011 Elsevier B.V.

photodiodes).[128,129] ICCD is a CCD on which an image intensifier is mounted to achieve high sensitivity and very fast gate time.[129–131] The intensifier consists of a photocathode, an MCP, and a phosphor screen (Figure 3-3).[129–131] Incident photons are converted into electrons as they strike a photocathode, and the photoelectrons are drawn towards the MCP by an electric field.[129–131] Then, they are multiplied inside the MCP and accelerated towards the phosphor screen, converting back into photons detected by the CCD coupled to a fibre optic.[129–131] Using ICCD, PL spectra for the different time steps can be obtained, and the decay kinetics are generally extracted by the integration of the spectra at each time. In this thesis, an Andor spectrometer setup (Andor SR303i) with an electrically gated ICCD camera (AndoriStar DH740 CCI-010) was utilised, and sample excitation was provided by a frequency-doubled 800 nm pulse from Ti:sapphire amplifier (Spectra Physics Solstice Ace, 100 fs pulses at 800 nm, 7 W output at 1 kHz).

The transient PL data provide valuable information such as the nature of the excited states, exciton energy transfer kinetics, exciton decay lifetime, and decay pathways.[126,127] The measured exciton decay lifetime (τ) is expressed with the combination of radiative and non-radiative processes modelled approximately as unimolecular decay processes, which is given by[126]

$$\tau = \frac{1}{k_{\mathrm{r}}+k_{\mathrm{nr}}} \tag{3-4}$$

where k_{r} and k_{nr} are the radiative and non-radiative decay rate constants, respectively. Furthermore, the value of PLQE is used to calculate the radiative and non-radiative decay constants in conjunction with transient PL measurements.[124] It can be determined with k_{r} and k_{nr}, which is formulated as[126]

$$\eta = \frac{k_{\mathrm{r}}}{k_{\mathrm{r}}+k_{\mathrm{nr}}} \tag{3-5}$$

Given that the effect of concentration quenching should be taken into account, the

concentration quenching rate constant (k_{CQ}) is applied to Equation 3-4 and 3-5, which are denoted as[132]

$$\tau = \frac{1}{k_r + k_{nr} + k_{CQ}} \tag{3-6}$$

$$\eta = \frac{k_r}{k_r + k_{nr} + k_{CQ}} \tag{3-7}$$

In general, τ is obtained by the exponential fitting of transient PL profiles, expressed by

$$I = A_1 e^{-t/\tau_1} + A_2 e^{-t/\tau_2} \ldots + A_n e^{-t/\tau_n} \tag{3-8}$$

where I is the PL intensity, A_n is the fitting parameter, t is the time. When the materials have one decay lifetime constant, their transient PL plots tend to be easily fitted mono exponentially ($n = 1$). However, when exciton energy transfer between two materials or spin states is considered, the transient PL profiles have more than one decay lifetime constant, so two or more exponential terms are necessary. For example, when hole transport and electron transport materials are mixed, an exciplex is formed with a narrow singlet-triplet energy gap resulting in rapid prompt emission and strong delayed emission.[117,133,134] Even from a single material, transient PL profiles can have multiple decay lifetime constants, such as TADF materials.[16]

3.1.5 Transient absorption

Transient absorption (TA) is another important technique of time-resolved spectroscopy, enabling the investigation of exciton dynamics in organic semiconductors.[135] The kinetics of singlet and triplet excited states and energy transfer

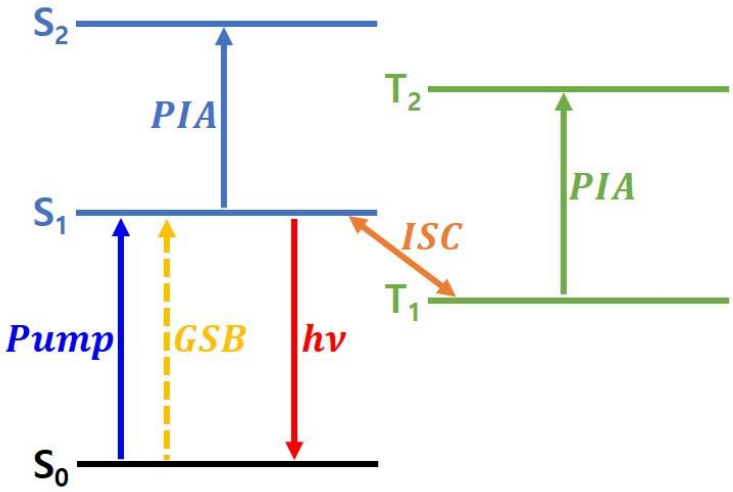

Figure 3-4. Schematic diagram of the transitions probed by transient absorption measurement.

mechanisms are studied by recording excited state absorption energies and probing their change in terms of wavelength and time.[135–138] Since the technique was firstly introduced in 1950,[139] it has been substantially developed, reaching time resolutions on the femtosecond scale.[140,141] In general, singlet excited states and fast processes, such as FRET, are probed by femtosecond-picosecond TA, while triplet excited states and other slow processes, such as TTA and ISC, are examined by the nanosecond TA.[135–141]

The recorded TA spectra are analysed based on the result of the following equation,

$$\Delta T/T = \frac{T_{pump} - T}{T} \tag{3-9}$$

where T_{pump} and T are the transmitted spectra with and without pump pulse, respectively. Figure 3-4 shows a schematic representation of the transitions probed by a TA measurement. Before the pump beam reaches a sample, only the singlet ground state (S_0) → singlet excited states (S_n) absorption is recorded as the probe beam passes

through the sample. When the pump beam hits the sample, numerous molecules in S_0 are excited to S_1. As a result, the $S_1 \rightarrow$ higher-lying singlet excited state (S_2) absorption, termed photo-induced absorption, is detected. In the meantime, the intensity of the $S_0 \rightarrow S_1$ absorption is decreased due to the absence of electrons in S_0, which is termed ground state bleach (GSB). In addition, the triplet excited state (T_1) $\rightarrow$ higher-lying triplet excited state (T_2) PIA can be detected when the ISC between S_1 and T_1 is possible. Also, the relaxation of excited electrons by emitting photons is detected, termed stimulated emission.

Figure 3-5 shows the schematic illustration of the TA measurement. It was performed on setups pumped at a rate of 1 kHz by a regenerative Ti:sapphire amplifier (Solstice Ace, Spectra-Physics) emitting sub-100 fs laser pulses centred at 800 nm. Sample excitation with 400 nm pump pulses was provided by frequency-doubled 800 nm pulse from Ti:sapphire amplifier in picosecond–nanosecond TA studies. Short-

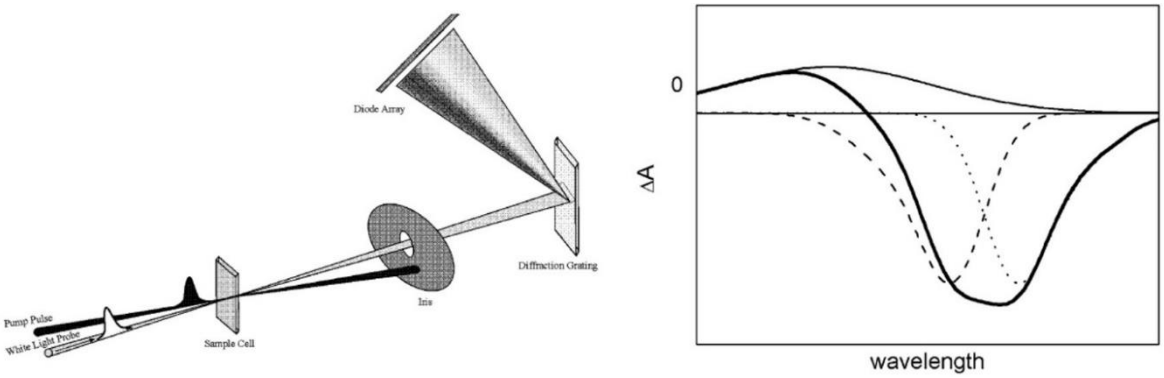

Figure 3-5. Schematic depiction of the transient absorption spectroscopy principle and Contributions to ΔA (the absorption spectrum of the excited sample minus the absorption spectrum of the sample in the ground state): ground state bleach (dashed line), stimulated emission (dotted line), excited-state absorption (solid line), and sum of these contributions (gray line). Reproduced from the reference 135 (*Photosynthesis Research* **101**, 105–118 (2009), open access). Copyright 2009, Springer Nature.

time TA studies at different wavelengths of excitation were achieved from the wavelength tuneable output of TOPAS commercial optical parametric amplifier (Light Conversion), which was pumped by the 800 nm laser pulses from the Ti:sapphire amplifier. The pump pulses were chopped at 500 Hz to enable shot-to-shot referencing, which accounted for intensity fluctuations in the amplifier. Probe pulses for TA were obtained from a set of home-built non-colinear optical parametric amplifier (NOPA) systems for the visible (510-790 nm) and infrared (1250-1650 nm) wavelength ranges. The NOPA probe pulses were divided into two identical beams by a 50/50 beamsplitter; this allowed for the use of a second reference beam for improved signal:noise. The probe pulses were detected by Si (Hamamatsu S8381-1024Q) and InGaAs (Hamamatsu G11608-512DA) dual-line array with a custom-built board from Stresing Entwicklungsbüro.

3.2 Device physics

3.2.1 Device fabrication

All OLED devices studied in this thesis were fabricated by a vacuum process utilising an evaporator manufactured by Angstrom Engineering. ITO coated substrates were cleaned with acetone and isopropyl alcohol, and then oxygen plasma treatment was applied to align the energy level with an HTL. Loading/unloading the substrates to/from a vacuum chamber was conducted in a nitrogen environment (glove box) to prevent degradation by air. All organic layers and a LiF/Al cathode were thermally evaporated on the substrates in a vacuum chamber under a high vacuum (~10^7 Torr). The evaporation process for each organic layer was calibrated in the same way as described in Section 3.1.1. The deposition rate of the organic layers was 1 Å/s for

thicker layers (>20 nm) and 0.5 Å/s for thinner layers (< 20 nm). Regarding an EML, host and dopant materials were loaded in separate crucibles and were co-deposited based on the target doping concentration. For example, for 3% doping, the deposition rate of the host is 0.97 Å/s, and that of the dopant is 0.03 Å/s. The doping concentration in Chapter 4 means volume percentage, and that in Chapter 5~7 means weight percentage. In terms of the deposition for LiF and Al, LiF powder and Al pellets were loaded on the alumina coated boat (S38B) and the Al deposition boat (QA00-00011), respectively. Then, they were thermally deposited in a vacuum chamber with a thickness of 1 nm (0.1 Å/s) and 100 nm (1 Å/s), respectively.

3.2.2 Device characterisation

Figure 3-6 shows the schematic diagram of the OLED device measurement. In this thesis, current, voltage, and luminance data were recorded by a Keithley 2635 sourcemeter and a calibrated Si photodiode, and EL spectra were obtained by an Ocean Optics Flame spectrometer. Based on them, several important values representing device performance are extracted, such as EQE (%), power efficiency (PE, lm/W), luminance (cd m^{-2}), and radiance (W sr^{-1} m^{-2} or mW sr^{-1} m^{-2}). Also, from the EL spectra, colour coordinates are calculated based Commission Internationale de l'Éclairage (CIE) 1931 colour space.

One of the essential parameters for OLEDs is an EQE, which can be defined as the ratio of the number of photons outcoupled from the EL device to the number of electrons flowing through the EL device,

$$\mathrm{EQE} = \frac{number\ of\ photons\ emitted\ from\ the\ EL\ device}{number\ of\ electrons\ flowing\ through\ the\ EL\ device} = \frac{pq\pi}{I} \tag{3-10}$$

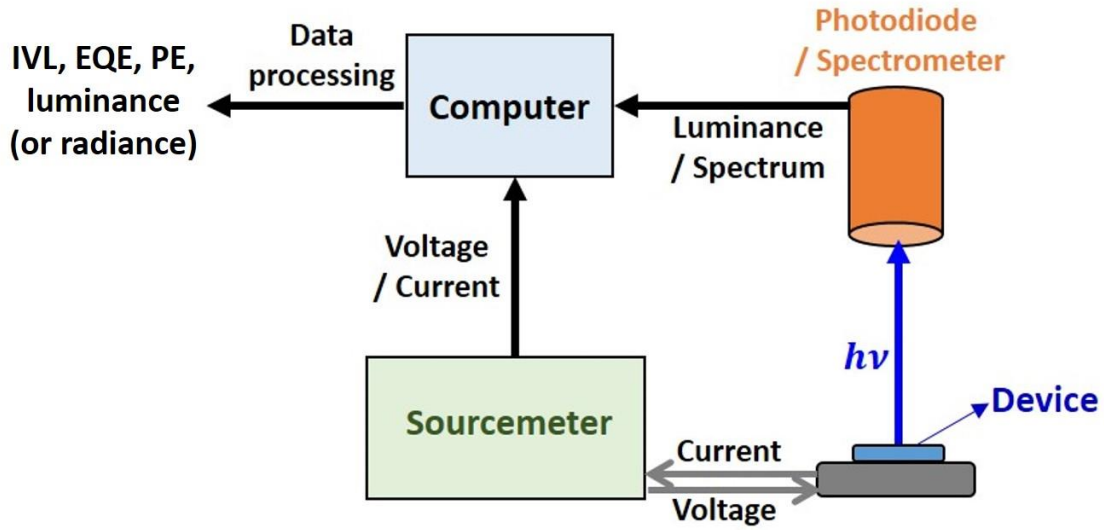

Figure 3-6. Schematic diagram of the OLED device measurement setup.

where p is the number of photons per second per steradian, q is the value of an electron charge (1.602×10^{-19} C), and I is the electric current, the electric charge passing through the device per second (1 A = 1 C/s). p is obtained from a photodiode, calculated by

$$p = \frac{LFd^2}{ACq \times 10^6} \tag{3-11}$$

where L is the photodiode output voltage, F is the photodiode calibration factor, d is the distance between a device and a photodiode, A is the photodiode area, C is the average photodiode quantum efficiency of the photodiode weighted EL spectrum, expressed as $\frac{\int Q(\lambda)S(\lambda)d\lambda}{\int S(\lambda)d\lambda}$ where Q is the photodiode quantum efficiency (the fraction of incident photons and electrons generated by incident photons), and S is the device EL spectrum. The factor of 10^6 originates from a 1 MΩ resistor in the photodiode to obtain the photodiode output voltage.

PE is defined as the ratio of the luminous flux (lm), which is the measure of the power of visible light weighted by the human eye sensitivity (P), to the total power

applied to a device, calculated by

$$\text{PE} = \frac{\int P(\lambda)S(\lambda)d\lambda}{I \cdot V} \tag{3-12}$$

where V is the voltage, and λ is the wavelength.

Luminance is defined as the luminous intensity (luminous flux per unit steradian) per unit area of a device (R), calculated by

$$\text{Luminance} = \frac{\int P(\lambda)S(\lambda)d\lambda}{\pi \cdot R} \tag{3-13}$$

As luminance is not applicable to NIR EL devices, radiance is utilised instead. Radiance is defined as radiant flux (radiant energy per unit time) per steradian per R, calculated by

$$\text{Radiance} = \frac{p\int S(\lambda)d\lambda}{R\int \frac{S(\lambda)}{hc/\lambda}d\lambda} \tag{3-14}$$

where h is the Planck constant (6.226×10^{-34} J·Hz^{-1}) and c is the speed of light (2.998×10^{8} m·s^{-1}).

CIE colour coordinates ($CIE_{x,y}$) were created by the International Commission on Illumination (or its French name: Commission Internationale de l'Éclairage) in 1931, and they can be calculated utilising the 1931 CIE standard observer colour matching functions ($\bar{x}(\lambda)$, $\bar{y}(\lambda)$, and $\bar{z}(\lambda)$) displayed in Figure 3-7.[142,143] The XYZ tristimulus values are calculated by the following equations,[142,143]

$$\text{X} = \int \bar{x}(\lambda)S(\lambda)d\lambda \tag{3-15}$$

$$\text{Y} = \int \bar{y}(\lambda)S(\lambda)d\lambda \tag{3-16}$$

$$\text{Z} = \int \bar{z}(\lambda)S(\lambda)d\lambda \tag{3-17}$$

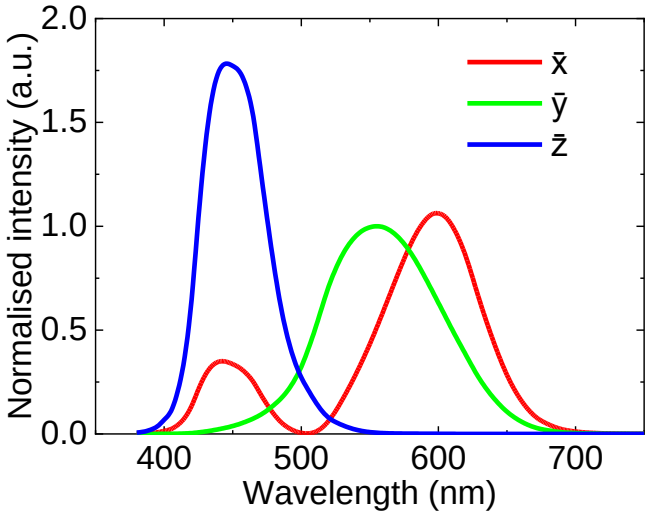

Figure 3-7. CIE standard observer colour matching functions.

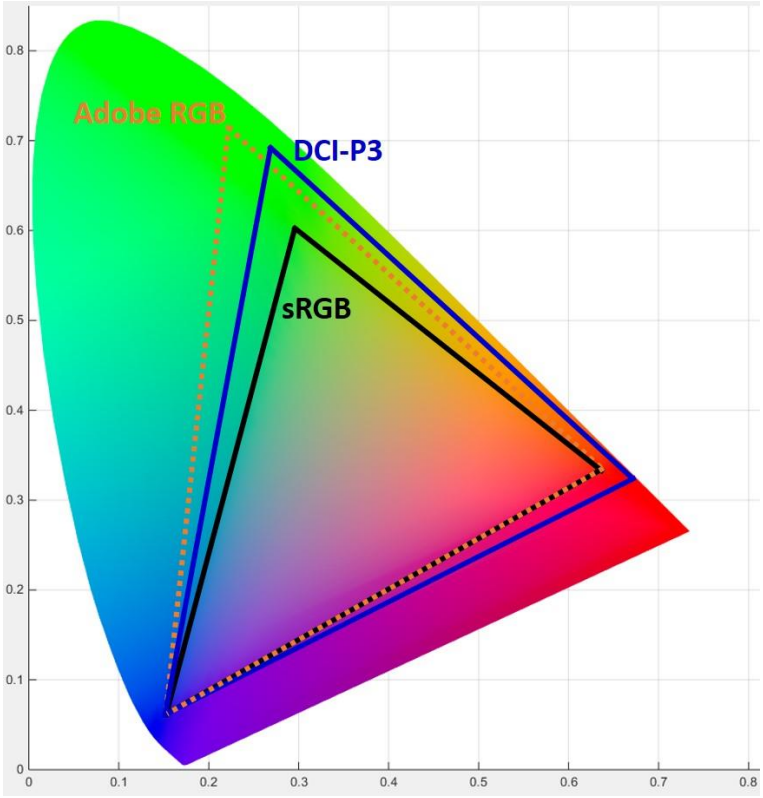

Figure 3-8. The CIE chromaticity diagram with the colour spaces of sRGB, Adobe RGB, and DCI-P3.

Table 3-1. The colour coordinates of sRGB, Adobe RGB, and DCI-P3.

	Blue		Green		Red	
	CIE_x	CIE_y	CIE_x	CIE_y	CIE_x	CIE_y
sRGB	0.150	0.060	0.300	0.600	0.640	0.330
Adobe RGB	0.150	0.060	0.210	0.710	0.640	0.330
DCI-P3	0.150	0.060	0.265	0.690	0.680	0.320

From these values, the colour coordinates of x and y are calculated by,[142,143]

$$x = \frac{X}{X+Y+Z} \tag{3-18}$$

$$y = \frac{Y}{X+Y+Z} \tag{3-19}$$

Figure 3-8 shows the CIE chromaticity diagram and the three representative standard colour spaces that have been applied to displays, and Table 3-1 shows the specific colour coordinates of the colour spaces.[142–146]

3.2.3 Single-carrier device and space-charge-limited current

There are several experimental techniques to estimate the carrier mobility of organic molecules. In general, the most common way which has been widely exploited for obtaining carrier mobility is the time-of-flight (TOF) technique.[147] The carrier transport in organic semiconductor films can be directly observed under laser excitation,

and the mobility is measured based on the transient photocurrent monitoring as holes or electrons drift to the charge-collecting electrode. Nonetheless, the main disadvantage of the method is the requirement of the micrometre scale thick organic layer resulting from the low electrical signal. It is challenging to form such a thick film through a thermal evaporation process due to enormous material consumption and the long time necessary for depositing the material. Also, the direct application of the mobility from TOF may not be possible in the sense that the thickness of organic layers in OLEDs is generally under 100 nm.

A useful alternative to the method mentioned above is to utilise the space-

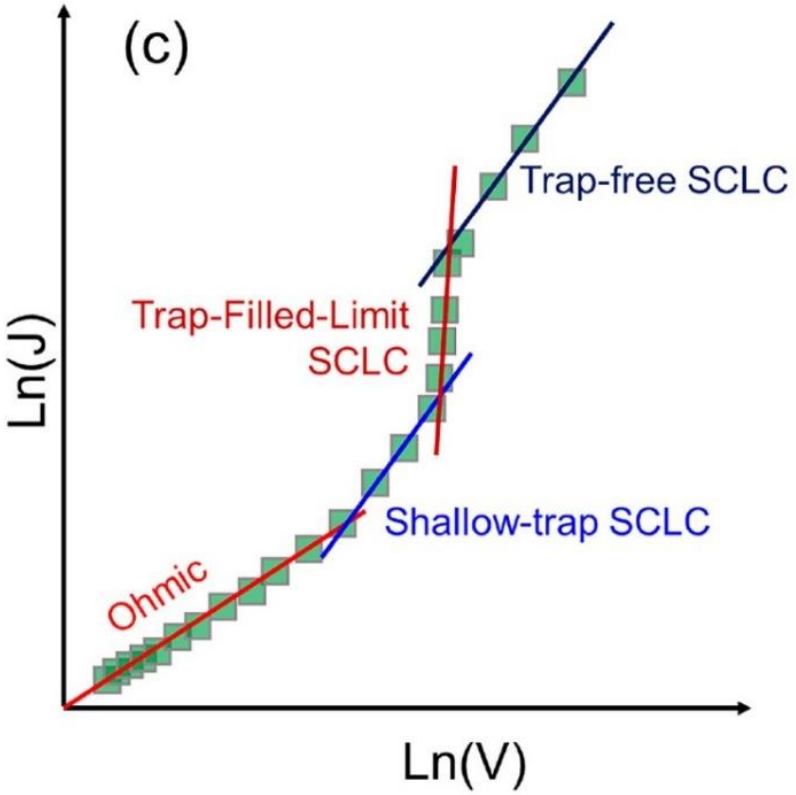

Figure 3-9. Schematic diagram of the typical current density-voltage curves in dielectric materials. Reproduced with permission from the reference 150 (*Journal of Applied Physics* **129**, 100902-1–32, (2021)). Copyright 2021 AIP Publishing LLC.

charge-limited current (SCLC) model based on single-carrier devices.[148–151] Figure 3-9 shows the schematic representation of the current density-voltage (J-V) curve in dielectric materials. The model assumes trap-free solids, but in practice, current flow is limited by trap states. However, as voltage increases, trap states are filled, and consequently, the J-V curve shows the trap-free SCLC behaviour at high voltage.[150–152]

The principal merit of this technique is that the carrier mobility of organic semiconductors can be directly estimated by the equation defined by the Mott-Gurney law. Therefore, the steady-state SCLC from single-carrier devices has been exploited to derive both hole and electron mobility of organic materials.[153–156] To analyse the charge mobility of organic materials, the J-V characteristics of single-carrier devices are examined utilising the Mott-Gurney law, expressed as

$$J = \frac{9}{8}\varepsilon\varepsilon_0\mu\frac{V^2}{L^3} \tag{3-20}$$

where J is the current density, ε is the relative dielectric constant, ε_0 is the permittivity of the free space, μ is the carrier mobility, L is the thickness of the organic layer, and V is the voltage. However, μ is electric-field dependent ascribed to energetic disorder in an amorphous film resulting from the interaction of each hoping charge with randomly oriented and located dipoles.[157–159] Hence, μ can be expressed by the Poole-Frenkel equation,

$$\mu(E) = \mu_0\exp(\gamma\sqrt{E}) \tag{3-21}$$

where μ_0 is the zero-field mobility, γ is the field activation of the mobility, E is the electric field (V/L). From Equation 3-20 and 21, the filed-dependent SCLC equation can be approximated as[148,157,158]

$$J = \frac{9}{8}\varepsilon\varepsilon_0\frac{V^2}{L^3}\mu_0\exp\left(0.891\gamma\sqrt{E}\right) \tag{3-22}$$

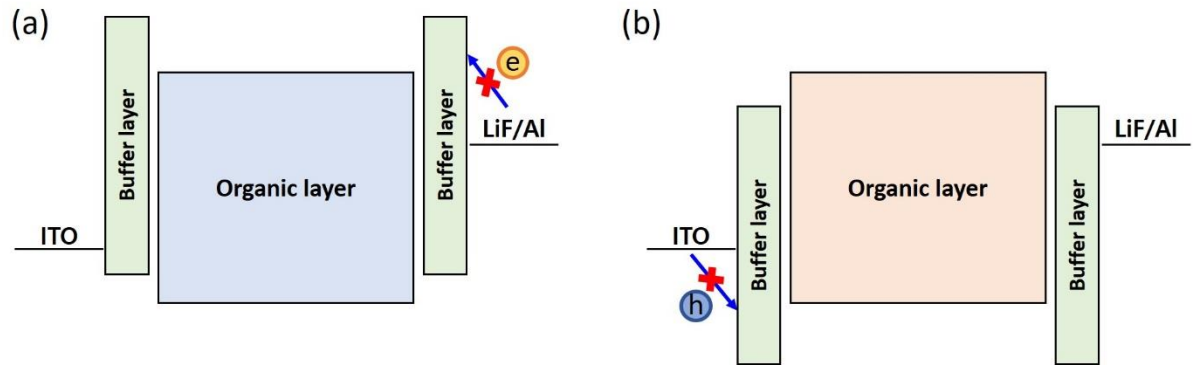

Figure 3-10. Schematic diagram of (a) hole-only device (HOD) and (b) electron-only device (EOD) structures with buffer layers to make a single-carrier current.

In general, hole transporting and electron transporting materials can show a single carrier flow without additional buffer layers.[154–156] However, for bipolar materials incorporating both electron donating and accepting moieties in a single molecule, the proper buffer layers between a layer of the testing organic material and the two electrodes are necessary to make electron- and hole-only devices (EODs and HODs), as shown in Figure 3-10. For HODs, the organic layer is sandwiched by hole transporting materials having high LUMO to block electron injection and allow hole-only current. In contrast, for EODs, the organic layer is sandwiched by electron transporting materials having deep HOMO to block hole injection and achieve an electron-only current. Single-carrier devices studied in this thesis were designed based on this concept. For better electron blocking for HODs, 1,4,5,8,9,11-hexaazatri phenylene hexacarbonitrile (HATCN) can be selected as buffer layers (Section 4.8).[108]

3.2.4 Transient electroluminescence

Transient EL is a powerful method to explore the fundamentals of device physics associated with the characteristics of OLEDs, such as charge transport, charge trapping,

charge carrier accumulation, exciton formation, exciton energy transfer, and exciton annihilation.[160–166] Accordingly, it has been widely applied to investigate the emission mechanism of OLEDs as the transient EL profiles show the results of the exciton dynamics in the EL devices. Figure 3-11 shows the schematic diagram of the transient EL setup utilised in the research in this thesis. The transient EL characteristics were recorded by an Andor spectrometer setup (Andor SR303i) with an electrically gated ICCD camera (AndoriStar DH740 CCI-010). The voltage pulse was given by a Keithley 2401 function generator.

One of the most commonly observed transient EL features is the EL overshoot after turn-off. The interpretation for this is highly dependent on how device architectures and host-dopant combinations are designed, but these EL features are typically ascribed to the delayed recombination of remaining trapped charge carriers in

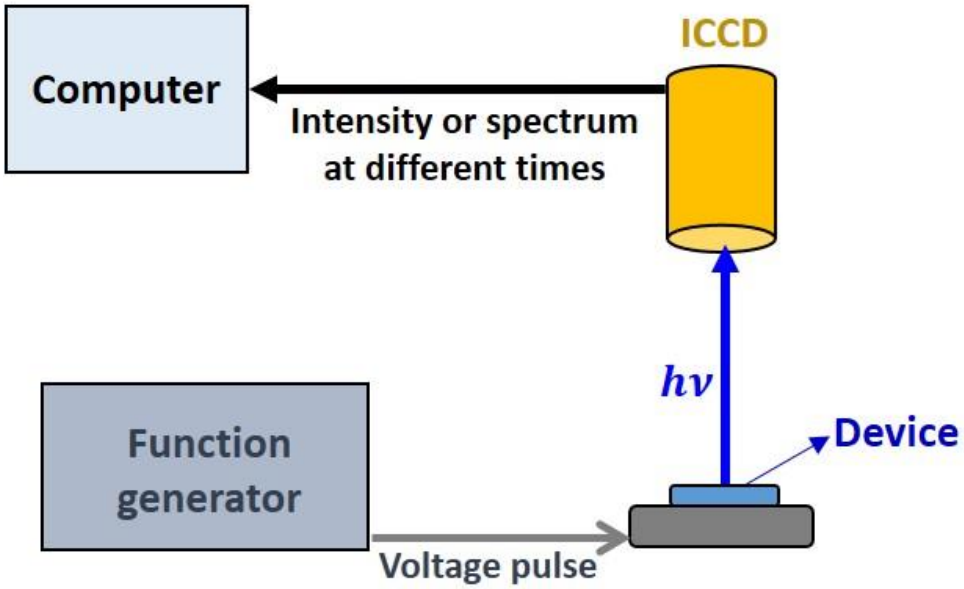

Figure 3-11. Schematic diagram of the transient EL setup.

devices.[160,164–166] It was reported that due to a relatively wide energy gap difference between host and dopant, charges tend to be trapped and stored at dopant sites during operation, causing the EL overshoot after turn-off.[160,165,166] Also, as the charges are accumulated at the interface of EML and charge transporting layers, the accumulated charges can contribute to the additional emission after turn-off.[160] However, charge trapping or accumulation causes large efficiency roll-off and low device stability.[78,79] However, they are substantially reduced by exploiting ambipolar hosts or mixed hosts in an EML, leading to improved charge transport and balance, which is proved by the transient EL profiles not showing or showing considerably reduced EL overshoot after turn-off.[78,79,165]

Furthermore, triplet contribution to the EL in fluorescent OLEDs has been proved by harnessing the transient EL measurement.[89,91–94] As mentioned in Section 2.2.1, transient EL profiles show delayed emission resulting from the additional singlet excitons generated by TTA. Transient PL is unable to show the TTA-induced delayed emission as only singlets are formed by photoexcitation. However, due to the three times higher population of triplet excitons than singlet excitons under electrical excitation, strong delayed emission can be observed in transient EL profiles if TTA effectively occurs.[89,91–94]

3.2.5 Magneto electroluminescence

Magneto EL (MEL) has been widely utilised to investigate exciton dynamics in EL devices. A magnetic field induces the Zeeman splitting, which is the splitting of atomic energy level in the presence of the external magnetic field,[167] in organic semiconductors resulting in different MEL tendencies in different systems owing to magnetic interactions.[168–180] MEL is understood based on the polaron-pair model

(Figure 3-12).[181–184] As holes and electrons are injected from an anode and a cathode, free charge carriers (positive and negative polaron, P^+ and P^-) are weakly bound at an EML to form singlet and triplet polaron pairs (^{S}PP and ^{T}PP) with a statistical ratio of 1:3.[181–184] They can either dissociate to polarons or recombine to form singlet and triplet excitons (SE and TE). The density of ^{S}PP and ^{T}PP relies on the effective decay rates of ^{S}PP and ^{T}PP, $k_S = k_D + k_{SE}$ and $k_T = k_D + k_{TE}$ as well as the ISC between ^{S}PP and ^{T}PP.[183,184] The Zeeman splitting induced by an external magnetic field affects hyperfine interaction between each polaron and its neighbouring nuclei and SOC between the spin of polaron-pairs and the molecule orbital moment, leading to the disturbance of the ^{S}PP and ^{T}PP spin mixing and changes in interconversion between ^{S}PP and ^{T}PP, which can result in positive or negative MEL.[174,175,177,182–184] MEL is defined by

$$\text{MEL}\ (\%) = \frac{\text{EL}(B) - \text{EL}(0)}{\text{EL}(B)} \times 100 \tag{3-23}$$

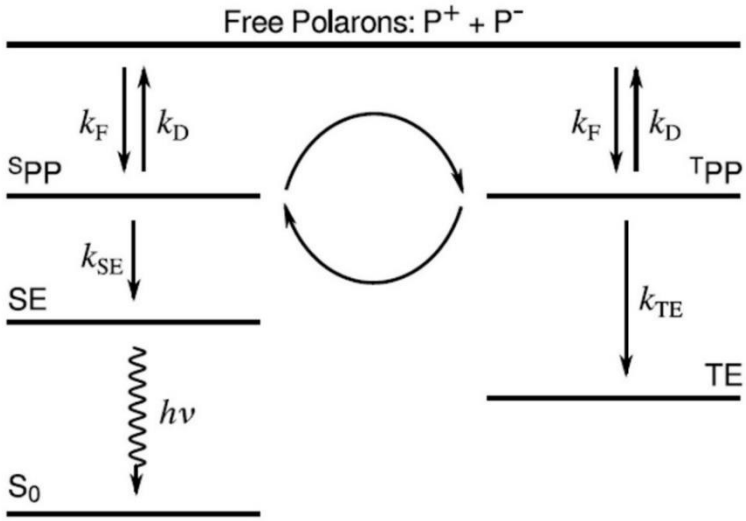

Figure 3-12. Schematic diagram of the dissociation and recombination for polaron pairs in an EML in OLEDs. Reproduced with permission from the reference 184 (*Journal of Chemical Physics* **144**, 1–10 (2016)). Copyright 2016 AIP Publishing LLC.

where EL(B) is the EL under a magnetic field (B), and EL(0) is the EL without a magnetic field ($B = 0$).

Figure 3-13 shows the schematic diagram of the MEL measurement setup. A sourcemeter controls voltage and current applied to the device, and a magnetic field applied to the device is measured by a gauss meter. An EL device was positioned between magnet cores (GMW 3470 electromagnet), and a Keithley 2635 sourcemeter was utilised to apply the voltage to the device. Its EL spectrum was recorded by an Andor spectrometer (Shamrock 303i and iDus camera) with and without a magnetic field.

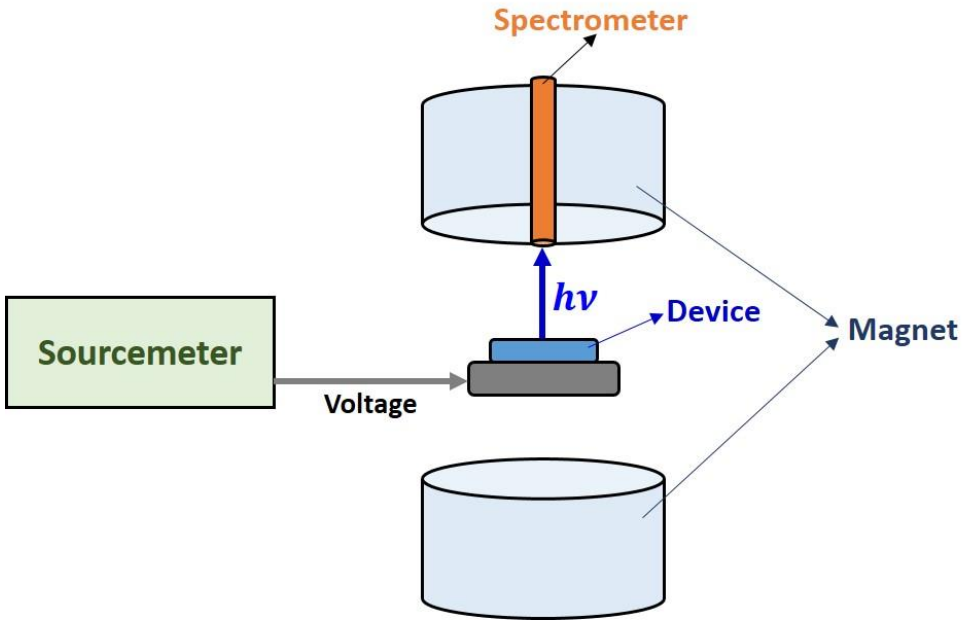

Figure 3-13. Schematic illustration of the MEL measurement setup.

3.3 Measurement uncertainty and error

Measurement is the set of operations to determine a value of a quantity that is intended to be measured and conducted to investigate and compare the properties of research subjects, which is one of the essential parts of experimental studies.[185–187] As described in Section 3.1 and 3.2, various measurements were utilised to quantify the characteristics, exploiting appropriate measuring instruments. However, when the experimental data are analysed, measurement uncertainty and error should be taken into account, which is briefly described in this section.

3.3.1 Measurement uncertainty

No measurement is perfect, despite the measuring instruments being set up as carefully as possible; in other words, there is always a margin of doubt about the measurement result, which is uncertainty.[185,186] There are many factors affecting the measurement results, such as the resolution and performance of the instruments, operator skills, the quality of the item being measured, sampling issues, the measurement conditions and environment, and the measurement process, in addition to the unknown factors that are not recognised.[185,186] Due to these factors, repeated measurements tend to give different results with some variations. Therefore, basic statistical calculations are used to ensure the measurement results, such as the average (arithmetic mean) and standard deviation.[185,186] Also, it is vital to minimise the uncertainties for the credibility of the measurement results. To be specific, it is necessary to calibrate the measuring instruments and set them up based on the instructions provided by the suppliers. In addition, following the standard measuring process with making it traceable is important to obtain reliable results and correct them

if they deviate from the expected range, and software and calculations are needed to be inspected.[185,186] For example, when the device characteristics are measured, several factors affecting the results have to be considered. The device intended to be measured should be placed perpendicularly to the photodiode, and the distance between them should be measured as accurately as possible. Also, the quality of each pixel in the device is needed to be inspected by checking the leakage current level so that the device performance cannot be underestimated, and the input parameters for the software should be checked to ensure the measured device characteristics. In addition, the spectrometer is necessary to be well calibrated to obtain the correct emission spectrum, and the accuracy of the Keithley source metre (±0.02%) may be checked if issues related to the input voltage are encountered.

3.3.2 Measurement error

Error is different from uncertainty. Uncertainty is a doubt about the measurement results, while error is the difference between the 'measured' value and the 'true' value.[185,186] There are two aspects that should be considered for measurement error: random and systematic error.[185,186] Random error means an error that randomly occurs in the repeated measurements, giving different results with unpredictable or stochastic variations.[185,186] If more measurements are conducted, a better estimate will be obtained by averaging the measured values, leading to the reduction of the error.[185,186] On the other hand, the systematic error originates from a recognised effect, such as the inherent measurement setup or procedure, so it is predictable and can be corrected by appropriate calibration or calculation.[185,186]

Chapter 4 Investigations of exciton energy transfer and charge transport in hyperfluorescent OLEDs with carbene-metal-amides

4.1 Introduction

FRET from triplet-harvesting assistant dopants to singlet emitters has been identified as a concept with the potential to improve operational stability and colour purity simultaneously.[19,188–194] The particular approach utilising TADF-type molecules as the assistant dopants in conjunction with conventional fluorescent emitters is termed 'hyperfluorescence'.[20] Hyperfluorescent EMLs use composites of multiple functional materials. Transport is typically handled by a host matrix, and interconversion of singlet and triplet states is managed by an assistant dopant, while the shape of the emission spectrum is managed by a fluorescent dopant. Dispersal of emissive components in a host matrix also acts to suppress concentration quenching and parasitic DET to the fluorescent dopant. The requirement for a host matrix means that a considerable increase in driving voltage is inevitable. Two-component exciplex-forming hosts may be capable of addressing this problem, though the concept requires at least four materials to be used in the EML, which is one reason why hyperfluorescence is not widely implemented in displays.[22,100,121,123]

In 2017, coinage metal-based organometallic emitting materials (carbene-metal-amides, so-called CMAs) exhibiting TADF-like characteristics were introduced with exceptionally rapid mixing of spin states and large oscillator strengths.[195] Interestingly,

even in a neat solid film, high PLQE of 83% was achieved for some CMA compounds. This implies an absence of significant concentration quenching, potentially due to weak intermolecular interactions, in part arising due to the tendency of many CMAs to anti-align in the solid phase.[196,197] This suggests that CMA-type organometallic compounds may be good candidates for realising efficient hyperfluorescent OLEDs without a host matrix, in the sense that the assistant dopant could fulfil the role normally played by the host. If the host may be removed without a significant drop in quantum efficiency, PE will be dramatically increased. Moreover, an emitting system with only two components is advantageous for eventual OLED manufacture.

This chapter explores matrix-free hyperfluorescene (MFHF) OLEDs with a simple device structure achieving comparable quantum efficiency and significantly improved PE versus equivalent devices employing a host matrix. Compounds CMA1 and CMA4 are employed as hosts,[195] (synthesised by Dr Alexander Romanov, Department of Chemistry, University of Manchester) and 5,6,11,12-tetraphenyl naphthacene (rubrene) and 2,8-di(*tert*-butyl)-5,11-di[4-(*tert*-butyl)phenyl]-6,12-diphenylnaphthacene (TBRb) are examined as dopants.[198,199] From the absorption and PL spectra of the hosts and dopants, Förster radii are calculated to predict the effectiveness of FRET between them. In order to investigate exciton energy transfer more directly, PL quenching measurements are performed. PLQE and transient PL measurements are employed to show the influence of *tert*-butyl substituents and doping concentration on FRET and DET. Next, the characteristics of the hyperfluorescent OLEDs are explored. In CMA1-based devices, the driving voltage of the MFHF devices is considerably reduced at 1000 cd/m^2, in line with the approximately two-fold increase in PE compared to devices employing a host matrix. Maximum EQEs of 15.2% and 16.5% for CMA1 and CMA4 MFHF devices are observed, versus 16.3% and 18.1%, respectively, when employing a host matrix. To further investigate the different features

of CMA1 and CMA4 in EL devices, the charge transporting abilities of CMA1 and CMA4 are examined based on analysing single-carrier devices. Hole and electron mobility for CMA1 is extracted from SCLC measurement. It is shown that faster charge transport in CMA1 than in CMA4 is correlated with their different device characteristics.

4.2 Förster resonance energy transfer

CMAs can achieve high PLQE even in neat films. Table 4-1 shows the values of absolute PLQE for thermally evaporated films of CMA1 and CMA4 diluted in 1,3-bis(N-carbazolyl)benzene (mCP) and their neat films, which were measured in an integrating sphere under a nitrogen flow with a calibrated spectrometer.[124] The comparable and high PLQE values (81±5 %) imply that CMAs can serve as a single host for hyperfluorescent OLEDs.

First, exciton energy transfer between exciton donors and exciton acceptors is examined. Once singlet and triplet excitons are generated on a donor, they may transfer to nearby acceptors via FRET and DET mechanisms. Minimising DET and maximising FRET is a way to optimise the performance of hyperfluorescent OLEDs. Even though high PLQE is available in neat films for CMAs, if a host matrix is not utilised, triplet diffusion via DET to the fluorescent sites will be possible since the CMAs and fluorescent emitters are in close contact.[200] It was recently demonstrated that the adoption of appropriate substituents attached to fluorescent emitters for the separation of donors and acceptors is a useful method for suppressing DET since the likelihood of transfer varies exponentially with chromophore spacing.[190] In this work, CMA1, CMA4, rubrene, and TBRb (molecular structures shown in Figure 4-1) are employed to

explore the influence of steric bulk, introduced via *tert*-butyl substituents (TBRb is *tert*-butyl substituted rubrene, and CMA4 is *tert*-butyl substituted CMA1), on DET efficiency between CMAs and fluorescent emitters.

Table 4-1. The PLQE values of CMAs and those diluted in mCP and the Förster radii for each combination of those with rubrene and TBRb.

		CMA1 100%	mCP:CMA1 20%	CMA4 100%	mCP:CMA4 20%
PLQE (%)		83	86	76	82
Rubrene	R_0 (nm)	3.48	3.40	3.30	3.34
TBRb		3.79	3.70	3.62	3.64

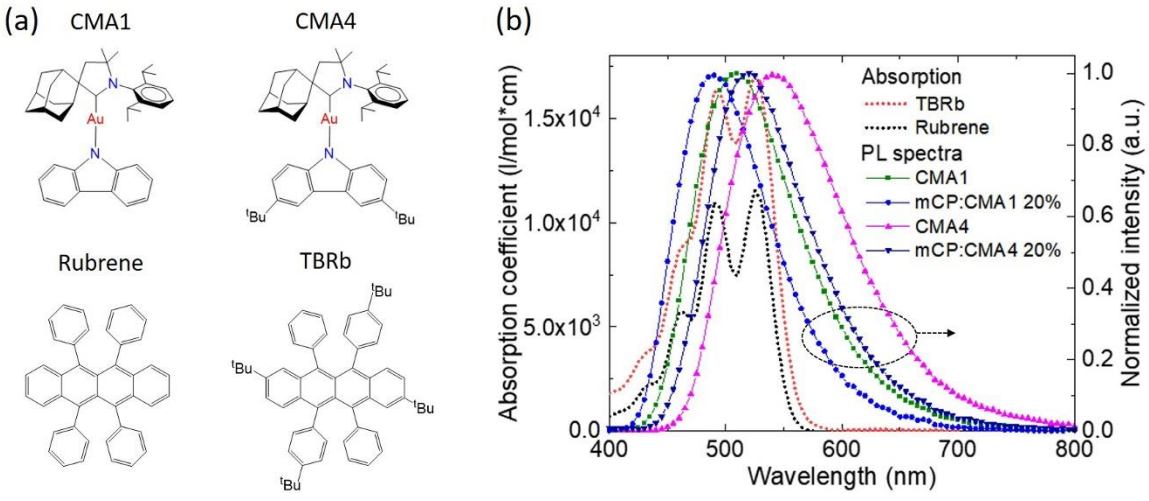

Figure 4-1. (a) Chemical structures and (b) PL and absorption spectra of CMA1, CMA4, rubrene, and TBRb.

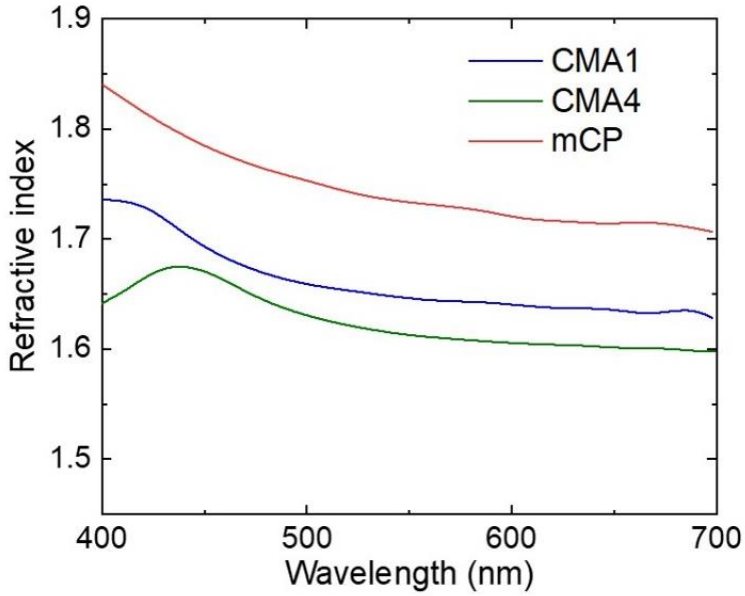

Figure 4-2. Refractive index of CMA1, CMA4, and mCP.

FRET operates on the basis of resonant dipole coupling, with long-range energy transfer between the singlet excited states of two molecules achieved by virtual emission and absorption processes.[81] As such, the spectral overlap between the PL of the donor and the absorption of the acceptor is vital for effective FRET. FRET between CMAs and fluorescent emitters is studied via the calculation of the Förster radius (R_0), which is the critical distance that 50% of singlet excited states of donors can be transferred to those of acceptors, expressed as[81–84]

$$R_0^6 = \frac{9000 \ln 10 \eta_D \kappa^2}{128 \pi^5 N_A n^4} \int \lambda^4 F_{\mathrm{D}}(\lambda) \epsilon_{\mathrm{A}}(\lambda) d\lambda \quad (4\text{-}1)$$

where N_{A} is Avogadro's number, n is the refractive index, η_{D} is the PLQE of the donor, κ is the dipole orientation factor, λ is the wavelength, F_{D} is the PL spectrum of the donor normalised to unity, and ϵ_{A} is the molar decadic absorption coefficient of the acceptor. Absorption and PL spectra are shown in Figure 4-1(b). Figure 4-2 presents refractive index measurements of neat CMA1, CMA4, and mCP, obtained by

ellipsometry. At 550 nm, the values of n are 1.65, 1.61, and 1.74, respectively. κ in a randomly orientated amorphous film is $0.845\sqrt{2/3}$, which is used for the calculation of R_0.[201] As shown in Table 4-1, the calculated values of R_0 for CMA1 and CMA4 with rubrene are 3.48 nm and 3.30 nm, and with TBRb are 3.79 nm and 3.62 nm, respectively. Those for CMA1 and CMA4 diluted in mCP with rubrene are 3.40 nm and 3.34 nm, and with TBRb are 3.70 nm and 3.64 nm, respectively, indicating that FRET is achievable at low doping concentration. The absorption spectra of rubrene and TBRb and the PL spectra of CMAs are well-overlapped with each other, and the absorption coefficient of TBRb is higher than that of rubrene, resulting in a larger R_0.

4.3 Photoluminescence quenching measurement

In order to explore exciton energy transfer in a CMA-based host-guest emitting system in detail, PL quenching measurements in a CMA4:mCP:rubrene system were performed to obtain exciton quenching efficiency (η_{EQ}).[202,203] As presented in Figure 4-3(a), mCP was adopted as a host to dilute rubrene and as a spacer layer to separate CMA4 from rubrene. After 10 nm of an mCP:rubrene 95:5% quencher layer is deposited on glass, a pure mCP spacer layer is deposited on top, followed by a 10 nm CMA4 sensitisation layer. The thickness of the mCP spacer layer varies from 0 nm to 10 nm. From the measurements of quenched PL (PL_Q) and non-quenched PL (PL_{NQ}), η_{EQ} of CMA4 is constructed by 1-PL_Q/PL_{NQ}.[202] In this structure, when CMA4 is excited, excitons formed in CMA4 are transferred to diluted rubrene via FRET (singlets) or DET (triplets). mCP is not expected to directly participate in exciton energy transfer since its singlet and triplet energy levels are much higher than those of either CMA4 or

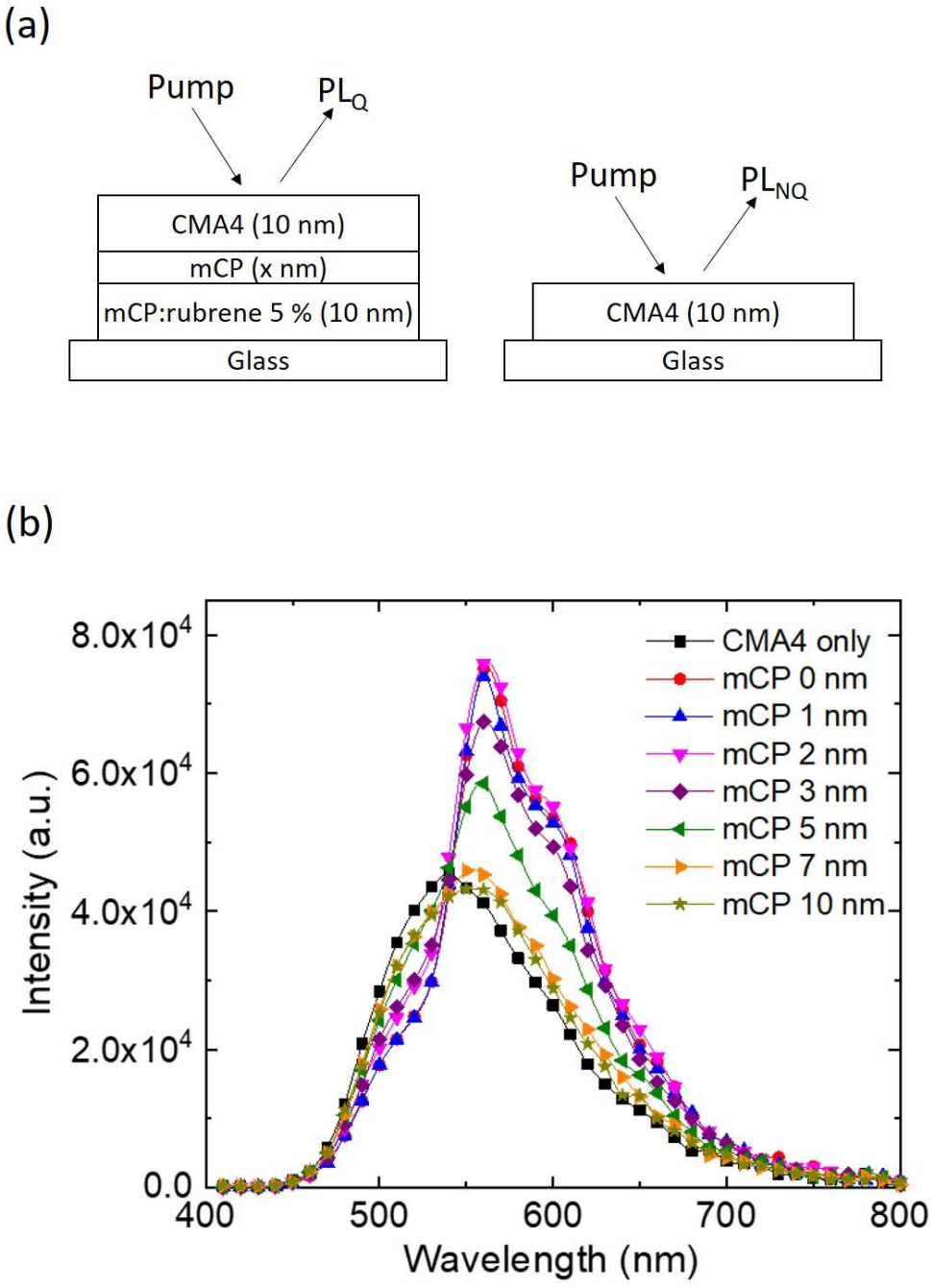

Figure 4-3. (a) Schematic illustration of the structures for PL quenching measurements. (b) PL spectra variation with the different thickness of an mCP spacer layer.

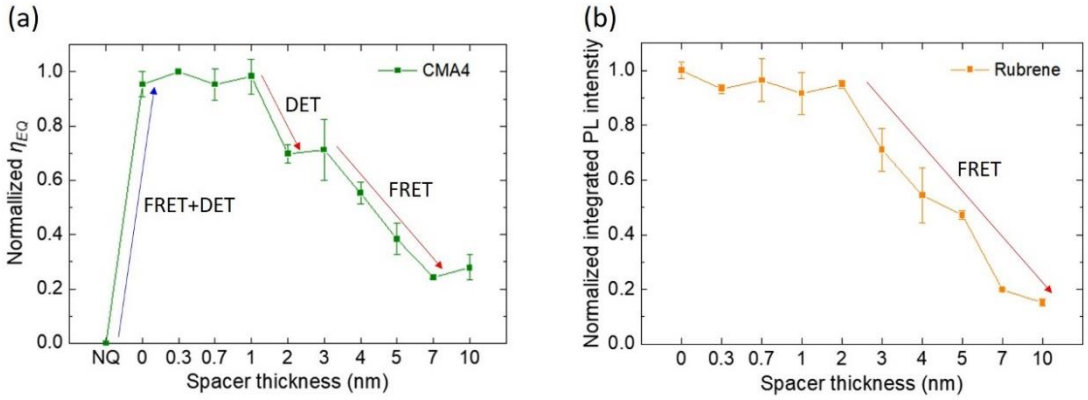

Figure 4-4. (a) Variation of the exciton quenching efficiency of CMA4 and (b) normalised integrated PL intensity from rubrene as a function of spacer layer thickness. Exciton quenching for CMA4 is attributed to both FRET and DET between 0 nm and 1 nm thick spacer layer. For higher spacer thicknesses, the regimes in which first DET, and then FRET, are turned off are shown. The PL of rubrene is sensitised only via FRET, so no signature from the change in DET efficiency is seen.

rubrene, so it acts primarily as an inert spacer. For PL_{NQ}, CMA4 10 nm was directly deposited on glass without the spacer and quencher layer as a control sample. Figure 4-3(b) displays the PL spectral dependence on the thickness of the spacer layer. When the mCP layer thickness is below 2 nm, the strong emission from rubrene with a peak wavelength at around 560 nm is observed with the reduced emission contribution from CMA4, meaning that singlet excitons formed in CMA4 are effectively transferred to rubrene via FRET. As the mCP layer thickness increases, the proportion of rubrene emission decreases and that of CMA4 emission increases. At a spacer thickness of 10 nm, the PL spectrum almost recovers that of the neat CMA4 control, since the CMA4 layer and mCP:rubrene 5% layer are sufficiently separated to block exciton energy transfer. η_{EQ} of CMA4 and the normalised integrated PL intensity of rubrene are obtained from the decomposed CMA4 and rubrene spectra, which are extracted by subtracting a linearly-scaled CMA4-only spectrum from the total PL spectrum.

Figure 4-4(a) and (b) show the variation of normalised η_{EQ} and normalised integrated PL intensity with spacer thickness. While η_{EQ} of CMA4 drops significantly for greater than 2 nm of the spacer layer, the normalised integrated PL intensity of rubrene only falls substantially for greater than 3 nm of the spacer layer. This is interpreted as originating from the difference between FRET and DET characteristics. Since DET is an electron exchange process, it typically occurs below 1 nm intermolecular distance. Accordingly, both DET and FRET are expected to contribute between 0 nm and 1 nm spacer layer thickness. However, for spacer layers of 2 nm and greater, excitons primarily migrate via FRET. Therefore, the decrease in η_{EQ} of CMA4 observed up to 2 nm spacer thickness is attributed to the proportion of quenching due to DET, while the decrease in η_{EQ} from 3 nm onwards results from reduced quenching due to FRET, in qualitative agreement with the expected Förster radius between CMA4 and rubrene. Concomitantly, light emission from rubrene drops for spacer layers beyond 3 nm as indirect excitation of rubrene singlets reduces. It is shown that DET causes triplet excitons generated in donors to be partly wasted, not contributing to an emission process. Also, FRET is not effective over distances greater than around 4 nm, in agreement with calculations. If a longer Förster radius were achieved, a greater proportion of excitons would be able to be transferred to acceptors via FRET.

4.4 Photoluminescence quantum efficiency

To explore the behaviour of different material combinations, PLQE was measured for the CMA-based hyperfluorescent films with and without a host matrix and varying doping concentrations. The values are summarised in Table 4-2. The PL spectra of the films are also measured using a fluorimeter, as shown in Figure 4-5,

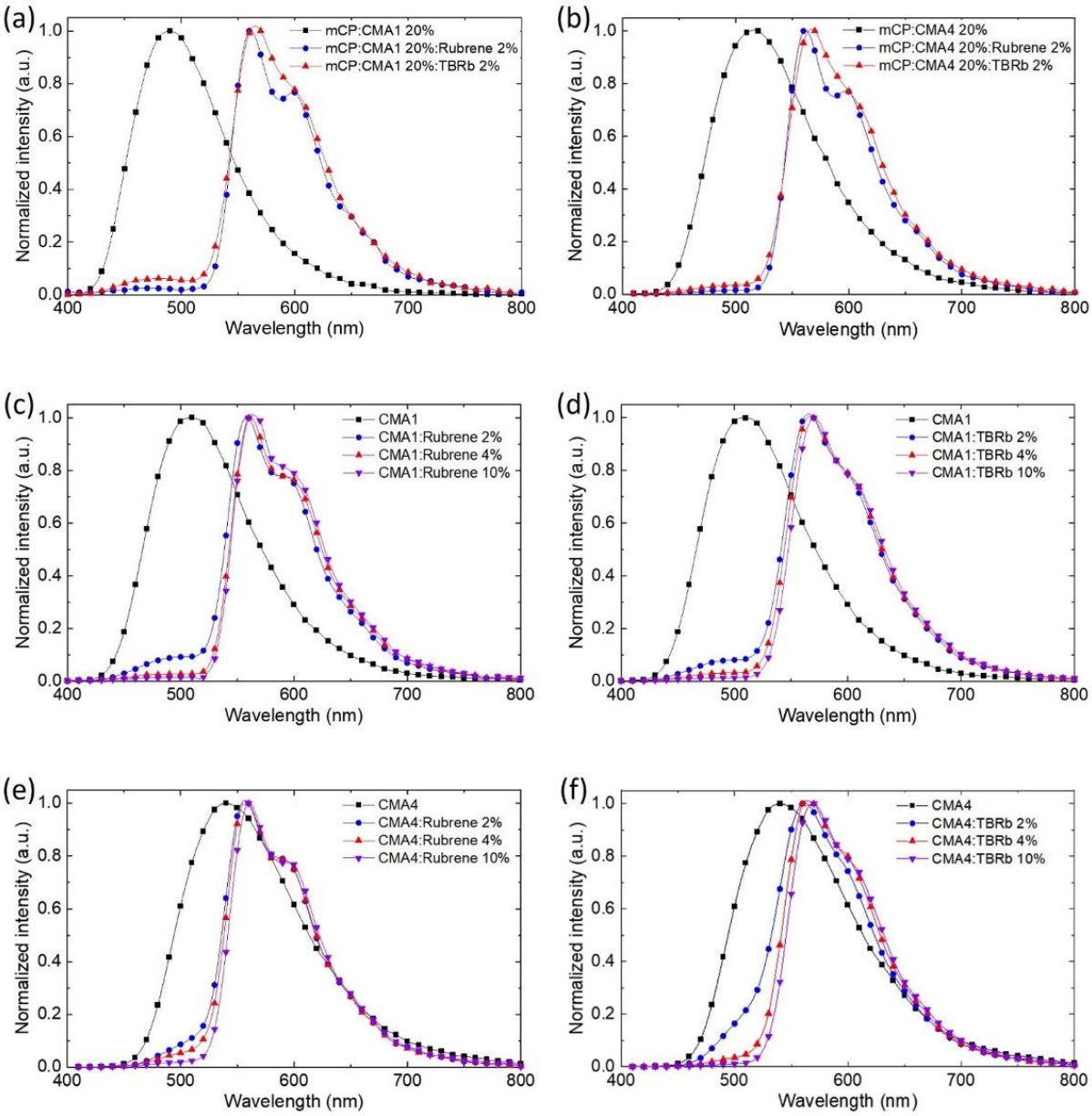

Figure 4-5. (a) and (b) show PL spectra of 2% rubrene or TBRb doped in mCP:CMA1 20% and mCP:CMA4 20% films. PL spectra of rubrene or TBRb doped in CMA1 or CMA4 films are plotted in (c), (d), (e), and (f), respectively, with the variation of doping concentration.

indicating that in all cases, most of the emission is from rubrene or TBRb. As expected, as doping concentration increases, the PLQE values are substantially reduced, which is interpreted as arising from the increased probability of triplet DET between the CMAs and the emitters. There may also be an effect of concentration quenching, but rubrene and TBRb are known to experience negligible concentration quenching at low doping concentrations (<5%).[198,199] The highest quantum efficiency is observed for conventional hyperfluorescent films where both donor and acceptor are dispersed in a matrix, reducing the probability of DET. In matrix-free films, rubrene shows relatively poor performance, achieving 34-38% PLQE at 2% concentration. By contrast, the performance of bulkier TBRb is better, and when paired with the bulkier derivative CMA4, the relative drop in performance at higher doping concentration is considerably reduced. This is ascribed to suppressed DET resulting from larger inter-chromophore spacing due to *tert*-butyl substituents in both CMA4 and TBRb.

Table 4-2. The PLQE values of rubrene or TBRb doped in CMA1, CMA4 and those diluted (at 20%) in mCP.

		Rubrene			TBRb		
Doping (%)		2	4	10	2	4	10
CMA1	PLQE (%)	38	25	8	57	37	24
CMA4		34	19	8	45	50	40
mCP:CMA1		78	-	-	74	-	-
mCP:CMA4		67	-	-	73	-	-

4.5 Exciton decay kinetics and energy transfer pathway

To better understand these implied exciton dynamics, transient PL was measured by TCSPC. Figure 4-6(a) illustrates a schematic representation of the exciton energy transfer mechanism and decay pathways for CMA-based hyperfluorescence. Once excitons are formed in CMAs, they convert rapidly between singlet and triplet excited states via RISC and ISC and migrate to fluorescent emitters via FRET or DET. Transient PL kinetics were measured at the peak emission wavelengths, which are 510 nm and 535 nm for CMA1 and CMA4, 490 nm and 515 nm for mCP:CMA1 20% and mCP:CMA4 20%, and 560 nm for rubrene and TBRb, respectively, depicted in Figure 4-7. CMAs and the acene emitters are expected to be dispersed with a broad range of intermolecular distances. Accordingly, decay kinetics are not mono-exponential since both FRET and DET are strongly dependent on intermolecular distance. From a multi-exponential fit with three components, the average (intensity-weighted) decay time (τ) of rubrene and TBRb diluted in CMA1, CMA4, mCP:CMA1 20%, and mCP:CMA4 20% were calculated as $\tau = \frac{\sum_{i=1}^{3} A_i {\tau_i}^2}{\sum_{j=1}^{3} A_j \tau_j}$, where A_i and τ_i are the amplitude and lifetime of the i^{th} decay component, respectively. The kinetics of CMA1, CMA4, mCP:CMA1 20%, and mCP:CMA4 20% without fluorescent dopants were fitted with double exponential decays to derive τ. In general, k_{r} and τ are expressed as[126]

$$k_{\text{r}} = \frac{\eta}{\tau} \tag{4-2}$$

$$\tau = \frac{1}{k_{\text{r}} + k_{\text{nr}}} \tag{4-3}$$

where η is the value of PLQE, and where k_{r} and k_{nr} are the overall radiative and nonradiative rates of the system, respectively. The system is parameterised in terms of the individual radiative (r) and nonradiative (nr) rates shown in Figure 4-6(a), with

k_{FRET} and k_{DET}, the characteristic FRET and DET rates from CMA to fluorescent dopant, respectively. The decay of triplets on the fluorescent dopant (k_{T}) is taken to be entirely nonradiative. Note that for brevity, $k_{\mathrm{nr,CMA}}$ incorporates both nonradiative singlet and triplet decay, and it is assumed that ISC rapidly mixes the singlet and triplet populations on the CMA materials.

Under the assumptions that $k_{\mathrm{r,F}} \gg k_{\mathrm{nr,F}}$ and $k_{\mathrm{r,F}} \gg k_{\mathrm{FRET}}$ where $k_{\mathrm{r,F}}$ and $k_{\mathrm{nr,F}}$ are the fluorescent radiative and nonradiative decay rate, respectively, the following equations are obtained as

$$k_{\mathrm{r}} \approx k_{\mathrm{r,CMA}} + k_{\mathrm{FRET}} \tag{4-4}$$

$$k_{\mathrm{nr}} \approx k_{\mathrm{nr,CMA}} + k_{\mathrm{DET}} \tag{4-5}$$

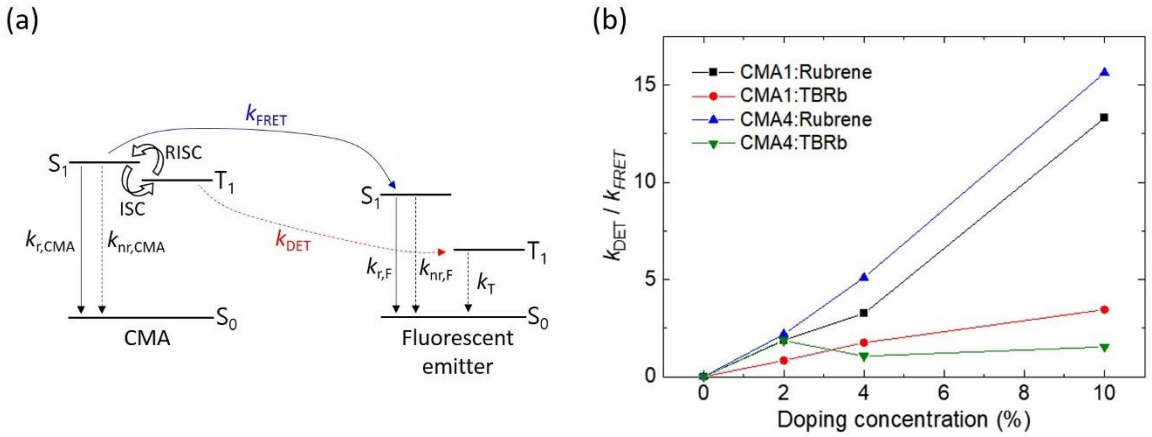

Figure 4-6. (a) Schematic representation of the energy diagram for exciton decay and energy transfer pathways for CMA-based hyperfluorescence. (b) The ratio of DET and FRET rates for the films of rubrene or TBRb doped in CMA1 or CMA4 with the variation of doping concentration. The FRET rate was derived from Equation 4-8, and the DET rate was calculated from Equation 4-7.

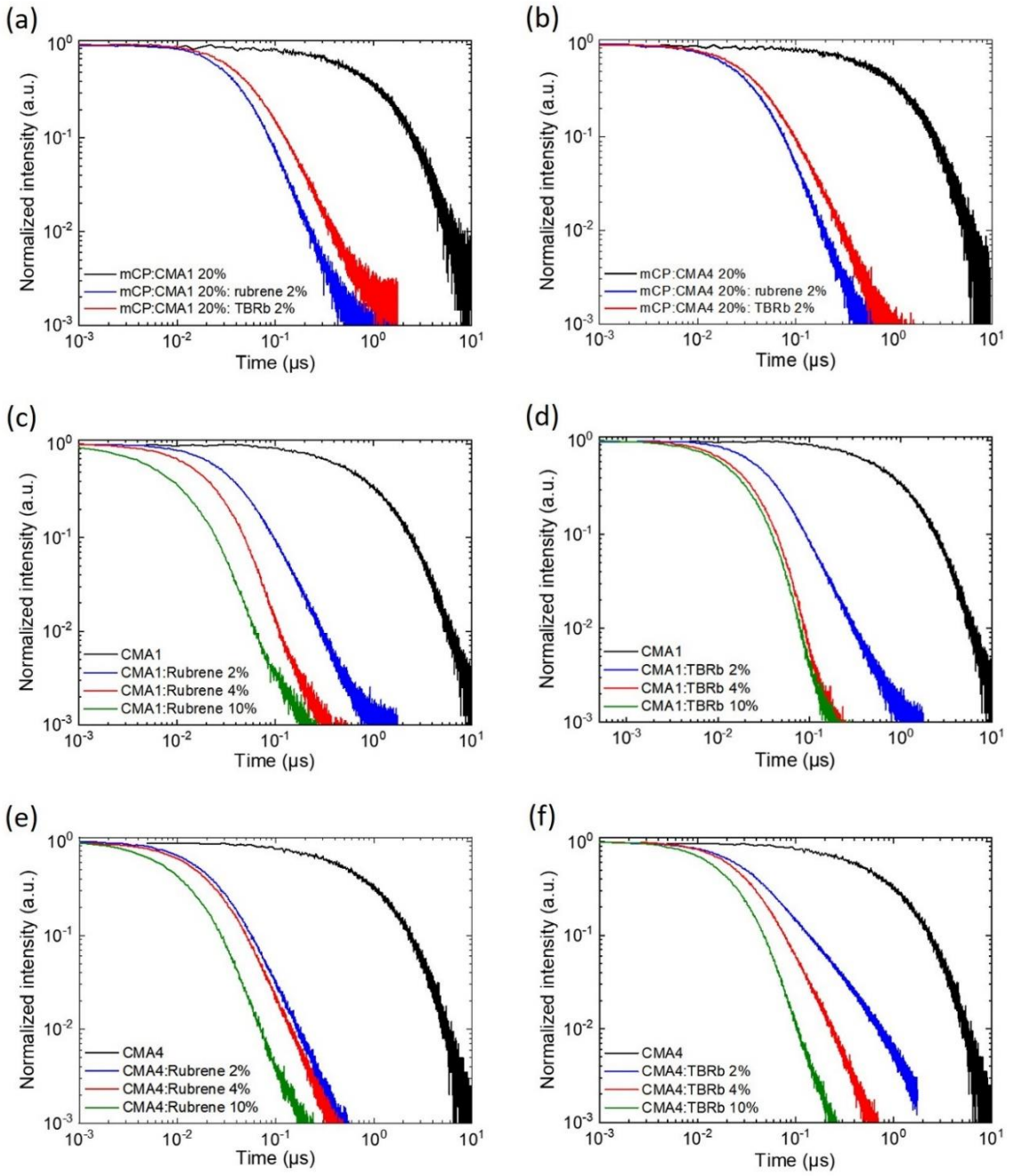

Figure 4-7. Comparison of transient PL kinetics. (a) and (b) show the transient PL for dopant-free mCP:CMA1 or CMA4 20% and rubrene or TBRb doped in mCP:CMA1 or CMA4 20% films. (c), (d), (e), and (f) display the transient PL for dopant-free CMA1 or CMA4 and rubrene or TBRb doped in CMA1 or CMA4 films.

$$\eta = \frac{k_{\mathrm{r,CMA}} + k_{\mathrm{FRET}}}{k_{\mathrm{r,CMA}} + k_{\mathrm{nr,CMA}} + k_{\mathrm{FRET}} + k_{\mathrm{DET}}} \tag{4-6}$$

i.e., the fluorescent emitter acts as a radiative sink for singlets and a nonradiative sink for triplets. These expressions are valid, assuming the fluorescent dyes have close to unity PLQE with radiative decay rates much higher than $k_{r,\mathrm{CMA}}$. PLQE for both rubrene and TBRb is close to unity, negligible concentration quenching is expected, and their radiative rates are of order 10^9 s^{-1}.[198,199] k_{DET} can, therefore, be approximated from Equation 4-3~6 as

$$k_{\mathrm{DET}} \approx \tau^{-1} - k_{nr,CMA} - k_{\mathrm{r,CMA}} - k_{\mathrm{FRET}} \tag{4-7}$$

while k_{FRET} may be obtained from Equation 4-2 and 4-4 as

$$k_{\mathrm{FRET}} \approx \frac{\eta}{\tau} - k_{\mathrm{r,CMA}} \tag{4-8}$$

η and τ are determined for each experiment, and $k_{\mathrm{r,CMA}}$ and $k_{\mathrm{nr,CMA}}$ are obtained from single-component films. The decay time and rate constants are summarised in Table 4-3. Figure 4-6(b) shows the ratio of k_{FRET} and k_{DET} depending on the host-dopant combination and doping concentration. Regarding the CMA:rubrene mixed films, the dominance of DET over FRET at all doping concentrations explains their poor PLQE performance and precludes the use of rubrene-based composites in MFHF OLEDs. k_{DET} and k_{FRET} for CMA:TBRb mixed films are much more similar, with CMA4:TBRb, which is the most promising candidate by this metric, explaining its relatively good PLQE performance even at higher doping concentrations. Thus, it is inferred that steric hindrance between the bulkier hosts and dopants is effective in suppressing DET in these composites. The slight deviation from the monotonic increase at CMA4:TBRb 2% is probably due to the fact that tert-butyl substituents in both CMA4 and TBRb increase intermolecular distance causing less efficient FRET at low doping.

Table 4-3. Summary of decay lifetime, radiative decay rate, FRET rate, DET rate, and FRET efficiency with respect to the doping concentration in CMA1, CMA4, mCP:CMA1, and mCP:CMA4.

Doping (%)		Rubrene				TBRb		
		0	2	4	10	2	4	10
mCP:CMA1	τ (μs)	1.19	0.046	-	-	0.077	-	-
	k_r (/μs)	0.70	17.02	-	-	9.64	-	-
	k_{FRET} (/μs)	-	16.30	-	-	8.92	-	-
	k_{DET} (/μs)	-	4.80	-	-	3.39	-	-
	E_{FRET} (%)	-	95.7	-	-	92.5	-	-
CMA1	τ (μs)	1.15	0.063	0.027	0.018	0.068	0.021	0.018
	k_r (/μs)	0.72	5.98	9.21	4.52	8.31	17.48	12.72
	k_{FRET} (/μs)	-	5.26	8.49	3.80	7.59	16.76	12.00
	k_{DET} (/μs)	-	9.93	27.62	50.57	6.35	29.38	41.40
	E_{FRET} (%)	-	88.0	92.2	84.1	91.4	95.9	94.3
mCP:CMA4	τ (μs)	1.22	0.042	-	-	0.066	-	-
	k_r (/μs)	0.67	15.71	-	-	11.18	-	-
	k_{FRET} (/μs)	-	15.04	-	-	10.51	-	-
	k_{DET} (/μs)	-	7.74	-	-	3.93	-	-
	E_{FRET} (%)	-	95.6	-	-	93.7	-	-
CMA4	τ (μs)	1.10	0.041	0.033	0.017	0.23	0.051	0.023
	k_r (/μs)	0.69	8.32	5.68	4.29	2.00	9.93	17.38
	k_{FRET} (/μs)	-	7.63	4.99	3.60	1.31	9.24	16.69
	k_{DET} (/μs)	-	16.21	24.38	52.94	2.44	9.77	25.64
	E_{FRET} (%)	-	91.7	87.9	83.9	65.6	93.1	96.0

4.6 Device characterisation

In light of these photophysical results, TBRb was chosen as a dopant for MFHF OLEDs. Figure 4-8(a) shows the device structure and schematic energy level diagram. 1,1-bis[(di-4-tolylamino)phenyl]cyclohexane (TAPC) and 2,2',2''-(1,3,5-benzinetriyl)-tris(1-phenyl-1-H-benzimidazole) (TPBi) were employed as a HTL and an ETL, respectively. 1,4-bis(triphenylsilyl) benzene (UGH2) with 10% of TPBi was applied to improve charge balance in the EML.[197] The layers of TBRb 0, 2, 4, and 10% doped in CMA1 or CMA4 served as an EML for MFHF. For comparison, mCP was used as a host matrix for conventional hyperfluorescent devices using the same donor-acceptor mix. CMA1- and CMA4-based hyperfluorescent devices were successfully fabricated; their EL spectra are displayed in Figure 4-8(b)-(d). As anticipated, as doping concentration increases, the proportion of CMA1 and CMA4 emission decreases as per the PL spectra shown in Figure 4-5.

The device characteristics are summarised in Table 4-4, and Figure 4-9 shows plots of EQE versus current density and PE versus luminance as the doping concentration of TBRb varies. Also, the characteristics of current density and luminance versus voltage are plotted in Figure 4-10. It is noticeable that CMA1-based devices show much lower turn-on voltage than CMA4-based ones (3.3 V vs 4.3~4.5 V for the MFHF devices and 3.5 V vs 4.3 V for the devices with a host matrix), mainly due to the difference of electrical properties between CMA1 and CMA4. In terms of CMA1-based devices, the devices with a host matrix exhibit somewhat higher EQE than the MFHF counterparts. MFHF devices with higher doping concentrations of TBRb show lower EQEs, which is well-correlated with the values of PLQE shown in Table 4-2. The maximum EQE of the CMA1-based MFHF OLED is 15.2% at 2% doping

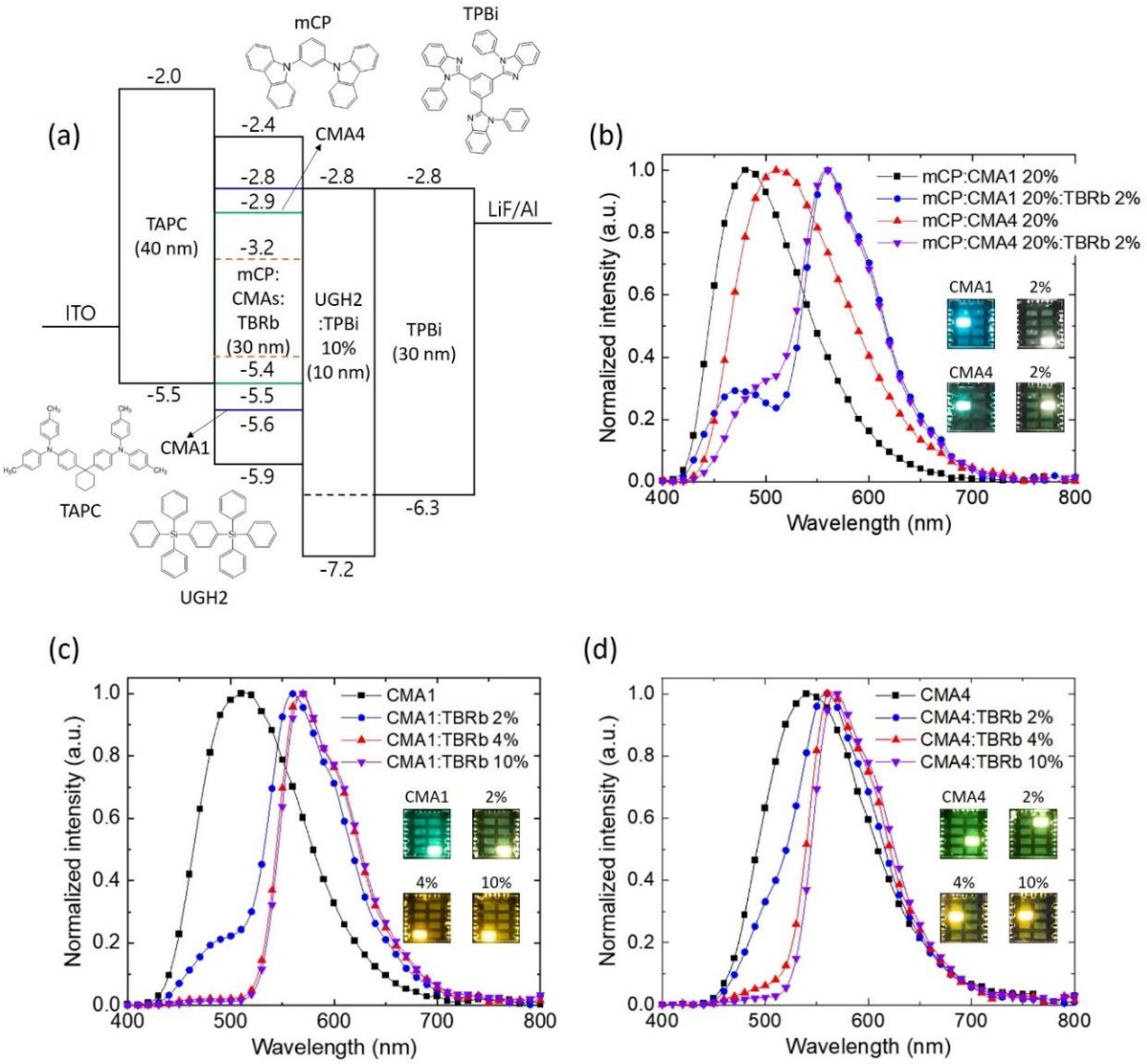

Figure 4-8. (a) Device structure and energy diagram of CMA-based hyperfluorescent OLEDs. (b) EL spectra of the mCP:CMA1- and mCP:CMA4-based devices with and without TBRb doping. (c) and (d) show EL spectra of the devices based on CMA1 and CMA4 with varying TBRb concentration.

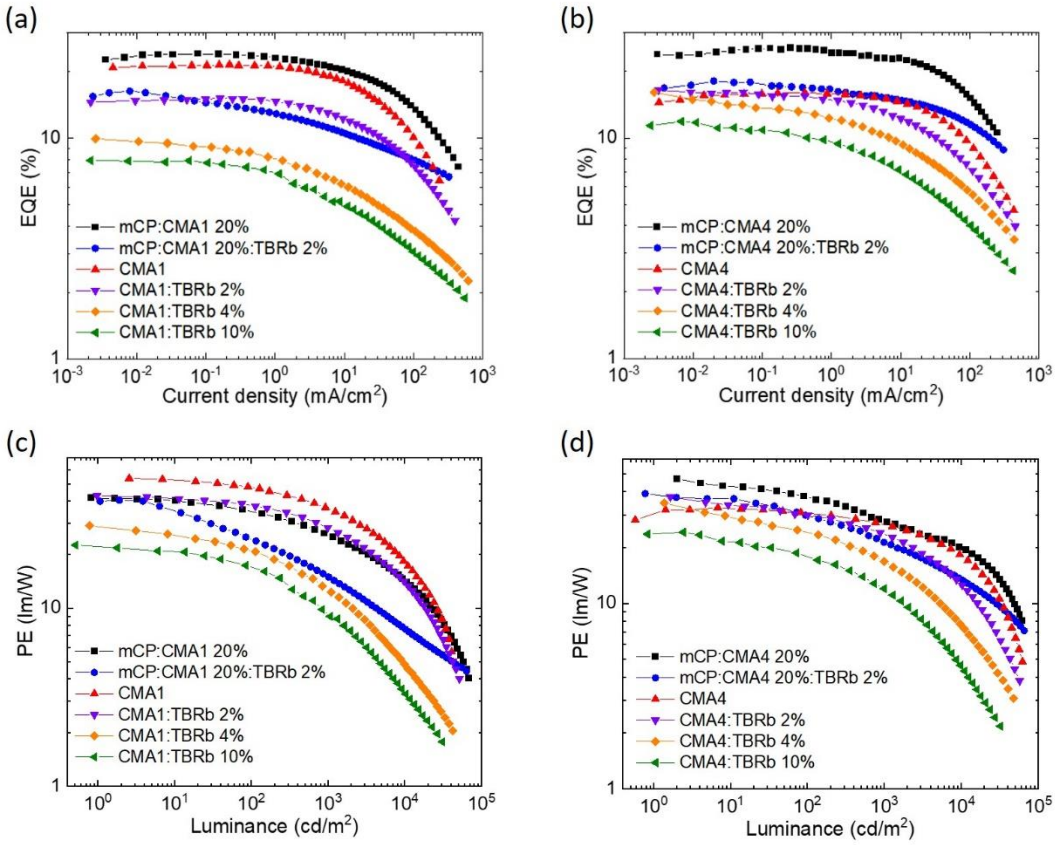

Figure 4-9. Characteristics of hyperfluorescent OLED devices based on CMA1 and CMA4 with TBRb doping. (a) and (b) present EQE vs current density. (c) and (d) show PE vs luminance.

concentration. As shown in Table 4-4, at 2% doping concentration, the MFHF device shows 2.6 V lower driving voltage and nearly two-times higher PE at a brightness of 1000 cd/m^2 than the device incorporating a host matrix. In addition, 40% higher PE at 1000 cd/m^2 is observed in the dopant-free CMA1-based device compared to the mCP:CMA1-based counterpart. This clearly shows that the wide-gap host matrix adversely affects device efficiency. Regarding the CMA4-based hyperfluorescent devices, the maximum EQE for the MFHF device at 2% doping concentration is 16.5%, while that for the device with mCP is 18.1%. Like the CMA1-based devices, the driving

voltage for the CMA4-based MFHF devices is reduced compared to the mCP:CMA4-based devices, showing about 10% higher PE at 1000 cd/m^2 despite the lower EQE at 2% TBRb concentration. From this, it is concluded that both CMA4 and the mCP host act to increase driving voltage. In addition, even in 10% doping concentration, the EQE of the CMA4-based device is still high, over 11.9%, which is associated with the high PLQE value and the suppressed DET, as shown in Table 4-2 and Figure 4-6(b).

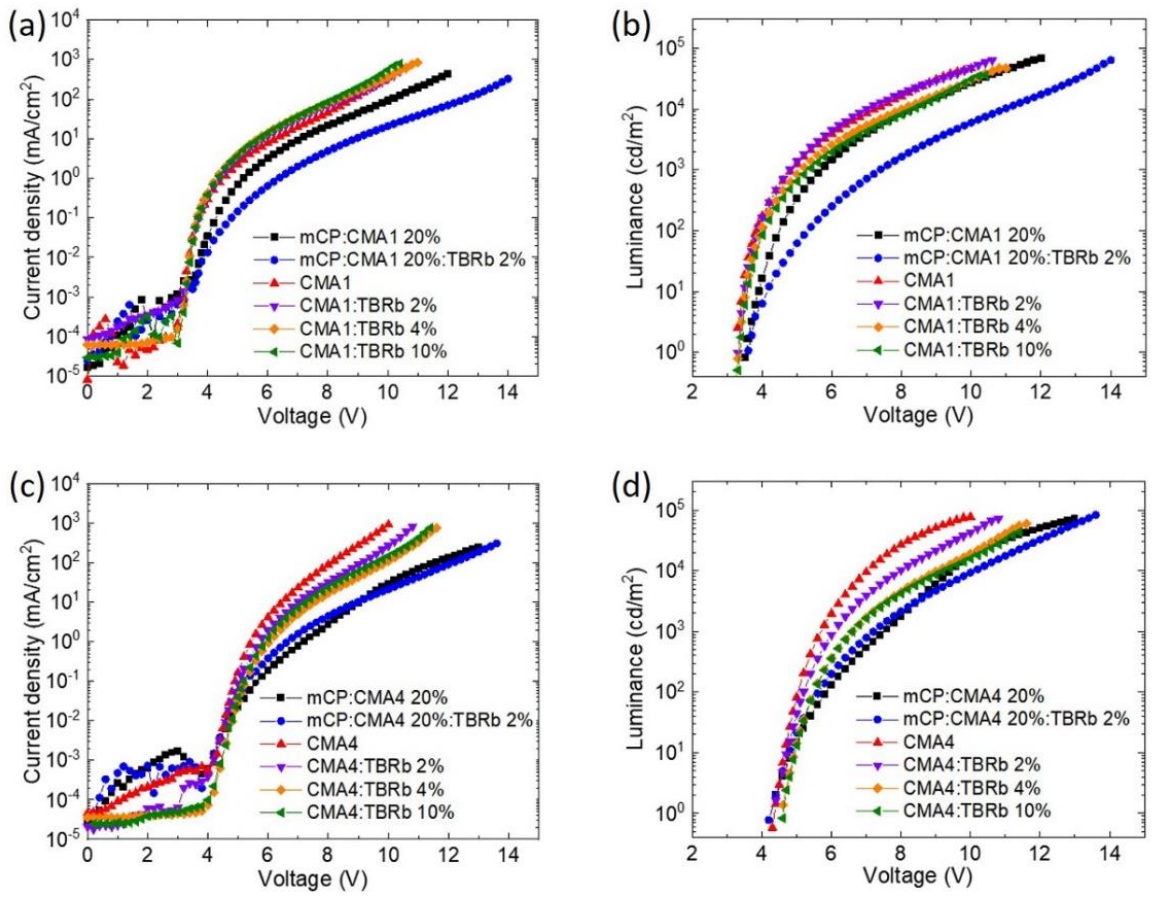

Figure 4-10. Characteristics of current density vs voltage and luminance vs voltage. (a), (b) CMA1-based devices. (c), (d) CMA4-based devices.

Table 4-4. Summary of the performance for the hyperfluorescent OLED devices.

	Doping (%)	V_{on}[a)] (V)	$V_{1000\ nit}$ (V)	EQE_{Max} (%)	$EQE_{1000\ nit}$ (%)	PE_{Max} (lm/W)	$PE_{1000\ nit}$ (lm/W)	CIE (x,y)
mCP:CMA1	0	3.5	5.7	24.1	22.4	41.5	25.8	(0.206, 0.336)
	2	3.6	7.4	16.3	11.9	40.3	15.0	(0.405, 0.453)
CMA1	0	3.3	4.8	21.5	20.7	55.5	36.3	(0.274, 0.466)
	2	3.3	4.8	15.2	14.0	43.5	29.0	(0.431, 0.494)
	4	3.3	5.1	9.9	6.8	29.0	12.7	(0.501, 0.486)
	10	3.3	5.3	7.9	5.2	22.6	9.2	(0.508, 0.481)
mCP:CMA4	0	4.3	7.5	25.6	24.2	47.0	27.8	(0.294, 0.473)
	2	4.3	7.2	18.1	15.8	39.1	21.3	(0.411, 0.497)
CMA4	0	4.4	5.7	16.0	15.7	32.9	26.7	(0.375, 0.541)
	2	4.4	6.1	16.5	14.3	37.6	23.7	(0.423, 0.524)
	4	4.6	6.6	16.1	11.2	34.8	16.9	(0.481, 0.502)
	10	4.6	6.6	11.9	8.3	24.2	12.0	(0.503, 0.487)

[a)]At 1 cd/m^2

4.7 Analysis of charge transporting properties based on device characteristics

When the host matrix is not applied, the TADF donors have to play a role in charge transport usually handled by the host matrix, as well as energy transfer. Therefore, it is vital to understand the charge transporting properties of CMAs in addition to energy transfer between CMAs and fluorescent acceptors for designing

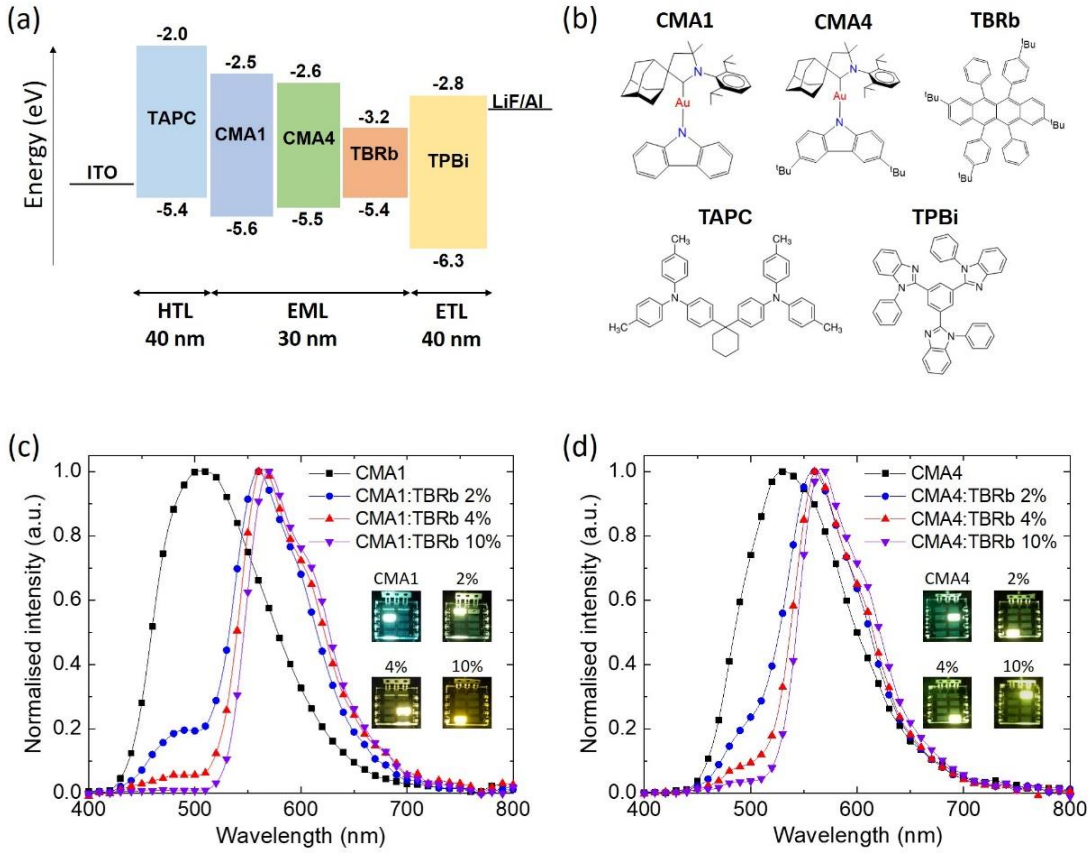

Figure 4-11. (a) Device architecture and energy level diagram with (b) chemical structures of CMA1, CMA4, TBRb, TAPC, and TPBi. (c) and (d) show EL spectra of the devices based on CMA1 and CMA4 with varying TBRb concentration.

appropriate device architectures for high efficiency.

To compare the different electrical properties between CMA1 and CMA4 more directly in EL devices, the UGH2:TPBi 10% 10 nm layer was removed from the device structure, as shown in Figure 4-11(a). This layer was inserted between EML and ETL as a HBL for high efficiency, as shown in Figure 4-8(a), but it was not utilised here for investigating the effect of the different donors on device performance in terms of the charge transporting properties since it impedes electron injection and transport to the

EML. The CMA-based EL devices shown in Figure 4-11(a) were successfully fabricated by a thermal evaporation process with variation of doping concentrations. Figure 4-11(c) and (d) show the EL spectra of the CMA1- and CMA4-based devices. As the doping concentration of TBRb is increased, the proportion of the CMA1 and CMA4 contribution to EL is reduced, like the EL spectra in Figure 4-8(c) and (d).

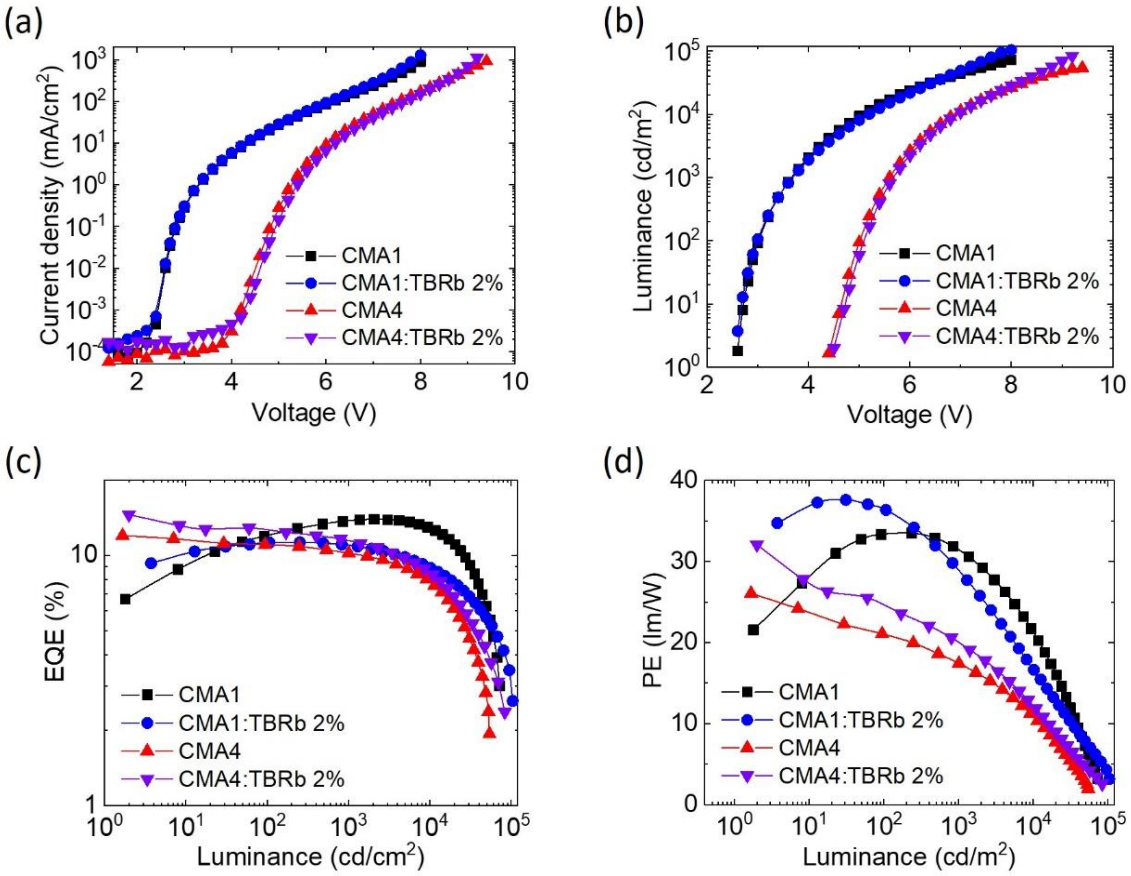

Fig. 4-12. Optoelectronic performance of the OLED devices based on CMA1 and CMA4 and with 2% TBRb doping concentration. (a) Current density versus voltage. (b) Luminance versus voltage. (c) EQE versus luminance. (d) PE versus luminance.

The device performance of the CMA1- and CMA4-based devices at 2% doping is shown in Figure 4-12 to directly compare the differences between them, and the specific device performance of all devices with varying doping concentrations is shown in Table 4-5 and Figure 4-13 and 4-14. Figure 4-12(a) and (b) show the J-V and luminance-voltage (L-V) characteristics of the CMA1- and CMA4-based devices with and without TBRb 2% doping. The turn-on and driving voltage of the devices employing CMA4 rose substantially compared to those using CMA1. It is noticeable that the CMA1-based devices reach high current density and luminance much faster than the CMA4-based counterparts corresponding to the faster charge transporting properties of CMA1 than CMA4. The turn-on and driving voltages of CMA4 are 4.3 V and 5.7 V, almost 2 V higher than CMA1, 2.5 V and 3.7 V, respectively.

Figure 4-12(c) exhibits the EQE vs luminance plots. The EQEs of the CMA1-based devices below 100 cd/m^2 are lower than those of the CMA4-based counterparts. It can be interpreted that while both hole and electron transport in CMA4 are quite slow, the higher hole transport than electron transport in CMA1 causes charge imbalance in the low current density region, reducing EQE. The maximum EQE values for CMA1-based devices with and without TBRb doping are 11.3% and 13.9%, whereas 14.5% and 12.0% are recorded from the CMA4-based counterparts, respectively. When it comes to PE shown in Figure 4-12(d), the maximum PE values of the CMA1-only and TBRb-doped devices are 33.5 lm/W and 37.6 lm/W, which are higher than the CMA4-based counterparts, 26.1 lm/W and 32.1 lm/W, respectively. As luminance increases, the disparity of the PE between the devices becomes more prominent. For example, at 1000 cd/m^2, the PE values of the CMA4-based devices are 17.4 lm/W and 20.1 lm/W, whereas those of the CMA1-based counterparts are 31.5 lm/W and 29.0 lm/W, showing approximately 80% and 50% higher values, respectively. This result originates from the substantial difference in turn-on (2.5 V vs 4.3 V) and driving voltage (3.7 V vs

Table 4-5. Summary of the device performance.

	Doping (%)	V_{on}[a)] (V)	V_{1000}[b)] (V)	EQE_{Max} (%)	EQE_{1000}[b)] (%)	PE_{Max} (lm/W)	PE_{1000}[b)] (lm/W)	CIE (x,y)
CMA1	0	2.5	3.7	13.9	13.7	33.5	31.5	(0.267,0.444)
	2	2.5	3.7	11.3	11.0	37.6	29.0	(0.429,0.494)
	4	2.5	3.8	9.6	8.7	31.8	21.3	(0.477,0.493)
	10	2.5	4.1	7.1	5.4	24.0	12.0	(0.513,0.480)
CMA4	0	4.3	5.6	12.0	10.2	26.1	17.4	(0.349,0.536)
	2	4.3	5.7	14.5	11.5	32.1	20.1	(0.426,0.524)
	4	4.3	5.7	12.8	10.7	27.9	18.7	(0.461,0.512)
	10	4.4	5.9	10.8	8.1	22.4	13.1	(0.491,0.495)

[a)]Voltage at 1 cd/m^2, [b)]At 1000 cd/m^2

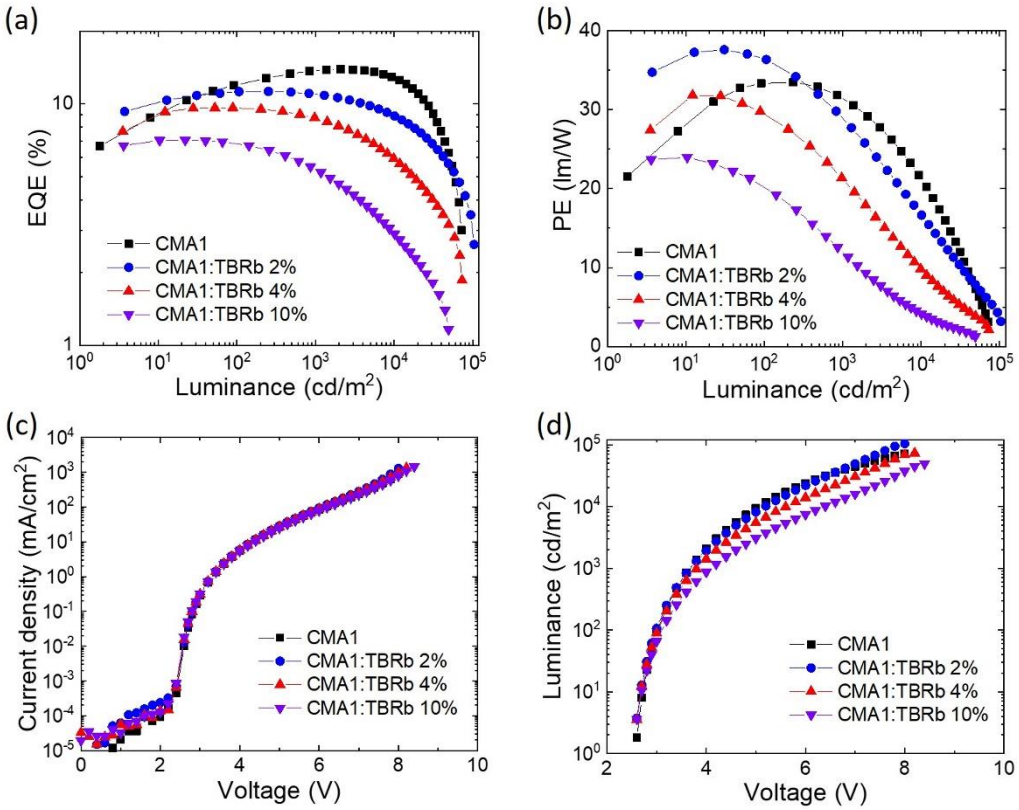

Fig. 4-13. Characteristics of hyperfluorescent OLED devices employing CMA1 with varying TBRb concentration. (a) and (b) EQE and PE versus luminance. (c) and (d) current density and luminance versus voltage.

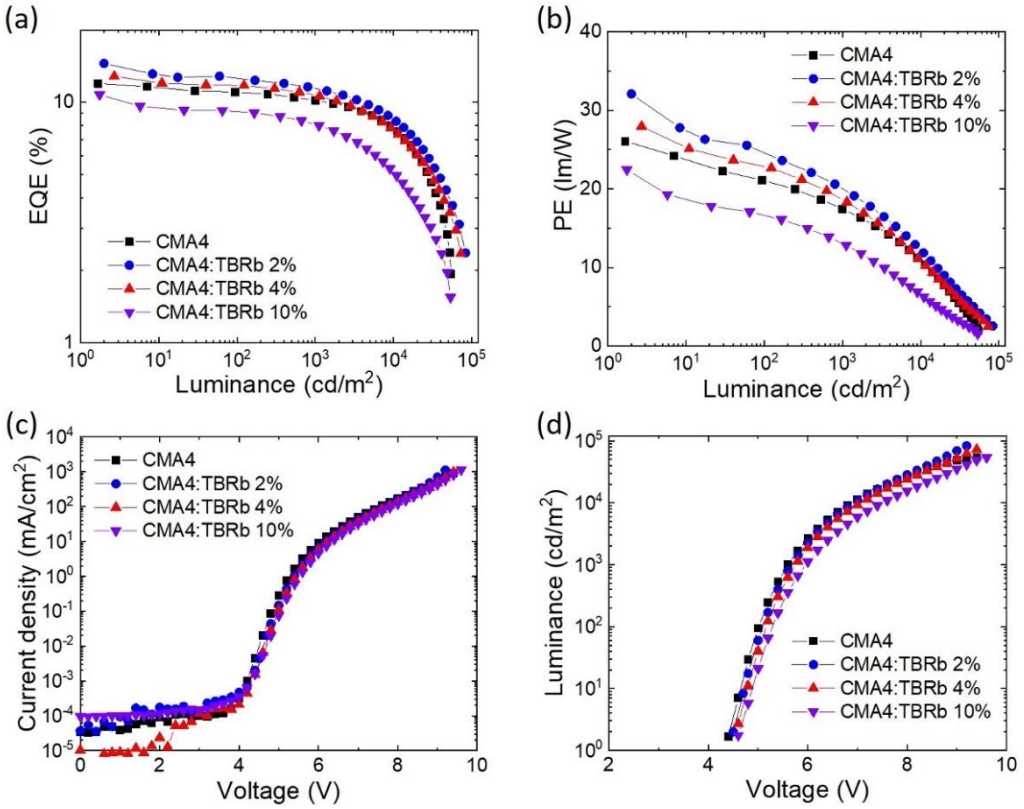

Fig. 4-14. Characteristics of hyperfluorescent OLED devices employing CMA4 with varying TBRb concentration. (a) and (b) EQE and PE versus luminance. (c) and (d) Current density and luminance versus voltage.

5.7 V) between the CMA1- and CMA4-based devices. Accordingly, it can be inferred that the considerable disparity in the device performance originates from the different electrical properties between CMA1 and CMA4 since all other conditions and materials utilised in the devices are identical. Furthermore, it can interpreted why the turn-on voltages for the CMA4-based devices stay almost the same regardless of the presence of the HBL while those for the CMA1-based devices are reduced from 3.3 V to 2.5 V when the HBL is excluded. Due to the much slower charge transport in CMA4 than in CMA1, the turn-on voltages do not change in the CMA4-based devices even though the HBL hindering electron transport is removed.

4.8 Single-carrier device analysis

To confirm the different charge transporting properties, single-carrier devices were fabricated. Figure 4-15(a) displays the chemical structures of CMA1, CMA4, 1,4,5,8,9,11-hexaazatriphenylene hexacarbonitrile (HATCN), and bis-4,6-(3,5-di-3-pyridylphenyl)- 2-methylpyrimidine (B3BYMPM), and Fig. 4-15(b) and (c) show the

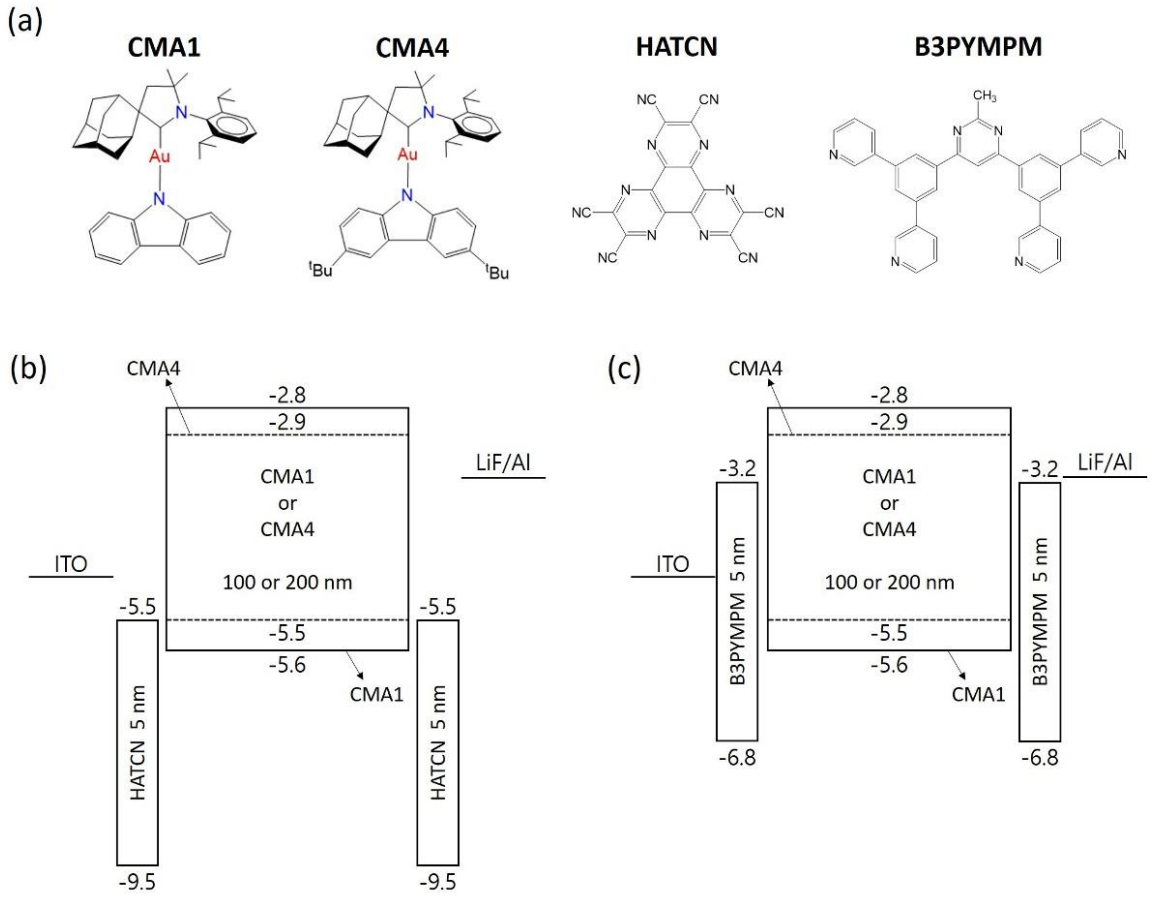

Figure 4-15. (a) Chemical structures of CMA1, CMA4, HATCN, and B3PYMPM. (b) and (c) show the device architectures of HOD and EOD. CMA1 and CMA4 are sandwiched by HATCN and B3PYMPM for HOD and EOD, respectively, to allow hole- and electron-only current.

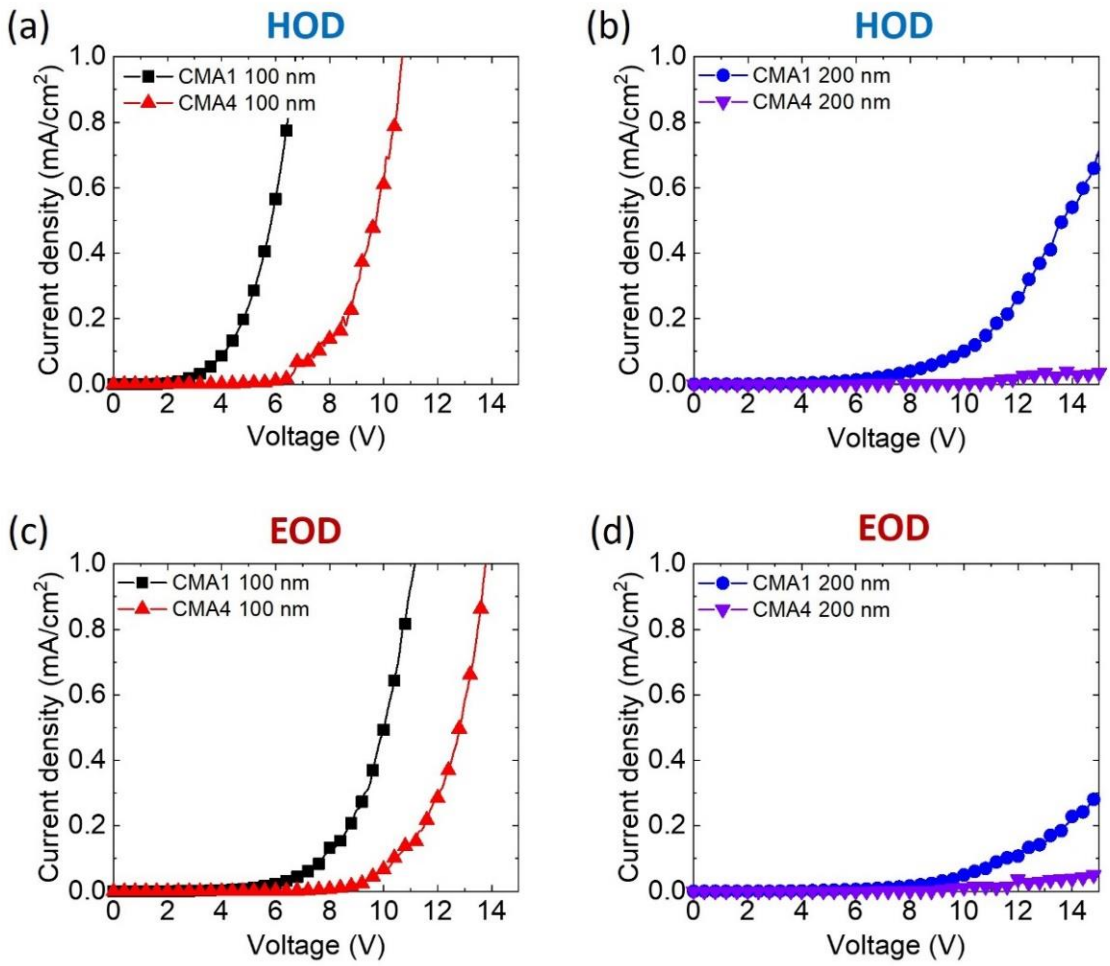

Figure 4-16. J-V characteristics of HOD and EOD for CMA1 and CMA4 with the thickness of 100 nm and 200 nm. (a) and (b) show HOD plots, and EOD curves are depicted in (c) and (d). Both hole and electron transport for CMA4 are much slower than CMA1. Also, hole current is faster than electron current.

device structure of HOD and EOD. As CMAs are bipolar-type materials consisting of electron-donating (carbazole part) and electron-accepting (carbene part) moieties, it is important to design HOD and EOD structures with proper buffer layers to leave a single carrier current in the CMA layer. HATCN has been widely utilised as a HIL or charge generation layer (CGL) due to its distinct energy level.[70–75] The LUMO of HATCN is

-5.5 eV, well-aligned with an anode, improving hole injection to an EML. Also, HATCN effectively prevents electron injection considering more than a 2 eV difference in LUMO energy levels between HATCN and CMAs. On the other hand, B3PYMPM is capable of effectively blocking hole injection due to its HOMO energy level of -6.8 eV. Therefore, HATCN and B3BYMPM with a thickness of 5 nm were employed to sandwich CMA1 and CMA4 layers for HODs and EODs to make the single carrier current. Also, the thickness of 100 nm and 200 nm for CMA1 and CMA4 layers were used to compare charge-transporting properties in the different thicknesses of the layers.

Figure 4-16 shows the comparison of the J-V characteristics of HODs and EODs for CMA1 and CMA4. Overall, the charge transporting abilities of CMA4 are much lower than CMA1, considering the much shallower J-V curves. This is attributed to the addition of *tert*-butyl substituents in CMAs, given that the inert moieties significantly affect carrier mobility in an amorphous film by increasing structural disorder and separation distance, reducing intermolecular interaction.[99,190,204] Also, hole transport is faster than electron transport for both CMA1 and CMA4, suggesting that the additional layer between EML and ETL for preventing hole leakage in an EML is necessary to enhance efficiency in EL devices. To examine the charge transporting properties in CMAs specifically, the charge mobility of CMA1 was estimated from SCLC behaviour.

With the increase of voltage, the variation of current density follows SCLC characteristics, which can be expressed by the Mott-Gurney law,

$$J = \frac{9}{8}\varepsilon\varepsilon_0\mu\frac{V^2}{L^3} \tag{4-9}$$

where J is the current density, ε is the relative dielectric constant, ε_0 is the permittivity of the free space, μ is the carrier mobility, L is the thickness of the organic layer, and V is the voltage. However, μ is dependent on the electric field due to the randomly

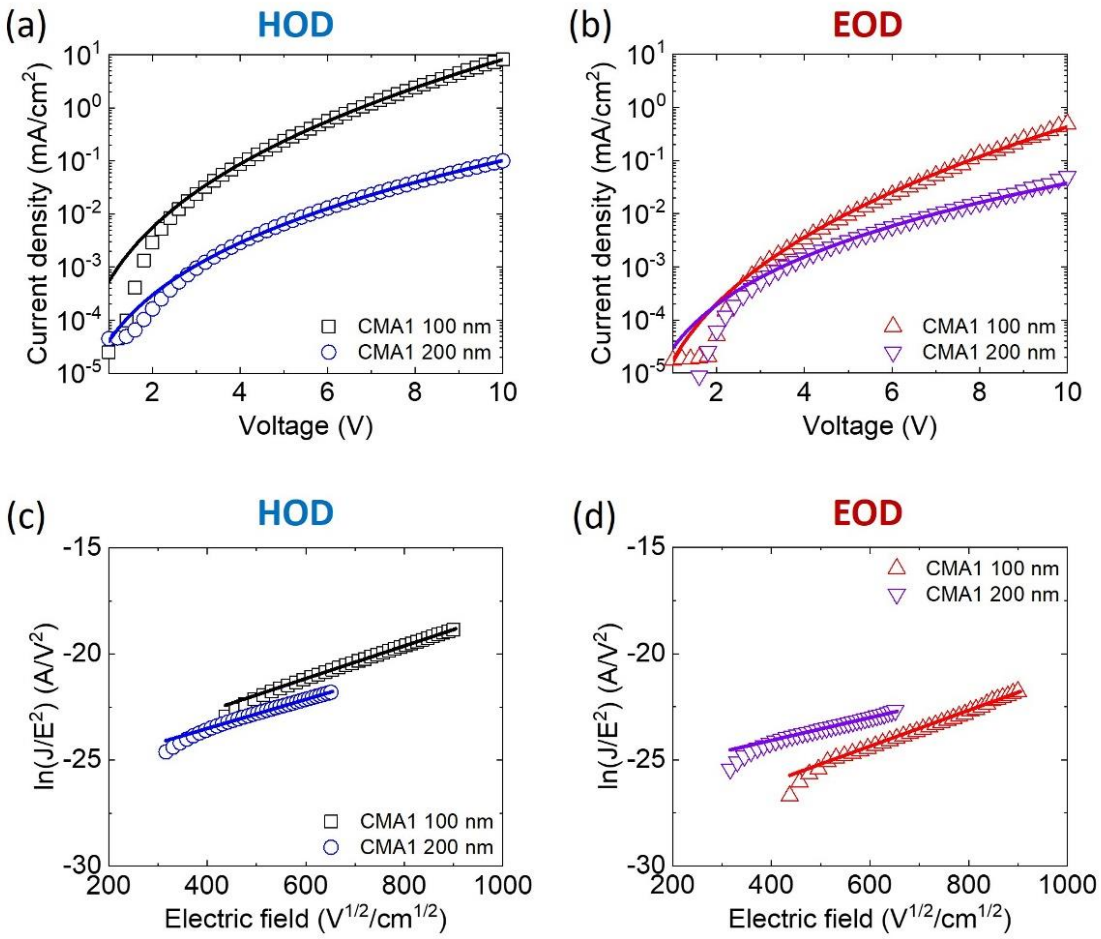

Fig. 4-17. The HOD and EOD characteristics of CMA1. (a) and (b) show J-V characteristics of HOD and EOD for CMA1 with the fitting by the SCLC equation. Slight deviation from the measured values under 3V means the presence of traps. The characteristics of $\ln(J/E^2)$ vs $\sqrt{E}$ for CMA1 are depicted in (c) and (d). The solid lines represent fits to SCLC behaviour.

oriented and located dipoles in the organic film, which can be generally expressed by the Poole-Frenkel equation,

$$\mu(E) = \mu_0 \exp(\gamma\sqrt{E}) \tag{4-10}$$

where μ_0 is the zero-field mobility, γ is the field activation of the mobility, E is the

electric field (V/L). From equation 4-9 and 10, Murgatroyd approximated the SCLC equation expressed as[148]

$$J = \frac{9}{8}\varepsilon\varepsilon_0\frac{V^2}{L^3}\mu_0\exp(0.891\gamma\sqrt{E}) \quad (4\text{-}11)$$

Figure 4-17(a) and (b) show the J-V characteristics of HODs and EODs for CMA1 with the thickness of 100 nm and 200 nm. The solid curves are fits by Equation 4-11, and the slight deviation from the measured current density at the low voltage region means the presence of traps. In general, there are three regions in J-V curves, ohmic region, trap-SCLC region, and trap-free SCLC region.[150–152] As the electric field begins to be applied, J-V curves initially follow the ohmic region and reach the trap-SCLC region. As more voltage is applied, traps are filled with charges, and the J-V characteristics become highly associated with electric field-dependent SCLC behaviour described by Equation 4-11. Figure 4-17(c) and (d) show the electric field dependent J/E^2. The fitted lines and the experimental data coincide with each other, showing that the current follows electric field-dependent SCLC in the selected region. γ and μ_0 can be obtained from the slope and the intercept, respectively. ε_0 is 8.8542×10^{-12} C/V·cm, and ε for CMA1 is set by 3.

Figure 4-18 shows the calculated hole and electron mobility for CMA1 dependent on the electric field. The solid lines mean the fitting by Equation 4-11. Concerning the thickness effect, while the hole mobility is less affected by the thickness increase, the electron mobility rises as the thickness increases. This tendency was also observed in the previous reports studying the charge mobility of organic semiconductors based on SCLC analysis, suggesting an interface effect.[155,156] In the EOD structure of this work, there is an energy barrier of 0.4 eV between the LUMO energy levels of CMA1 and B3PYMPM (Figure 4-15), preventing fluent electron

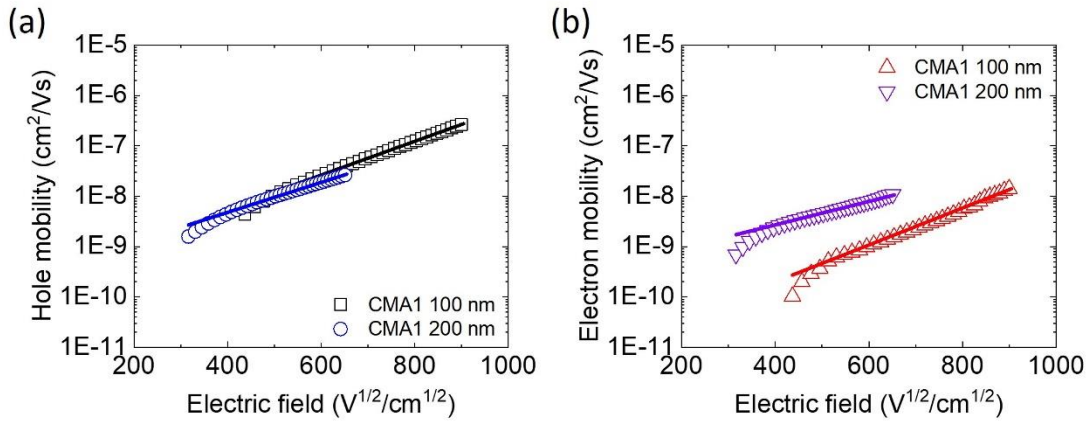

Figure 4-18. Electric field dependent (a) hole and (b) electron mobility for CMA1 in the 100 nm and 200 nm thick layers. The solid lines are fits by Equation 4-11.

Table 4-6. Zero-field mobility, field activation, carrier mobility at 0.7 MV/cm for the thickness of 100 nm and at 0.3 MV/cm for the thickness of 200 nm.

		μ_0 (cm^2/Vs)		γ (cm/V)		μ (cm^2/Vs)	
		hole	electron	hole	electron	hole	electron
CMA1	100 nm	2.58×10^{-10}	6.81×10^{-12}	8.65×10^{-3}	9.47×10^{-3}	1.63×10^{-7}	7.87×10^{-9}
	200 nm	3.08×10^{-10}	3.17×10^{-10}	7.69×10^{-3}	6.02×10^{-3}	1.34×10^{-8}	5.83×10^{-9}

injection at a low electric field and causing the slight deviation of electron mobility depending on thickness. Regarding HOD, due to the distinct energy levels of HATCN, the LUMO energy level of HATCN and the HOMO energy levels of CMA1 and CMA4 are well-aligned (Fig. 4-15(b)). Thus, under this energy level arrangement, electrons in CMA1 and CMA4 layers can be easily transported to HATCN with a negligible energy barrier, leading to the hole mobility being insensitive to thickness. The calculated values of zero-field mobility, field activation, and carrier mobility at 0.7 MV/cm and

0.3 MV/cm for the 100 nm and 200 nm thick layers are summarised in Table 4-6. As expected from the J-V characteristics, hole mobility is 1.63×10^{-7} cm^2/Vs at 0.7 MV/cm for 100 nm and 1.34×10^{-8} cm^2/Vs at 0.3 MV/cm for 200 nm, higher than electron mobility, 7.87×10^{-9} cm^2/Vs at 0.7 MV/cm for 100 nm and 5.83×10^{-9} cm^2/Vs at 0.3 mV/cm for 200 nm, respectively.

4.9 Summary

In summary, MFHF OLEDs were successfully demonstrated with CMA materials as a donor of excitons. High PLQE in neat films and effective energy transfer to exciton acceptors (fluorescent dopants) indicate the high suitability of CMA materials in this role. This two-component device architecture is particularly sensitive to DET processes, which can be reduced through the addition of steric *tert*-butyl substituents on both donor and acceptor molecules. It is shown that the MFHF system is able to achieve up to a 90% increase in PE compared with equivalent three-component hyperfluorescent OLEDs, and this increase in performance arises due to the significantly reduced driving voltage in the MFHF devices. The maximum EQEs of the CMA1 and CMA4 MFHF devices (15.2% and 16.5%) are reduced by only 5-10% versus devices incorporating a host matrix (16.3% and 18.1%), which was identified as the result of increased DET.

Also, the charge transporting properties of CMAs were investigated on the basis of single-carrier and EL devices. The CMA1-based EL devices showed far higher PE with nearly 2.0 V lower turn-on and driving voltages than the CMA4-based counterparts. These results show that steric hindrance in chemical structure considerably affects the electrical properties of CMAs associated with optoelectronic

properties. To understand the different electrical abilities between CMA1 and CMA4, HODs and EODs for CMA1 and CMA4 were examined. The hole and electron transport in CMA4 were much slower than in CMA1 due to the bulkier chemical structure of CMA4 resulting from *tert*-butyl substituents increasing intermolecular spacing and weakening intermolecular interaction. From single-carrier devices with SCLC analysis, the carrier mobility of CMA1 was obtained. It was interpreted that the higher hole mobility of CMA1 than the electron resulted in the lower EQE of the devices when an HBL was not utilised.

In conclusion, the exciton energy transfer and charge transport in CMA-based hyperfluorescent OLEDs were investigated with photophysical studies and device characterisation. It was demonstrated that CMAs could play a role in effective exciton donors to fluorescent acceptors for realising efficient MFHF OLEDs. Also, the effect of inert moieties on the charge transporting properties of the exciton donor molecules was explored based on the investigation of single-carrier devices and device characterisation. On the basis of the results, it is envisaged that with further work, two-component hyperfluorescent OLEDs may become the next industry-preferred method to enhance OLED device performance.

Chapter 5 Covalently encapsulated fluorophors for efficient deep blue hyperfluorescent OLEDs with narrow emission

5.1 Introduction

Hyperfluorescence is considered one of the most promising contemporary solutions to the blue OLED problem, combining the high efficiency of TADF with the stability and colour purity of conventional fluorescent emitters. There have been a variety of studies on this concept utilising diverse combinations of TADF sensitisers and fluorescent acceptors to afford almost 100% IQE.[188–194] The realisation of efficient blue hyperfluorescent devices has been considered quite challenging as, naturally, a deep blue TADF sensitiser is necessary for efficient FRET to a blue fluorescent emitter. However, even though the donor PL and acceptor absorption were not perfectly overlapped, high efficiency and stability with narrow emission have been attained from blue hyperfluorescent OLEDs utilising MR TADF emitters as exciton acceptors, indicating the promise of the hyperfluorescence strategy towards stable blue devices satisfying the requirement for the application to displays.[21,22]

In conventional-type hyperfluorescence (CTHF) devices, the EML is a three-component system consisting of a host matrix, TADF donor, and fluorescent acceptor. Fundamentally, the primary role of the host matrix is to suppress concentration quenching and aggregation of the TADF donors as well as DET of triplets from the donor to the acceptor – two phenomena that can lead to substantial reductions in EQE.

Nevertheless, it should be taken into account that a wide-gap host matrix can reduce PE, resulting from a considerable increase in driving voltage. A three-component EML also increases the complexity of device fabrication.

In Chapter 4, a MFHF emissive system was investigated based on the combination of CMA exciton donors and the conventional fluorescent exciton acceptor, TBRb, with higher than 15% EQE and substantially improved PE over three-component CTHF reference devices. However, the complete exclusion of DET and aggregation, causing an efficiency drop for the donors and acceptors, was not possible with bulky *tert*-butyl substituents. Hence, it is essential to research more effective methods to prevent energy losses. Theoretical studies on HF OLEDs have been reported, showing that the DET from an exciton sensitiser to an exciton acceptor could be minimised by steric protection in molecular structure.[205] One of the most effective ways to achieve such steric protection is to encapsulate organic molecules.[206,207] It was demonstrated that encapsulated diphenylanthracene dyes show higher than 80% PLQE even in neat films, indicating that concentration quenching is effectively suppressed by the steric protection.[207]

In this chapter, encapsulated fluorescent dyes are studied to achieve efficient deep blue OLEDs. Firstly, the encapsulated diphenylanthracene-based fluorescent emitter is investigated with a deep blue TADF donor. Thin-film steady-state and transient photophysical studies are conducted to examine how encapsulation influences efficiency and exciton energy transfer processes. Also, CTHF and MFHF devices employing the encapsulated emitter are fabricated, and their device performance is compared. It is shown that MFHF devices using the encapsulated emitter considerably outcompete the CTHF counterparts in terms of PE, luminance, and stability. Secondly, newly designed indolocarbazole-based MR emitters are explored for high efficiency deep blue hyperfluorescent OLEDs with ultra-narrow emission. It is shown that the

encapsulation of the MR emitter core substantially prevents aggregation and energy losses via DET, which is proved by steady-state and transient photophysical studies. Also, higher than 20% EQEs are achieved in both CTHF and MFHF devices showing the disruptive potential of MFHF in deep blue EL devices. In addition, the MR emitters are applied in conventional fluorescent OLEDs, showing higher than 8% EQE with pure blue emission.

5.2 Encapsulated diphenyl anthracene for deep blue OLEDs

5.2.1 Characterisation of diphenyl anthracene derivatives: MeO-DPA and En-DPA

Synthetic details for the encapsulated 9,10-diphenylanthracene (En-DPA) and the non-encapsulated En-DPA analogue, MeO-DPA, are described in reference 207 (synthesised by Dr Dan Congrave, Department of Chemistry, University of Cambridge). En-DPA has a larger calculated Onsager cavity radius (volume) than MeO-DPA (6.54 vs 6.05 Å). Hence, the intermolecular distance between the anthracene core of En-DPA and neighbouring chromophores is expected to be larger than MeO-DPA. The increase in volume of En-DPA is due to the inclusion of nonconjugated alkyl straps. Electronic communication with neighbouring chromophores is therefore expected to be reduced, suppressing excimer formation and aggregation while also potentially suppressing DET, which requires direct chromophore orbital overlap. To clarify the difference between the two molecules in detail, the steady-state and transient PL measurements were conducted. The PL spectra of En-DPA and MeO-DPA obtained from evaporated neat films and dilute toluene solutions are compared in Figure 5-1.

The PL spectrum obtained from the neat film of En-DPA is near-identical to that recorded in solution, as expected from the literature.[207] In contrast, the MeO-DPA neat film shows a red-shifted PL spectrum compared to the solution with an increased full-

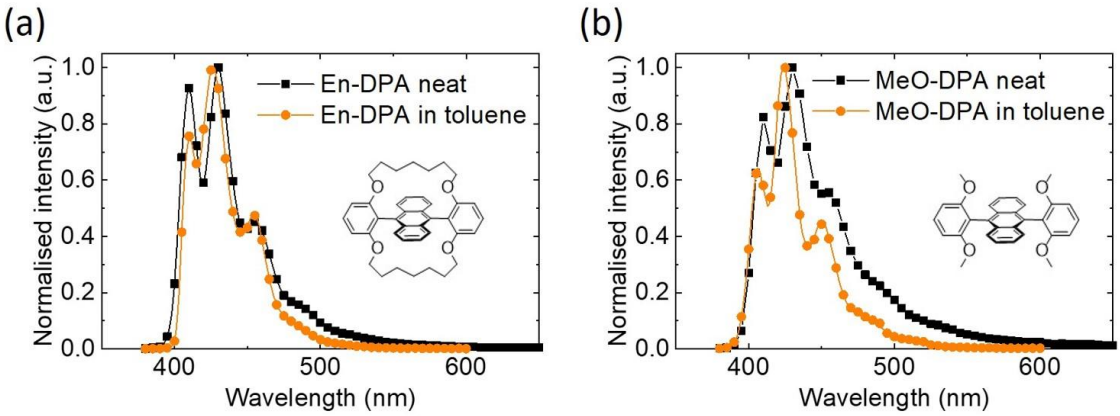

Figure 5-1. Comparison of the neat film and solution PL for (a) En-DPA and (b) MeO-DPA.

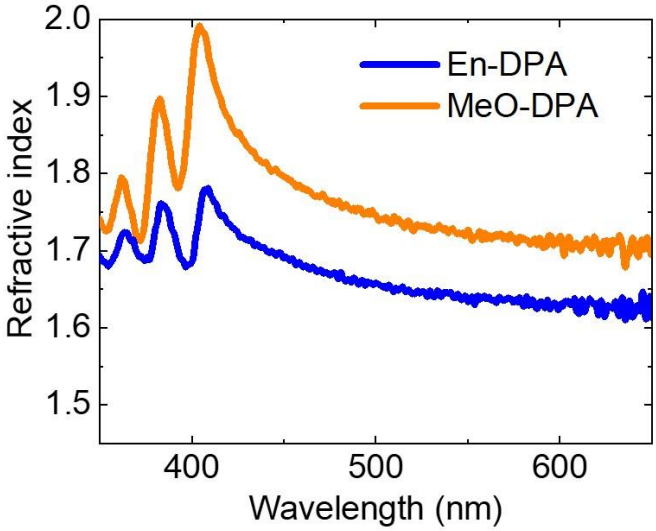

Figure 5-2. The refractive index plots measured by ellipsometry for En-DPA and MeO-DPA.

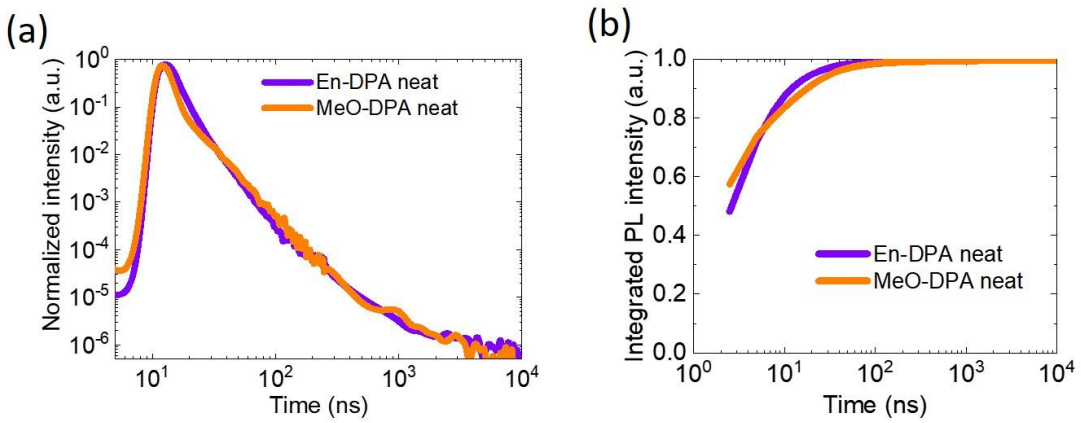

Figure 5-3. (a) Transient PL profiles and (b) integrated PL intensity for En-DPA and MeO-DPA neat films.

Table 5-1. PLQE, decay time, radiative and nonradiative decay rate for En-DPA and MeO-DPA neat films.

	PLQE (%)	τ (ns)	k_r (/ns)	k_{nr} (/ns)
En-DPA neat	84	3.28	0.255	0.050
MeO-DPA neat	43	3.38	0.128	0.168

[a)]Derived from the time when the integrated PL intensity reaches 1-(1/e).

width-half maximum (FWHM) suggestive of some contribution to the PL from aggregates. The PLQE of the En-DPA neat film is 84%, much higher than for MeO-DPA (43%), in line with the previous report,[207] indicating a reduction in aggregation and concentration quenching due to the encapsulated chemical structure of En-DPA. The relatively lower refractive index of En-DPA than MeO-DPA also supports that encapsulation increases intermolecular distance (Figure 5-2). In addition, the transient PL decays are distinctly different for MeO-DPA and En-DPA (Figure 5-3 and Table 5-1). A faster initial decay was recorded for MeO-DPA than En-DPA,

suggesting that an additional decay channel induced by intermolecular interaction is expected in MeO-DPA.

5.2.2 Steady-state photophysics

To examine En-DPA and MeO-DPA in a hyperfluorescence system, 9,9'-(4,4'-sulfonylbis(4,1-phenylene))bis(3,6-di-*tert*-butyl-9H-carbazole) (CZ-PS), which was reported as a deep blue TADF dye,[208] was selected. The molecular structures of the materials used in this study are displayed in Figure 5-4(a). Figure 5-4(b) shows the PL spectra of evaporated films of CZ-PS (neat and 20% doped into DPEPO) alongside the absorption coefficient plots for En-DPA and MeO-DPA. The En-DPA and MeO-DPA absorption spectra are almost identical. The PL spectrum of the CZ-PS neat film has an emission peak at 424 nm, slightly red-shifted compared to DPEPO:CZ-PS 20%, which shows a peak wavelength of 417 nm. Figure 5-4(c) and (d) show the PL spectra of the CZ-PS and DPEPO:CZ-PS 20% hosted films with varying doping concentrations of En-DPA and MeO-DPA. As the doping concentration is increased, the FWHM values of the PL spectra are slightly reduced, ascribed to an increased proportion of the emission from En-DPA and MeO-DPA due to more efficient energy transfer from CZ-PS at higher doping. Two peaks at around 410 nm and 430 nm are observed for all cases, similar to the neat film PL spectra of En-DPA and MeO-DPA (Figure 5-1).

The PLQEs of the blends were measured to confirm the superiority of En-DPA over MeO-DPA as an exciton acceptor in a donor-acceptor emissive system (Table 5-2). Regarding the MeO-DPA-based blends, the blends for 2% and 5% doping concentrations show higher than 90% PLQEs. However, the PLQE for MeO-DPA 10% doped in CZ-PS drops considerably to 64%. From the studies of the intrinsic

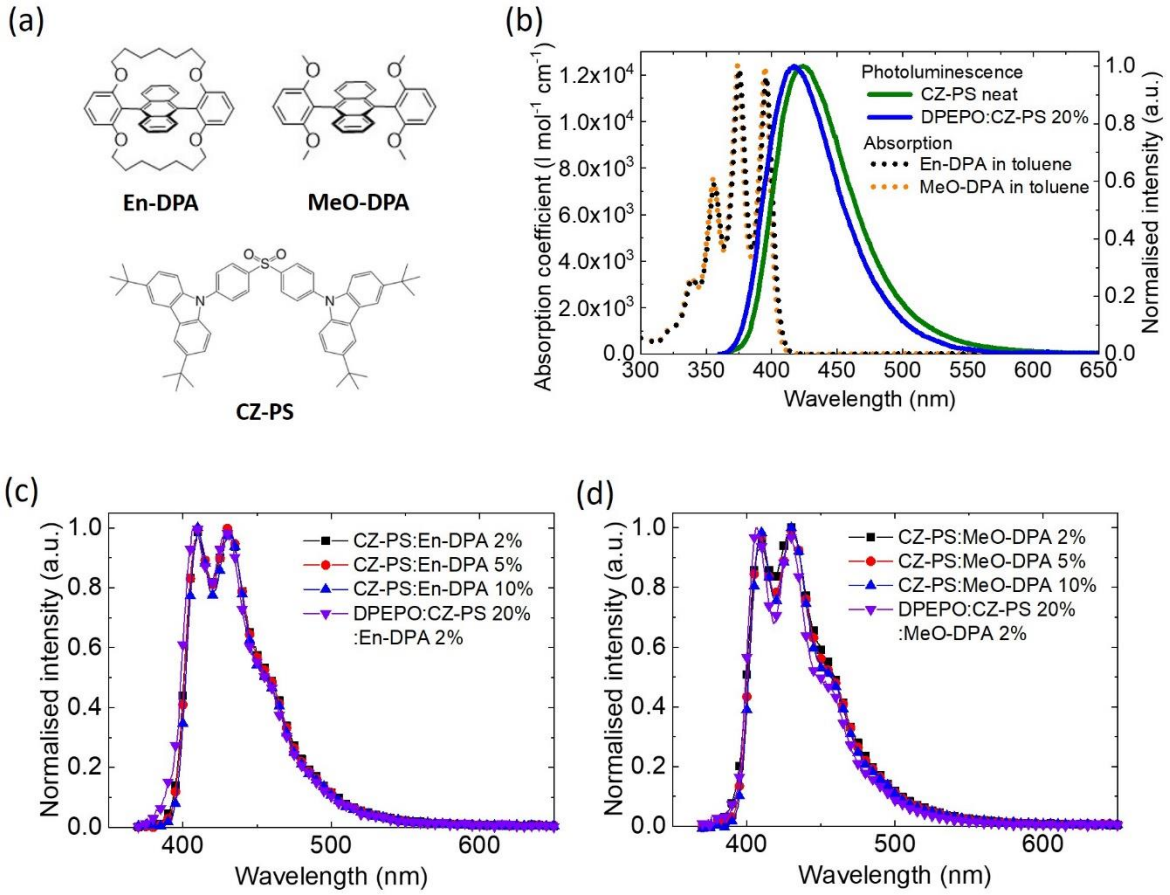

Figure 5-4. (a) Chemical structures of En-DPA, MeO-DPA, and CZ-PS. (b) PL spectra of CZ-PS neat and DPEPO:CZ-PS 20% films and absorption coefficient of En-DPA and MeO-DPA. (c) and (d) show PL spectra of En-DPA and MeO-DPA doped in CZ-PS and DPEPO:CZ-PS 20% with variation of doping concentration.

photophysical properties for En-DPA and MeO-DPA in Section 5.2.1, it is anticipated that the efficiency drop could result from concentration quenching, aggregation, and potential energy loss via DET. In contrast, for En-DPA, a PLQE of 100% was measured at 2% doped into DPEPO:CZ-PS 20%. Importantly, without the host matrix (DPEPO), the PLQEs of En-DPA doped into CZ-PS at 2%, 5%, and 10% are 100%, 99%, and 96%, respectively. Higher than 95% PLQE was maintained even at the highest doping

concentration. This is ascribed to the encapsulated chemical structure of En-DPA, which can potentially inhibit the loss mechanisms caused by close contact between molecules, as mentioned above.

Table 5-2. The summary of the PLQE values for the blends.

	CZ-PS							DPEPO:CZ-PS 20%		
	En-DPA				MeO-DPA			En-DPA		MeO-DPA
Doping (%)	0	2	5	10	2	5	10	0	2	2
PLQE (%)	74	100	99	96	97	94	64	77	100	95

5.2.3 Exciton decay kinetics

Figure 5-5 shows the decay kinetics of the doped films, and the decay constants are summarised in Table 5-3. CZ-PS and DPEPO:CZ-PS 20% undoped films show a combination of rapid nanosecond prompt decay and slow microsecond delayed emission, in accordance with the previous work.[208] However, due to the large singlet-triplet energy gap of CZ-PS (0.34 eV),[208] the delayed PL contribution is notably weak compared to efficient TADF materials with an S-T energy gap < 0.1 eV.[16] From the normalised integrated PL plots (Figure 5-6), the intensity proportion of the delayed emission for CZ-PS neat and DPEPO:CZ-PS 20% films are only 1.4% and 2.8%, respectively, whereas the intensity proportion of delayed emission for 4CzIPN, one of the representative TADF materials, is higher than 70%.[16] Hence, the triplet yield of CZ-PS upon photoexcitation is expected to be rather low, which is expected to contribute to the high PLQE of MeO-DPA. As the energy loss channel via DET is only

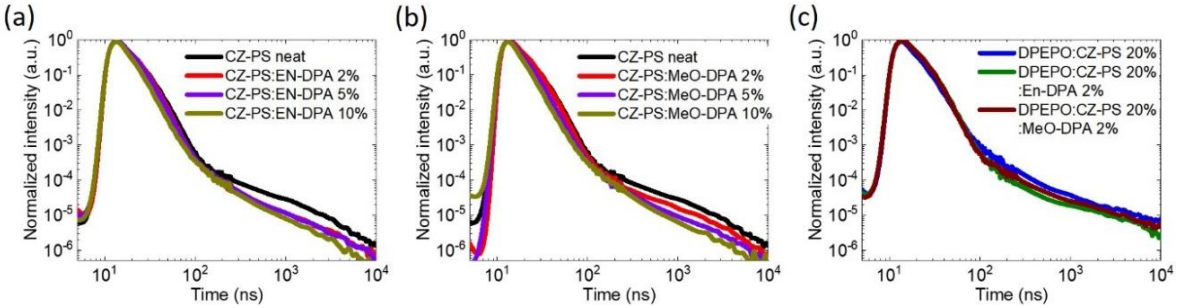

Figure 5-5. Transient PL characteristics for (a) En-DPA 0~10% doped in CZ-PS, (b) MeO-DPA 0~10% doped in CZ-PS, and (c) En-DPA and MeO-DPA 0~2% doped in DPEPO:CZ-PS 20%.

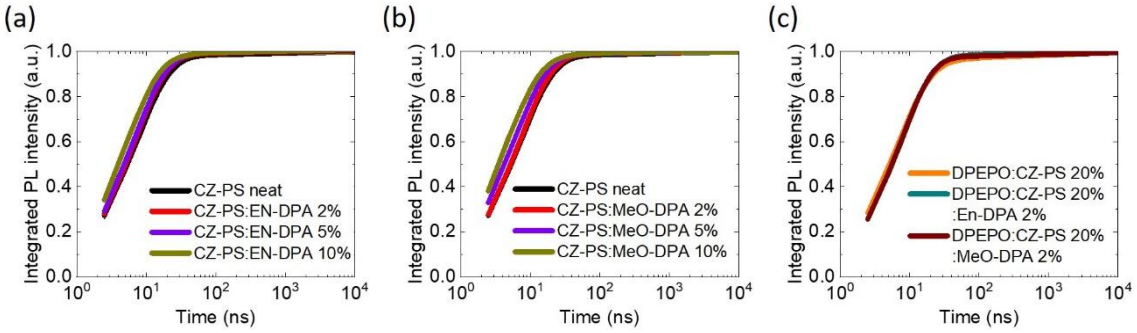

Figure 5-6. Normalised integrated PL profiles for (a) En-DPA 0~10% doped in CZ-PS, (b) MeO-DPA 0~10% doped in CZ-PS, and (c) En-DPA and MeO-DPA 0~2% doped in DPEPO:CZ-PS 20%.

applied to triplets interconverted from singlets via ISC, it is anticipated that the energy loss via DET is very small even in the MeO-DPA-based blends, allowing high PLQEs (> 90%) for them at low doping concentrations.

As the delayed emission components for the blends are low, the average (intensity-weighted) decay time (τ_{avr}) is extracted from the multi-exponential fit with

three components and calculated by $\tau = \frac{\sum_{i=1}^{3} A_i \tau_i^2}{\sum_{j=1}^{3} A_j \tau_j}$ where A_i and τ_i are the amplitude and lifetime of the i^{th} decay component, respectively, and the rate constants were obtained based on these results (Table 5-3). As the doping percentage of the emitters is increased, a shorter τ_{avr} is recorded. Also, as En-DPA and MeO-DPA are doped into the CZ-PS and DPEPO:CZ-PS 20% systems, both initial and delayed decay rates become faster, indicating that excitons formed in the hosts by photoexcitation are rapidly transferred to the emitters via FRET. As the fluorescence lifetimes of the emitters are much shorter than for CZ-PS (Table 5-1 and 5-3), a faster decay with increased doping indicates enhanced FRET to the emitters.

Table 5-3. The summary of average decay time and the rate constants of radiative and nonradiative decay for the blends.

	CZ-PS							DPEPO:CZ-PS 20%		
	En-DPA				MeO-DPA			En-DPA		MeO-DPA
Doping (%)	0	2	5	10	2	5	10	0	2	2
τ_{avr} (ns)[a)]	9.1	8.5	8.0	6.7	8.7	7.5	6.5	8.7	9.0	8.6
k_r (10^7 /s)	8.1	11.7	12.5	14.2	11.1	12.5	9.8	8.9	11.2	11.1
k_{nr} (10^7 /s)	2.8	-	0.1	0.6	0.4	0.8	5.6	2.7	-	0.6

a) The average intensity-weighted decay time obtained by $\tau = \frac{\sum_{i=1}^{3} A_i \tau_i^2}{\sum_{j=1}^{3} A_j \tau_j}$ from tri-exponential fit.

5.2.4 Analysis of exciton energy transfer

For the investigation of the FRET between CZ-PS and the two emitters, the Förster radius (R_0), which is the critical distance that 50% of singlet excited states of

donors can be transferred to those of acceptors, was calculated (refer to Section 2.1.4 and 4.2). The calculated values for En-DPA and MeO-DPA with CZ-PS are 2.05 nm and 2.00 nm, and En-DPA and MeO-DPA with DPEPO:CZ-PS 20% are 2.28 and 2.24 nm, respectively.

Also, the characteristic FRET rate (k_{FRET}) can be extracted by[81]

$$k_{\mathrm{FRET}} = \frac{1}{\tau_{\mathrm{D}}}\left(\frac{R_0}{R_{\mathrm{avr}}}\right)^6 \tag{5-2-1}$$

where τ_{D} is the radiative decay lifetime of the donor, and R_{avr} is the average intermolecular distance between donor and acceptor molecules. Assuming $k_{\mathrm{FRET}} \gg k_{\mathrm{nr,D}}$ (the nonradiative decay rate of the donor) and all photoexcited excitons formed at donors can be transferred to acceptors via FRET, The FRET efficiency (E_{FRET}), which is the proportion of photoexcited excitons transferred via FRET from donor to acceptor, can be calculated by[61]

$$E_{\mathrm{FRET}} = \frac{k_{\mathrm{FRET}}}{k_{\mathrm{r,D}}+k_{\mathrm{FRET}}} = \frac{1/\eta \int P_{\mathrm{A}}(\lambda)d\lambda}{\int P_{\mathrm{D}}(\lambda)d\lambda+1/\eta \int P_{\mathrm{A}}(\lambda)d\lambda} \tag{5-2-2}$$

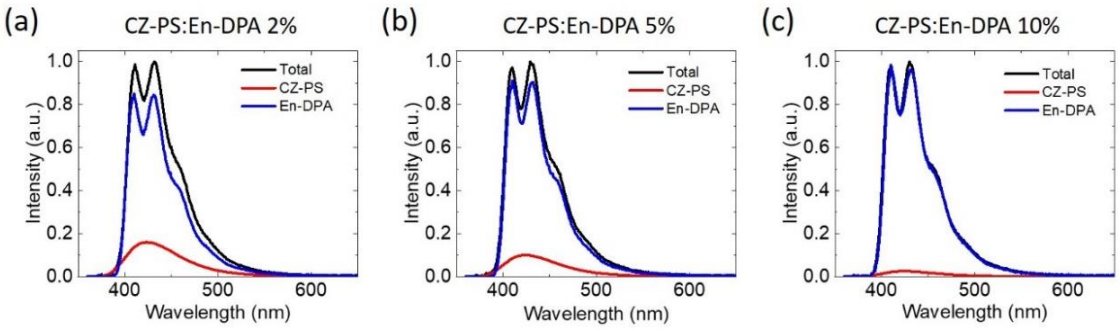

Figure 5-7. The PL spectra of the CZ-PS:En-DPA 2~10% films with the decomposed CZ-PS and En-DPA emission spectra.

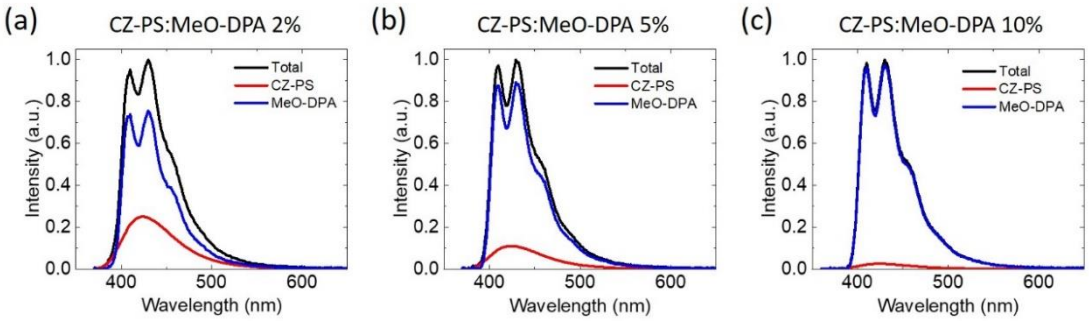

Figure 5-8. The PL spectra of the CZ-PS:MeO-DPA 2~10% films with the decomposed CZ-PS and En-DPA emission spectra.

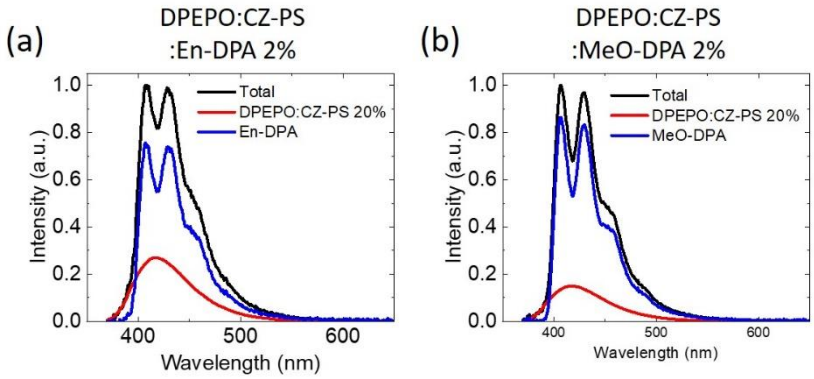

Figure 5-9. The PL spectra of the DPEPO:CZ-PS 20%:En-DPA and MeO-DPA 2% films with the decomposed DPEPO:CZ-PS 20% and En-DPA emission spectra.

where $k_{r,D}$ is the radiative decay rate of the donor, P_D and P_A are the donor and acceptor emission spectra, and η is the PLQE of the blends. P_D and P_A are obtained from the decomposed donor and acceptor spectra, which are extracted by subtracting a linearly-scaled donor-only spectrum from the total PL spectrum (Figures 5-7~9). Figure 5-10 shows the plots for PLQE, E_{FRET}, k_{FRET}, and R_{avr} with varying doping concentrations in CZ-PS, and the calculated values are summarised in Table 5-4. As doping concentration increases, PLQE and R_{avr} are decreased while E_{FRET} and k_{FRET} are increased for both

En-DPA and MeO-DPA. However, the influence of the doping concentration of MeO-DPA on the values is much more significant than for En-DPA. At 10% doping concentration, the R_{avr} for MeO-DPA considerably drops to 1.14 nm, which is close to the spacing between adjacent molecules, with a very rapid FRET rate. In contrast, En-DPA maintains a relatively longer R_{avr} (1.31 nm at 10%), with approximately half of the FRET rate than that observed for MeO-DPA. This indicates that the encapsulation is capable of maintaining intermolecular distance, causing the FRET efficiency to increase less drastically with varying doping concentrations.

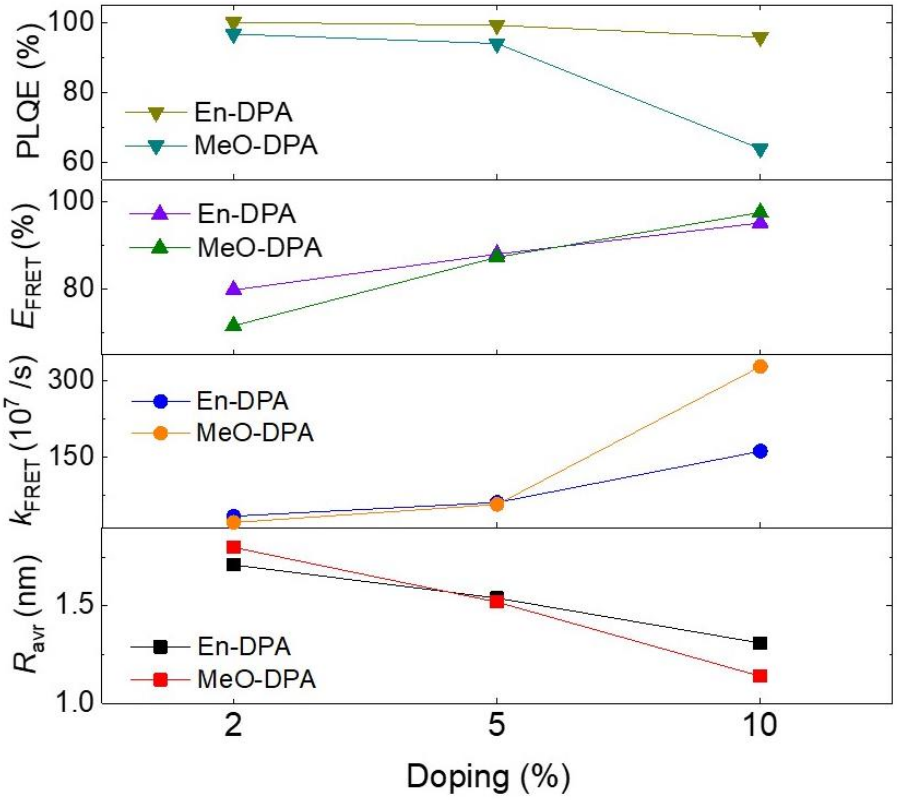

Figure 5-10. PLQE, E_{FRET}, k_{FRET}, and R_{avr} for En-DPA and MeO-DPA doped in CZ-PS with varying doping concentration.

Table 5-4. The summary of the FRET efficiency, Förster radii, FRET rate, and average donor-acceptor distance.

	CZ-PS						DPEPO:CZ-PS 20%	
	En-DPA			MeO-DPA			En-DPA	MeO-DPA
Doping (%)	2	5	10	2	5	10	2	2
E_{FRET} (%)	79.8	88.1	95.2	71.6	87.4	97.6	69.9	82.2
R_0 (nm)		2.05			2.00		2.28	2.24
k_{FRET} (10^8 /s)	3.22	6.00	16.10	2.06	5.62	32.72	2.06	4.09
R_{avr} (nm)	1.71	1.54	1.31	1.80	1.52	1.14	2.07	1.81

5.2.5 Device characterisation

Deep blue fluorescent OLEDs were successfully characterised utilising CZ-PS and En-DPA as an exciton donor and acceptor. Figure 5-11(a) shows the device structures employed for this study. 1,1-bis[(di-4-tolylamino)phenyl]cyclohexane (TAPC), 4,4′,4″-tris(carbazol-9-yl)triphenylamine (TCTA), and 1,3-bis(N-carbazolyl) benzene (mCP) constituted an HTL part, and bis[2-(diphenyl phosphino)phenyl]ether oxide (DPEPO) and 2,2',2"-(1,3,5-benzinetriyl)-tris(1-phenyl-1-H-benzimidazole) (TPBi) were employed for an ETL. Also, CZ-PS and En-DPA were used as an exciton sensitiser and a fluorescent acceptor in an EML, respectively. 2~10% doping of the emitter was applied to explore the dependence of doping concentration on MFHF devices (MF 1-3), and a wide-gap host matrix, DPEPO, was used for the CTHF device (CT 1). The device performance of CZ-PS and DPEPO:CZ-PS 20% without doping is presented in Figure 5-12. A maximum EQE of the DPEPO:CZ-PS 20% device is 9.3%, comparable to the previous work.[208]

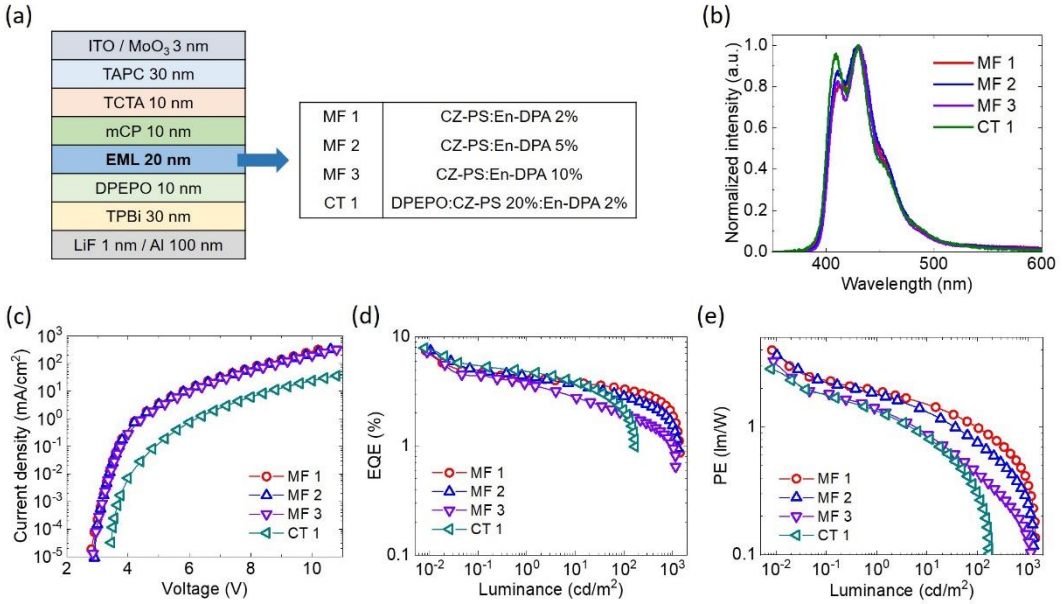

Figure 5-11. Optoelectronic performance of the En-DPA-based devices. (a) Device architecture. (b) EL spectra of the devices. (c) Current density-voltage plots. (d) EQE-luminance plots. (e) PE-luminance plots.

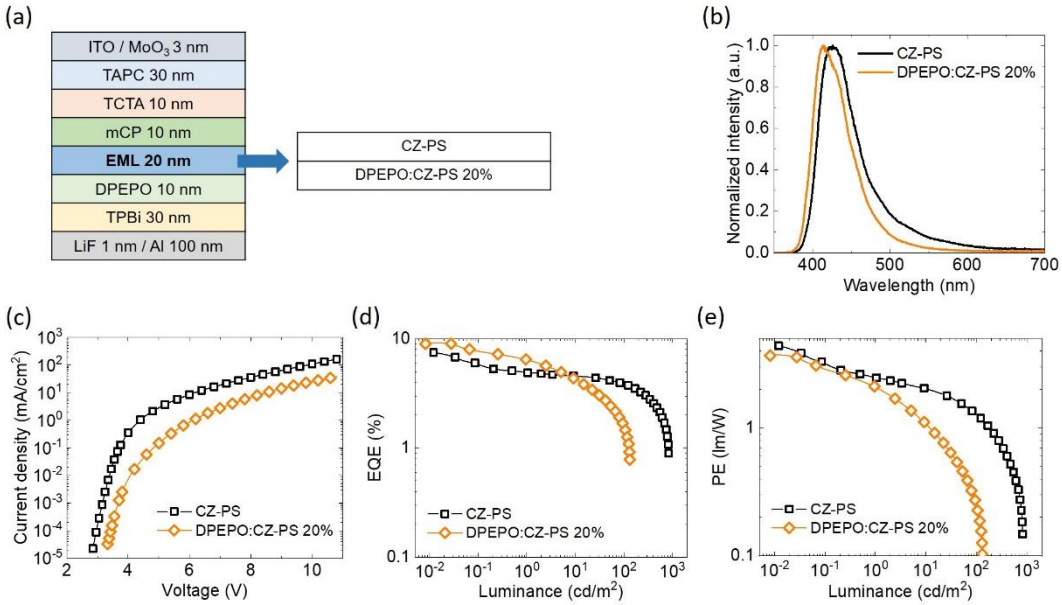

Figure 5-12. Optoelectronic performance of the CZ-PS and DPEPO:CZ-PS TADF devices without En-DPA doping.

The device characteristics of MFHF and CTHF devices based on En-DPA are summarised in Figure 5-11(b)-(d) and Table 5-5. Figure 5-11(b) shows the EL spectra of the devices. They are similar with two emission peaks at 410 nm and 430 nm and deep blue spectra with $CIE_y \leq 0.060$. As doping concentration increases, CIE_y becomes smaller (from 0.060 at 2% to 0049 at 10%) due to increased emission from En-DPA. J-V plots are depicted in Figure 5-11(c). As expected, the J-V plot for CT 1 is much shallower than MF 1-3 since the wide-gap host matrix interferes with charge transport in the EML. This leads to much higher maximum luminances (1,421 cd/m^2 for MF 1 vs 172 cd/m^2 for CT 1) and far lower turn-on and driving voltages for the MFHF devices than the CTHF device (V_{on}: 2.8 V and V_{100}: 5.2 V for MF 1 vs V_{on}: 3.4 V and V_{100}: 8.8 V for CT 1), as shown in Table 5-5 and Figure 5-13. The EQE and PE-luminance curves for the En-DPA devices are exhibited in Figure 5-11(d) and (e). MF 1~3 show maximum EQEs of 7.5%, 7.5%, and 7.3%, with negligible dependence on doping concentration, in line with PLQE values, comparable to CT 1 (7.9%), although

Table 5-5. Summary of the device performance for En-DPA-based devices.

	V_{on}[a)] (V)	EQE_{Max} (%)	V_{100}[b)] (V)	EQE_{100}[b)] (%)	PE_{Max} (lm/W)	$Luminance_{Max}$ (cd·m^{-2})	λ_{peak} (nm)	FWHM (nm)	CIE (x,y)
MF 1	3.0	7.5	5.4	3.3	4.0	1,421	410, 430	46.6	0.172, 0.060
MF 2	3.0	7.5	5.6	2.8	3.6	1,304	410, 430	49.0	0.168, 0.055
MF 3	3.1	7.3	6.2	2.0	3.3	1,169	410, 430	44.6	0.167, 0.049
CT 1	3.6	7.9	8.8	2.1	2.8	172	410, 430	44.6	0.163, 0.049

a) Voltage at 0.01 cd/m^2.
b) Values at 100 cd/m^2.

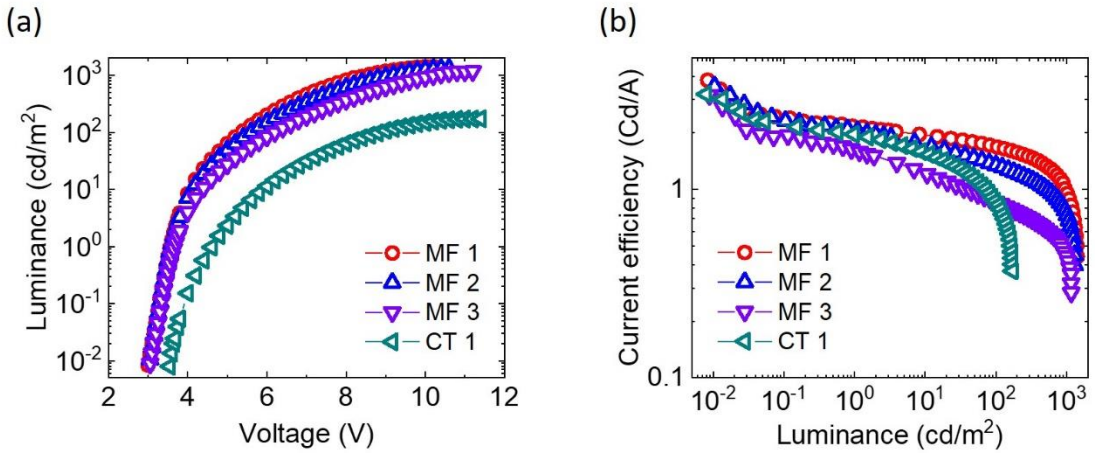

Figure 5-13. (a) Luminance-voltage and current and (b) Current efficiency-luminance plots for MF 1-3 and CT 1.

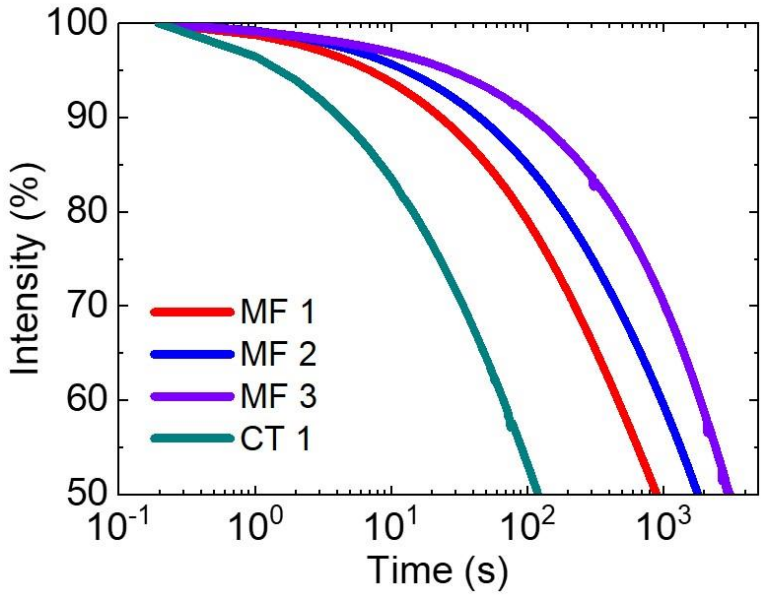

Figure 5-14. Lifetime profiles for MF 1-3 and CT 1 measured under constant current at starting brightness of 10 cd/m^2.

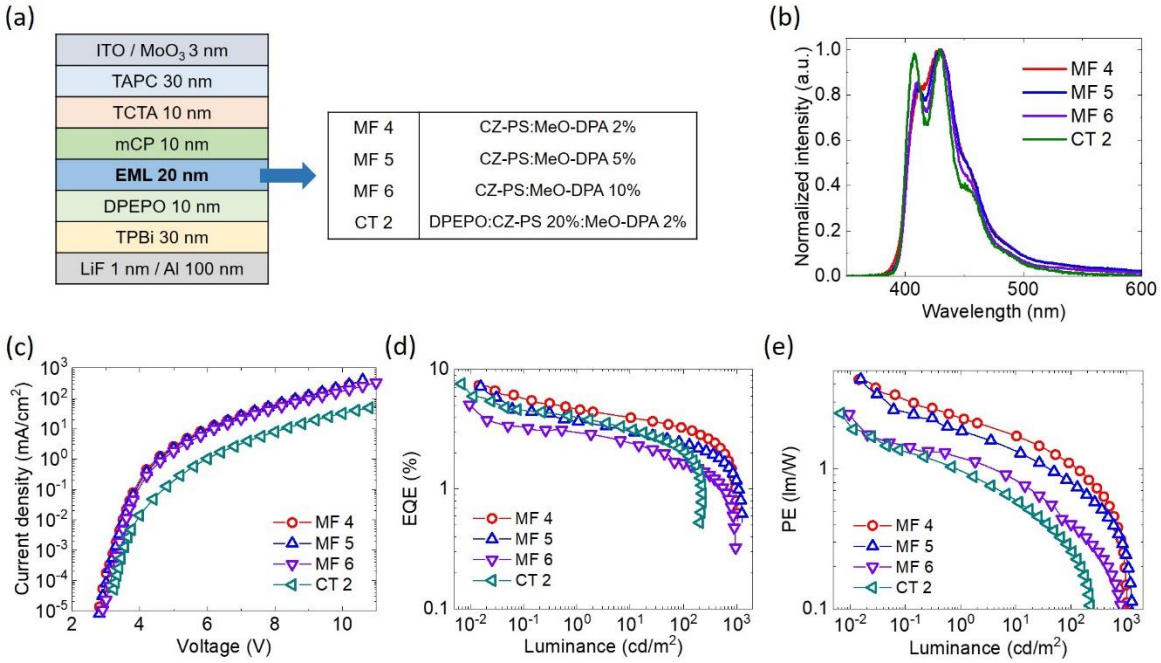

Figure 5-15. Optoelectronic performance of the devices using MeO-DPA.

Table 5-6. Summary of the device performance for MeO-DPA-based devices.

	V_{on} [a] (V)	EQE_{Max} (%)	V_{100} [b] (V)	EQE_{100} [b] (%)	PE_{Max} (lm/W)	$Luminance_{Max}$ ($cd \cdot m^{-2}$)	λ_{peak} (nm)	FWHM (nm)	CIE (x,y)
MF 4	3.1	7.4	5.5	3.2	4.3	1,036	410, 430	49.7	0.172, 0.070
MF 5	3.1	7.2	5.8	2.4	4.3	1,267	410, 430	49.4	0.173, 0.073
MF 6	3.3	5.1	6.4	1.6	2.5	958	410, 430	44.6	0.169, 0.058
CT 2	3.4	7.6	8.7	3.2	2.5	228	410, 430	42.7	0.160, 0.041

a) Voltage at 0.01 cd/m^2.
b) Values at 100 cd/m^2.

efficiency roll-off becomes larger with increasing doping concentration since bimolecular exciton quenching is accelerated at high doping. A maximum PE of MF 1 is 4.0 lm/W, about 43% higher than CT 1, 2.8 lm/W, and the disparity between them becomes more prominent as luminance increases. EQE and PE for CT 1 are recorded just until 172 cd/m^2 since DPEPO hinders charge transport, while MFHF devices give values over 1000 cd/m^2 due to improved charge injection and transport in the EML. Also, device lifetime was compared as depicted in Figure 5-14. More than one order of magnitude increase in lifetime is attained in the MF devices compared to CT 1. The optoelectronic performance of the MeO-DPA-based devices (MF 4~6 and CT 2) are shown in Table 5-6 and Figure 5-15. The maximum EQE of the MF device at 2% (MF 4) is 7.4%, comparable to the En-DPA-based devices, but as doping concentration increases, the values of EQE fall considerably associated with the PLQE results.

Overall, the En-DPA-based MFHF devices significantly outcompete the CTHF counterparts with respect to PE, luminance, driving voltage, and stability. However, due to the relatively poor performance of CZ-PS, the absolute EQE is quite lower than efficient hyperfluorescent OLEDs, usually showing higher than 20% EQE.

5.3 Encapsulated multiple resonance deep blue emitters with ultra-narrow emission

5.3.1 Necessity of new material design for efficient deep blue matrix-free hyperfluorescence

The working mechanism for hyperfluorescence is an energy cascade from a triplet-harvesting TADF donor to a fluorescent acceptor, with the spectral overlap between the donor PL and the acceptor absorption governing the key step of FRET. Accordingly, the singlet excited state energy of the TADF must exceed that of the acceptor, which is especially important when moving into the blue because the number of efficient TADFs reported in the literature drops off drastically with increasing singlet excited state energy. It is clear from Section 5.2 that the poor performance of high energy TADF materials (such as CZ-PS) can limit the efficiency of deep blue hyperfluorescent devices.

Rational fluorescent acceptor design provides the avenue to minimise the required singlet energy level for true blue hyperfluorescence. Beyond the base requirements of a unity PLQE and short fluorescence lifetime (τ), a narrow Stokes shift, small PL FWHM, and intense 0-0 absorption are all essential to lower the singlet energy level of the acceptor and hence the singlet energy level of the TADF donor. Recent advances have been made toward obtaining narrowband MR emitters that combine these properties, allowing the fabrication of efficient CTHF OLEDs with the $CIE_{x,y}$ colour coordinates approaching display requirements.[21,22]

In CTHF devices, a high gap host material is typically incorporated alongside the TADF sensitiser and the emitter molecule, leading to a three-component EML (or even four in the case of exciplex hosts). CTHF devices are the status quo for two

predominant reasons: Firstly, dilution into a high triplet energy host increases the average TADF-emitter distance to eliminate the DET of triplets as a loss pathway. Secondly, it suppresses aggregation of the TADF donor. As well as the possibility of concentration quenching, the neat film luminescence of TADF materials is usually red-shifted compared to diluted films, out of the useful region for HF with the current true blue acceptors.

However, the incorporation of additional high-gap materials into the EML of CTHF devices is a compromise, not without disadvantages: it substantially increases the complexity of device fabrication and reduces PE due to higher turn-on and driving voltages. In principle, the EML of a true blue hyperfluorescent OLED only requires two components: a TADF host and a narrowband emitter, a simpler device structure that is termed MFHF in this thesis. An MFHF device with display-relevant true blue $CIE_{x,y}$ colour coordinates would afford a new paradigm in OLED technology, but to achieve this, the challenge is substantial. An emitter with ideal spectral properties for matching with the sparse selection of suitable high energy TADF hosts is required, and an alternative strategy to suppress the short-range loss pathway, DET, must be developed.

5.3.2 Design and characterisation of novel multiple resonance emitters: tb-DBPICz and En-DBPICz

Recently, boron-free polycyclic aromatic hydrocarbons (PAHs) based on indolo[3,2,1-jk]carbazole (ICz) units have been of much interest for efficient deep blue fluorescent emitters due to their high efficiency and narrow emission in addition to relatively easier synthetic procedure with a higher yield.[209–212] These indolocarbazole-based fluorophors have a rigid chemical structure with small structural relaxation

between ground and excited states with MR effect by the different electronegativity of carbon and nitrogen, leading to a narrow Stokes shift and a small PL FWHM. Using this concept, novel dibenzo[2,3:5,6]pyrrolizino[1,7-bc]indolo[1,2,3-lm]carbazole (DBPICz)-based ultra-narrowband fluorescent emitters were designed (by Dr Dan Congrave, Department of Chemistry, University of Cambridge), which are isomeric with BisICz.[210,213,214] The chemical structures of BisICz and DBPICz are shown in Figure 5-16. From time-dependent density functional theory (TDDFT) calculations (conducted by Dr Dan Congrave and Dr Weixuan Zheng, Department of Chemistry, University of Cambridge), it is shown that the HOMO and LUMO are locally separated in the atoms by the MR effect.

Based on the DBPICz core structure, *tert*-butyl substituted DBPICz (tb-DBPICz) and covalently encapsulated DBPICz (En-DBPICz) were synthesised (by Dr Dan Congrave, Department of Chemistry, University of Cambridge), and their chemical structures are displayed in Figure 5-17, in addition to the steady-state PL and absorption spectra for them diluted in toluene. Interestingly, tb-DBPICz and En-DBPICz show

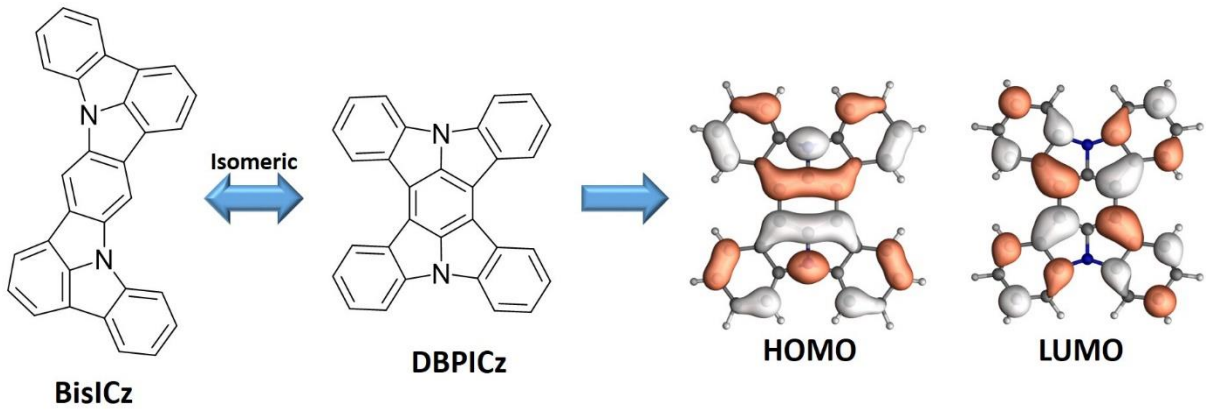

Figure 5-16. Molecular structure of BisICz and DBPICz and the HOMO and LUMO distributions of DBPICz by TD-DFT.

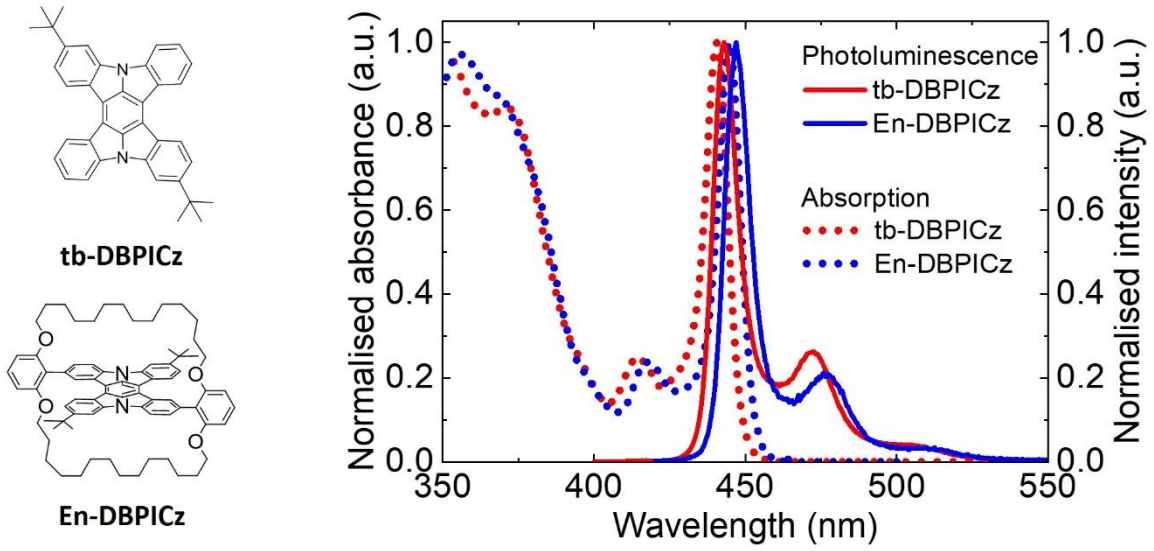

Figure 5-17. Chemical structures of tb-DBPICz and En-DBPICz and normalised absorption and PL spectra for tb-DBPICz and En-DBPICz diluted in toluene.

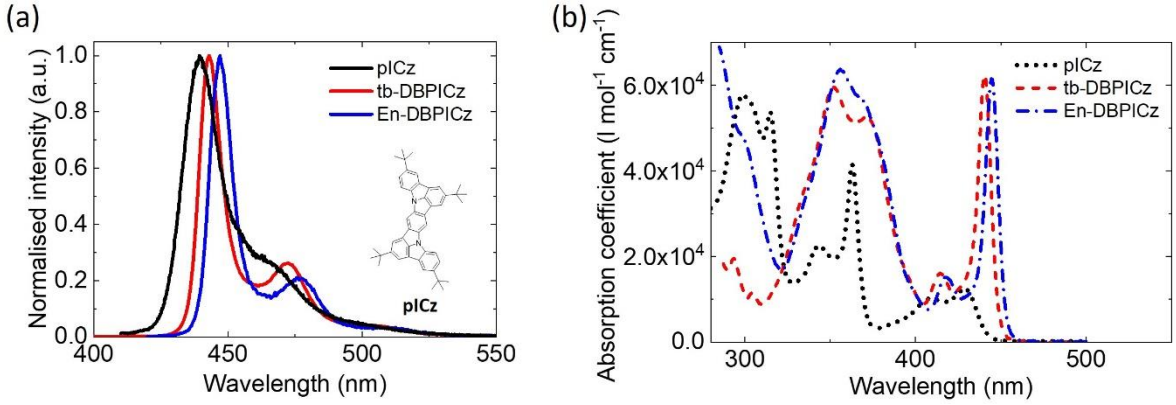

Figure 5-18. Comparisons of solution (a) PL spectra and (b) absorption coefficients for pICz, tb-DBPICz, and En-DBPICz.

ultra-narrow emission with ~10 nm FWHM and the $CIE_{x,y}$ of (0.15, 0.05), satisfying the blue coordinate of the OLED display colour spaces shown in Section 3.2.2 (Figure

3-8 and Table 3-1). En-DBPICz shows 447 nm peak emission, slightly red-shifted compared to the spectrum of tb-DBPICz, 443 nm. The redshift is ascribed to a small increase in conjugation by the encapsulating phenyl rings. As well as a Stokes shift of just 3 nm, strong 0-0 absorption is observed, which is highly advantageous for efficient FRET. Moreover, PLQEs for tb-DBPICz and En-DBPICz solutions are 100% and 96%, respectively, showing great potential as an efficient fluorescent acceptor for deep blue hyperfluorescent OLEDs. The PL and absorption spectra of *tert*-butyl substituted BisICz (pICz)[211] and DBPICz-based emitters are compared in Figure 5-18. The PL spectrum of pICz shows 439 nm peak emission with 17 nm FWHM, which is more blue-shifted with wider FWHM than tb-DBPICz and En-DBPICz. In addition, the high energy deep blue light between 415 nm and 455 nm could cause eye damage.[215,216] A large amount of harmful blue emission below 450 nm is included in pICz spectrum, while most of it is quenched in En-DBPICz due to ultra-narrowband emission with a peak wavelength of around 450 nm, which is beneficial for practical display applications (Figure 5-18(a)). Moreover, the absorption coefficients for the three emitters are compared in Figure 5-18(b). Intense 0-0 absorption coefficients of around 6.2×10^4 l mol^{-1} cm^{-1} are observed for tb-DBPICz and En-DBPICz at wavelengths of

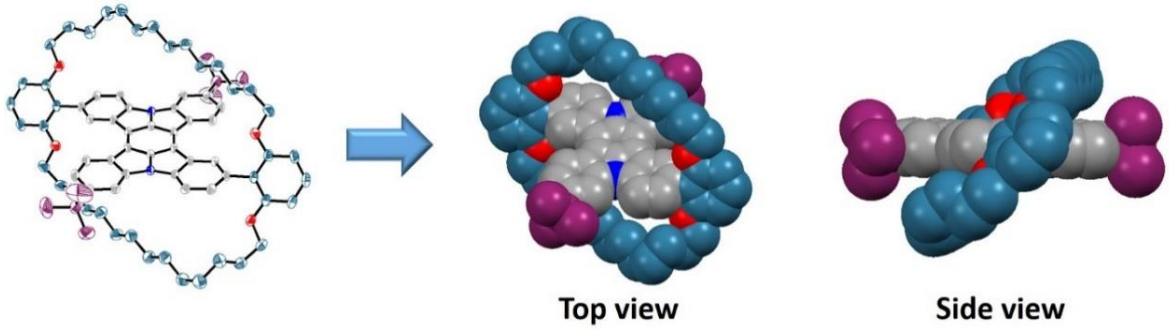

Figure 5-19. Ellipsoid and spacefill plots of the crystal structure for En-DBPICz from XRD.

440 nm and 445 nm, respectively. In contrast, for pICz, the 0-0 absorption coefficient is less than a fifth of the values for tb-DBPICz and En-DBPICz, 1.2×10^4 l mol^{-1} cm^{-1}.

An encapsulating alkyl chain was incorporated to sterically protect the DBPICz core structure in En-DBPICz. Consequently, En-DBPICz is expected to be more resistant to aggregation than tb-DBPICz, with the potential for substantially suppressed triplet DET from host molecules. Figure 5-19 shows the single crystal molecular structure from X-ray diffraction (XRD) (conducted by Dr Andrew Bond, Department of Chemistry, University of Cambridge). A thermal ellipsoid plot is shown (probability 50%) in addition to spacefill plots from top to side perspectives. The spacefill plots show the Van der Waals radii of the atoms with the size of the atomic electron clouds at 100% probability to help visualise the effective size of the molecule and emphasise the considerable steric protection around the DBPICz core from *tert*-butyl groups (purple) and the encapsulating rings (dark blue).

To help quantify the degree of steric protection, the volumes of the molecules were calculated using the marching tetrahedron model (by Dr Dan Congrave and Dr Weixuan Zheng, Department of Chemistry, University of Cambridge), which is approximately the sum of the volumes of all atoms calculated from their Van der Waals radii.[217] The calculated DBPICz core volume is 476 $Å^3$, whereas tb-DBPICz and En-DBPICz display values of 647 $Å^3$ and 1496 $Å^3$, much larger than the core structure. Accordingly, as the alkyl group encapsulating the core is not electronically coupled to the DBPICz chromophore, it can be inferred that the extra volume of 1020 $Å^3$ can be seen as insulating the core, contributing to the suppression of aggregation and the short-range energy transfer, DET.

Next, HOMO and LUMO energy levels for tb-DBPICz and En-DBPICz were obtained from cyclic voltammetry (CV) and DFT calculations (Dr Dan Congrave and

Dr Weixuan Zheng, Department of Chemistry, University of Cambridge), as shown in Figure 5-20 and Table 5-7. The onset of oxidation for tb-DBPICz is unconventionally shaped, likely due to its poor solubility, which complicates a detailed comparison of the electrochemical data. However, it can be reasonably concluded that the HOMO energy levels for tb-DBPICz and En-DBPICz obtained from CV are similar, around 5.4 eV. The difference in the DFT (B3LYP/6-31G*) calculated HOMO energies is more pronounced than for the experiment, with En-DBPICz displaying a significantly shallower HOMO than tb-DBPICz. This is rationalised based on the encapsulating alkoxy groups of En-DBPICz, which have electron donating properties to destabilise the HOMO of En-DBPICz relative to tb-DBPICz. Also, the vertical excitation energies of the first singlet (E_{S_1}) and triplet (E_{T_1}) excited states were calculated using TDDFT (PBE0/def2svp). E_{S_1} for tb-DBPICz is 3.05 eV, slightly higher than that for En-DBPICz, 3.00 eV, in line with the slightly blue-shifted experimental absorption and

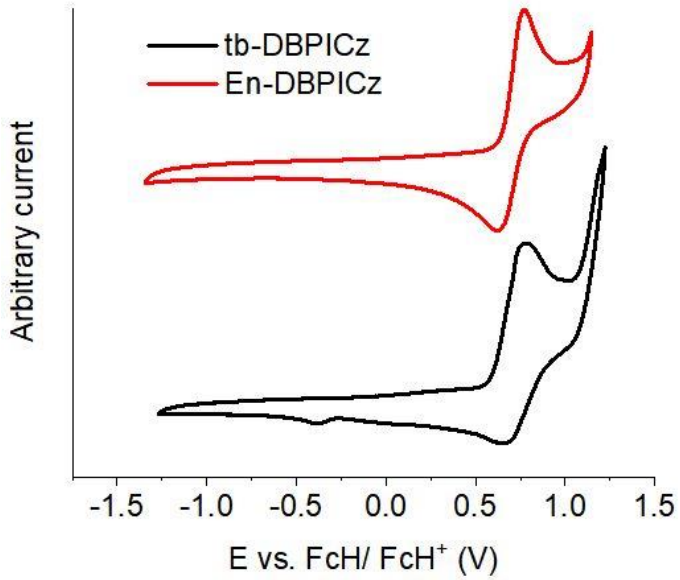

Figure 5-20. Cyclic voltammograms of tb-DBPICz and En-DBPICz.

Table 5-7. The electrochemical properties of tb-DBPICz and En-DBPICz obtained from CV, DFT, and TDDFT.

Compound	CV				DFT / TDDFT				
	E_{onset}^{ox} (V)[a]	HOMO (eV)[b]	LUMO (eV)[c]	E_g^{opt} (eV)[d]	HOMO (eV)[e]	LUMO (eV)[e]	E_{S_1} (eV)[e]	E_{T_1} (eV)[e]	ΔE_{ST} (eV)[e]
tb-DBPICz	0.59	-5.39	-2.62	2.77	-5.15	-1.75	3.05	2.30	0.75
En-DBPICz	0.65	-5.45	-2.71	2.74	-4.95	-1.59	3.00	2.31	0.69

[a]Referenced to $E_{1/2}$ of the fcH/ fcH^+ redox couple; [b]HOMO level calculated from CV potentials using the HOMO of ferrocene (–4.8 eV) as the standard, HOMO = $-4.8 + (-E_{1/2}^{ox})$; [c]LUMO = HOMO + E_g^{opt}; [d]Onset of the UV-Vis spectrum in toluene; [e]B3LYP/6-31G*

PL spectra observed for tb-DBPICz compared to En-DBPICz. Interestingly, the E_{T_1} for both emitters are relatively low, at around ~2.3 eV, leading to a singlet-triplet energy gap (ΔE_{ST}) of around ~0.7 eV. Hence, the emitters are expected not to show TADF characteristics, in contrast to other boron-incorporated or pICz-based MR emitters.[17,210] This will be investigated experimentally in Section 5.3.4.

5.3.3 Steady-state photophysics

As an efficient blue TADF donor, 10,10'-(4,4'-Sulfonylbis(4,1-phenylene)) bis(9,9-dimethyl-9,10-dihydroacridine) (DMAC-DPS) was selected since it shows very high EQE in both doped and nondoped devices.[115,218] Approximately 20% EQE was reported even in DMAC-DPS-based host-free TADF devices, giving high potential for incorporation alongside the novel MR emitters in the MFHF system. Firstly, the steady-

state photophysical properties of the DMAC-DPS and the DBPICz-based MR emitter components of the hyperfluorescent system are investigated. Figure 5-21(a) shows the schematic diagram of the hyperfluorescence emission mechanism. As described above, excitons formed in TADF donors have to be transferred to fluorescent acceptors via FRET while experiencing ISC and RISC, and triplet transfer via DET must be suppressed to prevent the efficiency loss and realise 100% IQE. The PL-absorption overlap of the donor and acceptor considerably affects the long-range energy transfer, FRET, and is shown in Figure 5-21(b). The PL peaks of DPEPO:DMAC-DPS 20% and DMAC-DPS neat films are observed at 475 nm and 479 nm, respectively, which are quite red-shifted compared to the absorbance peaks for tb-DBPICz and En-DBPICz. However, due to the very intense 0-0 absorption coefficients of the acceptors (Figure 5-18(b)), a potential for effective FRET is still expected considering the apparent PL-absorption overlap. Figure 5-21(c) and (d) show the PL spectra for tb-DBPICz and En-DBPICz 0.5% and 1.0% doped in DMAC-DPS. Interestingly, tb-DBPICz doped films show quenching of the expected emission peak at 449 nm with red-shifted spectra upon increasing the doping concentration to 1%. A tendency for broadened emission upon increasing the doping concentration has been previously reported for pICz and was ascribed to aggregation.[211] In contrast, En-DBPICz shows a narrowing of the emission towards a profile similar to the solution PL spectrum (Figure 5-17) as doping concentration is increased. Thus, aggregation is considerably suppressed in En-DBPICz by the sterically protected chemical structure of En-DBPICz that inhibits close contact between molecules (Section 5.3.2).

Furthermore, the PLQEs of the MR emitter doped and undoped films were measured with 330 nm laser excitation. A PLQE of 96% was obtained from a DMAC-DPS neat film, in line with the previous report.[218] Regarding the DMAC-DPS

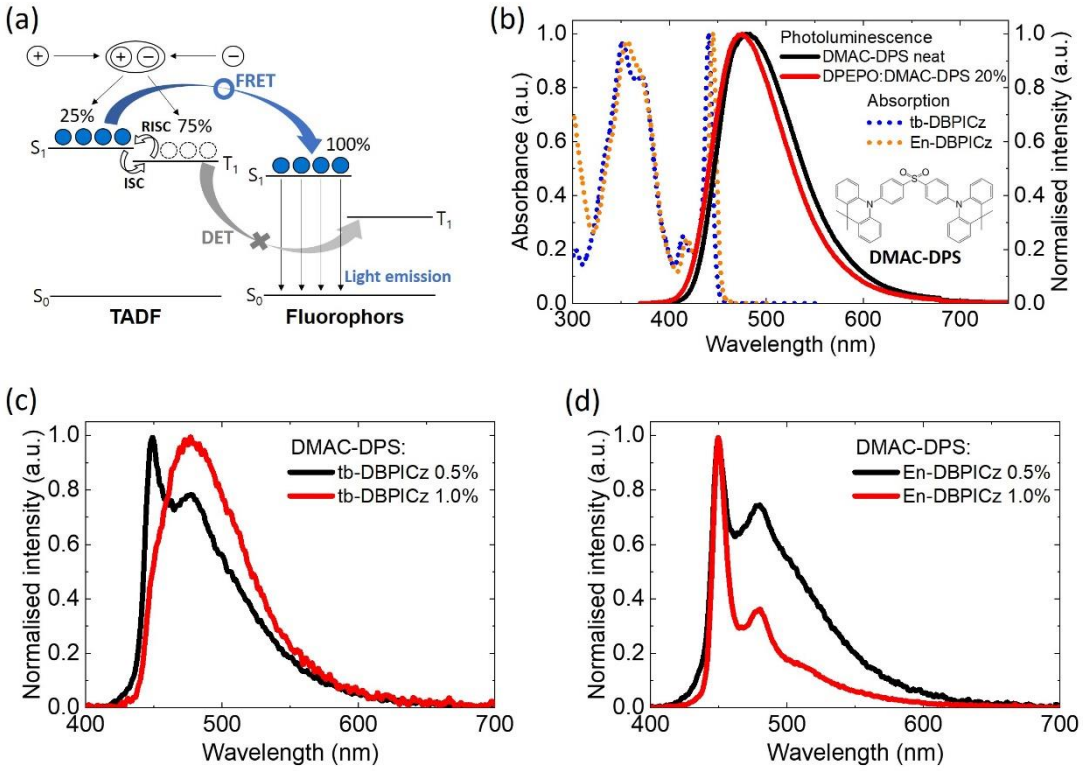

Figure 5-21. (a) Schematic diagram of hyperfluorescence emission mechanism. (b) The absorbance for tb-DBPICz and En-DBPICz diluted in toluene and the PL spectra for DMAC-DPS and DPEPO:DMAC-DPS 20% films. (c),(d) show the PL spectra for tb-DBPICz and En-DBPICz doped in DMAC-DPS without a host matrix.

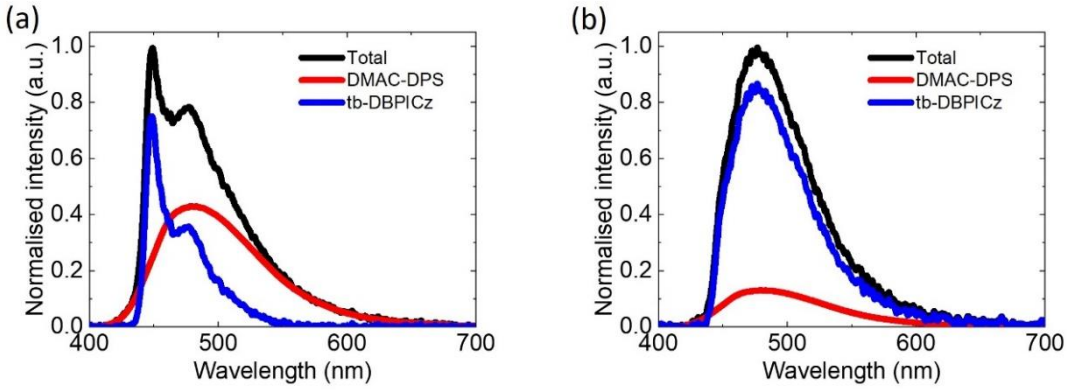

Figure 5-22. The total PL spectra of (a) the DMAC-DPS:tb-DBPICz 0.5% and (b) 1.0% films with the decomposed PL spectra for DMAC-DPS and tb-DBPICz.

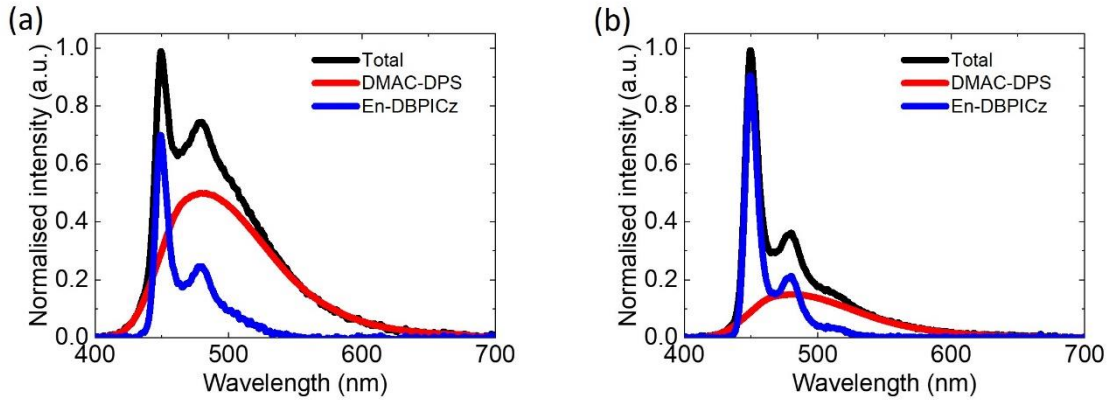

Figure 5-23. The total PL spectra of (a) the DMAC-DPS:En-DBPICz 0.5% and (b) 1.0% films with the decomposed PL spectra for DMAC-DPS and En-DBPICz.

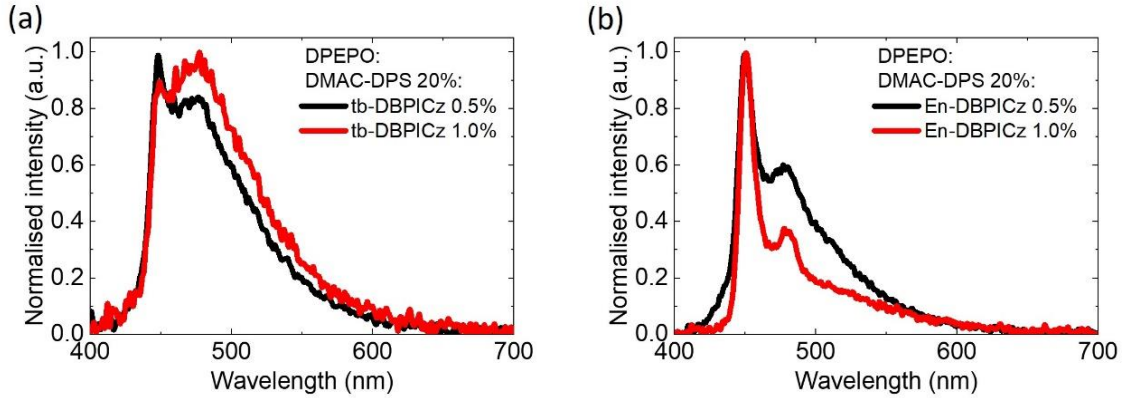

Figure 5-24. The PL spectra for (a) tb-DBPICz and (b) En-DBPICz doped in DPEPO:DMAC-DPS 20%.

hosted films, those doped with tb-DBPICz show much lower PLQEs (43% for 0.5% doping and 35% for 1% doping) than with En-DBPICz (75% for 0.5% doping and 63% for 1.0% doping). The difference in PLQEs between the two emitters in DMAC-DPS is likely related to the lower PLQE of the aggregates present in the tb-DBPICz doped films, potentially increasing triplet DET for tb-DBPICz, compared to the En-DBPICz molecules. Meanwhile, in contrast to the solution PL spectra in Figure 5-17, a long

emission tail over 520 nm is not perfectly removed in the DMAC-DPS hosted film PL for En-DBPICz, which probably originates from the remaining DMAC-DPS emission contribution due to its broad PL spectrum (92 nm FWHM). Figure 5-22 and 5-23 show the decomposed PL spectra of DMAC-DPS and the emitters for the DMAC-DPS hosted films, indicating that DMAC-DPS emission is included in the total PL spectra of the films. As displayed in Figure 5-21(b), the PL-absorption overlap between DMAC-DPS and the MR emitters is not sufficient to transfer all excitons formed on DMAC-DPS to the MR emitters at low doping concentrations; there are residual excitons on DMAC-DPS molecules not transferred to En-DBPICz via FRET at a sufficient rate to quench all DMAC-DPS emission. Additionally, Figure 5-24 shows the PL spectra for the CTHF films, and the tendency dependent on doping concentrations is almost the same as those for the MFHF films in Figure 5-21(c) and (d).

5.3.4 Exciton decay kinetics

To study exciton decay kinetics in this hyperfluorescence system, transient PL measurements were conducted with 330 nm laser excitation. Figure 5-25 shows the transient PL data for the tb-DBPICz and En-DBPICz doped films and the DMAC-DPS neat film. The radiative decay rate constants of prompt (k_p) and delayed (k_d) fluorescence for the films can be calculated by,[116,117,119]

$$k_\mathrm{p} = \frac{\Phi_\mathrm{p}}{\tau_\mathrm{p}} \tag{5-3-1}$$

$$k_\mathrm{d} = \frac{\Phi_\mathrm{d}}{\tau_\mathrm{d}} \tag{5-3-2}$$

where Φ_p and Φ_d are the PLQEs of prompt and delayed emission, and τ_p and τ_d are the decay lifetime of prompt and delayed emission. The total PLQE (Φ_total) is expressed

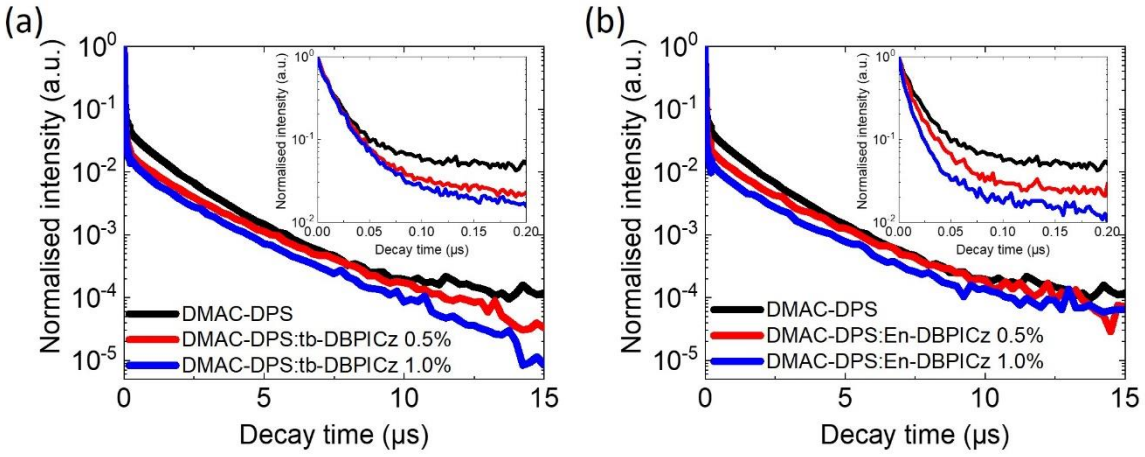

Figure 5-25. Transient PL profiles for (a) tb-DBPICz and (b) En-DBPICz doped in DMAC-DPS.

Table 5-8. The summary of PLQEs (total, prompt, and delayed), decay time, and decay rate for DAMC-DPS neat and tb-DBPICz and En-DBPICz doped in DMAC-DPS.

Host	DMAC-DPS				
Dopant	tb-DBPICz			En-DBPICz	
Doping (%)	0	0.5	1	0.5	1
Φ_{total}	0.96	0.43	0.35	0.75	0.63
r_1	0.15	0.24	0.32	0.15	0.23
r_2	0.85	0.76	0.68	0.60	0.77
Φ_p	0.14	0.11	0.11	0.20	0.14
Φ_d	0.82	0.32	0.24	0.55	0.49
τ_p (10^{-9} s)	13.80	13.75	13.60	11.37	8.57
τ_d (10^{-6} s)	1.24	1.37	1.15	1.47	1.43
k_p (10^7 /s)	1.04	0.76	0.81	1.32	1.67
k_d (10^5 /s)	6.61	2.36	2.08	4.08	3.40

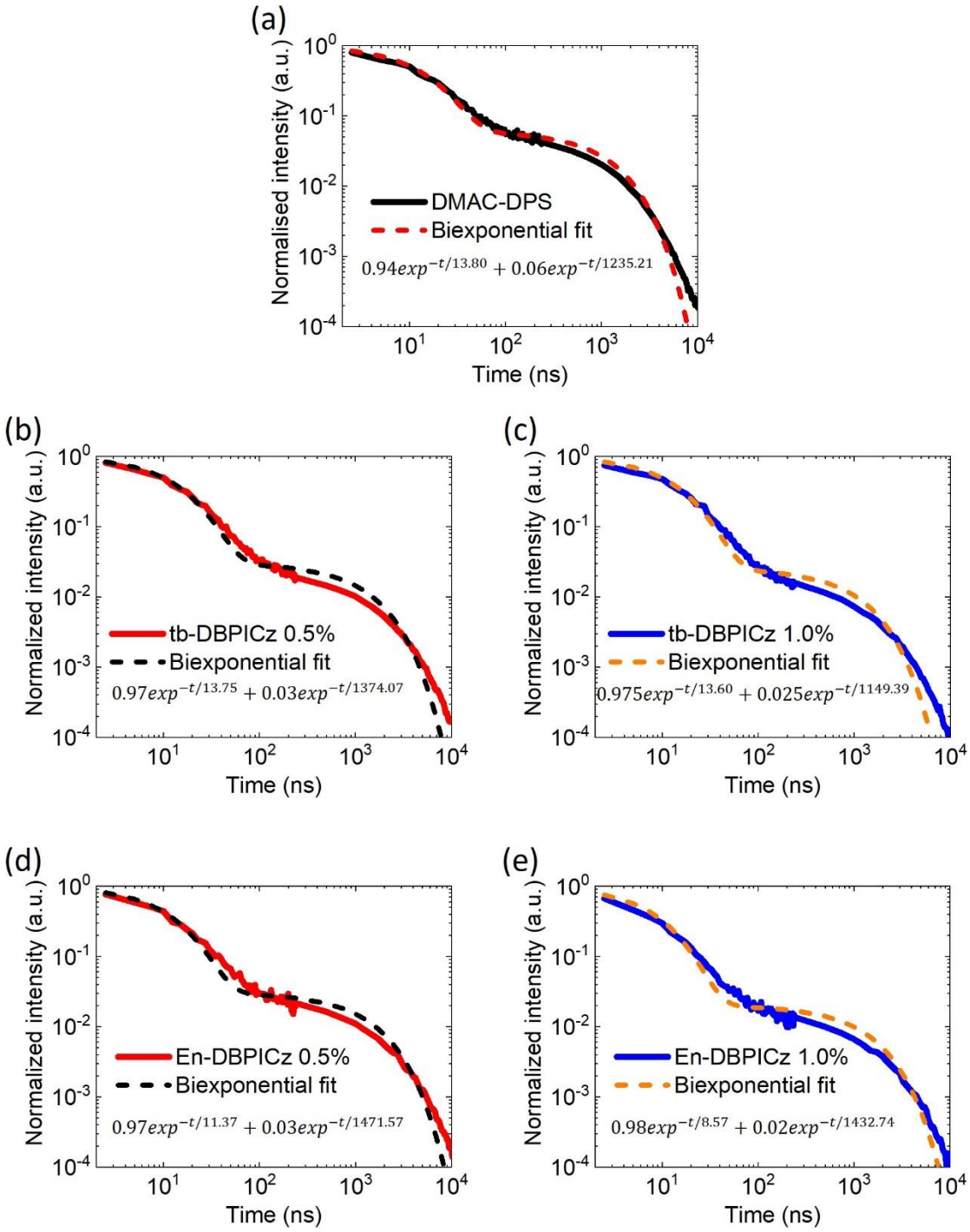

Figure 5-26. Biexponential fits for the transient PL profiles of DMAC-DPS-based films. (a) DMAC-DPS. (b),(c) tb-DBPICz 0.5% and 1.0%. (d),(e) En-DBPICz 0.5% and 1.0%.

by the sum of Φ_p and Φ_d, expressed by the following equations,

$$\Phi_{total} = \Phi_p + \Phi_d \quad (5\text{-}3\text{-}3)$$

$$\Phi_p = r_1 \Phi_{total} \quad (5\text{-}3\text{-}4)$$

$$\Phi_d = r_2 \Phi_{total} \quad (5\text{-}3\text{-}5)$$

where r_1 and r_2 are the intensity ratio of prompt and delayed components, defined by

$$r_1 = \frac{A_1\tau_p}{A_1\tau_p + A_2\tau_d} \quad (5\text{-}3\text{-}6)$$

$$r_2 = \frac{A_2\tau_d}{A_1\tau_p + A_2\tau_d} \quad (5\text{-}3\text{-}7)$$

where A_1 and A_2 are the fitting parameters in the double exponential equation ($A_1 e^{-t/\tau_p} + A_2 e^{-t/\tau_d}$). Figure 5-26 shows the biexponential fitting for the transient PL profiles of the films. Based on these results, the decay time and rate constants for the films are calculated from Equation 5-3-1 to 5-3-7, as summarised in Table 5-8.

DMAC-DPS shows nanosecond prompt fluorescent emission with microsecond delayed emission in line with the previous report.[115] As the MR emitters are doped into DMAC-DPS, the overall PLQE drops, accompanied by a change in the ratios of prompt and delayed emission. The ratio of the prompt to delayed emission increases (inset in Figure 5-25) as the doping concentration of both MR emitters is increased. There are likely multiple factors that lead to the increase in prompt emission compared to delayed. The change in ratio could be ascribed 1) to an increase in prompt emission due to FRET from DMAC-DPS to the DBPICz emitters outcompeting ISC from the initial DMAC-DPS S_1 state formed during photoexcitation, and also 2) a decrease in delayed emission due to quenching via triplet DET from DMAC-DPS to the DBPICz emitters. Additionally, Figure 5-27 shows the integrated normalised PL intensity of the transient

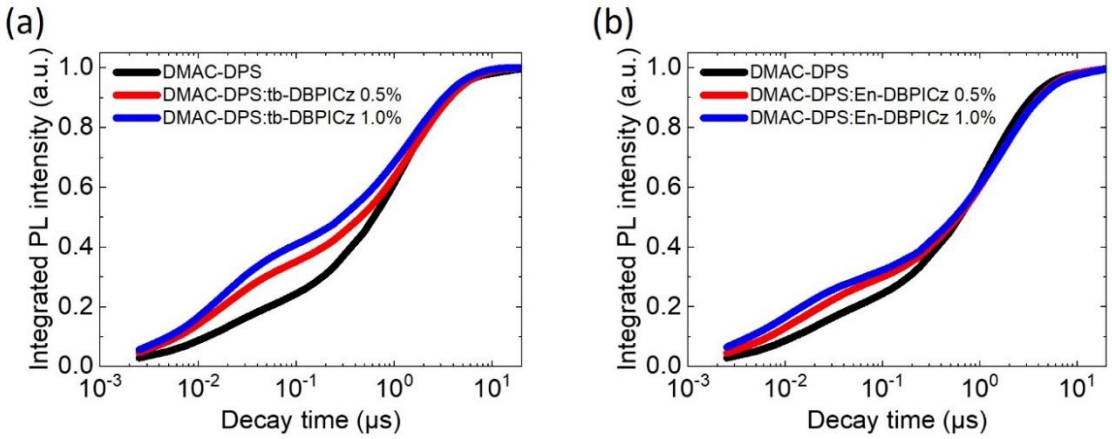

Figure 5-27. Normalised integrated PL intensity for (a) tb-DBPICz and (b) En-DBPICz doped in DMAC-DPS.

PL profiles indicating an increase in the prompt emission proportion with a decrease in the delayed emission proportion.

Meanwhile, the prompt fluorescent emission of En-DBPICz is faster than tb-DBPICz (inset in Figure 5-25(a) and (b)), and as doping concentration is increased, the prompt fluorescent emission of En-DBPICz becomes much shorter while that of tb-DBPICz is insensitive to doping concentration in the early time region. This tendency may be related to slower aggregate emission in tb-DBPICz and prompted a study of the intrinsic decay kinetics of the emitters in the wide energy hap host, CBP.

Figure 5-28 shows the transient PL characteristics and integrated PL intensity plots for the CBP hosted films. As expected from the large ΔE_{ST} (Table 5-7), delayed emission is negligible, and almost all emission is from initial fluorescence. However, En-DBPICz shows appreciably faster initial decay than tb-DBPICz (inset in Figure 5-28(a)), and this is attributed to the aggregate emission of tb-DBPICz originating from its chemical structure. The decay times of the films are taken for a fraction 1-(1/e) of

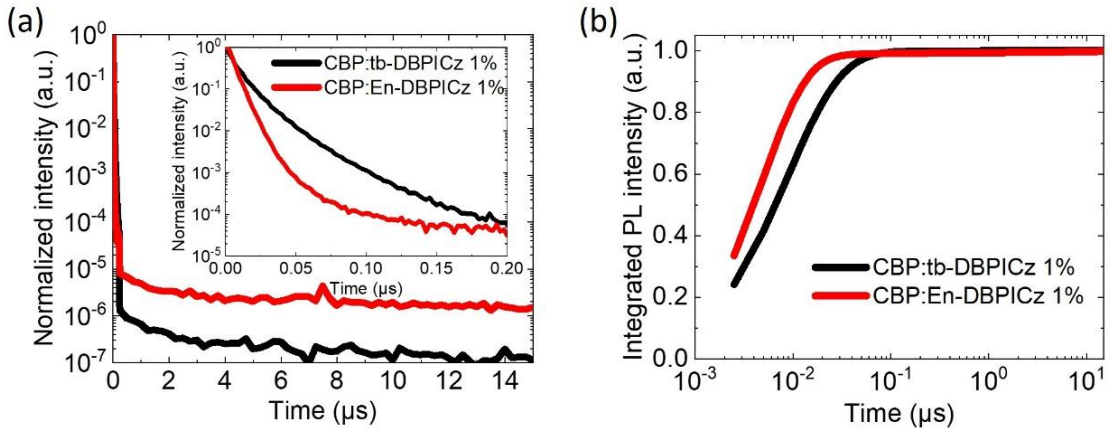

Figure 5-28. (a) Transient PL and (b) normalised integrated PL profiles for tb-DBPICz and En-DBPICz doped in CBP.

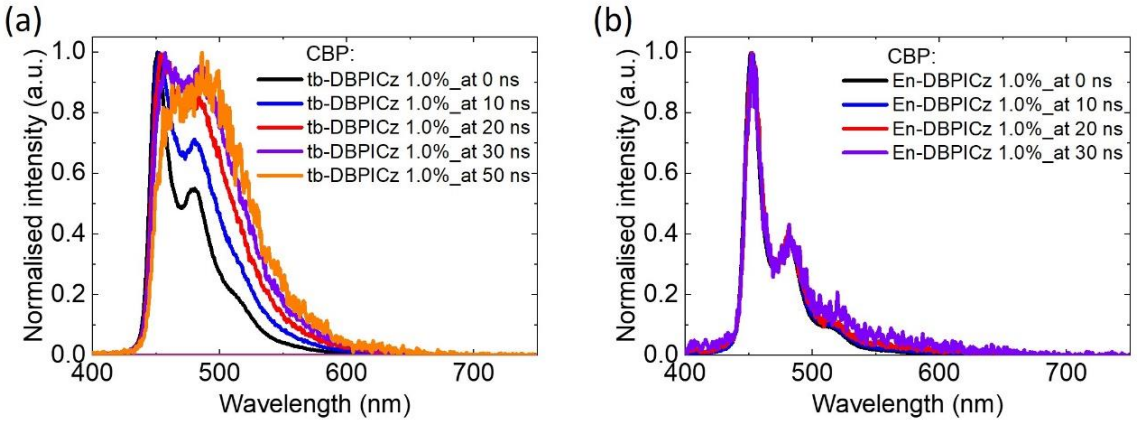

Figure 5-29. Normalised PL at different times for (a) tb-DBPICz and (b) En-DBPICz 1% doped in CBP.

the total emission to occur (Figure 5-28(b)), which are 10.1 ns and 5.7 ns for tb-DBPICz and En-DBPICz, respectively. Figure 5-29 shows the PL spectra at different times for the tb-DBPICz and En-DBPICz doped films. The PL spectra for the En-DBPICz doped films are maintained at almost the same spectral profile across all time scales (0-30 ns).

In contrast, for tb-DBPICz, the peak emission at 450 nm is comparatively quenched at all investigated timescales, and a broad secondary shoulder develops as time is increased. This disparity highlights that aggregation is prevalent for tb-DBPICz even when doped into a wide energy gap host at a low concentration, which can be effectively suppressed in En-DBPICz due to the sterically protected chemical structure.

5.3.5 Analysis of exciton energy transfer

Firstly, the exciton dynamics in DMAC-DPS are explored. Figure 5-30 shows the schematic diagram of the TADF process in DMAC-DPS. Assuming that the T_1-to-S_0 radiative and nonradiative transition in DMAC-DPS ($k_{\mathrm{r,T}}$ and $k_{\mathrm{nr,T}}$) is negligible, the decay rates and PLQEs of the prompt and delayed emission for DMAC-DPS ($k_{\mathrm{p,D}}$, $\Phi_{\mathrm{p,D}}$, $k_{\mathrm{d,D}}$, $\Phi_{\mathrm{d,D}}$) can be approximated as[16,116,117]

$$k_{\mathrm{p,D}} = k_{\mathrm{r,S}} + k_{\mathrm{nr,S}} + k_{\mathrm{ISC}} \tag{5-3-8}$$

$$\Phi_{\mathrm{p,D}} = \frac{k_{\mathrm{r,S}}}{k_{\mathrm{r,S}}+k_{\mathrm{nr,S}}+k_{\mathrm{ISC}}} = \frac{k_{\mathrm{r,S}}}{k_{\mathrm{p,D}}} \tag{5-3-9}$$

$$k_{\mathrm{d,D}} = \left(1 - \frac{k_{\mathrm{r,S}}}{k_{\mathrm{r,S}}+k_{\mathrm{nr,S}}+k_{\mathrm{ISC}}}\right) k_{\mathrm{RISC}} \tag{5-3-10}$$

$$\Phi_{\mathrm{d,D}} = \sum_{k=1}^{\infty} (\Phi_{\mathrm{ISC}}\Phi_{\mathrm{RISC}})^k \Phi_{\mathrm{p,D}} = \frac{\Phi_{\mathrm{ISC}}\Phi_{\mathrm{RISC}}}{1-\Phi_{\mathrm{ISC}}\Phi_{\mathrm{RISC}}} \Phi_{\mathrm{p,D}} \tag{5-3-11}$$

where $k_{\mathrm{r,S}}$ and $k_{\mathrm{nr,S}}$ are the radiative and nonradiative decay rates of the singlet state, k_{ISC} and k_{RISC} are the rate constants of ISC and RISC, and Φ_{ISC} and Φ_{RISC} are the efficiencies of ISC and RISC, respectively. From the above equations, k_{ISC} and k_{RISC} are described by the following equations,

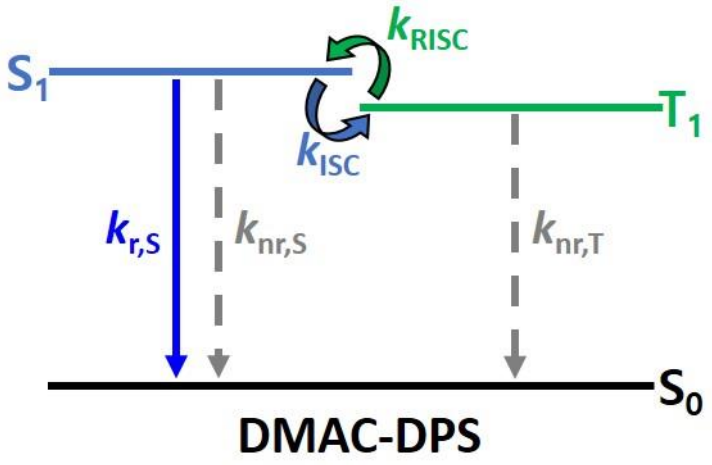

Figure 5-30. Schematic representation of the TADF process in DMAC-DPS.

$$k_{\mathrm{ISC}} = \frac{\Phi_{\mathrm{d,D}}}{\Phi_{\mathrm{p,D}}+\Phi_{\mathrm{d,D}}} k_{\mathrm{p,D}} \tag{5-3-12}$$

$$k_{\mathrm{RISC}} = \frac{k_{\mathrm{d,D}}\Phi_{\mathrm{RISC}}}{1-\Phi_{\mathrm{ISC}}\Phi_{\mathrm{RISC}}} = \frac{k_{\mathrm{p,D}}k_{\mathrm{d,D}}}{k_{\mathrm{ISC}}}\frac{\Phi_{\mathrm{d,D}}}{\Phi_{\mathrm{p,D}}} \tag{5-3-13}$$

Accordingly, k_{ISC} and k_{RISC} are obtained as 8.82×10^6 /s and 4.44×10^6 /s, respectively.

The schematic diagram of the hyperfluorsecent system where the MR emitters are doped in DMAC-DPS is depicted in Figure 5-31. Firstly, the FRET between DMAC-DPS and the MR emitters are explored. As studied in Section 5.3.3, the fluorescent emission from the DMAC-DPS hosted films consists of the MR emitter emission by excitons transferred from DMAC-DPS via FRET in addition to DMAC-DPS emission by the remaining excitons not transferred to the emitter molecules. To understand FRET between DMAC-DPS and the emitters, Forster radius (R_0) was calculated (refer to Section 2.1.4 and 5.2.4). The values of R_0 are 2.73 nm for tb-DBPICz and 2.88 nm for En-DBPICz, respectively.

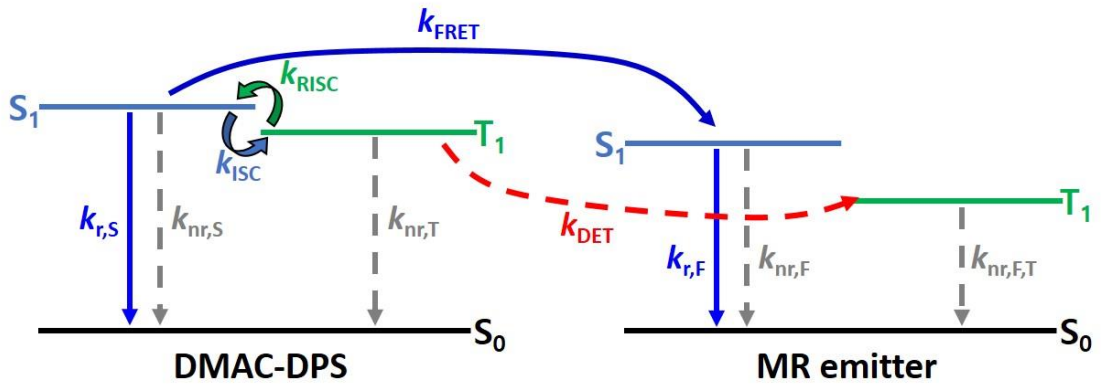

Figure 5-31. Schematic representation of exciton decay and energy transfer pathways between DMAC-DPS and MR emitter.

In transient PL profiles for the films (Figure 5-25), when the fluorescent MR emitters are doped in DMAC-DPS, strong delayed emission is still observed even though it is weaker than the DMAC-DPS neat film. To explore the difference in prompt and delayed emission more in detail, the PL spectra of prompt and delayed emission for the films at different times are plotted in Figure 5-32 and 5-33, respectively. Regarding the prompt emission (Figure 5-32), due to the strong aggregation features of tb-DBPICz, the peak emission is quickly quenched while the peak emission of En-DBPICz is maintained in line with Figure 5-29(b). However, with a slight increase of shoulder peaks at around 480 nm, the intensity of tail spectra over 500 nm is increased with time, suggesting that there is a small PL contribution from aggregate emission. In contrast, Figure 5-33 shows the normalised PL spectra of delayed emission for the films. Interestingly, the PL spectra of the delayed emission include negligible emission contribution from the MR emitters, meaning that delayed emission originates from the remaining excitons on DMAC-DPS, and FRET is completed at early times.

Assuming that the fluorescent emission of the MR emitter doped films originates

from the FRET of excitons initially formed in DMAC-DPS, the characteristic FRET efficiency and rate (E_{FRET} and k_{FRET}) can be described as

$$E_{\mathrm{FRET}} = \frac{k_{\mathrm{FRET}}}{k_{\mathrm{p,D}}+k_{\mathrm{FRET}}} = \frac{1/\Phi_{\mathrm{total}} \int P_{\mathrm{A}}(\lambda)d\lambda}{\int P_{\mathrm{D}}(\lambda)d\lambda+1/\Phi_{\mathrm{total}} \int P_{\mathrm{A}}(\lambda)d\lambda} \tag{5-3-14}$$

$$k_{\mathrm{FRET}} = \frac{E_{\mathrm{FRET}}k_{\mathrm{p,D}}}{1-E_{\mathrm{FRET}}} = \frac{1}{\tau_{\mathrm{D}}}\left(\frac{R_0}{R_{\mathrm{avr}}}\right)^6 \tag{5-3-15}$$

where P_{D} and P_{A} are the decomposed donor and acceptor emission spectrum, Φ_{total} is the total PLQE of the films, τ_{D} is the radiative decay lifetime of DMAC-DPS, and R_{avr}

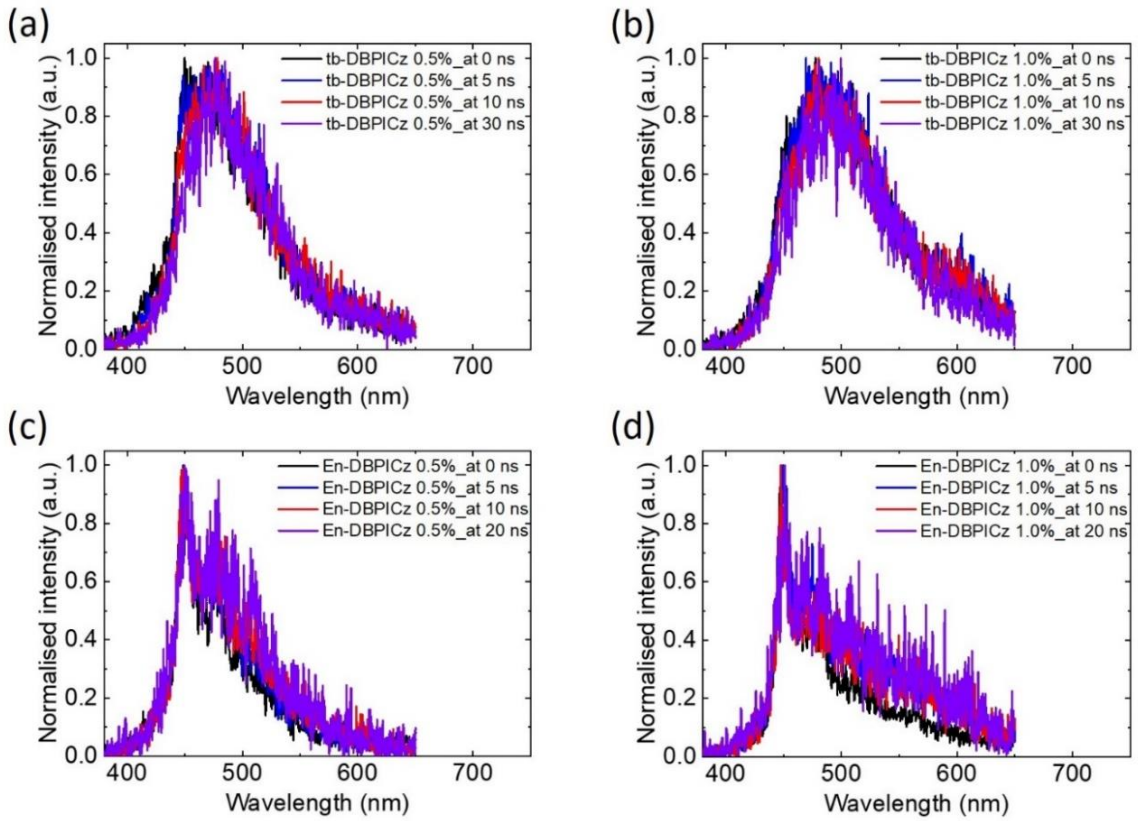

Figure 5-32. Normalised PL spectra of prompt emission for the DMAC-DPS: MR emitter films at different times. (a),(b) tb-DBPICz. (c),(d) En-DBPICz.

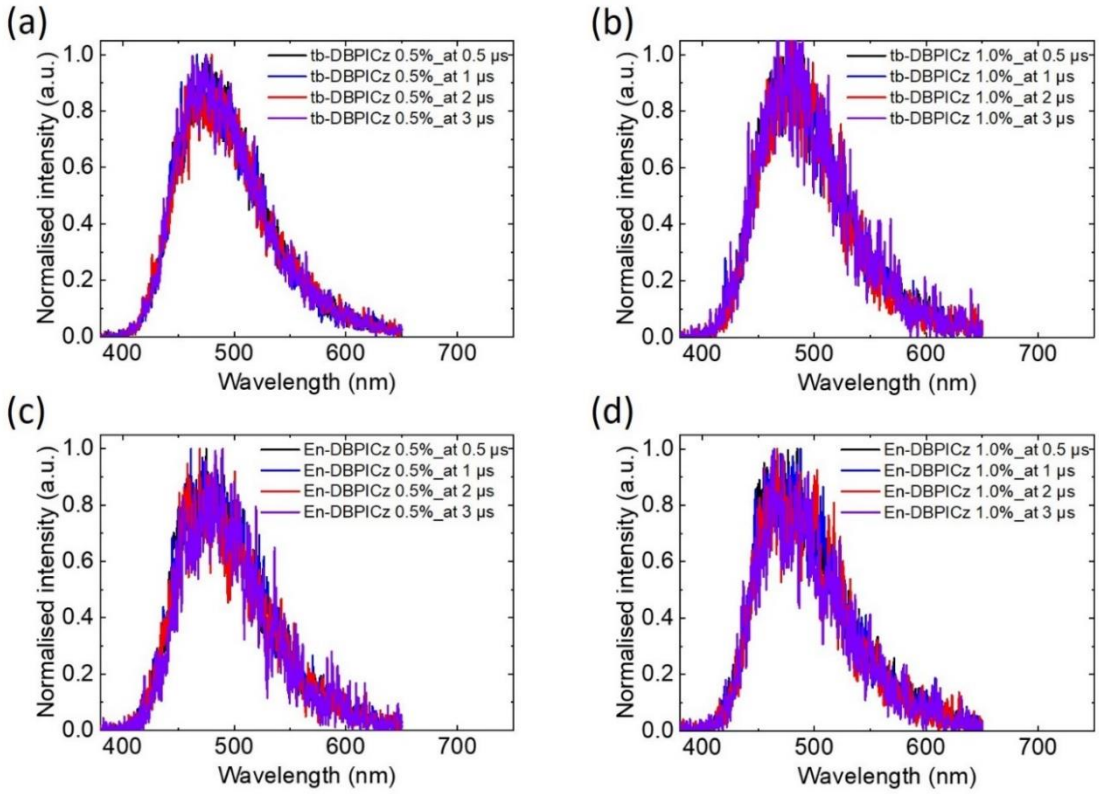

Figure 5-33. Normalised PL spectra of delayed emission for the DMAC-DPS: MR emitter films at different times. (a),(b) tb-DBPICz. (c),(d) En-DBPICz.

is the average intermolecular distance between donor and acceptor molecules. P_D and P_A are obtained by subtracting a linearly-scaled donor-only spectrum from the total PL spectrum (Figures 5-22 and 5-23). E_{FRET} for tb-DBPICz is 0.58 for 0.5% and 0.93 for 1.0%, respectively. In contrast, E_{FRET} for En-DBPICz is 0.31 for 0.5% and 0.64 for 1.0%, respectively, which is lower than that for tb-DBPICz. This result shows that as the encapsulating alkyl chain in En-DBPICz substantially increases intermolecular distance, E_{FRET} for the En-DBPICz doped films is lower than that for the tb-DBPICz doped films since k_{FRET} decreases rapidly with molecular spacing. From Equation 5-3-15, k_{FRET} for the DMAC-DPS:MR emitters films are calculated. As DMAC-DPS

and tb-DBPICz are in closer contact than En-DBPICz, k_{FRET} for the DMAC-DPS: tb-DBPICz blends (1.4×10^7 /s for 0.5% and 13.8×10^7 /s for 1.0%) is much faster than the DMAC-DPS:En-DBPICz blends (0.5×10^7 /s for 0.5% and 1.8×10^7 /s for 1.0%). As the values of k_{FRET} for the blends were obtained, the values of R_{avr} can also be extracted from Equation 5-3-15. As expected, R_{avr} of tb-DBPICz 0.5% and 1.0% doped in DMAC-DPS is 2.59 nm and 1.77 nm, quite shorter than that of En-DBPICz 0.5% and 1.0% doped in DMAC-DPS, 3.29 nm and 2.62 nm, respectively, indicating that the encapsulating ring in En-DBPICz increases the intermolecular distance effectively.

Next, the energy loss mechanisms, aggregation and DET, are examined. In principle, aggregation is the intrinsic properties of the dopant, not related to the interaction with the host, whereas DET is highly associated with the intermolecular orbital interaction between host and dopant molecules. As shown in Figure 5-32 and 33, FRET is almost completed in the early time range, and delayed emission only results from remaining excitons on DMAC-DPS. Accordingly, it is assumed that the efficiency loss in prompt emission and delayed emission results from aggregation and DET, respectively. Then, the efficiency and rate of aggregation (E_{agg} and k_{agg}) can be described by

$$E_{\mathrm{agg}} = 1 - \Phi_{\mathrm{total}} = \frac{k_{\mathrm{agg}}}{k_{\mathrm{p}} + k_{\mathrm{agg}}} \tag{5-3-14}$$

$$k_{\mathrm{agg}} = \frac{E_{\mathrm{agg}} k_{\mathrm{p}}}{1 - E_{\mathrm{agg}}} \tag{5-3-15}$$

Also, assuming that $k_{\mathrm{nr,T}}$ is negligible (k_{RISC} and $k_{\mathrm{DET}} \gg k_{\mathrm{nr,T}}$), the efficiency and rate of DET (E_{DET} and k_{DET}) can be expressed by

$$E_{\mathrm{DET}} = 1 - \Phi_{\mathrm{total}} = \frac{k_{\mathrm{DET}}}{k_{\mathrm{RISC}} + k_{\mathrm{DET}}} \tag{5-3-16}$$

$$k_{\mathrm{DET}} = \frac{E_{\mathrm{DET}} k_{\mathrm{RISC}}}{1 - E_{\mathrm{DET}}} \quad (5\text{-}3\text{-}17)$$

From Equation 5-3-15 and 17, k_{agg} and k_{DET} can be extracted. The rate constants of energy transfer and other important parameters are summarised in Table 5-9. As expected, the k_{agg} and k_{DET} of En-DBPICz are much slower than those of tb-DBPICz, which can lead to higher efficiency in devices.

Table 5-9. The summary of E_{FRET}, k_{FRET}, R_0, R_{avr}, k_{agg}, and k_{DET} for the tb-DBPICz and En-DBPICz doped in DMAC-DPS.

Host	DMAC-DPS			
Dopant	tb-DBPICz		En-DBPICz	
Doping (%)	0.5	1	0.5	1
E_{FRET}	0.58	0.93	0.31	0.64
k_{FRET} (10^7 /s)	1.43	13.77	0.47	1.84
R_0 (nm)	2.73		2.88	
R_{avr} (nm)	2.59	1.77	3.29	2.62
k_{agg} (10^7 /s)	1.01	1.51	0.44	0.98
k_{DET} (10^6 /s)	5.89	8.25	1.48	2.61

5.3.6 Device characterisation: hyperfluorescent OLEDs

Hyperfluorescent EL devices were fabricated utilising DMAC-DPS (exciton donor) and the two MR emitters, tb-DBPICz and En-DBPICz (exciton acceptor). It is expected that En-DBPICz could show much better performance in devices than tb-DBPICz on the basis of the chemical and photophysical studies in Section 5.3.2~5.

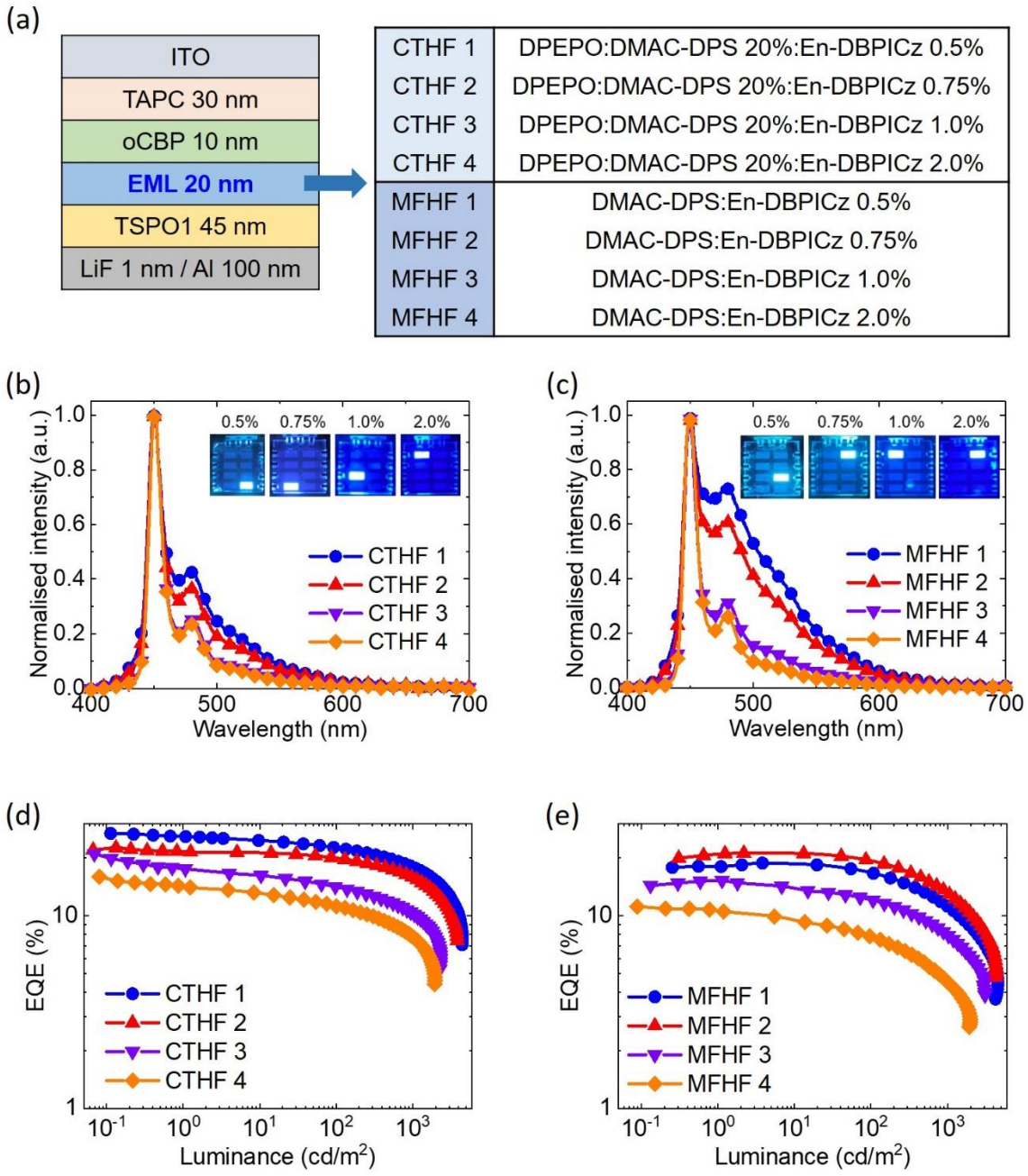

Figure 5-34. (a) Device structure for CTHF and MFHF devices employing En-DBPICz. Doping concentrations varies from 0.5% to 2.0% for both types of devices. (b),(c) EL spectra for CTHF and MFHF devices at 1 mA/cm^2. (d),(e) EQE-luminance plots for CTHF and MFHF devices.

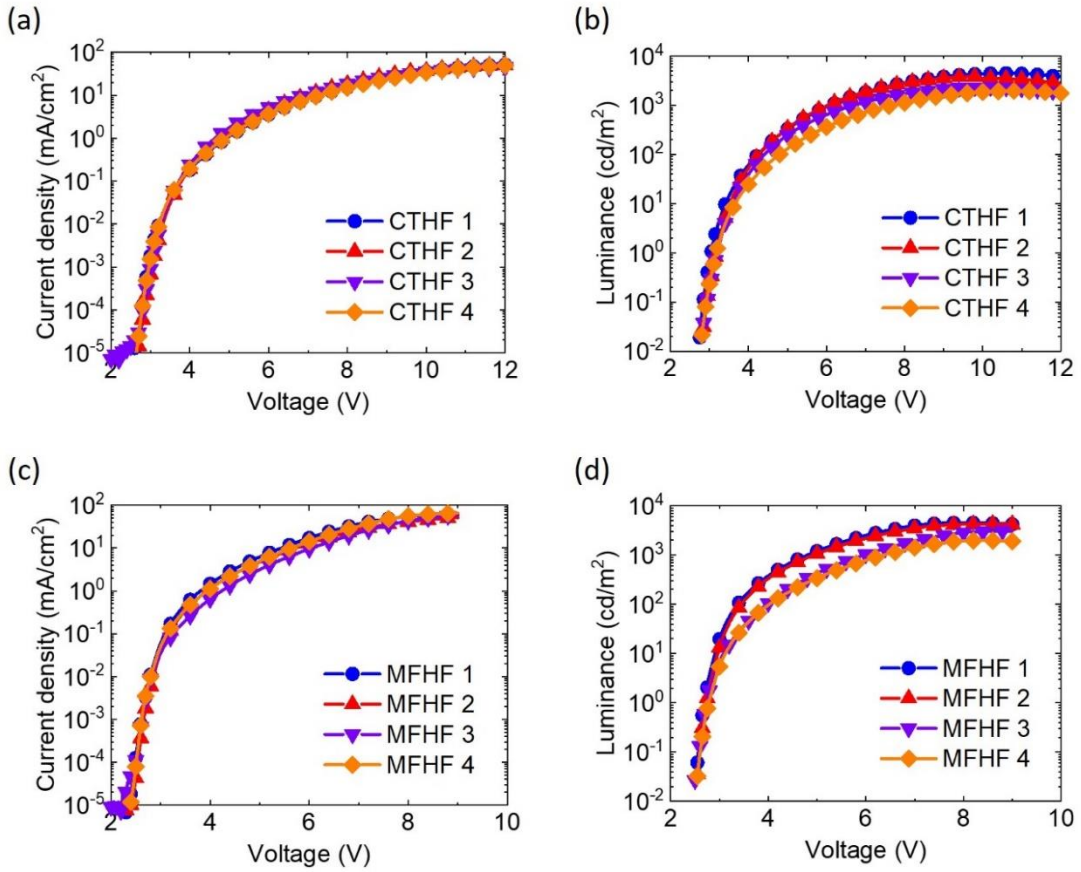

Figure 5-35. Comparison of current density-voltage plots and luminance-voltage plots for the CTHF and MFHF devices employing En-DBPICz. (a),(c) Current density-voltage plots. (b),(d) Luminance-voltage plots.

Accordingly, En-DBPICz was applied in hyperfluorescent OLEDs utilising the simple device structure shown in Figure 5-34(a). TAPC and 2,2′-di(9H-carbazol-9-yl)-1,1′-biphenyl (oCBP) were employed in an HTL part, and diphenyl-4-triphenylsilylphenyl phosphine oxide (TSPO1) was employed as an ETL.

To compare the device performance with and without a wide gap host matrix, MFHF and CTHF devices are explored with variation of emitter doping concentrations from 0.5% to 2.0%. Figure 5-34(b) and (c) show the EL spectra of the CTHF and MFHF

devices, respectively. Due to the better PL-absorption overlap in CTHF, the spectra at 0.5% and 0.75% doping in CTHF are narrower than those in MFHF. However, with increased doping to 1% and 2%, as the donors and acceptors are close enough for effective FRET, the EL of the MFHF devices is observed predominantly from En-DBPICz with EL spectra approaching the solution PL with an ultra-narrow FWHM (~12 nm). Figure 5-34(d) and (e) show the EQE-luminance plots. In CTHF devices, the maximum EQE of 26.7% is achieved at 0.5% doping, and as doping concentration is increased, EQE is gradually reduced, but higher than 20% maximum EQE was maintained at 1% doping where most excitons formed in DMAC-DPS are transferred to En-DBPICz (Figure 5-34(b)). Regarding MFHF devices, the maximum EQE of

Table 5-10. Summary of the device performance for En-DBPICz-based hyperfluorescent OLED devices.

	V_{on} [a] (V)	EQE_{Max} (%)	V_{100} [b] (V)	EQE_{100} [b] (%)	$Luminance_{Max}$ ($cd \cdot m^{-2}$)	λ_{peak} (nm)	FWHM (nm)	CIE (x,y)
CTHF 1	2.8	26.7	4.2	22.5	4477.5	449.5	15.5	0.163, 0.173
CTHF 2	2.9	22.5	4.3	19.9	3840.8	449.5	14.3	0.164, 0.159
CTHF 3	2.9	20.9	4.4	14.4	2327.5	450.5	12.3	0.159, 0.115
CTHF 4	2.9	15.9	4.8	11.2	1955.1	450.5	12.0	0.157, 0.105
MFHF 1	2.6	18.8	3.4	16.7	4531.8	449.0	60.3	0.176, 0.247
MFHF 2	2.6	21.1	3.4	19.3	4285.1	449.0	47.8	0.174, 0.225
MFHF 3	2.6	15.2	4.0	12.1	3086.6	449.0	12.5	0.166, 0.156
MFHF 4	2.6	11.2	4.0	7.8	1980.0	449.0	12.5	0.160, 0.116

a) Voltage at 0.1 cd/m^2. b) Values at 100 cd/m^2.

21.1% was attained even though the host matrix was not applied, meaning that the IQE is close to unity. In addition, at 1% doping, higher than a maximum EQE of 15% is maintained with CIE_y ~0.16, showing the disruptive potential of realising highly efficient pure blue MFHF OLEDs with ultra-narrowband emission. The J-V and L-V plots for the CTHF and MFHF devices are presented in Figure 5-35. Considering the insensitivities of J-V profiles to doping concentrations (Figure 5-35(a) and (c)), charge trapping is negligible, and EL primarily results from exciton energy transfer between the donors and acceptors. Also, as shown in Figure 5-35(b) and (d), luminance is decreased with reduced EQEs as doping concentrations are increased. The detailed device performance for the devices is summarised in Table 5-10.

Figure 5-36 shows the device results for conventional-type TADF (CT-TADF) and matrix-free TADF (MF-TADF) OLEDs. The maximum EQE for the CT-TADF device is 28.5%, much higher than MF-TADF, 17.0%, which led to the lower EQEs of the MFHF devices than those of the CTHF devices. Also, the slightly red-shifted and broader spectrum of the MF-TADF device compared to the CT-TADF one is not beneficial for effective FRET from DMAC-DPS to En-DBPICz. Better device performance could be realised in MFHF devices if more efficient blue TADF donors

Table 5-11. Summary of the device performance for DMAC-DPS TADF OLED devices.

	V_{on} [a)] (V)	EQE_{Max} (%)	V_{100} [b)] (V)	EQE_{100} [b)] (%)	$Luminance_{Max}$ ($cd \cdot m^{-2}$)	λ_{peak} (nm)	FWHM (nm)	CIE (x,y)
CT-TADF	2.8	28.5	3.7	25.8	5420.5	461.0	83.0	0.173, 0.242
MF-TADF	2.7	17.0	3.3	15.8	2261.7	475.5	88.3	0.185, 0.315

a) Voltage at 0.1 cd/m^2. b) Values at 100 cd/m^2.

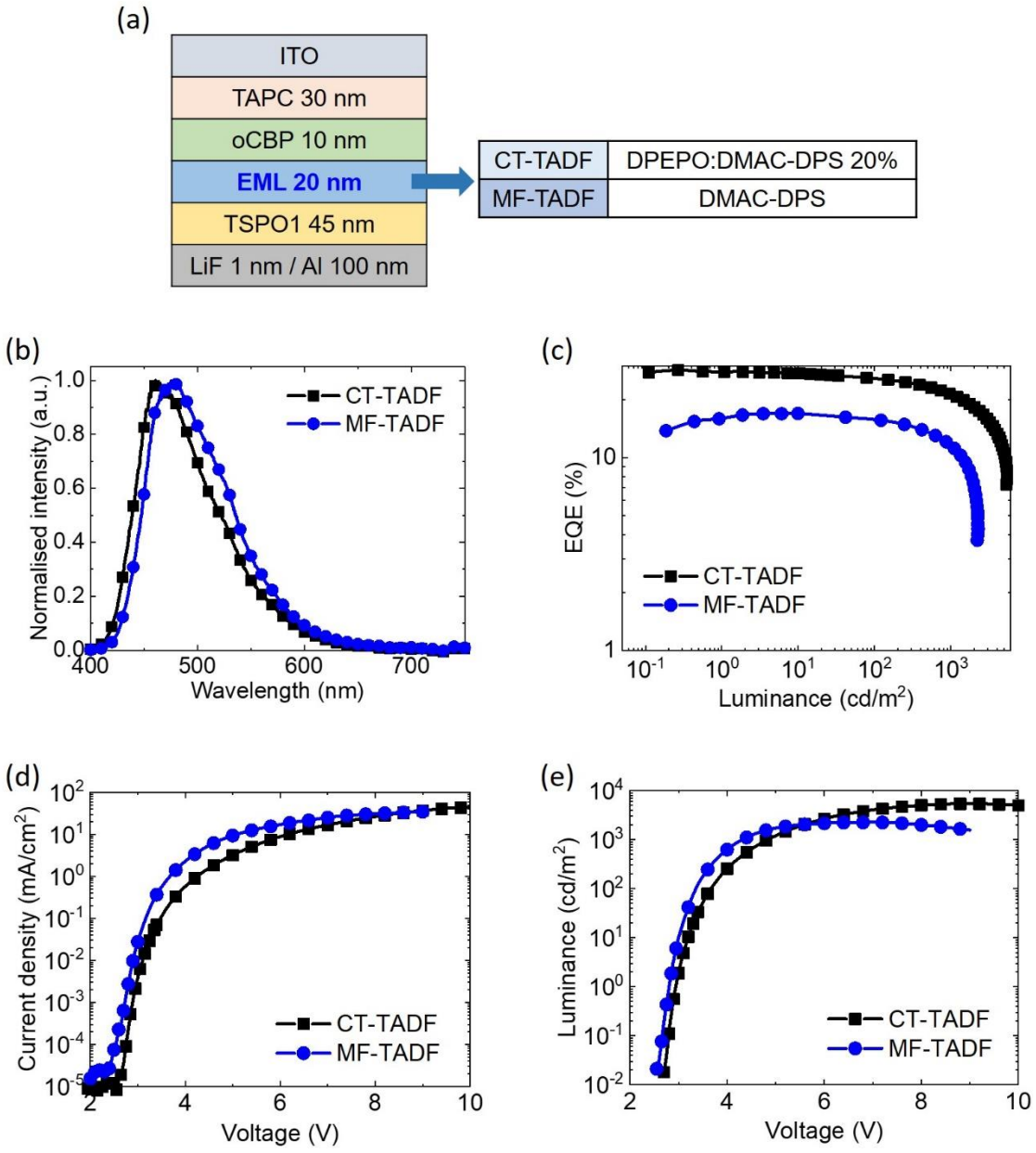

Figure 5-36. (a) Device structure for DMAC-DPS-based CT-TADF and MF-TADF devices (b) EL spectra for CT-TADF and MF-TADF devices at 1 mA/cm^2. (c) EQE-luminance plots for the CT-TADF and MF-TADF devices. (d),(e) show current density-voltage plots and luminance-voltage plots for the CT-TADF and MF-TADF devices, respectively.

with improved PL-absorption overlap could be combined with En-DBPICz. The detailed device performance of DMAC-DPS TADF devices is summarised in Table 5-11.

To confirm the superiority of En-DBPICz over tb-DBPICz in devices, tb-DBPICz is also employed in the same device structure and doping conditions used with En-DBPICz, and the device performance is shown in Figure 5-37 and Table 5-12. The EL spectra for the CTHF and MFHF devices are depicted in Figure 5-37(b) and (c). As anticipated from the steady-state photophysical studies in Section 5.3.3, the peak emission at 450 nm is quenched, and the EL spectra are red-shifted with broader FWHM as doping concentrations are increased. This result is associated with the PL spectra of the tb-DBPICz doped films with variation of doping concentrations in Figure 5-21(c) and 5-22(a). Figure 5-37(d) and (e) show the EQE-luminance plots. As

Table 5-12. Summary of the device performance for tb-DBPICz-based OLED devices.

	V_{on} [a)] (V)	EQE_{Max} (%)	V_{100} [b)] (V)	EQE_{100} [b)] (%)	$Luminance_{Max}$ ($cd \cdot m^{-2}$)	λ_{peak} (nm)	FWHM (nm)	CIE (x,y)
CTHF 5	2.9	17.5	4.6	15.3	2259.6	448.5	58.3	0.162, 0.194
CTHF 6	2.9	16.4	4.5	14.6	2108.1	448.5	62.5	0.162, 0.208
CTHF 7	2.9	12.5	4.4	10.7	1724.7	465.5	72.3	0.161, 0.231
CTHF 8	2.9	6.5	5.7	3.9	1251.0	480.5	66.5	0.163, 0.304
MFHF 5	2.6	14.1	3.7	12.9	2284.2	449	60.3	0.173, 0.234
MFHF 6	2.6	10.0	4.2	9.1	1699.7	449	61.3	0.165, 0.221
MFHF 7	2.6	5.2	4.4	4.2	1202.7	479	77.8	0.170, 0.293
MFHF 8	2.6	4.2	4.8	3.5	928.4	475.5	62.5	0.158, 0.266

a) Voltage at 0.1 cd/m^2. b) Values at 100 cd/m^2.

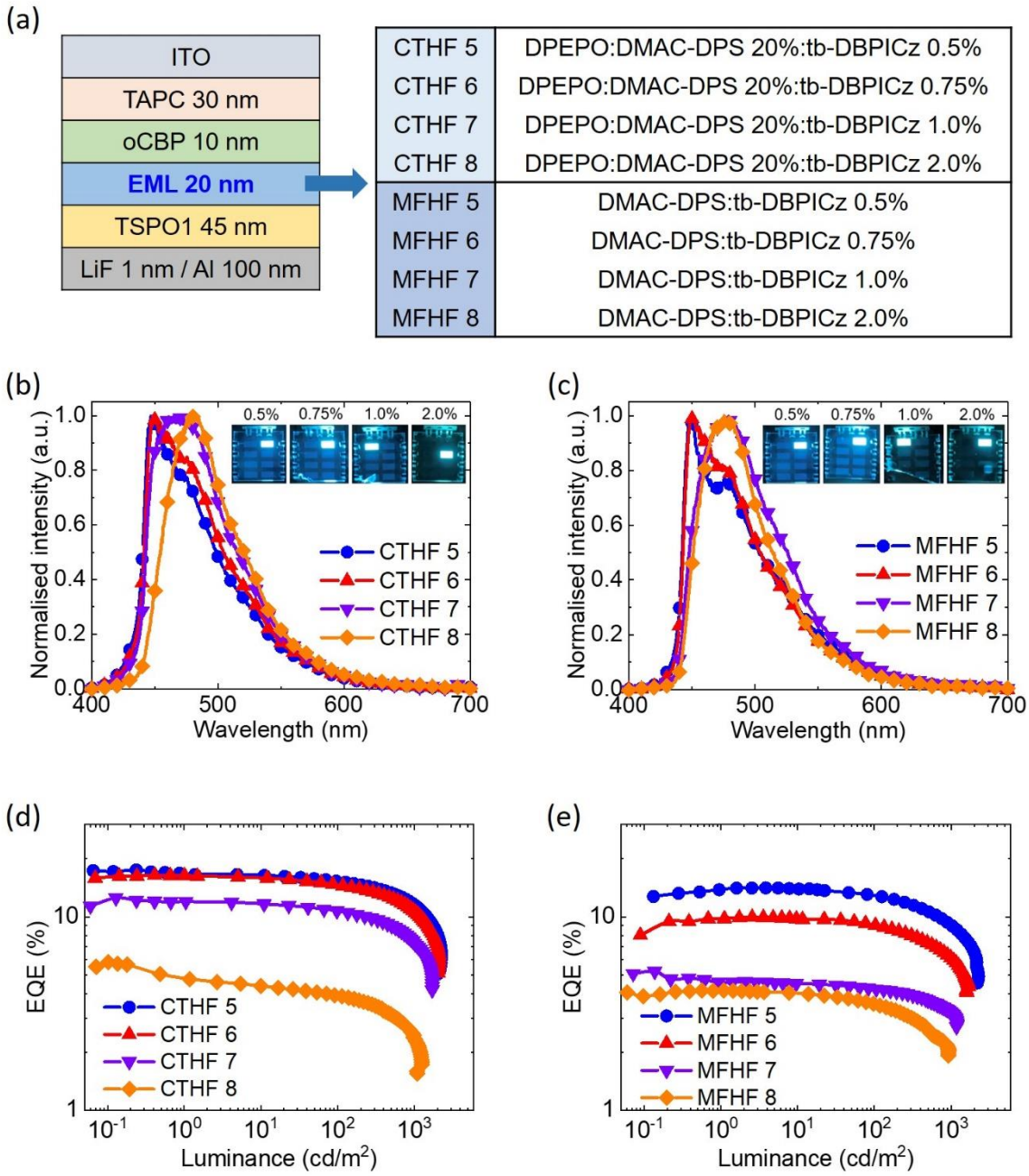

Figure 5-37. (a) Device structure for CTHF and MFHF devices employing tb-DBPICz. Doping concentrations varies from 0.5% to 2.0% for both types of devices. (b),(c) EL spectra for CTHF and MFHF devices at 1 mA/cm^2. (d),(e) EQE-luminance plots for CTHF and MFHF devices.

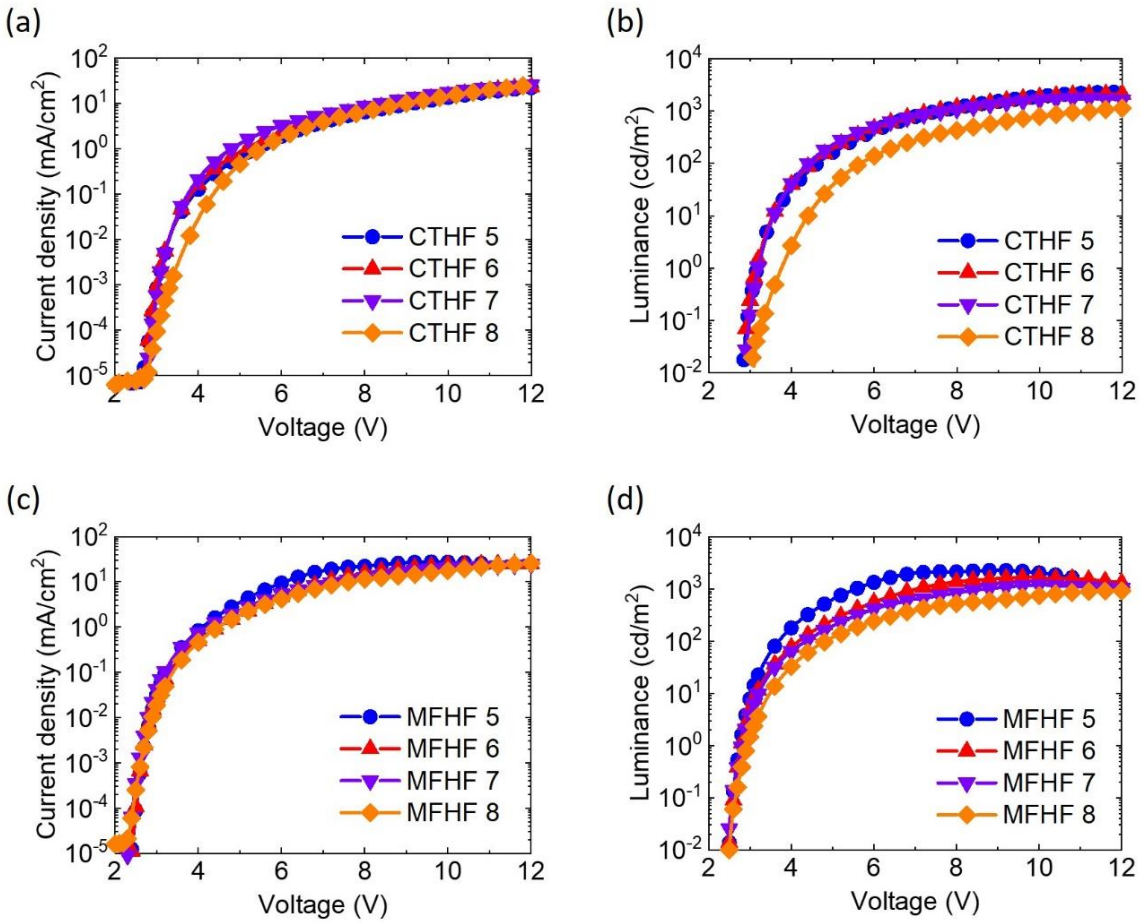

Figure 5-38. Comparison of current density-voltage plots and luminance-voltage plots for the CTHF and MFHF devices employing tb-DBPICz. (a),(c) Current density-voltage plots. (b),(d) Luminance-voltage plots.

expected, the maximum EQEs for the tb-DBPICz-based CTHF and MFHF devices are 17.5% and 14.1%, respectively, much lower than those for the En-DBPICz-based counterparts. Also, as doping concentrations are increased, EQEs steeply drop due to significant aggregation and triplet transfer via DET between the donors and acceptors, as studied in Section 5.3.3~5. Also, tb-DBPICz can act as trapping sites at high doping consistent with the slightly shallower J-V curves as doping concentrations are increased, as shown in Figure 5-38(a) and (c). The substantially reduced luminance with an

increase in doping concentrations (Figure 5-38(b) and (d)) is also relevant to the energy loss mechanisms mentioned above. Therefore, it can be concluded that sterically protected chemical structures by encapsulation can substantially enhance the device performance of hyperfluorescent OLEDs by suppressing energy losses via aggregation and triplet DET.

5.3.7 Device characterisation: fluorescent OLEDs

As studied in Section 5.3.2, the solution PL of En-DBPICz shows much narrower FWHM(~10 nm) than DABNA-type MR emitters (~20-30 nm FWHM),[17,21,22] with $CIE_{x,y}$: (0.15, 0.05). However, in the DMAC-DPS matrix, due to the remaining emission tail over 520 nm, CIE_y was slightly higher than 0.1 in DMAC-DPS-based hyperfluorescent OLEDs, as studied in Section 5.3.6. Recently, one of the blue boron-incorporated MR emitters, methyl-2,12-di-*tert*-butyl-5,9-bis(4-(*tert*-butyl)phenyl)-5,9-dihydro -5,9-diaza-13b-boranaphtho[3,2,1-de]anthracene (M-tDABNA) was applied to

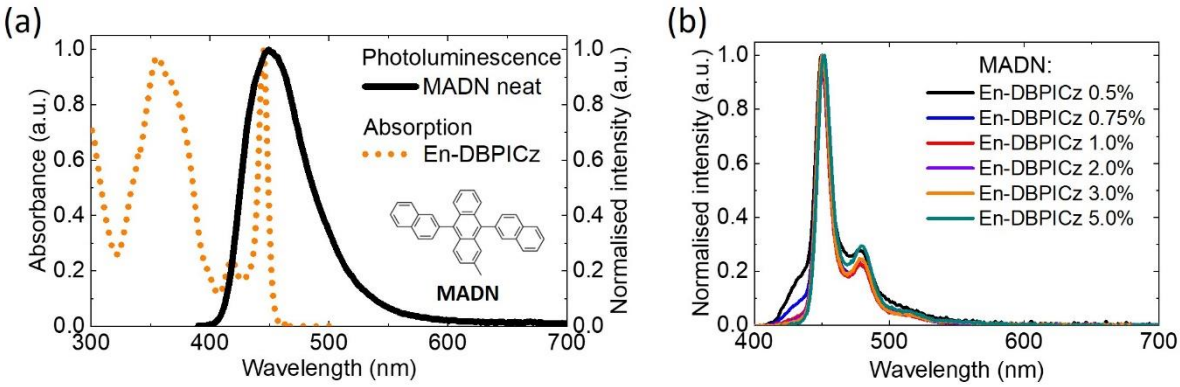

Figure 5-39. (a) The absorbance for En-DBPICz diluted in toluene and the PL spectrum for the MADN nest film. (b) The PL spectra for the En-DBPICz doped in MADN films with variation of doping concentrations from 0.5% to 5.0%.

conventional fluorescent OLEDs showing good colour purity (CIEx,y: 0.137, 0.076) in bottom emission OLEDs with higher than 8% EQE.[95] Therefore, En-DBPICz was also applied in conventional fluorescent OLEDs exploiting one of the anthracene derivatives, 2-methyl-9,10-bis(naphthalen-2-yl)anthracene (MADN), as an exciton donor, for realising pure blue En-DBPICz spectrum in OLEDs. Figure 5-39(a) shows the PL-absorption overlap between MADN and En-DBPICz. The 0-0 transition absorption peak for En-DBPICz is well-overlapped with the PL spectrum for MADN. In addition, FWHM for MADN is 61 nm, narrower than that for DMAC-DPS (92 nm) with a much smaller PL intensity over 550 nm, which could be beneficial for quenched emission tail beyond 520 in the MADN hosted films. Figure 5-39(b) shows the PL spectra for the MADN hosted films with the variation of doping concentrations from 0.5% to 5.0%. As expected from the excellent PL-absorption overlap, the PL spectra for the films are almost identical to the solution PL (Figure 5-17), with quenched MADN emission at over 1% doping.

Based on these results, the MADN:En-DBPICz combination was applied in the device architecture shown in Figure 5-40(a), and the device performance is shown in Figure 5-40(b) and (c) and Table 5-13. TAPC, TCTA, and mCP were used in an HTL part, and 2-(9,9'-spirobi[fluoren]-3-yl)-4,6-diphenyl-1,3,5-triazine (SF3-TRz) and bis-4,6-(3,5-di-3-pyridylphenyl)-2-methylpyrimidine (B3PYMPM) were employed for an ETL. The doping concentration of En-DBPICz varies from 0.5% to 5.0%, like the PL spectra. Figure 5-40(b) shows the EL spectra for the devices. As anticipated from the PL spectra, pure En-DBPICz emission is fully realised by effective FRET from MADN to En-DBPICz, showing pure deep blue emission spectra at ~450 nm peak wavelength and 11~12 nm FWHM. Furthermore, $CIE_{x,y}$: (0.15, 0.05) is attained (Table 5-13), with mostly quenched emission below 450 nm, which is considered as unfavourable and harmful deep blue emission range in displays.[215,216] Figure 5-40(c) shows EQE-

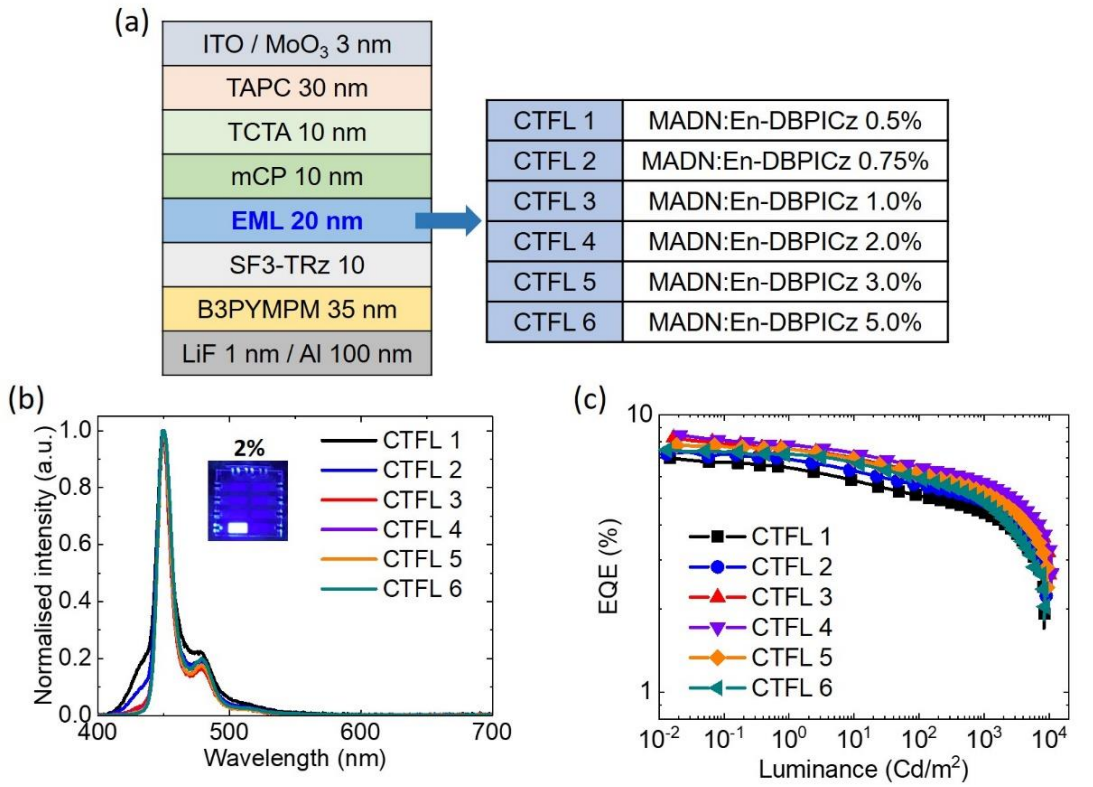

Figure 5-40. (a) Device structure for En-DBPICz-based conventional fluorescent OLEDs with variation of doping concentration from 0.5% to 5%. (b) EL spectra for the devices at 1 mA/cm^2. (c) EQE-luminance plots for the devices.

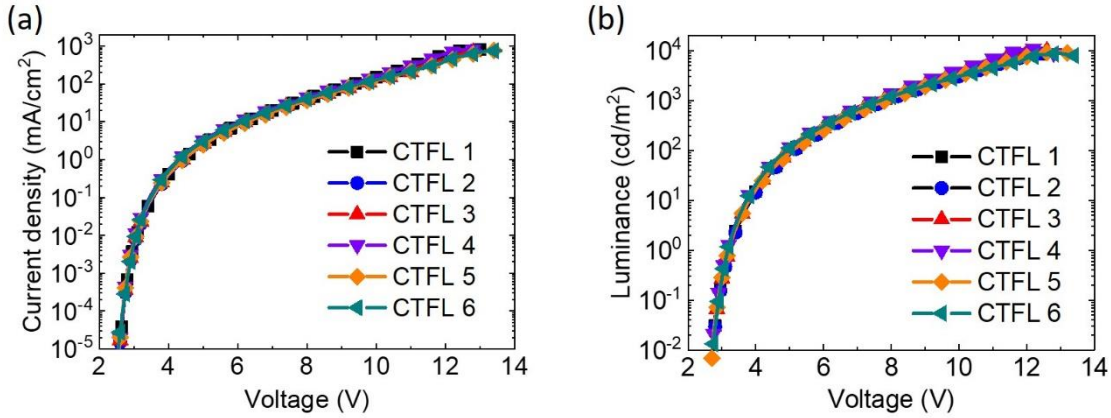

Figure 5-41. (a) Current density-voltage plots and (b) luminance-voltage plots for the devices.

luminance plots. The maximum EQE among the devices is 8.5%, attained at 2% doping (CTFL 4). At low doping, as MADN emission is included in EL due to incomplete FRET, EQE is relatively low, but at 1% and 2%, EQEs are higher than 8% as most excitons formed in MADN are mostly transferred to En-DBPICz via FRET. However, at higher than 3%, EQE drops due to concentration quenching, which is normally observed in host-guest emitting systems.[132,219] J-V and L-V curves are exhibited in Figure 5-41(a) and (b). Almost identical J-V and L-V curves for all devices indicate that the charge trapping effect is negligible, and most emission occurs by energy transfer, FRET, from the host to the dopant.

Table 5-13. Summary of the device performance for En-DBPICz-based fluroescent OLED devices.

	V_{on} [a)] (V)	EQE_{Max} (%)	V_{100} [b)] (V)	EQE_{100} [b)] (%)	$Luminance_{Max}$ ($cd \cdot m^{-2}$)	λ_{peak} (nm)	FWHM (nm)	CIE (x,y)
CTFL 1	2.7	7.0	5.1	5.1	8545.5	449.5	13.0	0.151, 0.060
CTFL 2	2.7	7.3	5.1	5.6	9028.8	449.5	11.8	0.149, 0.054
CTFL 3	2.7	8.3	5.0	6.2	10125.5	449.5	11.3	0.149, 0.049
CTFL 4	2.7	8.5	4.9	6.5	10908.6	449.5	11.9	0.149, 0.050
CTFL 5	2.7	7.8	5.1	6.1	9330.6	450.5	11.9	0.150, 0.051
CTFL 6	2.7	7.5	4.9	5.9	8694.0	450.5	12.6	0.150, 0.056

a) Voltage at 0.1 cd/m^2. b) Values at 100 cd/m^2.

5.4 Summary

Firstly, the influence of encapsulation on the performance of deep blue hyperfluorescent OLEDs with 9,10-diphenylanthracene based fluorescent acceptors was investigated. Doped into DPEPO:CZ-PS and a host-free CZ-PS system, En-DPA exhibits a maximum PLQE of 100% by effective FRET. Also, even at 10% doping in the TADF matrix CZ-PS, a PLQE greater than 95% was recorded, indicating that loss mechanisms resulting from close contact between molecules (such as aggregation and DET) are effectively suppressed by encapsulation. Furthermore, it was demonstrated that MFHF devices substantially outperform CTHF devices. Higher than 40% improved PE with nearly ten times higher maximum luminance and stability was attained with deep blue emission, maintaining the comparable maximum EQE of 7.5% to CTHF devices, 7.9%. This result shows the potential of efficient MFHF devices with the new design of fluorescent acceptors and TADF donors for effectively suppressing the energy loss pathways.

Next, the newly designed MR emitters were studied. The sterically encapsulated indolocarbazole-based new emitter, En-DBPICz, showed ultra-narrow emission at 450 nm peak wavelength with almost unity PLQE. With one of the efficient blue TADF materials, DMAC-DPS, En-DBPICz was utilised in the hyperfluorescent emissive system, and tb-DBPICz was compared as a control. The steady-state and transient photophysical studies proved that triplet transfer is substantially reduced in the En-DBPICz-doped films compared to the tb-DBPICz-doped film. Also, it was demonstrated that the aggregation effect of tb-DBPICz is severe, while En-DBPICz shows negligible aggregate emission due to its sterically protected chemical structure. Furthermore, the two MR emitters were employed in EL devices. In hyperfluorescent EL devices, the CTHF and MFHF devices show maximum EQEs of 26.7% and 21.1%,

respectively, indicating almost 100% IQE in both CTHF and MFHF devices, considering the 20~30% outcoupling efficiency of OLEDs.[16,218] Furthermore, higher than 15% EQE is maintained in the MFHF device with CIE_y ~0.16, showing the great potential of realising highly efficient deep blue MFHF devices with future work. For true blue EL devices, En-DBPICz is applied in conventional fluorescent OLEDs. Higher than a maximum EQE of 8% with $CIE_{x,y}$: (0.15,0.05) was attained. These results suggest that the encapsulated deep blue MR emitters could be a solution for realising highly efficient pure blue OLEDs.

Chapter 6 The optimisation of exciton formation and charge transport in organic radical LEDs

6.1 Introduction

Organic radicals have emerged as the basis of more efficient OLEDs with higher performance limits than typical molecular emitters. This is achieved by doublet fluorescence with nanosecond emission in contrast to standard singlet-triplet photophysics found in organic optoelectronics. Here, direct charge recombination at radical sites is considered the primary emission process. However, due to the low-energy radical orbitals, severe electron trapping occurs in devices with narrow emission zones at the interface of EML and ETL, which causes problems of significant efficiency roll-off, low radiance, and poor stability.

The most effective and widely used method for improving the balance of electron and hole transport in an EML is to mix electron-transporting and hole-transporting materials in a blended host.[78,79,220] This can be achieved by blending the materials used for the electron- and hole-transport layers (ETL and HTL). Mixed-host approaches have been widely applied not only to fluorescence-[221–223] and phosphorescence-based devices,[133,224–226] but also with TADF EL, and TADF- or phosphorescence-sensitised fluorescence.[100,102,121,122,227]

For efficient and stable NIR OLEDs, a new NIR emitter based on (3,5-dichloro-4-pyridyl)bis(2,4,6-trichlorophenyl)methyl (PyBTM) radical has been designed.[41] Triphenyl amine-substituted (2-chloro-3-pyridyl)bis(2,4,6-trichlorophenyl) methyl

(PyBTM') (TPA-PyBTM') shows efficient NIR emission around 820 nm and strong absorption between 400 and 550 nm, beneficial for effective FRET. The design of TPA-PyBTM' follows the previously established rules for obtaining emissive π-radicals with non-alternant hydrocarbon motifs (here -TPA and -PyBTM' components). TPA-PyBTM'-based devices were successfully fabricated with a maximum EQE of 6.4%: the highest value of published NIR emissive devices. By exploiting mixed hosts for the radical emitters, improved efficiency roll-off, radiance, and operational lifetime are obtained, despite the slightly reduced maximum EQEs. Furthermore, by enhanced electron transport in an EML, the comparable EQE to the CBP-based device is achieved with substantially improved efficiency, radiance, and device lifetime.

6.2 Studies of mixed host systems for organic radical

6.2.1 Characterisation of NIR organic radical: TPA-PyBTM'

The synthesis and characterisation of TPA-PyBTM' were conducted by Dr Shun Kimura, Department of Chemistry, University of Tokyo. TPA-PyBTM' is a new NIR radical emitter with energy level features that are suitable for testing radical-based OLEDs, as shown by studies of its spin, electrochemical, photophysical, and quantum-chemical properties. Quantitative electron spin resonance (ESR) spectroscopy confirmed the existence of one unpaired electron for each TPA-PyBTM' molecule. The ESR spectrum displays hyperfine splitting assigned to nitrogen and hydrogen atoms in the PyBTM' moiety, indicating delocalisation of the spin density over this group (Figure 6-1). CV demonstrated two reversible redox waves at $E^{0'}_{red} = -1.05$ V (vs ferrocenium/ferrocene) and $E^{0'}_{ox} = 0.15$ V, attributed to reduction centred at the

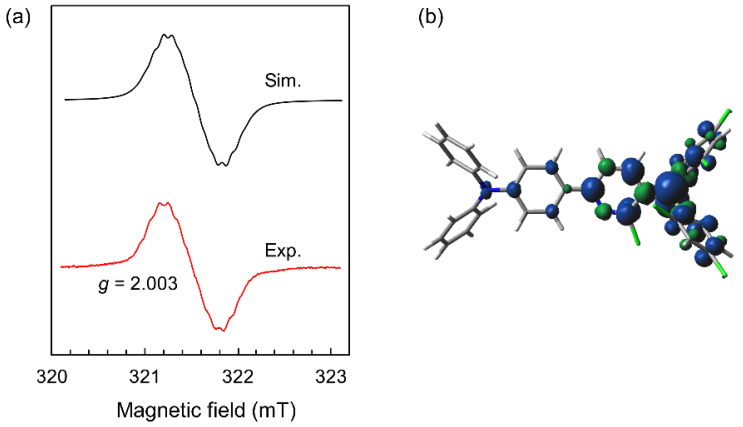

Figure 6-1. (a) ESR spectrum of TPA-PyBTM' in toluene at 175 K (2.0×10^{-4} M, red) and computed simulation (black). Hyperfine coupling constants used for the simulation were as follows: 0.2 mT for a nitrogen atom, 0.1 mT for four hydrogen atoms on two trichlorophenyl groups, and 0.1 and 0.15 mT for hydrogen atoms at 5- and 4-positions in the pyridyl ring, respectively. (b) Spin density distribution calculated using DFT.

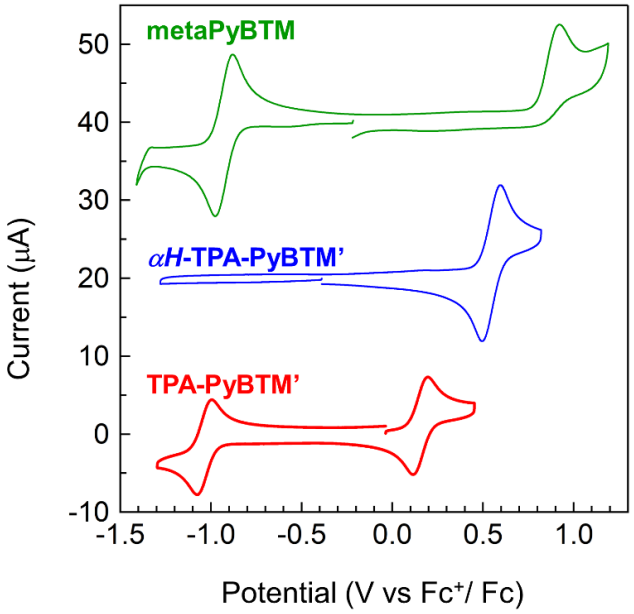

Figure 6-2. Cyclic voltammograms of TPA-PyBTM' Cyclic voltammogram of TPA-PyBTM' (red), *αH*-TPA-PyBTM'(blue), and metaPyBTM (green) in CH_2Cl_2 containing 0.1 M $^{n}(C_4H_9)_4NPF_6$, obtained with a scan rate of 0.1 V/s.

electron-poor PyBTM' moiety and oxidation that removes an electron from the highest occupied molecular orbital (HOMO), a π-orbital delocalised over the electron-rich TPA skeleton and the PyBTM' moiety (Figure 6-2 and Figure 6-4). From this, SOMO (reduction) and HOMO energies are estimated as 3.8 eV and 5.0 eV. TPA-PyBTM' displays PL in a variety of solvents (Figure 6-3 and Table 6-1), with PLQEs between 6 and 24%. The peak emission wavelength is redshifted from 742 nm (1.67 eV) to 875 nm (1.42 eV) with increasing solvent polarity, indicating the formation of an intramolecular charge-transfer excited state. These experimental characteristics are supported by density functional theory (DFT) and time-dependent density functional theory (TDDFT) calculations (done by Dr Shun Kimura, Department of Chemistry, University of Tokyo) as described in Figure 6-4.

Figure 6-4 shows the calculated molecular orbitals (MOs) of TPA-PyBTM'. The MOs are distributed on both the TPA and the PyBTM' moieties due to orbital hybridisation via efficient π-conjugation. The β-HOMO (184β) and β-SOMO (185β) are located mainly at the TPA and the PyBTM' moieties, while their α-counterparts are delocalised over the entire π-conjugated framework. TDDFT calculation shows that the

Table 6-1. Photophysical parameters of TPA-PyBTM' in solvents.

Solvent	λ_{ab} / nm	ε / $M^{-1}cm^{-1}$	λ_{em} / nm	Φ	τ / ns	k_f / $10^7 s^{-1}$	k_{nr} / $10^7 s^{-1}$
Cyclohexane	715	7230	742	0.17	8.0	2.1	10
Carbon tetrachloride	719	6636	753	0.22	9.4	2.3	8.3
Toluene	720	6520	800	0.24	8.5	2.8	8.9
Dioxane	713	5950	811	0.12	4.6	2.6	19
Diethyl ether	712	5730	830	0.06	2.3	2.4	41
Chloroform	713	5020	875	0.06	2.5	2.5	38

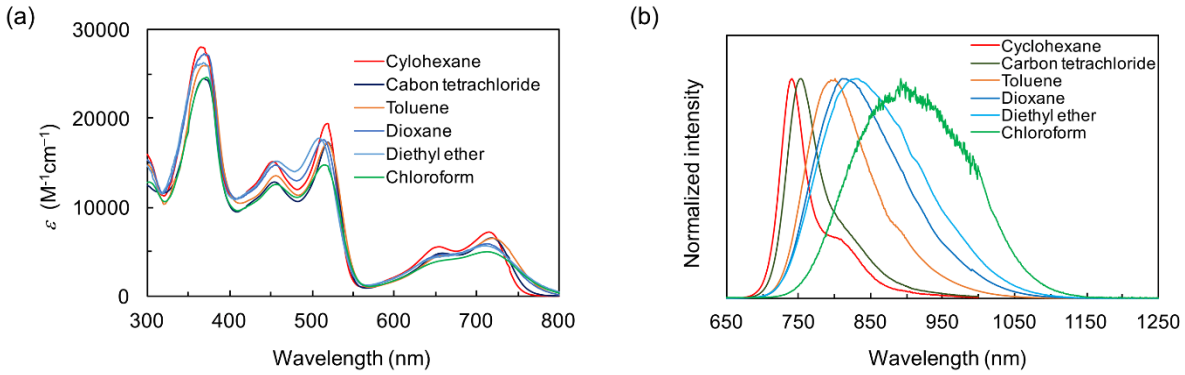

Figure 6-3. (a) Absorption and (b) emission spectra of TPA-PyBTM' in solvents.

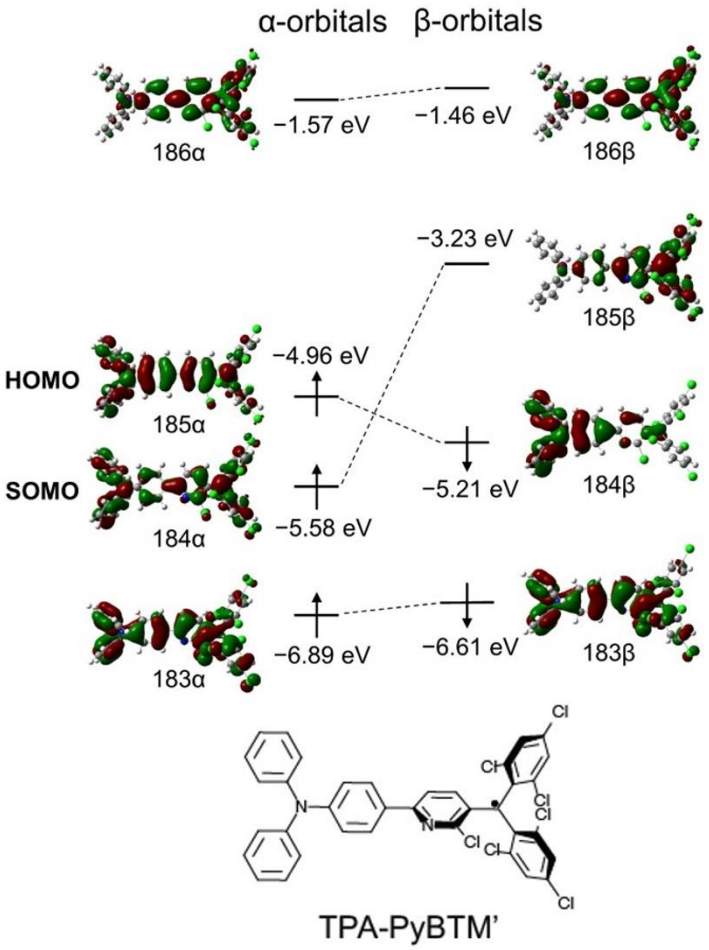

Figure 6-4. MO diagram of TPA-PyBTM' in cyclohexane calculated by DFT.

lowest energy excited state is formed mainly via a 185β←184β electronic transition. This transition corresponds to a charge transfer transition from the TPA to the PyBTM' moiety and is assignable to the transition bands observed around 600-750 nm in the absorption spectra. The modelled charge-transfer character of the doublet excited state is consistent with the solvatochromic effects mentioned above.

6.2.2 Design of mixed hosts

Figure 6-5(a) shows the molecular structures of TPA-PyBTM', 4,4'-bis(carbazol-9-yl)biphenyl (CBP), 4,4′,4″-tris(carbazol-9-yl)triphenylamine (TCTA), and bis-4,6-(3,5-di-3-pyridylphenyl)-2-methylpyrimidine (B3PYMPM). The three types of EML composition were designed using these materials, as shown in Figure 6-5(b). For standard devices, CBP was employed as a conventional host with TPA-PyBTM'. To control charge transport and improve charge balance in the EML, two types of mixed hosts were exploited using typical ETL and HTL materials: B3PYMPM was mixed with CBP to enhance electron transport, and CBP was replaced with TCTA to further increase hole transport. When B3PYMPM was mixed with CBP or TCTA in a 1:1 ratio, emission peaks were observed at 430 nm (CBP:B3PYMPM) and 510 nm (TCTA:B3PYMPM), which were red-shifted with respect to the individual host components and indicate exciplex formation (Figure 6-6). In this case, it is anticipated that when radical emitters are doped in an exciplex host matrix, both singlet and triplet exciplexes formed on the host can undergo energy transfer to form doublet excitons in the radical dopant for efficient and rapid light emission in EL devices. Direct charge capture on the dopant is also a possible mechanism that is tested in this design.

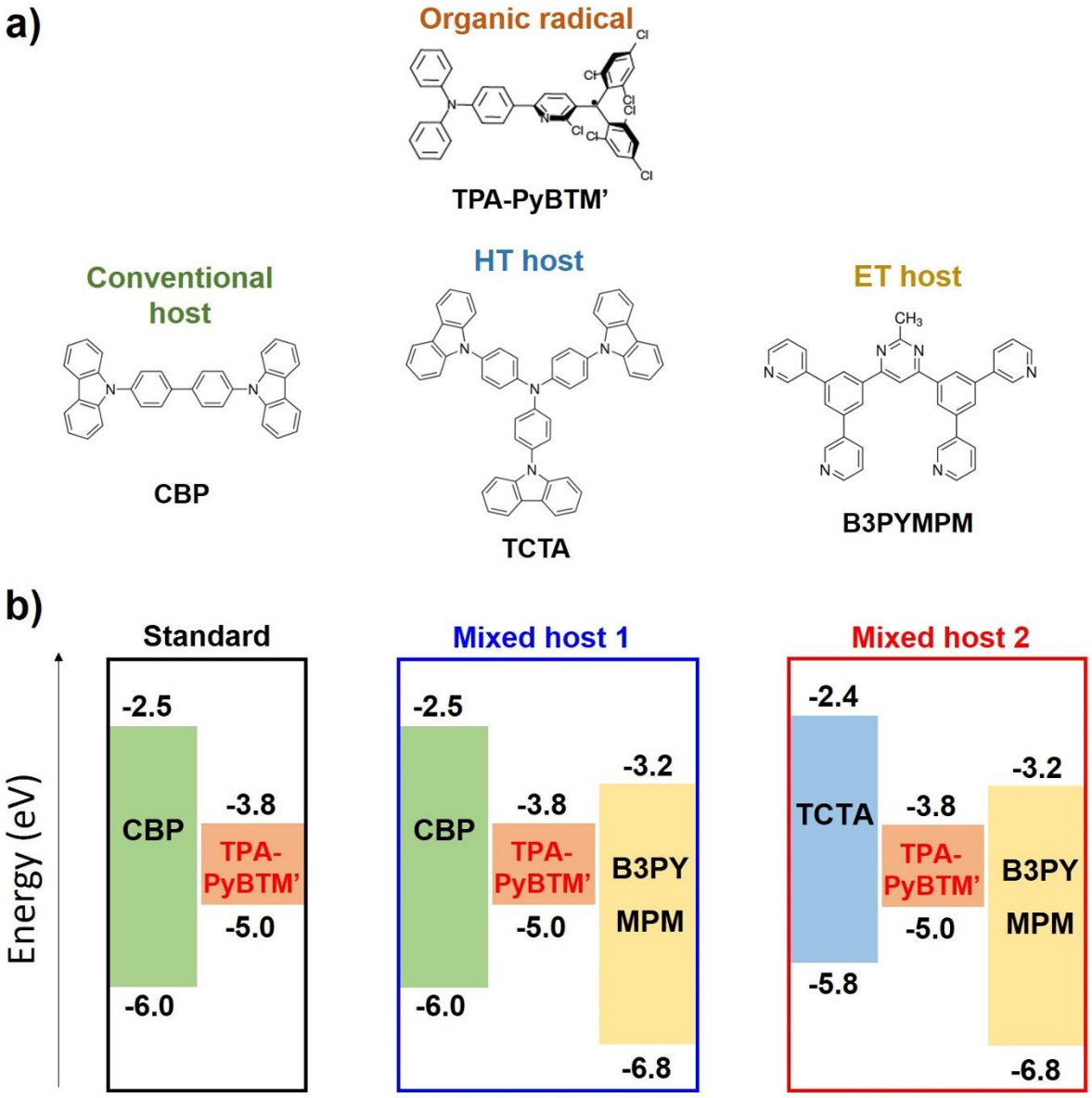

Figure 6-5. (a) Chemical structures of TPA-PyBTM', CBP, TCTA, and B3PYMPM. (b) Schematic representation of the energy level diagram for the three types of emissive system. CBP is selected for the standard, and B3PYMPM is combined with CBP and TCTA for the mixed hosts with TPA-PyBTM'.

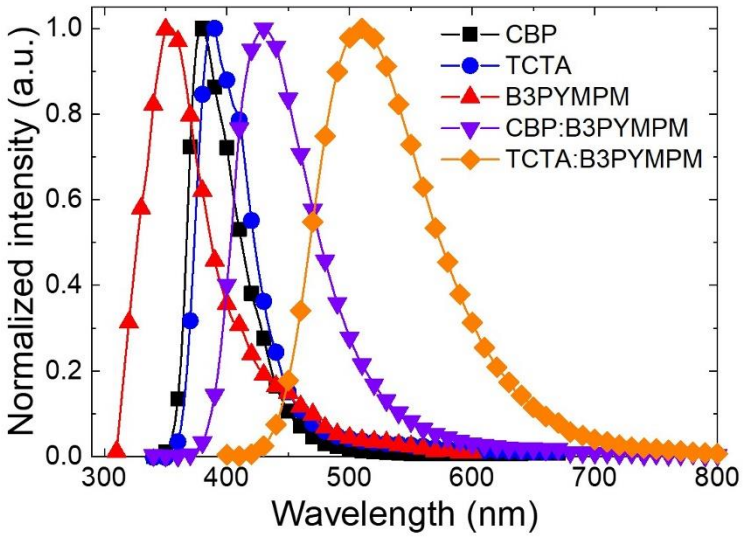

Figure 6-6. PL spectra of CBP, TCTA, B3PYMPM, CBP:B3PYMPM, and TCTA:B3PYMPM films.

6.2.3 Steady state and transient photophysics

Figure 6-7 shows the TPA-PyBTM' steady-state and transient photophysical studies. The PL of CBP, CBP:B3PYMPM, and TCTA:B3PYMPM neat films and the PL and absorption of TPA-PyBTM' diluted in toluene are depicted in Figure 6-7(a). The high absorption coefficient of TPA-PyBTM' between 400 nm and 550 nm allows the exciplex-forming hosts to be adopted as an energy donor, and overlap of (exciplex) PL and (radical) absorption enable efficient energy transfer. The steady-state PL spectra of TPA-PyBTM' 3% doped in CBP, CBP:B3PYMPM, and TCTA:B3PYMPM show TPA-PyBTM' emission spectra centred at 820 nm in all cases, with some residual emission contribution from the hosts due to low radical doping concentration (Figure 6-7(b)). As the films are excited by a 330 nm laser, NIR emission mainly originates from FRET from the hosts even though there is a small contribution by direct excitation

of TPA-PyBTM' (Figure 6-8). In addition, PLQEs for the TPA-PyBTM'-doped films were measured at the same excitation wavelength as above. The PLQE values for the TPA-PyBTM' 3% doped in CBP:B3PYMPM and TCTA:B3PYMPM films are 14% and 9%, respectively, which is lower than the value of 21% in CBP films.

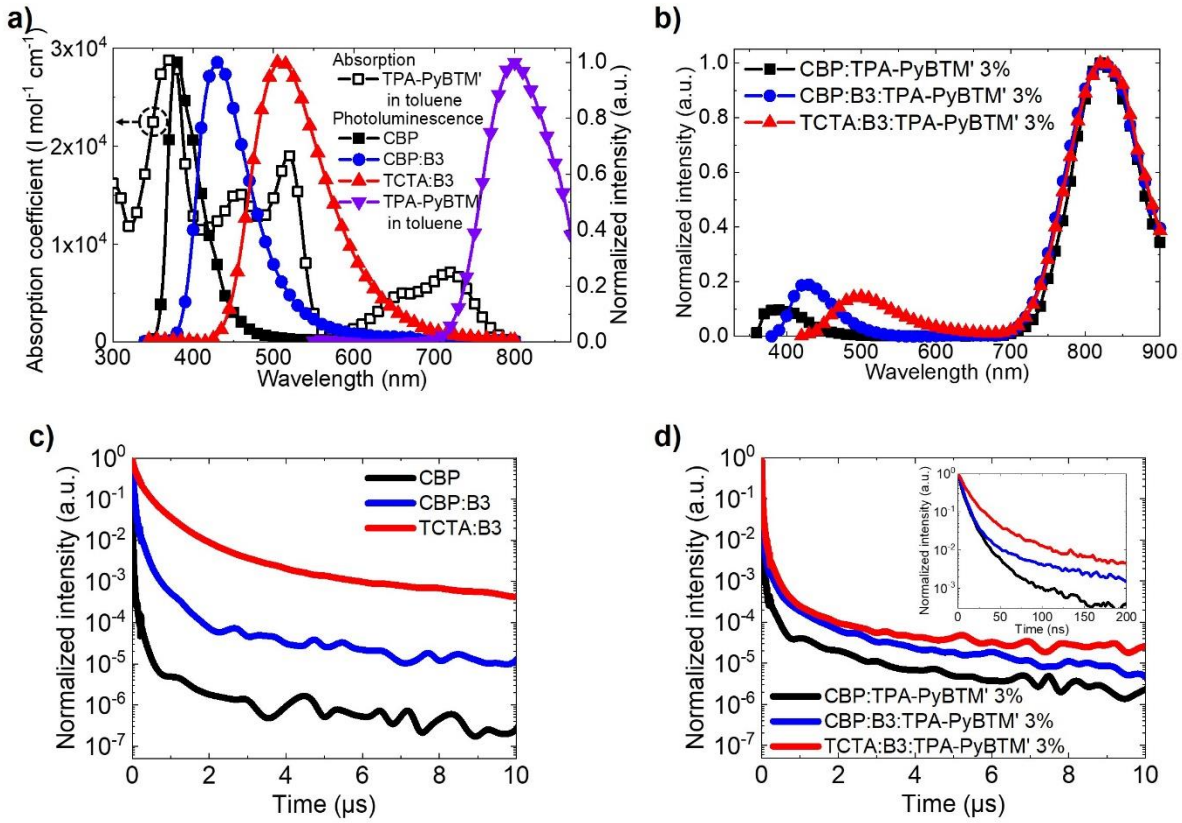

Figure 6-7. Steady-state and transient photophysics. (a) PL spectra of CBP, CBP:B3PYMPM, and TCTA:B3PYMPM neat films; and TPA-PyBTM' solution absorption and PL spectra. (b) PL spectra of TPA-PyBTM' doped at 3 wt% in CBP, CBP:B3PYMPM, TCTA:B3PYMPM films. (c) and (d) show transient PL characteristics of CBP, CBP:B3PYMPM, and TCTA:B3PYMPM films and the radical-doped films, respectively. The inset in (d) shows the same data at earlier times.

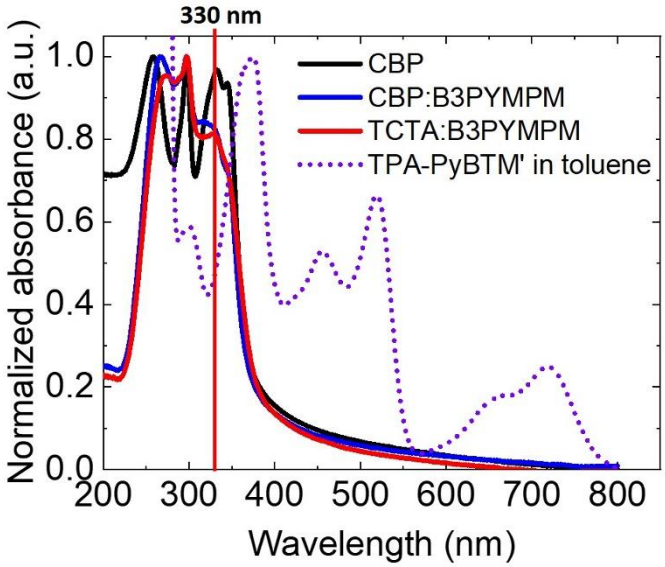

Figure 6-8**.** Absorbance of CBP, CBP:B3PYMPM, and TCTA:B3PYMPM films and TPA-PyBTM' in toluene.

For the investigation of the excited-state decay kinetics, transient PL measurements were conducted for the three host types with and without TPA-PyBTM' doping, as shown in Figure 6-7(c) and (d). Characteristic decay timescales were determined from the time-integrated PL intensity (Figure 6-9); the times taken for a fraction 1-(1/e) of the total emission to occur are shown in Table 6-2. As expected, due to reduced oscillator strength, the exciplex emission is slower than the rapid exciton emission seen in CBP. TCTA:B3PYMPM exhibits strong delayed emission in agreement with the previous work[134] where it was attributed to the formation and recovery of non-emissive triplet exciplex states. CBP:B3PYMPM also shows slow non-monoexponential decay, although the delayed components are not as prominent as in TCTA:B3PYMPM. TPA-PyBTM'-doped films show nanosecond decay (Figure 6-7(d)), with faster emission on all timescales than in the undoped mixed hosts. This implies rapid energy transfer from the singlet exciplex state onto the radical emitter.

The decay times for fluorescent doublet emission of TPA-PyBTM' doped in CBP, CBP:B3PYMPM, and TCTA:B3PYMPM are 7.8 ns, 11.3 ns, and 22.9 ns, respectively.

Table 6-2. Summary of TPA-PyBTM' decay kinetics doped in different hosts.

TPA-PyBTM'	CBP		CBP:B3PYMPM		TCTA:B3PYMPM	
Doping (%)	0	3	0	3	0	3
PLQE (%)	78	21	15	14	46	9
τ (ns)[a)]	3.4	7.8	45.9	11.3	418.1	22.9
k_r (/μs)	229.4	26.9	3.3	12.4	1.1	3.9
k_{nr} (/μs)	64.7	101.3	18.5	76.1	1.3	39.7

[a)]Derived from the time when the integrated PL intensity reaches 1-(1/e).

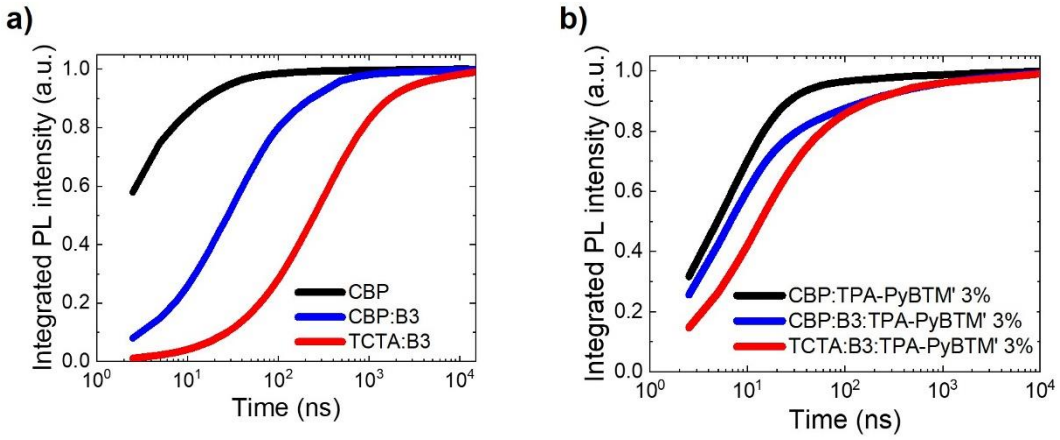

Figure 6-9. Normalised integrated PL intensity of (a) CBP, CBP:B3PYMPM, and TCTA:B3PYMPM films and (b) TPA-PyBTM' 3 wt% doped in CBP, CBP:B3PYMPM, and TCTA:B3PYMPM films.

Compared to the radical doped in CBP, the CBP:B3PYMPM and TCTA:B3PYMPM hosted films show longer decay time with delayed components (inset in Figure 6-7(d)), which suggests longer time energy transfer from the exciplex formed between CBP or TCTA and B3PYMPM (Figure 6-7(c)).

6.2.4 Single-carrier device analysis

Single-carrier devices were examined to probe charge transport in devices with different hosts. Figure 6-10(a) and (b) show the device structures for the HODs and EODs. For the HOD, 1,1-bis[(di-4-tolylamino)phenyl]cyclohexane (TAPC) and TCTA are used as the HTL, and TAPC is inserted between the EML and the cathode to block electron injection into the EML. For the EOD, the EML is sandwiched by the well-established ETL material B3PYMPM to achieve an electron-only current. Figure 6-10(c) and (d) show the J-V characteristics of single-carrier devices with and without radical emitter doping based on three different hosts: CBP (HOD 1 and EOD 1), CBP:B3PYMPM (HOD 2 and EOD 2), and TCTA:B3PYMPM (HOD 3 and EOD 3). On radical doping, the J-V curves for both HOD and EOD become shallower in all cases, suggesting that the direct recombination of holes and electrons at the radical sites will dominate the emission mechanism for radical EL. The severe electron trapping (Figure 6-10(d)) behaviour implies that the emission zone is located close to the EML/ETL interface in full OLED devices. The hole current in HOD 3 is much higher than in other devices due to the improved hole-transporting properties of TCTA compared with CBP,[228] and the introduction of B3PYMPM reduces hole transport as observed from the shallower J-V curve of HOD 2 than HOD 1 (Figure 6-10(c)). From EOD studies with and without radical doping, EOD 2 and 3 show steeper J-V curves than EOD 1, meaning that B3PYMPM considerably improves electron-transporting

properties. Enhanced electron transport is apparent despite substantial electron-trapping behaviour by the radical dopant.

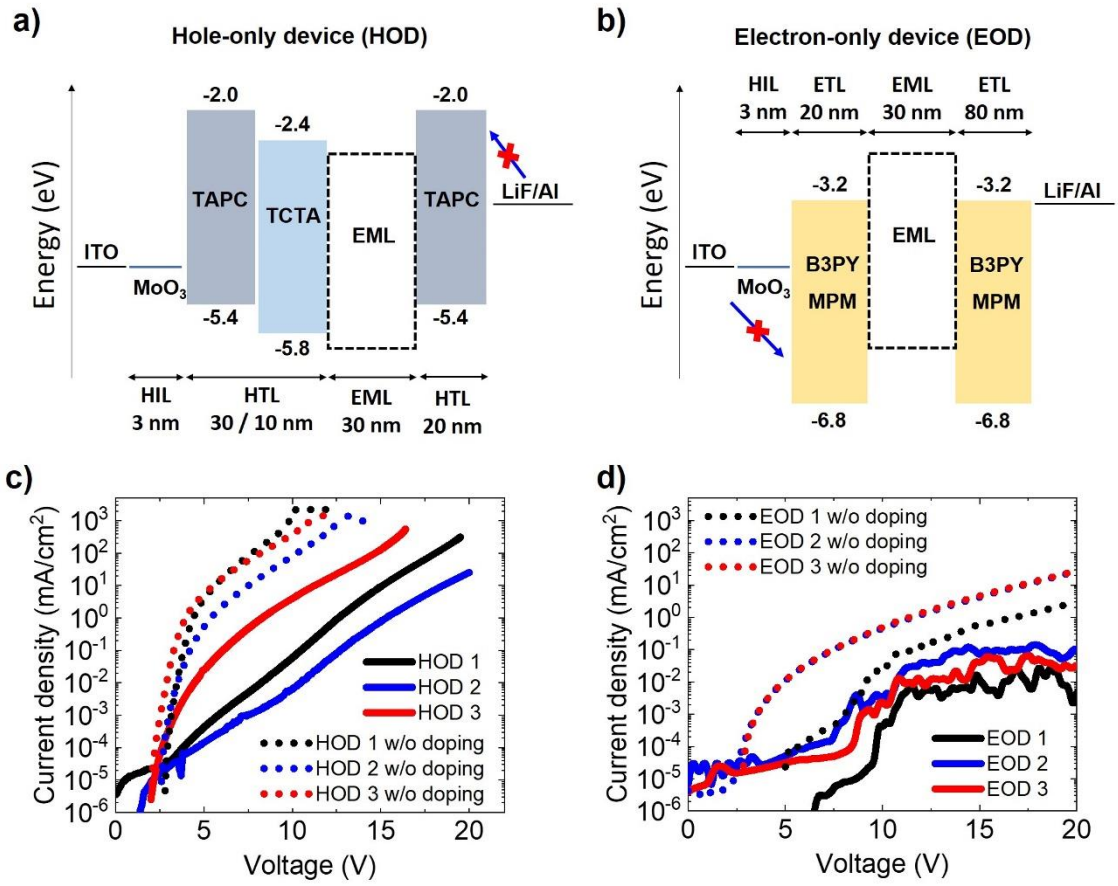

Figure 6-10. (a),(b) show the device architectures of HOD and EOD. For the direct comparison of the hole and electron-transporting properties in devices, the device structures are designed based on usable layers for a full device. For HOD, TAPC 20 nm is used between the EML and cathode to block electron injection. For EOD, B3PYMPM 20 nm is deposited at the anode to allow electron-only currents. The current density-voltage profiles for the HODs and EODs are plotted in (c) and (d). As TPA-PyBTM' is doped in the hosts, HOD and EOD plots become shallower, meaning that the radical plays a role in trapping both holes and electrons, but electron trapping is more severe.

6.2.5 Device characterisation

Radical EL devices were explored on the basis of the device layout displayed in Figure 6-11(a), with EML composition corresponding to the materials combinations studied above. The three types of devices were successfully characterised, and their performance is shown in Figure 6-11(b)~(d) and Table 6-3. Figure 6-11(b) shows current density-voltage-radiance characteristics. Device 3 exhibits a substantially lower turn-on voltage, 2.1 V, than other devices, 2.7 V (Device 1) and 3.3 V (Device 2), which is attributed to the negligible hole injection barrier between HTL and EML as TCTA is used in both layers. Additionally, Device 2 shows 0.6 V higher turn-on voltage than Device 1 as B3PYMPM partially inhibits hole injection to the EML, which is consistent with the HOD studies (figure 6-10(c)).

Figure 6-11(c) displays the recorded EQE-current density plots. The maximum EQE of 6.4% was attained from Device 1, with Devices 2 and 3 reaching 4.7% and 3.7%, respectively, and follows the same trend as the film PLQE values. The large efficiency roll-off in Device 1 is mainly ascribed to poor electron transport narrowing the recombination zone, while Devices 2 and 3 exhibit improved efficiency roll-off characteristics, with higher EQEs than Device 1 at current densities over 1 mA/cm^2 since the mixed-host design leads to reduced charge trapping and improved electron transport (Figure 6-11(c) and 6-12). This is also summarised in Table 6-3, which shows that at 10 mA/cm^2, the EQE for Device 1 drops to only 15% of the maximum EQE, while approximately 50% and 40% of the maximum EQEs are maintained in Device 2 and 3, respectively.

Figure 6-11(d) shows the EL spectra of the devices, where the emission can be seen to peak at wavelengths higher than 800 nm. No host emission is observable, which contrasts with the PL spectra shown in Figure 6-7(b), and suggests that direct electrical

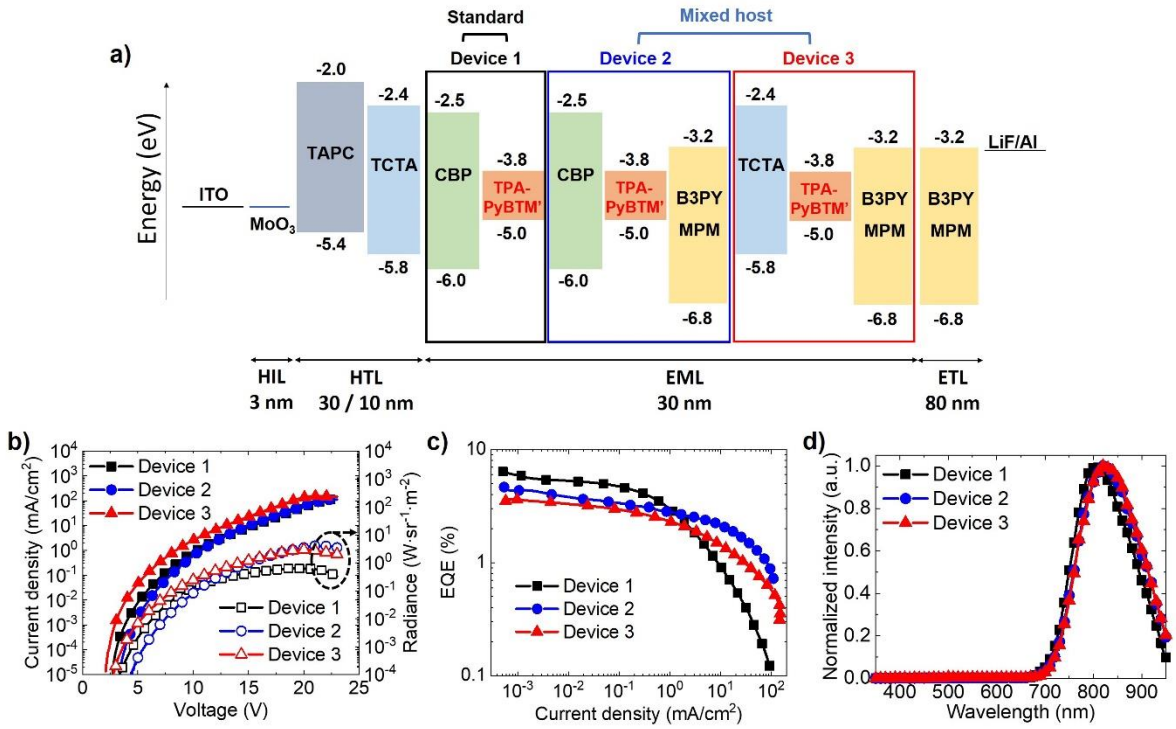

Figure 6-11. Device structures and optoelectronic performance of the TPA-PyBTM' radical-based OLEDs. (a) TPA-PyBTM' device layout with energy level diagram for the materials used for this study. (b) Current density-voltage-radiance plots. (c) EQE-current density curves. (d) EL spectra at 1 mA/cm^2

Table 6-3. Summary of device performance.

	V_{on}[a)] (V)	EQE_{Max} (%)	$EQE_{J\text{-}1.0}$[b)] (%)	$EQE_{J\text{-}10.0}$[c)] (%)	$Radiance_{Max}$ ($W \cdot sr^{-1} \cdot m^{-2}$)	λ_{max} (nm)
Device 1	2.7	6.4	3.0	0.9	0.6	805
Device 2	3.3	4.7	2.8	2.2	4.0	820
Device 3	2.1	3.7	2.3	1.4	3.0	820

[a)]Voltage at 10^{-5} mA/cm^2. [b)]EQE at 1 mA/cm^2, [c)]EQE at 10 mA/cm^2

excitation of the dopant dominates over possible energy transfer mechanisms from host excitons. The EL from Device 1 is slightly blue-shifted compared to Device 2 and 3 (not seen in the PL spectra). It is inferred that this is due to a recombination zone shift.[229] Concerning Device 1, the emission zone is close to the EML/ETL interface since the severe electron trapping due to the large energy gap disparity between CBP LUMO and TPA-PyBTM' SOMO is expected from the EOD studies (Figure 6-10(d)). In contrast, the recombination zone of Device 2 and 3 can be extended towards the HTL/EML interface because of the enhanced electron transport in B3PYMPM, leading to a slight spectrum change compared to Device 1 with increasing optical path length from cathode to the emission zone. Furthermore, device lifetime was measured at 1 mA/cm^2 (10.3 V for Device 1, 10.7 V for Device 2, and 8.4 V for Device 3) for the devices (Figure 6-13). As investigated, the mixed hosts are conducive to more balanced

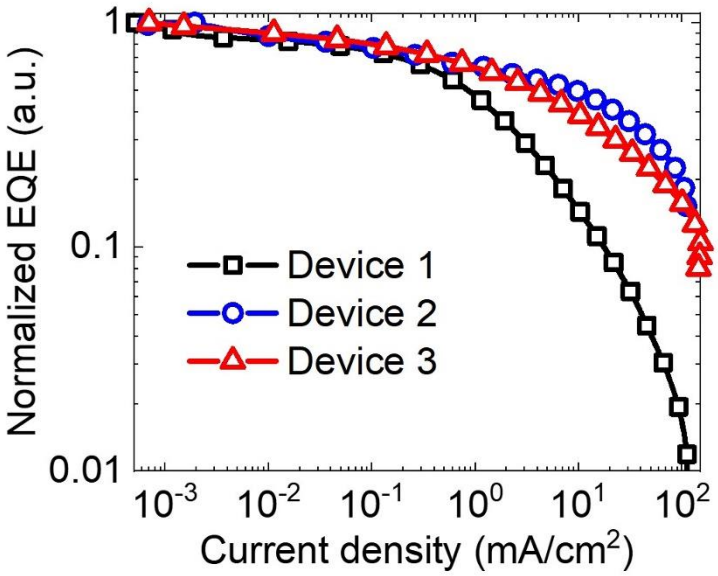

Figure 6-12. The normalised EQE-current density plots of the devices.

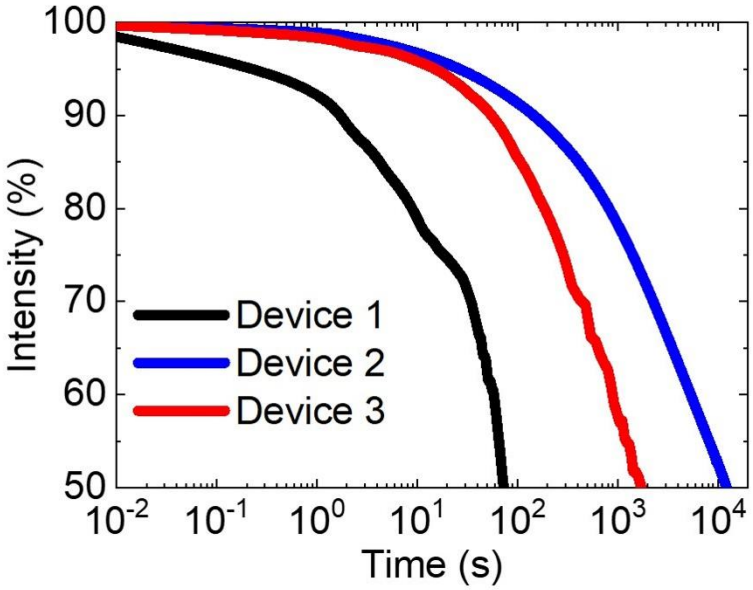

Figure 6-13. Comparison of device lifetime measured at 1 mA/cm^2.

charge populations in an extended recombination zone; this results in substantially improved device stability (70 s for Device 1, 3.4 hr for Device 2, and 0.5 hr for Device 3). The approximately seven times shorter lifetime of Device 3 than Device 2 is attributed to the higher hole mobility and shallower HOMO energy level in TCTA compared to CBP, leading to higher hole transport in the EML causing hole accumulation at the EML/ETL interface for increased exciton-polaron quenching.[78,79] Additionally, it is noted that as lifetime was measured at relatively high voltage in an ambient condition without encapsulation, the absolute device lifetime could be enhanced in more optimised device configurations and measurement conditions. Consequently, mixed hosts contributed to the considerable improvement of efficiency roll-off and device lifetime, whereas maximum EQEs compromised, prompting further work on the new design of mixed hosts.

6.3 New design of mixed hosts for enhanced electron transport

6.3.1 New mixed host design for TPA-PyBTM'

To further improve the optoelectronic performance of TPA-PyBTM'-based organic radical LEDs, higher electron transport with reduced electron trapping is required, considering the severe electron trapping examined in Section 6.2.4. For this purpose, B3PYMPM is replaced with 4,6-bis[3,5-(dipyrid-4-yl)phenyl]-2-methyl pyrimidine (B4PYMPM) as shown in Figure 6-14. B4PYMPM is known to have deeper

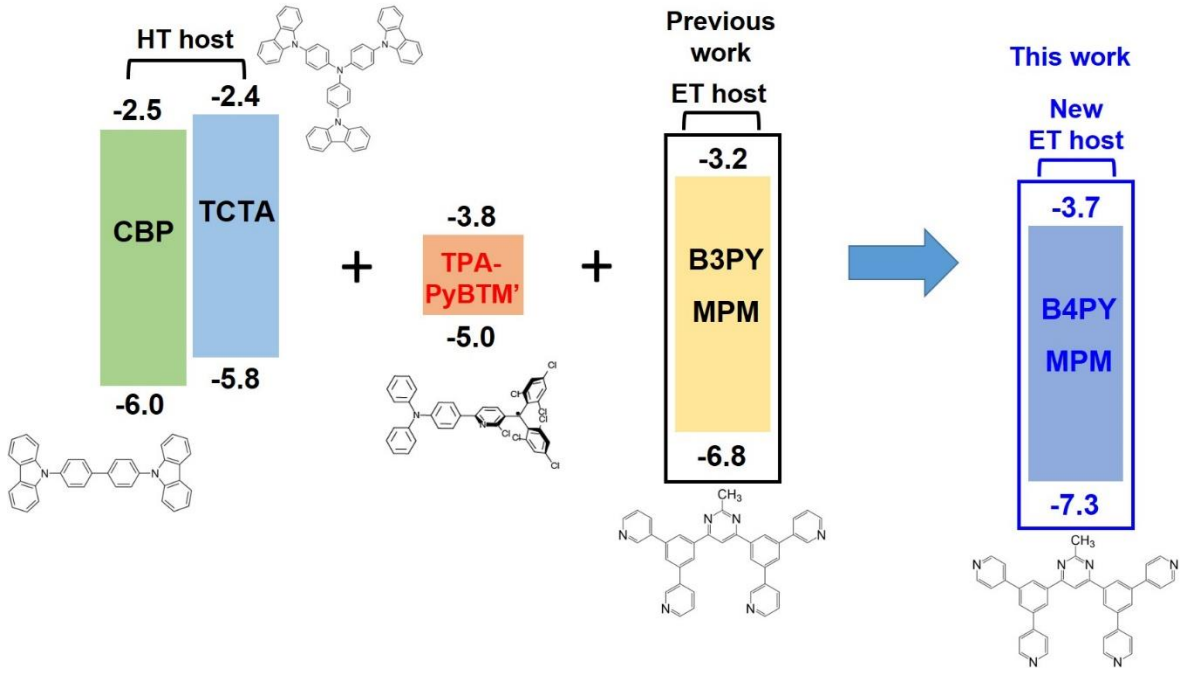

Figure 6-14. New design of mixed hosts for TPA-PyBTM'. B4PYMPM is adopted instead of B3PYMPM as a new ET host for enhanced electron transport and reduced electron trapping in an EML.

energy levels with one order higher electron mobility than B3PYMPM.[80] Accordingly, it is anticipated that B4PYMPM could substantially raise the electron transporting properties in an EML compared to B3PYMPM.

6.3.2 Steady-state and transient photophysics

Figure 6-15 shows the steady-state and transient photophysical properties for TPA-PyBTM' 3% doped and undoped films in different hosts. As studied in Section 6.2.3, the fundamental characteristics of B4PYMPM-based mixed hosts are almost the same as B3PYMPM-based ones. CBP:B4PYMPM and TCTA:B4PYMPM PL spectra are red-shifted compared to the PL of each element (Figure 6-16(a)), implying the formation of exciplexes. Figure 6-15(b) shows the PL spectra of the films with 820 nm peak wavelength excited by a 330 nm laser. Considering that the hosts are mainly excited by the laser (Figure 6-16(b)), NIR emission mainly results from FRET from the hosts, and a small proportion of host emission is detected, in line with the PL spectra of the TPA-PyBTM' doped films studied in Section 6.2.3. In addition, PLQEs for the films are measured with the same wavelength laser excitation. The CBP:B4PYMPM and TCTA:B4PYMPM hosted films show the PLQEs of 11% and 8%, which are lower than the PLQE of the CBP hosted film (21%), and these results are similar to the lower PLQEs of the CBP:B3PYMPM and TCTA:B3PYMPM hosted films studied in Section 6.2.3.

Figure 6-15(c) and (d) show transient PL characteristics of the TPA-PyBTM' doped and undoped films to explore the different decay kinetics in the three kinds of hosts. Overall, the basic decay features for the B4PYMPM-based mixed hosts are almost identical to the B3PYMPM-based ones. Figure 6-15(c) presents the decay

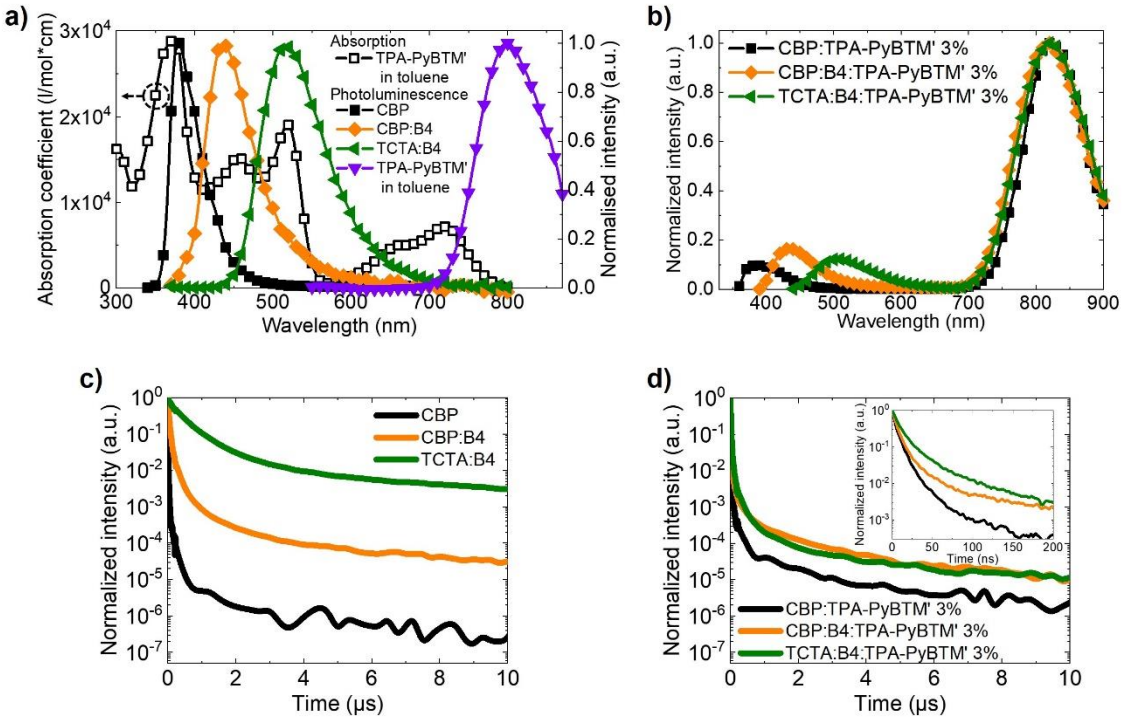

Figure 6-15. Steady-state and transient photophysics. (a) PL spectra of CBP, CBP:B4PYMPM, and TCTA:B4PYMPM neat films and the absorption and PL spectra of TPA-PyBTM' solution. (b) PL spectra of TPA-PyBTM' doped at 3 wt% in CBP, CBP:B4PYMPM, TCTA:B4PYMPM films. (c) and (d) show transient PL characteristics of CBP, CBP:B4PYMPM, and TCTA:B4PYMPM films and the radical-doped films, respectively. The inset in (d) shows the same data at earlier times.

Table 6-4**.** Summary of TPA-PyBTM' decay kinetics doped in different hosts.

TPA-PyBTM'	CBP		CBP:B4PYMPM		TCTA:B4PYMPM	
Doping (%)	0	3	0	3	0	3
PLQE (%)	78	21	14	11	65	8
τ (ns)[a)]	3.4	7.8	56.6	14.5	780.5	21.5
k_r (/μs)	229.4	26.9	2.5	7.6	0.83	3.7
k_{nr} (/μs)	64.7	101.3	15.2	61.4	0.45	42.8

[a)]Derived from the time when the integrated PL intensity reaches 1-(1/e).

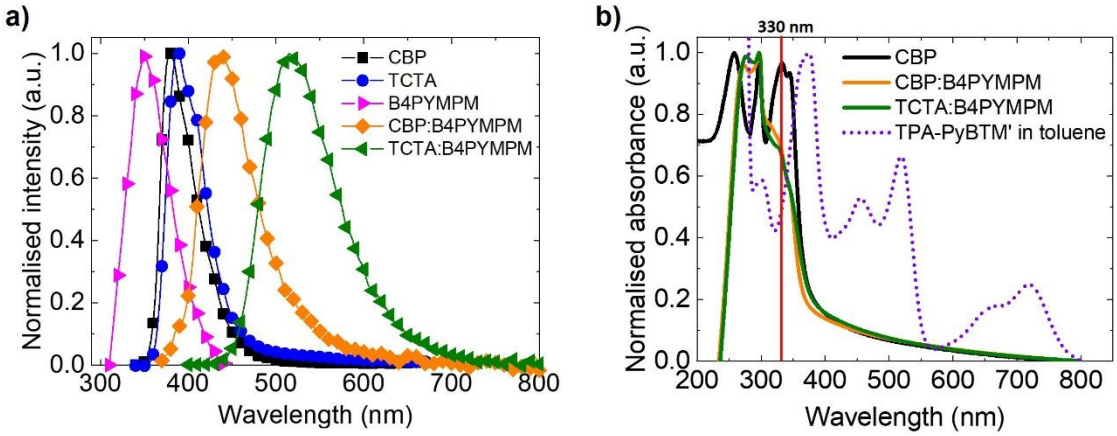

Figure 6-16. (a) PL spectra of CBP, TCTA, B4PYMPM, CBP:B4PYMPM, and TCTA:B4PYMPM films. (b) Absorbance of CBP, CBP:B4PYMPM, and TCTA:B4PYMPM films, and TPA-PyBTM' in toluene.

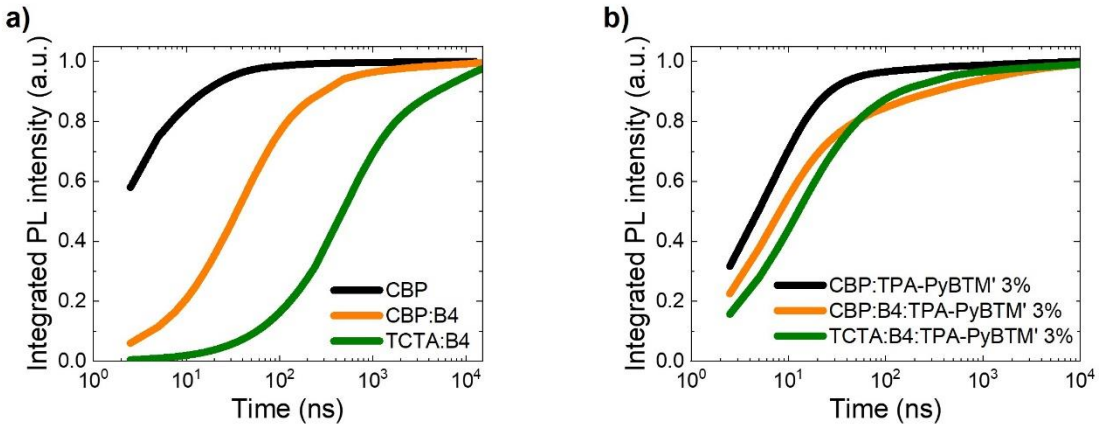

Figure 6-17**.** Normalised integrated PL intensity of (a) CBP, CBP:B4PYMPM, and TCTA:B4PYMPM films and (b) TPA-PyBTM' 3 wt% doped in CBP, CBP:B4PYMPM, and TCTA:B4PYMPM films.

kinetics of the hosts without radical doping. TCTA:B4PYMPM shows prominent delayed emission like TCTA:B3PYMPM, and it is correlated with the previous work.[230] Also, CBP:B4PYMPM shows faster emission decay than TCTA:B4PYMPM, meaning that RISC in CBP:B4PYMPM is not as effective as that in TCTA:B4PYMPM. With

radical doping, high-speed doublet fluorescence decay profiles are recorded in all hosts like in the previous study in Section 6.2.3. Table 6-4 shows the summary of the PLQE values and decay constants determined from the time when the integrated normalised PL intensity reaches 1-(1/e) (Figure 6-17). Compared to CBP:B3PYMPM and TCTA:B3PYMPM (Table 6-2), CBP:B4PYMPM and TCTA:B4PYMPM show longer decay time, indicating that RISC is more effective in B4PYMPM-based mixed hosts than B3PYMPM-based ones.

6.3.3 Single-carrier device analysis

To confirm the enhanced electron transport by the exploitation of B4PYMPM compared to B3PYMPM, single-carrier devices were fabricated. From the device structures in Figure 6-10(a) and (b), B3PYMPM was replaced with B4PYMPM, and the other layers are identical, as shown in Figure 6-18(a) and (b). EML thickness is reduced from 30 nm to 20 nm, which could lead to better device performance by improving J-V characteristics.

Figure 6-18(c) and (d) show the J-V characteristics of HODs and EODs for the three kinds of hosts with and without TPA-PyBTM' doping: CBP (HOD 1 and EOD 1), CBP:B4PYMPM (HOD 2 and EOD 2), TCTA:B4PYMPM (HOD 3 and EOD 3). The J-V plots for both HODs and EODs become shallower as TPA-PyBTM' is doped, which means that direct charge trapping to the radical would be dominant in EL devices. Regarding HODs (Figure 6-18(c)), TCTA increases hole transport in HOD 3 while the J-V curve for HOD 2 is shallower than HOD 1 as B4PYMPM interferes with hole transport in an EML.

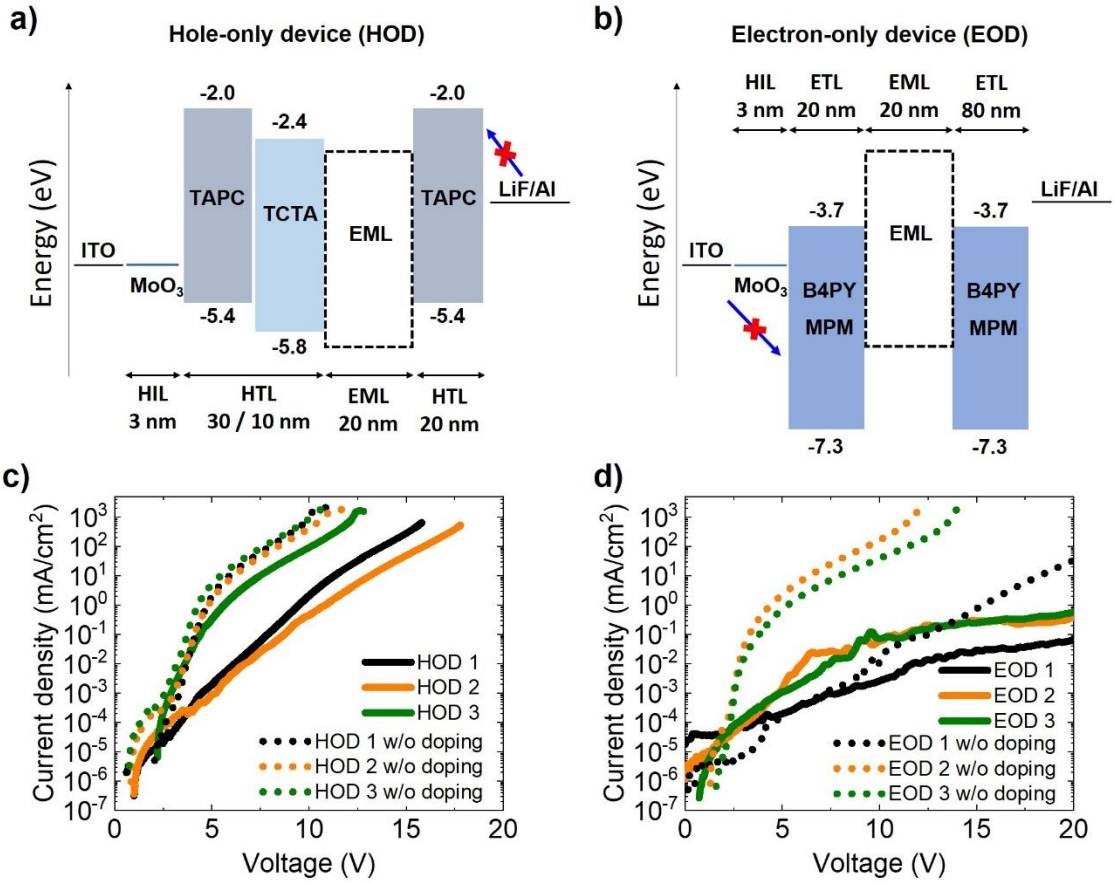

Figure 6-18. **(**a),(b) show the device architectures of HOD and EOD. For HOD, TAPC 20 nm is deposited between the EML and cathode to preclude electron injection. For EOD, the EML is sandwiched by B4PYMMPM to ensure electron-only currents. The J-V plots for the HODs and EODs are depicted in (c) and (d). As TPA-PyBTM' is doped in the hosts, the radical plays a role in trapping both holes and electrons, considering HOD and EOD plots become shallower, but electron trapping is more severe. Also, as B4PYMPM is mixed with CBP and TCTA, electron transporting abilities in an EML are substantially improved in the sense of the much steeper J-V curves.

On the other hand, as B4PYMPM is utilised instead of B3PYMPM, electron transporting properties for CBP:B4PYMPM and TCTA:B4PYMPM are substantially improved considering the much steeper J-V curves than CBP:B3PYMPM and TCTA:B3PYMPM (Figure 6-19(b)). Nevertheless, electron trapping is still severe

considering the much shallower J-V curves for EOD 1~3 with doping than EOD 1~3 without doping (Figure 6-18(d)). However, B4PYMPM substantially enhances electron transport in an EML compared to B3PYMPM, which could lead to the more balanced hole and electron transporting properties.

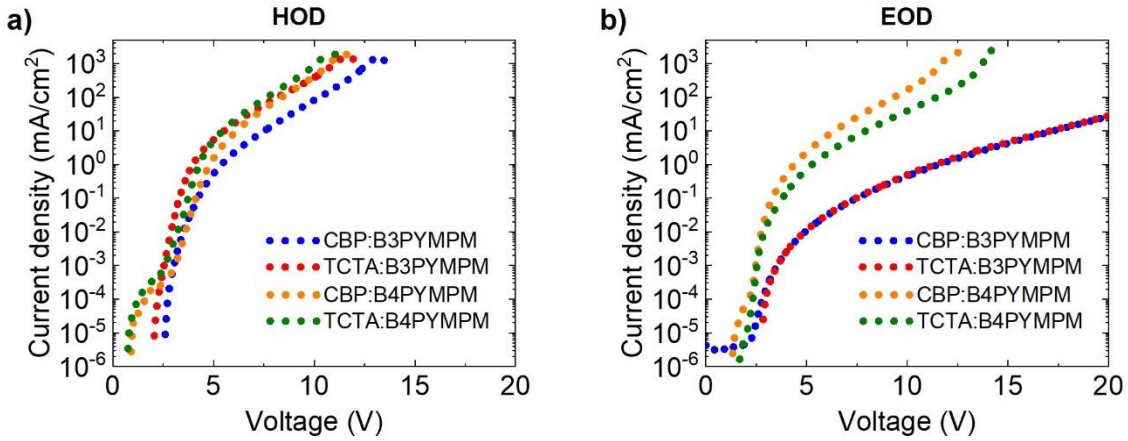

Figure 6-19. Comparisons of (a) HOD and (b) EOD for the B3PYMPM-based mixed hosts and B4PYMPM-based mixed hosts.

6.3.4 Device characterisation

On the basis of the photophysical studies and single-carrier device results, the three kinds of the full devices corresponding to the EML combinations explored above were successfully fabricated utilising the device layout shown in Figure 6-20(a). TAPC and TCTA were used in an HTL part with the thickness of 30 nm and 10 nm, respectively, and 80 nm thick B4PYMPM was employed as an ETL. To investigate the host effect on device performance, the three hosts (CBP, CBP:B4PYMPM, and TCTA:B4PYMPM) were compared in the same device architecture, corresponding to

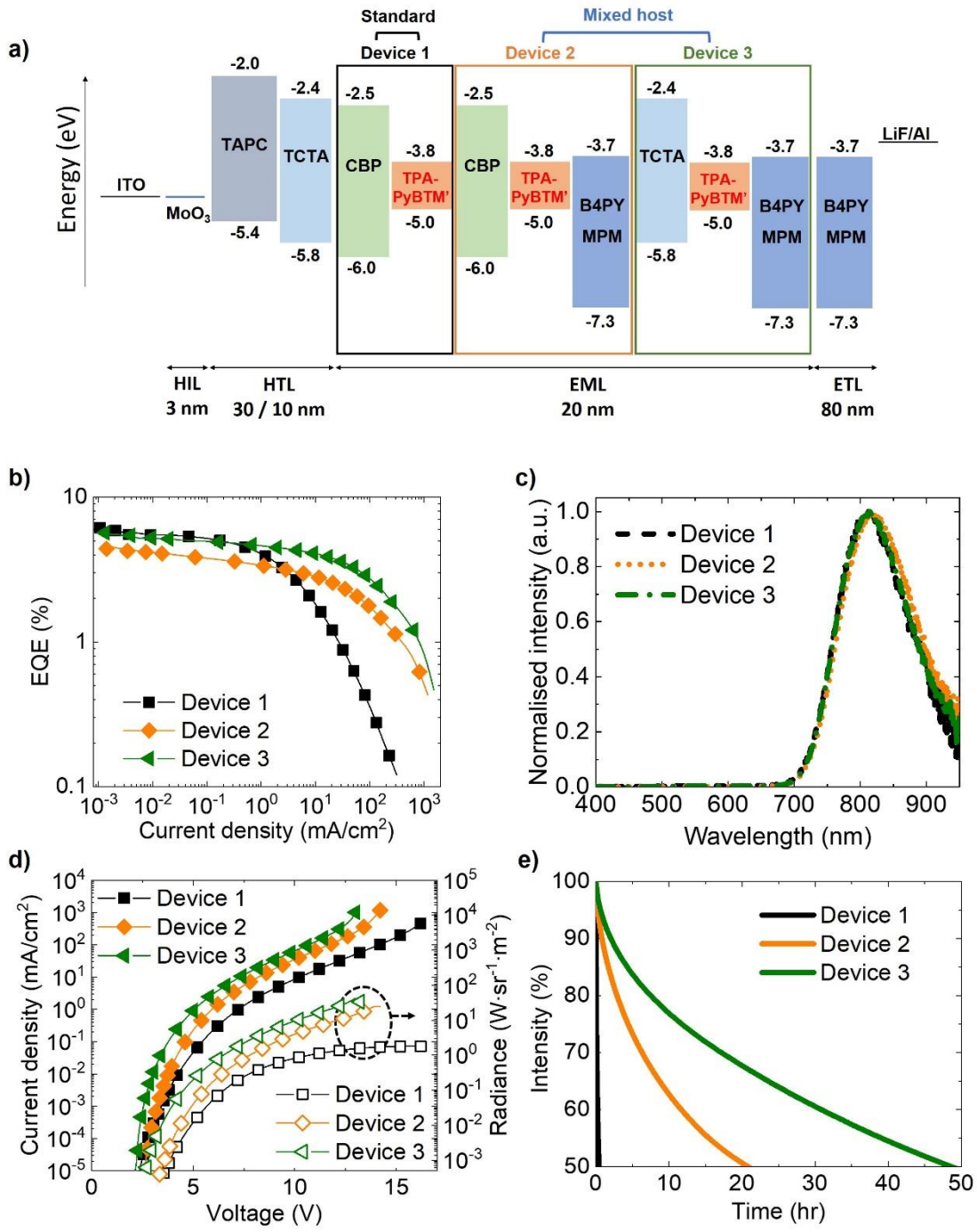

Figure 6-20. Device structures and device performance. (a) TPA-PyBTM' device layout with energy level diagram for the materials used for this study. (b) EQE-current density curves. (c) EL spectra at 1 mA/cm^2. (d) Current density-voltage-radiance plots. (e) Lifetime measured at 0.1 mA/cm^2.

Table 6-5. Summary of device performance.

	V_{on}[a)] (V)	EQE_{Max} (%)	$EQE_{J\text{-}0.1}$[b)] (%)	$EQE_{J\text{-}10.0}$[c)] (%)	$Radiance_{Max}$ ($W \cdot sr^{-1} \cdot m^{-2}$)	Lifetime[d)] (hr)	λ_{max} (nm)
Device 1	2.4	6.2	5.2	1.8	1.8	0.4	812
Device 2	2.6	4.6	3.8	2.8	24.6	20.8	818
Device 3	2.1	5.7	5.0	4.1	41.3	48.7	814

[a)]Voltage at 10^{-5} mA/cm^2. [b)]EQE at 0.1 mA/cm^2, [c)]EQE at 10 mA/cm^2, [d)]Lifetime at 0.1 mA/cm^2

Device 1, Device 2, and Device 3, respectively.

The optoelectronic performance of the devices is presented in Figure 6-20(b)~(e) and Table 6-5. Figure 6-20(b) shows the EQE-current density plots. The maximum EQE of Device 3 is 5.7%, comparable to Device 1, 6.2%, and the maximum EQE of Device 2 is slightly lower than others, 4.6%. As mixed hosts are employed, Device 2 and 3 show highly improved efficiency roll-off features. While the EQE for Device 1 drops substantially over 1 mA/cm^2, Device 2 and 3 keep relatively high EQEs and exceed Device 1. As a result, at 10 mA/cm^2, just 30% of the maximum EQE remains in Device 1, whereas Device 2 and 3 maintain higher than 60% and 70% of the maximum EQEs, respectively. Interestingly, it is noted that the PLQE of the TCTA:B4PYMPM hosted film is just 8%, lower than half of the PLQE of the CBP hosted film (21%), but the EQE of Device 3 is comparable to Device 1. This can be interpreted by the difference between photoexcitation and electrical excitation. As shown in Figure 6-15(b), there remains host emission in PL as NIR emission from TPA-PyBTM' is mainly from FRET from host molecules. In contrast, no host emission is observed in EL, as shown in Figure 6-19(c), meaning that the direct charge recombination at radical sites is the main emission mechanism in electrical excitation, and the contribution of

the energy transfer from hosts to radicals in EL is not dominant. Therefore, EL efficiency is mostly determined by the intrinsic efficiency of the dopant and charge recombination by hole and electron in the EML.

Figure 6-20(d) shows the current density-voltage-radiance plots. As expected from single-carrier device studies, Device 2 and 3 show much faster charge transport than Device 1 as B4PYMPM considerably increases electron transport, as shown in the EOD studies (Section 6.3.3). Moreover, as B4PYMPM having much faster electron mobility than B3PYMPM is utilised,[80] radiance for the B4PYMPM-based devices is

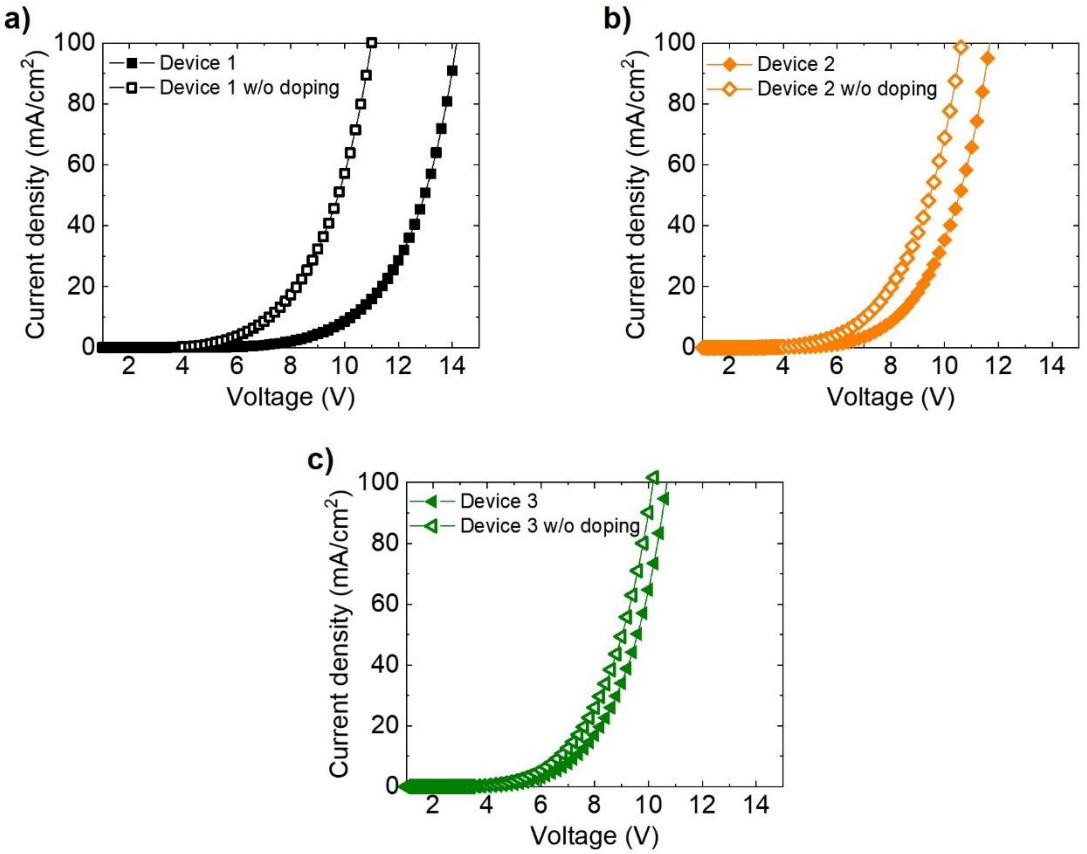

Figure 6-21. Comparison of the J-V characteristics between the devices with and without TPA-PyBTM' doping.

substantially enhanced compared to the devices using B3PYMPM. The maximum radiance for Device 3 is 41.3 $W \cdot sr^{-1} \cdot m^{-2}$ W, more than ten times higher than the B3PYMPM-based counterpart, 3.0 $W \cdot sr^{-1} \cdot m^{-2}$. Also, compared to the maximum radiance for Device 1 (1.8 $W \cdot sr^{-1} \cdot m^{-2}$), more than twenty times higher maximum radiance is achieved in Device 3. Furthermore, in order to prove the effect of mixing B4PYMPM with the HT hosts on device characteristics, the J-V curves for the devices with and without the radical doping are compared, as shown in Figure 6-21. In Device 1, as TPA-PyBTM' is doped, the J-V curve becomes much shallower (Figure 6-21(a)), indicating that most electrons are captured at radical sites near the interface of EML and ETL, causing bimolecular exciton quenching at high current density in line with the EOD study and large efficiency roll-off (6-18(d) and 6-20(b)). However, the J-V curve difference between with and without doping for Device 2 and 3 is substantially reduced compared to Device 1 as shown in Figure 6-21(b) and (c). As electron transporting properties are highly enhanced by B4PYMPM, electrons can travel more quickly and easily to meet holes at radical sites in an EML to form excitons by direct charge recombination, which is associated with low efficiency roll-off in Device 2 and 3. To confirm the superiority of the mixed hosts over the standard single host in terms of stability, device lifetime was measured at 0.1 mA/cm^2, as shown in Figure 6-20(e). Device 3 shows the lifetime of 48.7 hr, more than one hundred times longer lifetime than Device 1 (0.4 hr). The lifetime of Device 2 is 20.8 hr, lower than half of the lifetime of Device 3, probably due to relatively higher hole trapping resulting in relatively less balanced charge recombination and excessive radical cations causing lower efficiency and stability in Device 2 than Device 3.

6.3.5 Transient electroluminescence

Transient EL was measured to compare the difference of the emission process in the three devices and prove the higher device performance of Device 3 than others in terms of efficiency roll-off, radiance, and stability. Figure 6-22(a) shows transient EL kinetics for the devices without doping. The undoped Device 2 and 3 show longer decay profiles than Device 1, in line with the transient PL studies (Figure 6-15(c)). However, the transient EL decays for the radical doped devices show different characteristics compared to the undoped devices. As studied in single-carrier device studies, the radical molecules act as a trapping centre. In Device 1, as only CBP is used as a host, the strong additional emission decay is observed compared to the other devices (inset in Figures 6-22(b)), indicating that trapped electrons can be recombined with holes contributing to EL after turn-off.[160,164–166] As B4PYMPM is mixed with CBP, the additional emission is considerably reduced due to enhanced electron transport

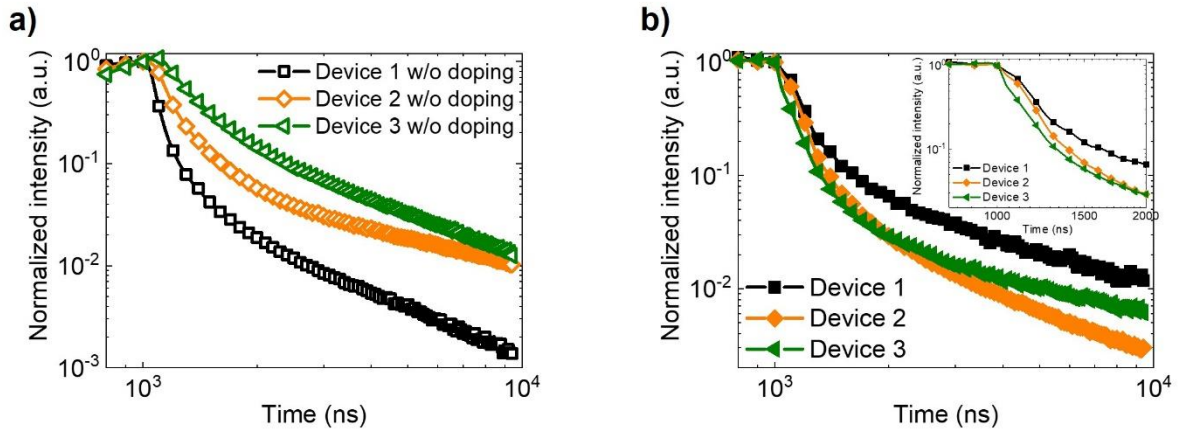

Figure 6-22. (a),(b) show the transient EL plots for the TPA-PyBTM' undoped and doped devices. The frequency was 100,000 Hz, and the pulse width was 1 μs. They were measured at the voltage corresponding to 1 mA/cm^2. Off voltage was -5 V for de-trapping the charge carriers after turn-off.

(Device 2). Also, Device 3 shows the negligible additional emission with rapid doublet fluorescence decay, meaning that the direct electron-hole capture at radical sites becomes more balanced in Device 3 than Device 1 and 2, supporting substantially improved efficiency roll-off and lifetime.

6.4 Summary

In conclusion, efficient NIR OLEDs were successfully demonstrated by utilising a novel radical emitter, and improved efficiency roll-off and device lifetime were shown by employing mixed hosts. The high absorption coefficient of TPA-PyBTM' in the range of 400 nm to 550 nm allows efficient energy transfer from the energy donor to the radical as an energy acceptor. It was demonstrated that improvement in charge balance of holes and electrons with the extended emission zone enables more stable devices with improved efficiency roll-off. From the conventional charge trapping-type device, a maximum EL EQE of 6.4% was achieved, and with B3PYMPM mixed hosts, not only the efficiency roll-off was improved, but also substantially better device lifetime was found: more than one hundred times longer than conventional devices.

However, the low-lying nature of the SOMO and HOMO energy levels of the radical causing severe electron trapping leads to the requirement of electron transport materials having lower energy levels with higher electron mobility than optimised for non-radical optoelectronics. For better electron transport with reduced electron trapping, B4PYMPM, which has one order faster electron mobility and 0.5 eV deeper LUMO energy level than B3PYMPM, was employed. It was shown that enhanced electron transport results in substantially improved optoelectronic performance, which

was proved by single-carrier devices and transient EL. A maximum EQE of 5.7% from the TCTA:B4PYMPM-based device was achieved, which is comparable to the CBP-based standard device (6.2%). Moreover, not only efficiency roll-off was substantially improved, but also more than ten times higher maximum radiance and two orders of magnitude increased device stability were attained, showing the disruptive potential of organic radical LEDs.

Consequently, it was shown that mixed host-based emissive systems are conducive to realising efficient and stable NIR organic radical LEDs based on doublet fluorescence. It was demonstrated that severe electron trapping in organic radicals results in low device performance, but it can be substantially enhanced by engineering EML and electron transport materials. It is noted that in electrical excitation, most doublet excitons are directly formed at radicals, which is opposite to photoexcitation resulting in doublet fluorescence mostly by FRET from hosts. As direct charge recombination at radical sites is dominant over energy transfer from hosts in doublet EL, it was shown that balanced hole and electron transport in an EML by mixing HTL and ETL materials results in high device performance. These results indicate a pathway for radical-based optoelectronic devices with doublet emission for infrared light-emitting technologies.

Chapter 7 Exploiting intersystem dual energy transfer for high efficiency organic radical LEDs

7.1 Introduction

In Chapter 6, efficient NIR OLEDs using a novel organic radical emitter, TPA-PyBTM', were studied with charge control by exploiting mixed hosts. Substantially improved efficiency roll-off and stability were achieved by exploiting mixed hosts while exploring the radical EL emission mechanism based on transient analysis and single-carrier device studies. However, although mixed hosts contribute to more balanced charge transport in an EML for improved device performance, direct charge recombination mechanisms still considerably dominate the overall emission process in doublet fluorescence in devices, and this has led to research for a new route to harvest excitons formed on host molecules by energy transfer for optimising doublet EL efficiency.

Anthracene derivatives have been widely applied in fluorescent OLEDs as exciton donors since they can show efficient TTA, which leads to overcoming the IQE limit of 25% in fluorescent OLEDs.[88–95] Interestingly, their triplet energy levels are generally around ~1.8 eV, which can be well-aligned with the doublet energy level of NIR emissive organic radicals, giving the potential of promoting triplet-to-doublet DET. Also, their fluorescent emission is well-overlapped with the absorption of radicals enabling effective FRET. Accordingly, excitons formed on the host molecules are capable of participating in doublet fluorescent emission by simultaneous intersystem dual energy transfer. This novel energy transfer mechanism can lead to realising highly

efficient NIR EL devices based on organic radicals.

In this chapter, highly efficient NIR OLEDs are demonstrated, exploiting organic radicals with intersystem dual energy transfer. One of the conventional anthracene derivatives, 2-methyl-9,10-bis(naphthalene-2-yl)anthracene (MADN), is selected as an exciton donor, and triphenyl amine-substituted tris(2,4,6-trichloro phenyl)methyl (TTM-TPA) presenting efficient NIR emission is employed as an exciton acceptor. Based on the MADN:TTM-TPA combination, a highly efficient NIR EL device with peak emission at 800 nm is successfully achieved, and its device performance easily outperforms the conventional charge trapping-type device. A maximum EQE of 9.6% is attained, which is approximately 60% higher than the conventional-type counterpart, 6.1%, with substantially reduced efficiency roll-off and enhanced radiance and device stability. To confirm and investigate the emission mechanism and energy transfer pathways in detail, the devices are examined using the transient EL and MEL measurements. Prominent delayed emission in the transient EL profile is recorded from the MADN-based device, indicating that as well as the FRET of singlets, the concurrent DET of triplets formed in MADN substantially contributes to doublet fluorescence. Also, this is confirmed by the distinct positive dependence of the EL on the magnetic field. Furthermore, transient PL and absorption profiles for the MADN-based blend clearly support the doublet-triplet interaction considering the much faster decay in transient absorption and prominent delayed emission in transient PL.

7.2 The design of intersystem dual energy transfer

Figure 7-1 shows the schematic diagram of the energy transfer pathways between

MADN and TTM-TPA with their energy levels. When TTM-TPA molecules are doped in a MADN matrix, it is expected that electrically excited singlet and triplet excitons formed on MADN molecules are capable of being transferred to the doublet excited states of TTM-TPA via the mechanism of FRET and DET. The schematic diagram of the spin configurations for the expected FRET and DET processes between MADN and TTM-TPA is displayed in Figure 7-2, corresponding to the following expressions,

$$S_1 + D_0 \rightarrow S_0 + D_2 \rightarrow S_0 + D_1 \text{ (FRET channel)} \quad (7\text{-}1)$$

$$T_1 + D_0 \rightarrow S_0 + D_1 \text{ (DET channel)} \quad (7\text{-}2)$$

where S_1 and T_1 are the first electronically excited states of the singlet and the triplet, S_0 is the ground singlet state, D_1 and D_2 are the first and second electronically excited states of the doublet, and D_0 is the ground doublet state. As shown in Figure 7-2, the intersystem energy transfer between the different spin states can be achieved with conservation of spin projection quantum number.

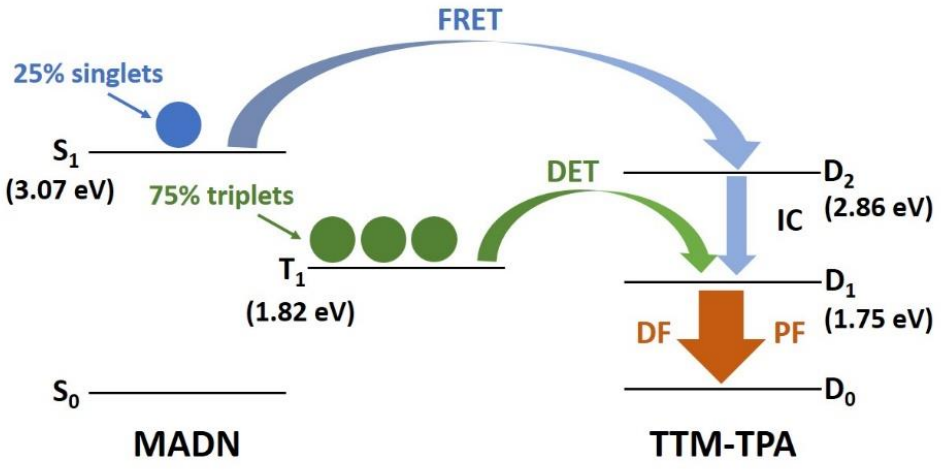

Figure 7-1. Schematic illustration of dual energy transfer between MADN and TTM-TPA in devices.

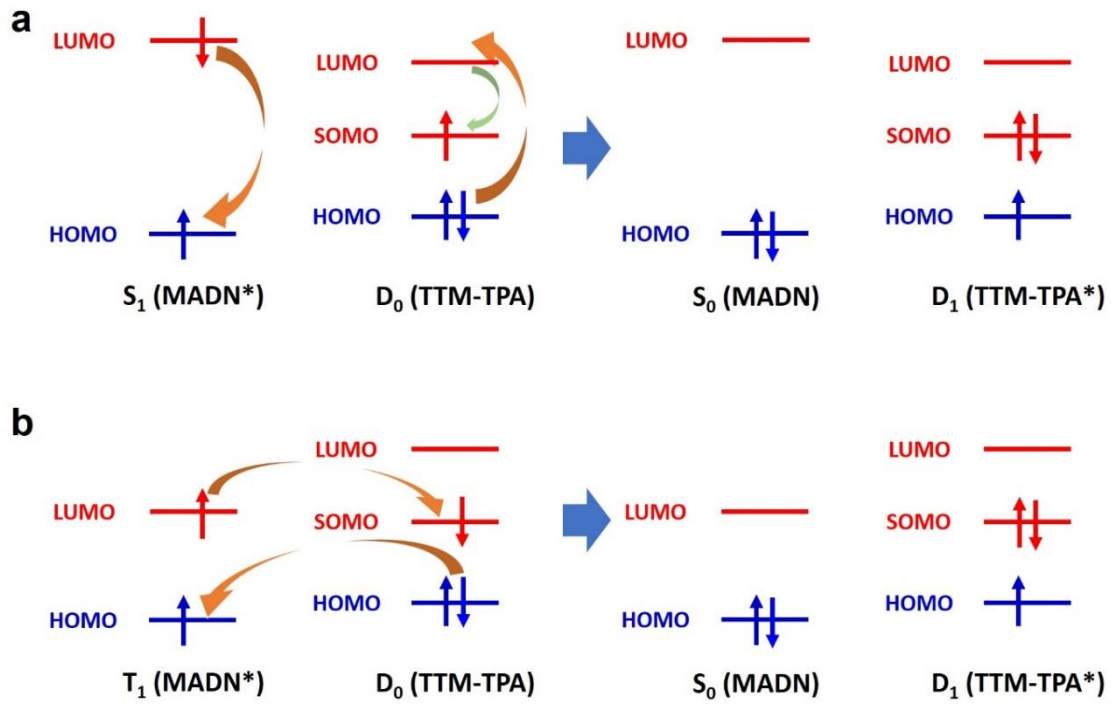

Figure 7-2. Schematic illustration of the spin configurations for the energy transfer mechanisms between MADN and TTM-TPA. (a) FRET. (b) DET.

As demonstrated from previous reports, FRET from the non-radical host (singlet states) to radical dopant (doublet states) occurs effectively considering high PLQE values and strong doublet fluorescence intensity by photoexcitation from the radical doped films.[50] Also, considering the small energy gap between MADN T_1 and TTM-TPA D_1 (< 0.1 eV), it is anticipated that triplet excitons formed on MADN molecules can be transferred to the doublet excited states of TTM-TPA via DET. Therefore, both singlet and triplet excitons formed at MADN molecules can contribute to doublet emission via effective concurrent dual energy transfer, in addition to the doublet exciton formation by the direct charge recombination at TTM-TPA sites, which could lead to substantially improved optoelectronic performance in doublet EL devices.

7.3 Steady-state photophysics

TTM-TPA was synthesised by Prof. Feng Li, College of Chemistry, Jilin University. Figure 7-3(a) shows the chemical structures of TTM-TPA, MADN, and 4,4'-Bis(carbazol-9-yl)biphenyl (CBP), and Figure 7-3(b) depicts their steady-state photophysical properties. As a control, CBP was utilised as a conventional host for TTM-TPA to be compared with MADN. CBP neat and CBP:TTM-TPA 3% films and TTM-TPA solution are excited by a 330 nm laser, and MADN neat and MADN: TTM-TPA 3% films are excited by a 370 nm laser. The PL of CBP and MADN neat films overlaps with the absorption of TTM-TPA so that photoexcited singlet excitons formed in CBP and MADN can be effectively transferred to the doublet excited states of TTM-TPA, emitting intense NIR fluorescence with the emission peak at around 800 nm (Figure 7-3(b)). This result indicates that the doublet excitons are formed from

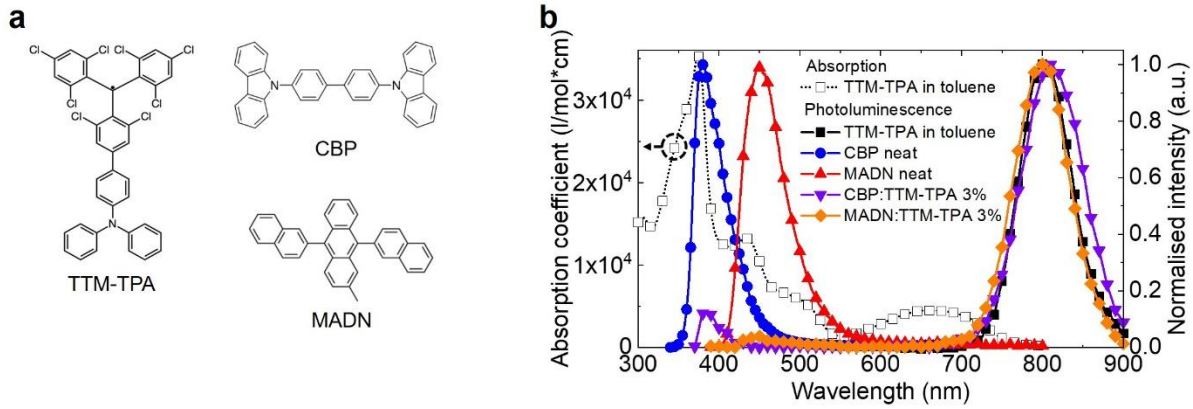

Figure 7-3. Chemical structures and steady-state photophysical properties. (a) Chemical structures of TTM-TPA, CBP, and MADN. (b) PL and absorption profiles for TTM-TPA, CBP, and MADN. The absorption coefficient for TTM-TPA and the PL spectra for CBP and MADN are well-overlapped, leading to effective FRET between them. The CBP- and MADN-hosted films show strong NIR emission with around 800 nm peak wavelength, in line with the TTM-TPA solution PL.

the singlet excitons generated in MADN via the effective FRET. A small contribution of the host emission to the total PL is observed since the small proportion of the remaining singlet excitons in CBP and MADN participates in the emission process. Also, PLQEs of the TTM-TPA solution and the TTM-TPA doped films are measured. The PLQE of TTM-TPA diluted in toluene is 24%, while the CBP and MADN hosted films show 19% and 27% PLQEs, respectively.

7.4 Device characterisation

To explore how MADN works with TTM-TPA under electrical excitation, the MADN:TTM-TPA combination was initially applied in doublet EL devices. The device structure and the energy level diagram of materials utilised in this work are displayed in Fig. 7-4(a). 1,1-bis[(di-4-tolylamino) phenyl] cyclohexane (TAPC) and 4,4′,4″-tris(carbazol-9-yl) triphenylamine (TCTA) were used in an HTL part, and bis-4,6-(3,5-di-3-pyridyl phenyl)-2-methyl pyrimidine (B3PYMPM) was employed as an ETL. For a control device, CBP was used as a host for TTM-TPA in an EML. In contrast, TTM-TPA was doped in MADN to compare device performance to the control device. The radical-based EL devices were fabricated, and their characteristics are shown in Figure 7-4(b)~(e) and Table 7-1. Regarding the EQE-current density plots shown in Figure 7-4(b), the MADN-based device shows a maximum EQE of 9.6%, nearly 60% higher than the CBP-based device, 6.1%. Also, whereas the CBP-based device shows a large efficiency drop beyond 10 mA/cm^2, the MADN-based device keeps a relatively high efficiency, 4.2%, even at 100 mA/cm^2. As a result, the maximum radiance of the MADN-based device reaches 68,000 mW·sr^{-1}·m^{-2}, which is the highest value of published NIR OLEDs with over 800 nm emission peak, and this is nearly ten times

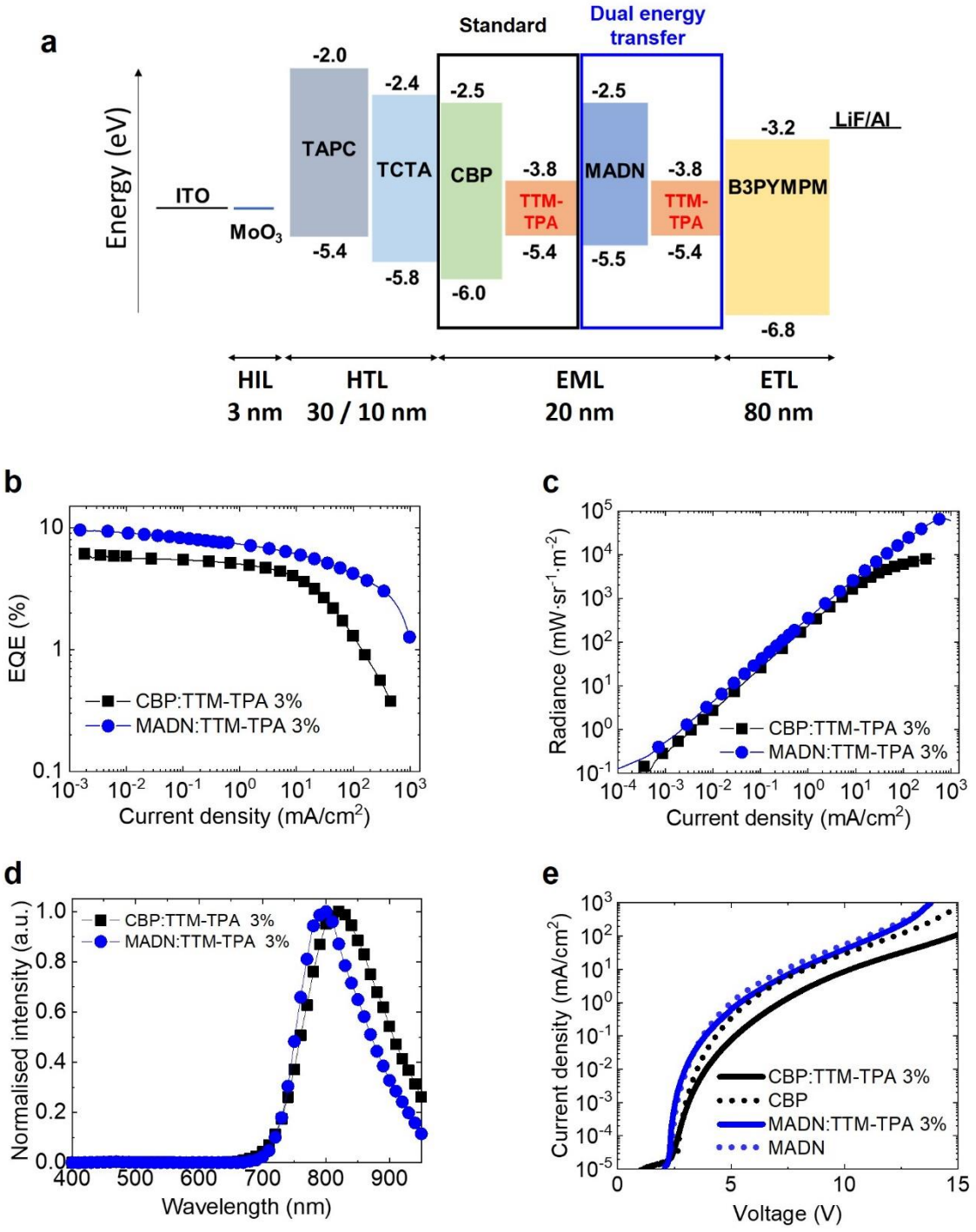

Figure 7-4. (a) Device structure with energy levels. (b) EQE-current density plots. (c) Radiance-current density plots. (d) EL spectra at 1 mA/cm^2. (e) The comparison of the J-V profiles for the devices with and without TTM-TPA doping.

Table 7-1. Summary of device performance.

	V_{on}[a)] (V)	EQE_{Max} (%)	$EQE_{J\text{-}1.0}$[b)] (%)	$EQE_{J\text{-}100.0}$[c)] (%)	$Radiance_{Max}$ ($mW \cdot sr^{-1} \cdot m^{-2}$)	λ_{max} (nm)	Lifetime[d)] (hr)
CBP:TTM-TPA 3%	2.8	6.1	4.9	1.3	8,100	820	6.9
MADN:TTM-TPA 3%	2.4	9.6	7.2	4.2	68,000	800	58.4

[a)]Voltage at 10^{-1} $mW \cdot sr^{-1} \cdot m^{-2}$. [b)]EQE at 1 mA/cm^2, [c)]EQE at 100 mA/cm^2, [d)]Lifetime at 0.1 mA/cm^2

higher than the CBP-based device, 8,100 $mW \cdot sr^{-1} \cdot m^{-2}$ (Fig. 7-4(c)). Fig. 7-4(d) shows the NIR doublet EL emission spectra for the devices. Interestingly, no host emission is recorded, unlike PL, indicating that the direct charge recombination contributes to the overall emission process as well as energy transfer from hosts. Also, the EL spectrum for the MADN-based device (800 nm) is slightly blue-shifted compared to the CBP-based device (820 nm). This is probably attributed to the host effect,[231] like the solvatochromic effect shown in Section 6.2.1 (Figure 6-3(b)). In order to investigate the influence of the radical doping and different hosts on the charge transport in devices, the J-V plots for the radical doped and undoped devices are compared, as shown in Figure 7-4(e). When MADN is employed, the J-V curves become steeper than CBP, showing the faster charge transporting properties of MADN than CBP. Moreover, as TTM-TPA is doped in CBP, the J-V curve becomes much shallower. In contrast, regarding the MADN-based devices, even though TTM-TPA is doped in MADN, the charge transport in the device stays almost the same. It is inferred that MADN shows much better electron and hole transporting properties than CBP, and potentially energy transfer dominates the overall emission process in the device.

Furthermore, the device lifetime was compared to support the superiority of the MADN-based device over the CBP-based device. Figure 7-5 shows the comparison of

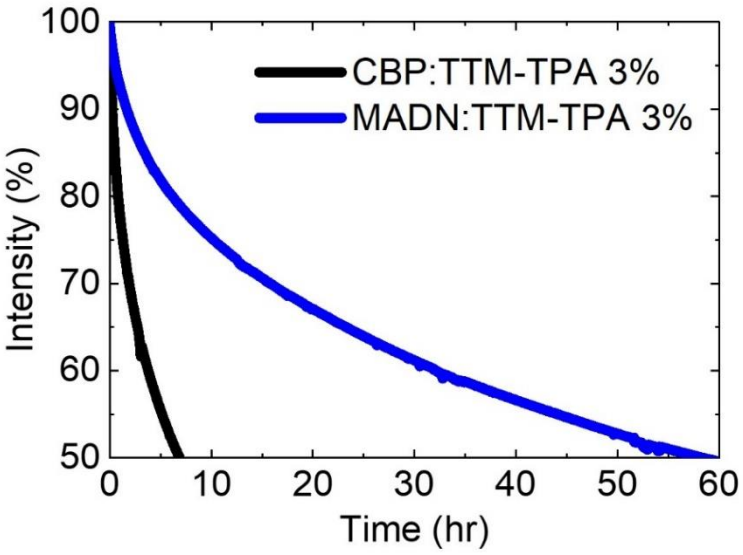

Figure 7-5**.** Comparison of device lifetime measured at 0.1 mA/cm^2.

lifetime for the devices measured at 0.1 mA/cm^2. The MADN-based device shows 58.4 hr, almost ten times longer than the CBP-based device, 6.9 hr. Compared to the previous reported lifetime result of radical-based OLEDs showing under 1 hr, the device stability was dramatically enhanced.[51] Furthermore, due to the very low efficiency and low material stability of NIR organic emitters resulting from the energy gap law, most NIR OLED papers do not tend to report device lifetime, possibly due to poor values.[23] Therefore, these results show the great potential of realising high stability as well as high efficiency in doublet EL devices.

Overall, the MADN-based device substantially outcompetes the CBP-based device in terms of all aspects of the device characteristics, such as EQE, efficiency roll-off, radiance, J-V profiles, and lifetime. To understand the driving force of the significantly enhanced device performance in detail, the devices are specifically investigated based on the examination and comparison of the charge transporting

properties and emission mechanism in the devices in the following sections.

7.5 Single-carrier device analysis

Single-carrier devices were fabricated to explore the influence of the different hosts on charge transporting abilities in an EML more in detail. They were designed based on the full device architecture to directly apply their characteristics to the full device performance, as shown in Figure 7-6(a) and (b). Regarding HODs, TAPC and TCTA are used in the HTL part, and TAPC is inserted between the EML and the cathode to block electron injection into the EML. In contrast, the EML is sandwiched by the ETL material, B3PYMPM, to achieve an electron-only current in EODs. The corresponding host-dopant compositions used in the full devices (CBP:TTM-TPA 3%, MADN:TTM-TPA 3%, CBP, and MADN) are applied in both HODs and EODs to examine the different charge transporting properties in devices depending on the different use of hosts and radical doping.

Figure 7-6(c) and (d) present the comparison of the J-V plots for HODs and EODs, respectively. Regarding HODs, hole transport in MADN is more rapid than in CBP, considering the steeper J-V curves. Also, holes are less trapped at radicals in MADN than CBP due to the shallower HOMO energy level of MADN. Also, electron transport in MADN is much faster than in CBP, leading to a more balanced population of charge carriers in the EML. Although electrons are captured at radicals in both MADN and CBP, much more enhanced electron transport in MADN is apparent compared to CBP. Therefore, MADN is capable of providing much more improved charge transport with better charge balance in the EML, leading to substantially enhanced device performance. Also, as holes are less captured in a MADN matrix, it is

expected that direct recombination of hole and electron at radical sites would be less dominant, whereas exciton energy transfer from MADN to TTM-TPA would dominate the overall emission process in this combination.

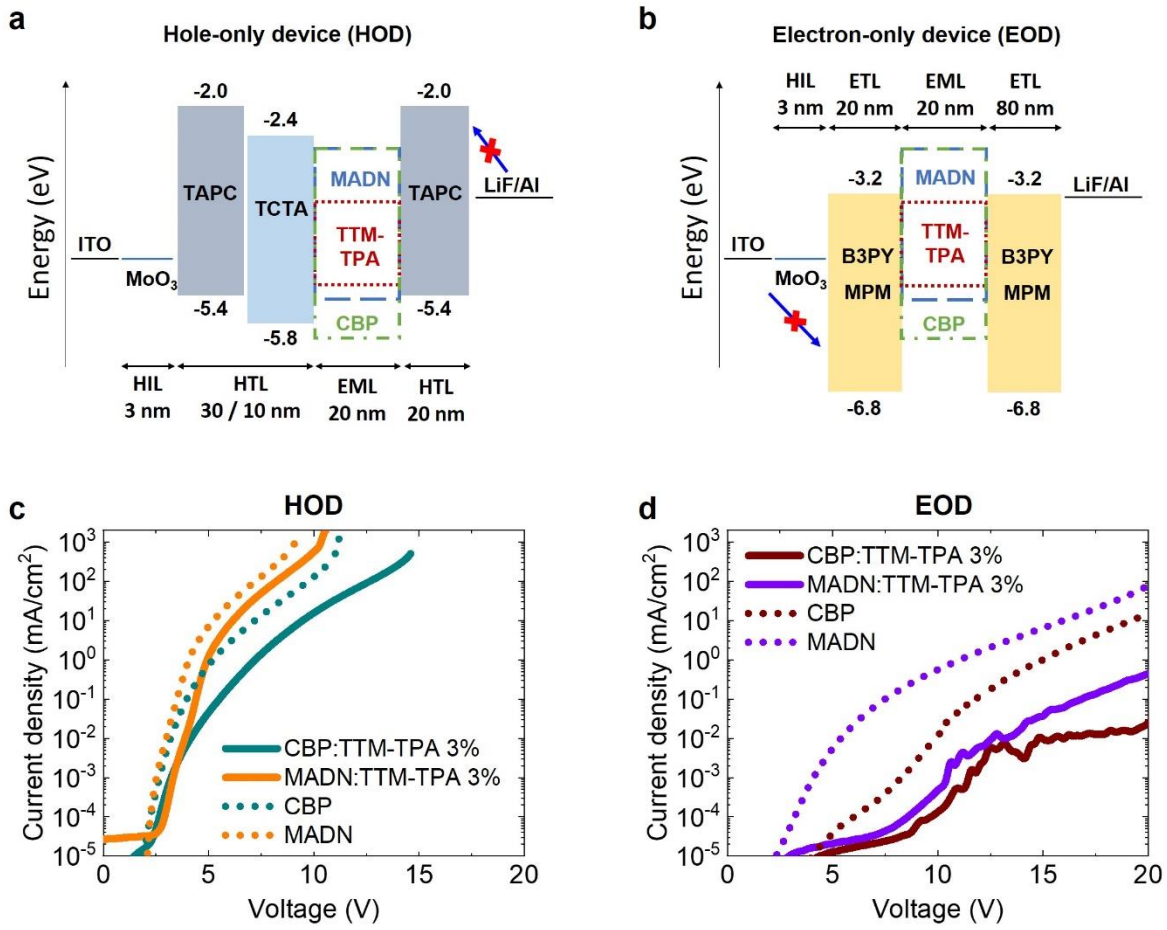

Figure 7-6 **(**a),(b) show the device architectures of HOD and EOD. For HOD, TAPC 20 nm is deposited between the EML and cathode to preclude electron injection. For EOD, EML is sandwiched by B3PYMMPM to ensure electron-only currents. The J-V plots for the HODs and EODs are depicted in (c) and (d). As TTM-TPA is doped in the hosts, the radical plays a role in trapping both holes and electrons, considering HOD and EOD plots become shallower, but electron trapping is more severe. Also, as MADN is employed, electron transporting abilities in EML are substantially improved in the sense of the much steeper J-V curves.

7.6 Transient and magneto electroluminescence

Despite the fact that the substantially improved charge transport and balance in an EML are proved by the comparison of the J-V characteristics for the full devices and single-carrier devices, it is necessary to explore the difference in the emission mechanisms for the two devices more in detail to clearly prove and support the substantial enhancement of the optoelectronic performance in the MADN-based device compared to the CBP-based counterpart. For this purpose, transient EL and MEL

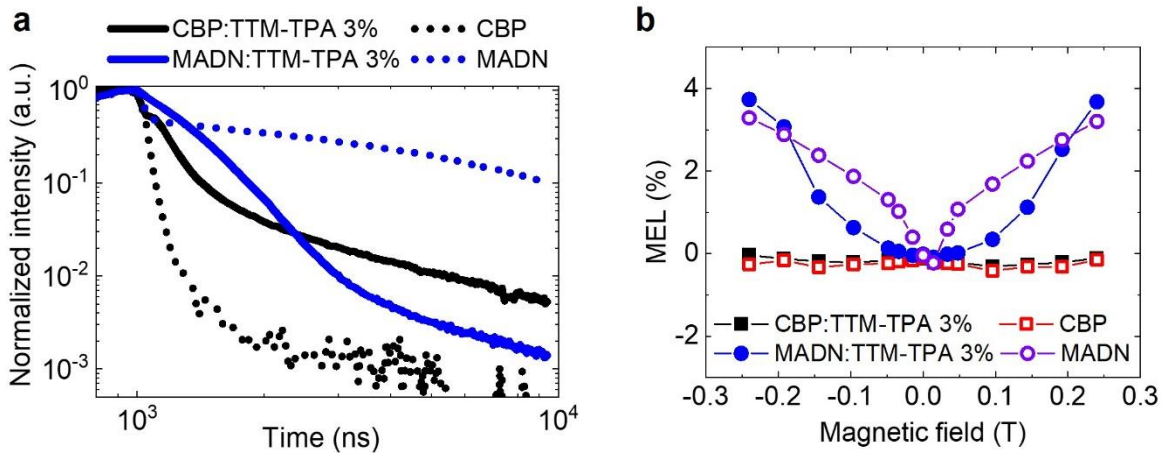

Figure 7-7. (a) Transient EL profiles for the TTM-TPA doped and undoped devices. The voltage pulse corresponds to 1 mA/cm^2, and off-voltage was -5V for de-trapping the charge carriers after turn-off. In the CBP-based devices, no delayed emission is observed, but additional emission after turn-off is recorded due to trapped charges. Interestingly, the MADN-based devices show strong delayed emission features, which is different from TTA shown in the undoped device. Hence, it is estimated that DET considerably contributes to the emission process. (b) Magneto EL for the devices at 1 mA/cm^2. The CBP-based devices show negligible MEL while the MADN based devices clearly show positive MEL, but the apparently different dependence on magnetic field is recorded. Unlike the MADN-only device, the TTM-TPA-doped device shows much lower MEL at low magnetic field, suggesting that DET dominates the emission process over TTA.

measurements were conducted. Transient EL and MEL results were interpreted with Dr. Emrys Evans, Department of Chemistry, Swansea University.

Firstly, transient EL profiles for the devices with and without TTM-TPA doping are exhibited in Figure 7-7(a). It is known that MADN shows effective TTA with distinct delayed emission in devices.[95,178] These characteristics were clearly recorded by the transient EL measurements on the MADN only device. In contrast, the CBP-only device shows no delayed emission but just rapid fluorescence emission, meaning that triplets formed in CBP do not contribute to the emission process. Regarding the radical-doped devices, as expected from the full device and single-carrier device results, the CBP-based device shows fast doublet fluorescence with the initial feature at 50~100 ns resulting from the remaining trapped charges at radical sites.[160,164–166] In contrast, the MADN-based device does not show fast prompt decay but much slower EL decay, which is also entirely different from the transient EL decay of the MADN-only device. If TTA occurred effectively in the MADN:TTM-TPA device, additionally generated singlet excitons would contribute to the emission process via FRET after prompt doublet fluorescence. Accordingly, the transient EL decay plot for the MADN:TTM-TPA device would be similar to the MADN-only device in this case. However, given that the far slower initial EL decay is recorded without prominent rapid prompt decay compared to other devices, it can be estimated that the triplet excitons formed on MADN molecules contribute to doublet EL by a different mechanism from TTA. Accordingly, it is inferred that with the singlet-to-doublet FRET, the coincident triplet-to-doublet DET between MADN and TTM-TPA substantially contributes to the formation of doublet excitons, as designed in the MADN:TTM-TPA emissive system (Figure 7-1).

To confirm and distinguish the different exciton dynamics in the MADN-based

devices with and without TTM-TPA doping, MEL was recorded (Figure 7-7(b)). MEL is defined by the following equation,

$$\text{MEL}\ (\%) = \frac{\text{EL(B)}-\text{EL(0)}}{\text{EL(B)}} \times 100 \qquad (7\text{-}3)$$

where EL(B) and EL(0) are the EL intensity with the presence and absence of magnetic field, respectively. MEL can reveal the different exciton mechanisms in devices since the Zeeman splitting of spin states in a magnetic field leads to different MEL tendencies arising from magnetic interactions in different systems, especially for those where singlet-triplet interconversion can happen effectively by ISC or TTA.[168–180]

For CBP-based devices, MEL shows almost negligible magnetic field dependence regardless of TTM-TPA doping. In contrast, the MADN-based devices show distinct positive MEL, meaning that magnetosensitive triplet excitons contribute to the emission process as deduced from transient EL studies. For the MADN-only device biased at 1 mA/cm^2, the net positive MEL suggests that magnetosensitivity of the polaron-pair hyperfine mechanism (positive MEL) must dominate magneto-sensitivity from TTA (negative MEL).[177,178,180,183,184] In the polaron-pair hyperfine mechanism, a positive MEL for S_1 emission occurs if triplet states of the polaron-pair precursor to excitons decay more rapidly than the singlet. On the applied magnetic field, the Zeeman splittings of polaron-pair T_+ and T_- make them energetically isolated from singlet-triplet conversion, and the singlet population is lost only via T_0.[184] In the TTA mechanism, a negative MEL for delayed S_1 emission occurs due to a reduced number of states with spin-conserving singlet-intermediate '{}' upon the applied magnetic field, when considering encounter eigenstates for: $T_1 + T_1 \rightarrow \{T_1\ T_1\} \rightarrow S_1 + S_0$.[180,232]

However, as TTM-TPA molecules are doped in a MADN matrix, the MEL profile shows a different dependence on the magnetic field with a non-Lorentzian shape.

If energy transfer from MADN S_1 to TTM-TPA D_1 for radical emission were dominant, MEL profiles for the MADN-only and MADN:TTM-TPA devices would be identical since the magnetic field does not affect the FRET. The MADN:TTM-TPA magnetosensitivity is attributed to contribution from the triplet-doublet energy transfer mechanism for EL. The triplet-to-doublet magnetosensitivity would give rise to negative MEL behaviour for TTM-TPA emission. This arises due to a reduced number of states with spin-conserving doublet-intermediate '{}', upon the applied magnetic field, when considering encounter eigenstates in: $T_1 + D_0 \rightarrow \{T_1\ D_0\} \rightarrow S_0 + D_1$.[233] The triplet-to-doublet transfer contributes to the total MEL in the MADN:TTM-TPA device, where the magnetic field response curve depends on the MADN T_1 zero-field splitting interaction. This gives a broader magnetic field response than for systems such as the MADN-only device, where smaller hyperfine interactions dominate the magnetosensitivity at a low magnetic field.

7.7 Exciton decay kinetics and energy transfer analysis

Transient absorption and PL measurements (done by Sebastian Gorgon, Department of Physics, University of Cambridge) were conducted to investigate the exciton dynamics and confirm the energy transfer pathways in the MADN:TTM-TPA combination. Both host excitation (330 nm laser for CBP and 400 nm laser for MADN) and radical excitation (532 nm laser) were applied to explore the difference of energy transfer and exciton decay kinetics between TTM-TPA 3% doped in CBP and MADN films (150 nm) on the basis of the absorbance spectra of CBP and MADN neat films (100 nm) shown in Figure 7-8.

Figure 7-9(a) shows the transient absorption profiles for the MADN only and

MADN:TTM-TPA 3% films excited at 400 nm. The singlet decay of the MADN: TTM-TPA 3% is much faster than the MADN-only, meaning that singlet excitons formed in MADN are rapidly transferred to TTM-TPA via FRET. The doublet signal in the MADN:TTM-TPA 3% is well fitted monoexponentially assigning singlet-to-doublet FRET with a time constant of just 8 ps. Therefore, although there may be a possible route for singlets to be converted to upper excited triplets via ISC,[234] it can be inferred that almost all singlet excitons formed by photoexcitation are rapidly transferred to doublet excited states via FRET. Furthermore, the CBP:TTM-TPA 3% and MADN:TTM-TPA 3% films were excited by a 532 nm laser to compare the different behaviour of TTM-TPA 3% doped in CBP and MADN, not considering FRET from the hosts (Figure 7-9(b)). Even though singlet-to-doublet FRET is excluded by the direct radical excitation, quicker decay of the MADN hosted blend (0.58 ns) than the CBP hosted blend (1.2 ns) is observed, which is evidence showing that intersystem doublet-to-triplet DET between TTM-TPA D_1 and MADN T_1 may decrease the doublet population.

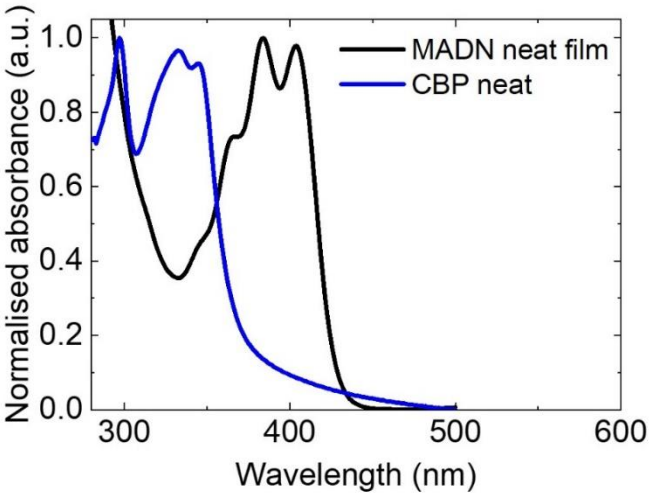

Figure 7-8. The normalised absorbance of CBP and MADN neat film (100 nm).

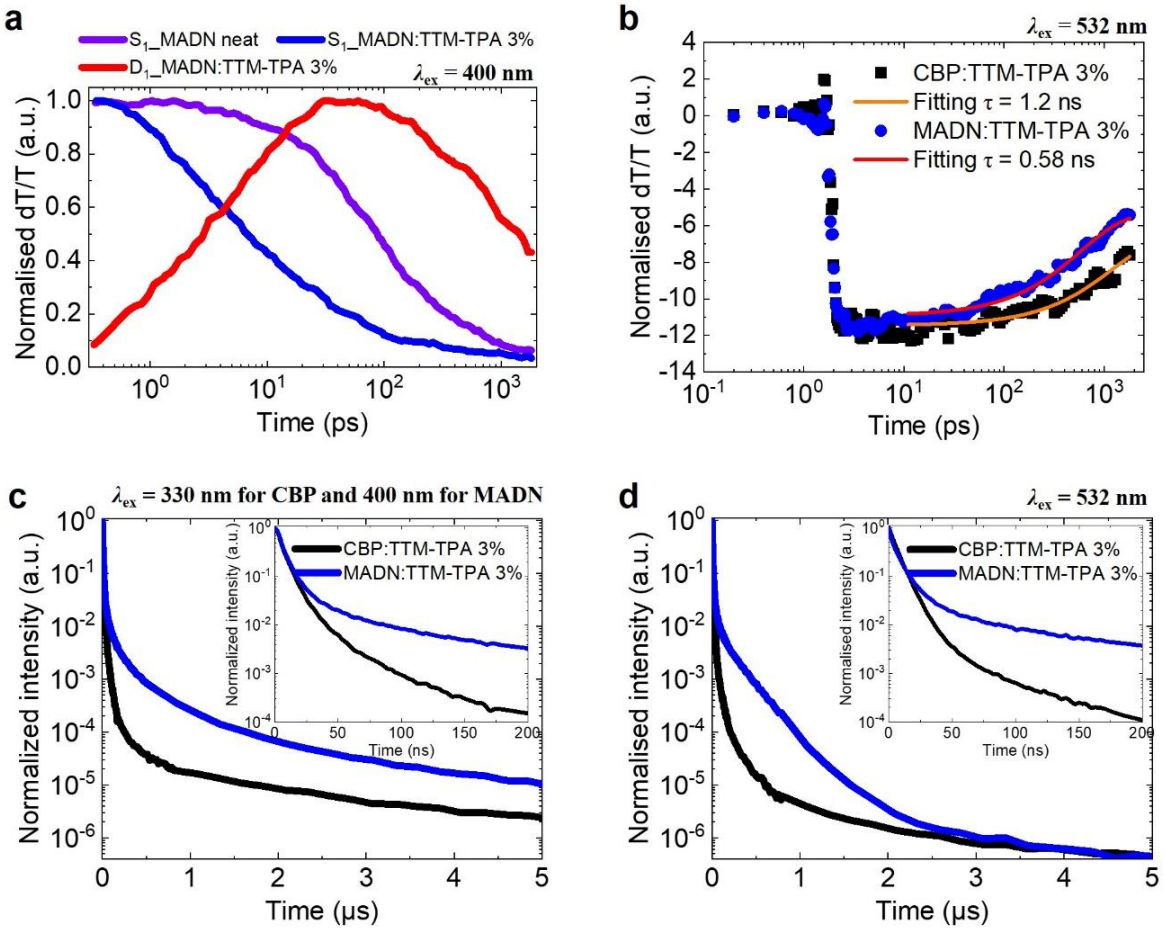

Figure 7-9. (a) Transient absorption profiles of MADN only and MADN:TTM-TPA 3% films for singlet and doublet signals. (b) Comparison of transient absorption profiles for CBP:TTM-TPA 3% and MADN:TTM-TPA 3% films excited by 532 nm laser. (c),(d) Transient PL profiles at 400 nm and 532 nm laser excitation.

In order to confirm the interaction between MADN T_1 and TTM-TPA D_1, transient PL for the two blends was compared, as shown in Figure 7-9(c) and (d). When the hosts, CBP and MADN, are excited (Figure 7-9(c)), the MADN hosted film shows distinct delayed emission, not observed in the CBP hosted film. Moreover, a similar delayed emission is recorded even by the direct excitation of TTM-TPA in the

MADN:TTM-TPA blend, clearly supporting the doublet-to-triplet DET (R-DET) in addition to triple-to-doublet DET (F-DET) in line with the transient absorption results.

Figure 7-10 shows the schematic diagram of exciton decay kinetics and energy transfer pathways in the MADN:TTM-TPA system. Assuming that the internal conversion (IC) time is negligibly short, and doublet excitons experiencing radiative and nonradiative decay ($k_{\mathrm{r,D}}$ and $k_{\mathrm{nr,D}}$) are generated by the FRET of singlet excitons formed by photoexcitation when MADN is excited by 400 nm, the FRET efficiency (E_{FRET}) can be extracted as,

$$E_{\mathrm{FRET}} = \frac{k_{\mathrm{FRET}}}{k_{\mathrm{r,MADN}}+k_{\mathrm{nr,MADN}}+k_{\mathrm{FRET}}} = \frac{1/\Phi_F \int P_{\mathrm{TTM-TPA}}(\lambda)d\lambda}{1/\Phi_{\mathrm{MADN}} \int P_{\mathrm{MADN}}(\lambda)d\lambda+1/\Phi_F \int P_{\mathrm{TTM-TPA}}(\lambda)d\lambda} \quad (7\text{-}4)$$

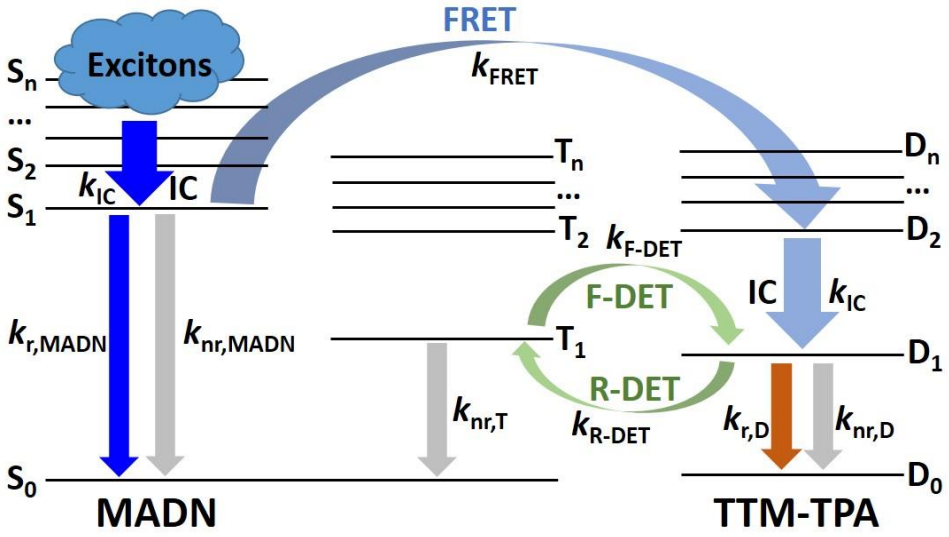

Figure 7-10. Schematic illustration of exciton decay kinetics and intersystem dual energy transfer pathways between MADN and TTM-TPA.

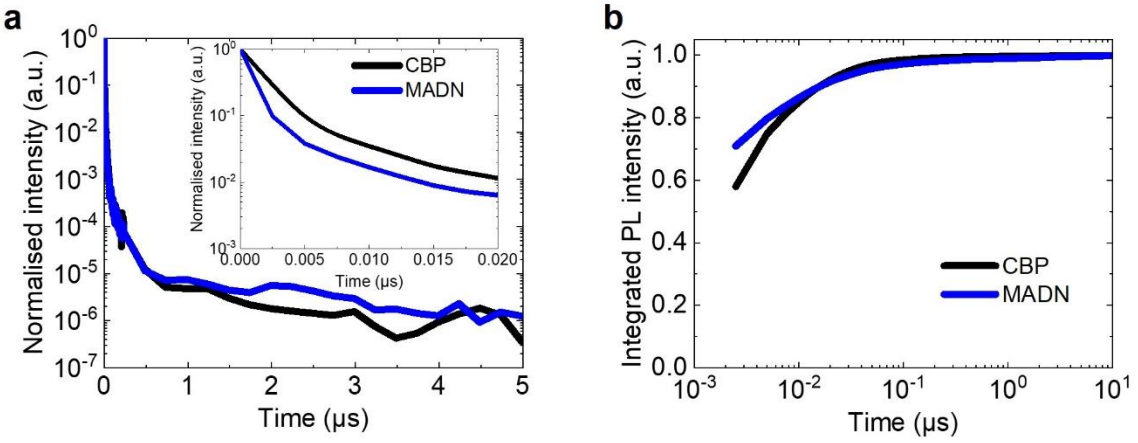

Figure 7-11. The transient PL and normalised integrated PL intensity profiles of the CBP and MADN neat films.

Table 7-2. Summary of PLQE, decay lifetime, and decay rate for CBP and MADN.

	PLQE	τ (10^{-9}s)[a)]	k_r (10^9/s)	k_{nr} (10^9/s)
CBP	0.78	3.27	23.85	6.73
MADN	0.41	2.23	18.39	26.56

[a)]Derived from the time when the integrated PL intensity reaches 1-(1/e).

Table 7-3. Summary of PLQE, decay lifetime, decay rate, FRET rate, and FRET efficiency for CBP:TTM-TPA 3% and MADN:TTM-TPA 3%.

Host	Dopant	PLQE	τ [a)] (10^{-9}s)	k_r (10^7/s)	k_{nr} (10^7/s)	k_{FRET} (10^9/s)	E_{FRET} (%)
CBP	TTM-TPA	0.19	8.27	2.30	9.79	20.08	98.5
MADN		0.27	14.33	1.88	5.09	21.97	98.0

[a)]Derived from the time when the integrated PL intensity reaches 1-(1/e).

where $k_{\mathrm{r,MADN}}$ and $k_{\mathrm{nr,MADN}}$ are the radiative and nonradiative decay rates of MADN (Figure 7-11 and Table 7-2), k_{FRET} is the rate constant of the characteristic FRET, Φ_{MADN} and Φ_F are the PLQEs of the MADN neat and the MADN hosted films, and P_{MADN} and $P_{\mathrm{TTM\text{-}TPA}}$ are the PL spectra of MADN and TTM-TPA emission components in the blend, respectively, obtained from the decomposed donor and acceptor spectra from the total spectra of the MADN hosted film. From Equation 7-4, k_{FRET} is calculated by

$$k_{\mathrm{FRET}} = \frac{E_{\mathrm{FRET}}(k_{\mathrm{r,MADN}}+k_{\mathrm{nr,MADN}})}{1-E_{\mathrm{FRET}}} \tag{7-5}$$

Hence, from Equation 7-5, k_{FRET} between MADN and TTA-TPA can be extracted as 21.97×10^9/s, in line with the rapid doublet signal rise (~8 ps) of the transient absorption profile (Figure 7-9(a)). The decay lifetime, decay rate, FRET rate, and FRET efficiency for the CBP-based and MADN-based blends are summarised in Table 7-3.

Furthermore, to understand the mutual DET between MADN T_1 and TTM-TPA D_1, the transient PL profile of the MADN:TTM-TPA blend by the direct excitation of TTM-TPA was investigated (Figure 7-9(d)). The decay profile can be separated by prompt and delayed components resulting from the intermolecular intersystem triplet-doublet mutual DET. Accordingly, under the direct excitation of TTM-TPA in the MADN hosted blend, the doublet and triplet exciton densities in TTM-TPA and MADN (D and T) are described by[116–118]

$$\frac{d\mathrm{D}}{dt} = -(k_{\mathrm{r,D}} + k_{\mathrm{nr,D}})\mathrm{D} - k_{\mathrm{R-DET}}\mathrm{D} + k_{\mathrm{F-DET}}\mathrm{T} \tag{7-6}$$

$$\frac{d\mathrm{T}}{dt} = -k_{\mathrm{nr,T}}\mathrm{T} - k_{\mathrm{F-DET}}\mathrm{T} + k_{\mathrm{R-DET}}\mathrm{D} \tag{7-7}$$

where $k_{\mathrm{r,D}}$ and $k_{\mathrm{nr,D}}$ are the radiative and nonradiative decay rates of the doublet, $k_{\mathrm{nr,T}}$

is the nonradiative decay rate of the triplet, $k_{\mathrm{R-DET}}$ and $k_{\mathrm{F-DET}}$ are the rate constants of R-DET and F-DET. The solutions to Equation 7-11 and 12 can be expressed as the simple form of the biexponential decay,[116–118]

$$\mathrm{D,T} = A_1 \exp(-k_{\mathrm{p}}\mathrm{t}) + A_2 \exp(-k_{\mathrm{d}}\mathrm{t}) \tag{7-8}$$

where A_1 and A_2 are the fitting parameters, and k_{p} and k_{d} are the rate constants of the prompt and delayed emission. With the intersystem mutual DET, k_{p} and k_{d} are given by Equation 7-9,[116–118]

$$k_{\mathrm{p}}, k_{\mathrm{d}} = \frac{k_{\mathrm{r,D}}+k_{\mathrm{nr,D}}+k_{\mathrm{R-DET}}+k_{\mathrm{nr,T}}+k_{\mathrm{F-DET}}}{2} \times$$

$$\left(1 \pm \sqrt{1 - \frac{4\left(k_{\mathrm{r,D}}+k_{\mathrm{nr,D}}+k_{\mathrm{R-DET}}\right)\left(k_{\mathrm{nr,T}}+k_{\mathrm{F-DET}}\right)-4k_{\mathrm{R-DET}}k_{\mathrm{F-DET}}}{\left(k_{\mathrm{r,D}}+k_{\mathrm{nr,D}}+k_{\mathrm{R-DET}}+k_{\mathrm{nr,T}}+k_{\mathrm{F-DET}}\right)^2}}\right) \tag{7-9}$$

Assuming $k_{\mathrm{r,D}}$, $k_{\mathrm{nr,D}}$, and $k_{\mathrm{R-DET}} \gg k_{\mathrm{nr,T}}$ and $k_{\mathrm{F-DET}}$, k_{p} and k_{d} are expressed by Equation 7-10 and 11,[116–118]

$$k_p = k_{\mathrm{r,D}} + k_{\mathrm{nr,D}} + k_{\mathrm{R-DET}} \tag{7-10}$$

$$k_{\mathrm{d}} = k_{\mathrm{nr,T}} + \left(1 - \frac{k_{\mathrm{r,D}}}{k_{\mathrm{r,D}}+k_{\mathrm{nr,D}}+k_{\mathrm{R-DET}}}\right) k_{\mathrm{F-DET}} = \frac{k_{\mathrm{p}}k_{\mathrm{F-DET}}-k_{\mathrm{r,D}}k_{\mathrm{F-DET}}}{k_{\mathrm{p}}} \tag{7-11}$$

Also, the PLQEs of the prompt and delayed emission (Φ_{P} and Φ_{d}) are given by Equation 7-12 and 13,

$$\Phi_{\mathrm{P}} = \frac{k_{\mathrm{r,D}}}{k_{\mathrm{r,D}}+k_{\mathrm{nr,D}}+k_{\mathrm{R-DET}}} \tag{7-12}$$

$$\Phi_{\mathrm{d}} = \sum_{k=1}^{\infty}(\Phi_{\mathrm{R-DET}}\Phi_{\mathrm{F-DET}})^k \Phi_{\mathrm{p}} = \frac{\Phi_{\mathrm{R-DET}}\Phi_{\mathrm{F-DET}}}{1-\Phi_{\mathrm{R-DET}}\Phi_{\mathrm{F-DET}}}\Phi_{\mathrm{p,D}} \tag{7-13}$$

where $\Phi_{\mathrm{R-DET}}$ and $\Phi_{\mathrm{F-DET}}$ are the efficiency of R-DET and F-DET, given by

$$\Phi_{\mathrm{R-DET}} = \frac{k_{\mathrm{R-DET}}}{k_{\mathrm{r,D}}+k_{\mathrm{nr,D}}+k_{\mathrm{R-DET}}} = \frac{k_{\mathrm{R-DET}}}{k_{\mathrm{p}}} \tag{7-14}$$

$$\Phi_{\mathrm{F-DET}} = \frac{k_{\mathrm{F-DET}}}{k_{\mathrm{F-DET}}+k_{\mathrm{nr,T}}} \approx 1 \tag{7-15}$$

Meanwhile, Φ_{p} and Φ_{d} are extracted experimentally from the total PLQE (Φ_{total}) and the intensity ratio of the prompt and delayed emission (r_1 and r_2) in the transient PL profile. Hence, Φ_{total}, Φ_{p}, and Φ_{d} are described by

$$\Phi_{\mathrm{total}} = \Phi_{\mathrm{p}} + \Phi_{\mathrm{d}} \tag{7-16}$$

$$\Phi_{\mathrm{p}} = r_1 \Phi_{\mathrm{total}} \tag{7-17}$$

$$\Phi_{\mathrm{d}} = r_2 \Phi_{\mathrm{total}} \tag{7-18}$$

where r_1 and r_2 are expressed by

$$r_1 = \frac{A_1\tau_{\mathrm{p}}}{A_1\tau_{\mathrm{p}}+A_2\tau_{\mathrm{d}}} \tag{7-19}$$

$$r_2 = \frac{A_2\tau_{\mathrm{d}}}{A_1\tau_{\mathrm{p}}+A_2\tau_{\mathrm{d}}} \tag{7-20}$$

where A_1 and A_2 are the fitting parameters of the biexponential decay ($A_1 e^{-t/\tau_{\mathrm{p}}} + A_2 e^{-t/\tau_{\mathrm{d}}}$) for the transient PL curve, and τ_{p} and τ_{d} are the decay lifetime of prompt and delayed emission (Figure 7-12). Thus, from the values of Φ_{p}, Φ_{d}, τ_{p}, and τ_{d}, the radiative decay rates of prompt and delayed emission (k_{p} and k_{d}) can be extracted by

$$k_{\mathrm{p}} = \frac{\Phi_{\mathrm{p}}}{\tau_{\mathrm{p}}} \tag{7-21}$$

$$k_{\mathrm{d}} = \frac{\Phi_{\mathrm{d}}}{\tau_{\mathrm{d}}} \tag{7-22}$$

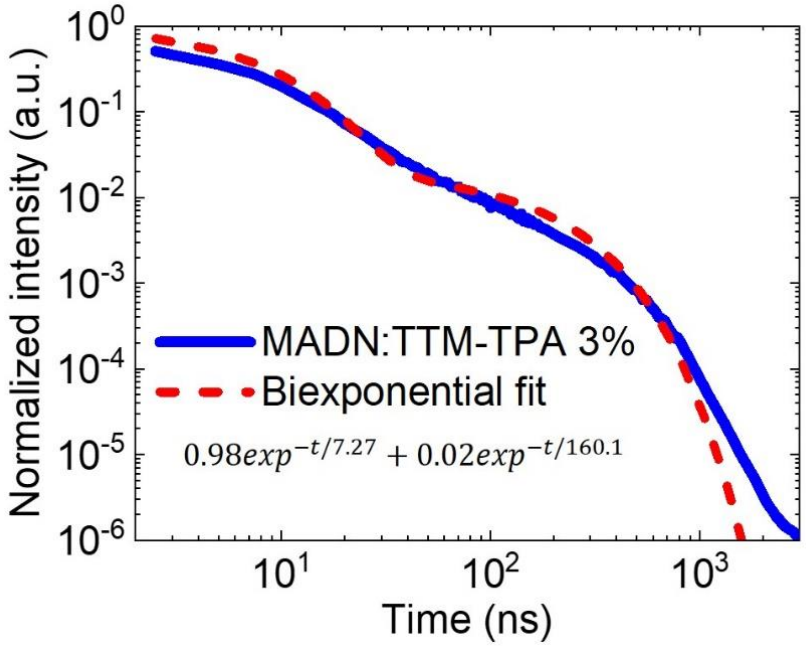

Figure 7-12. The biexponential fit of the transient PL profile obtained by 532 nm excitation for the MADN:TTM-TPA 3% film.

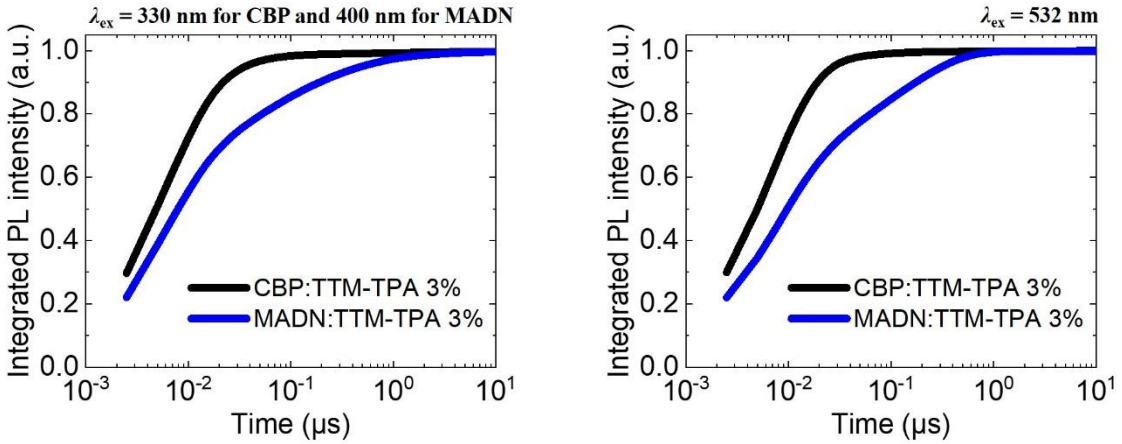

Figure 7-13. The normalised integrated PL intensity of the CBP:TTM-TPA 3% and MADN:TTM-TPA 3% films with different excitation wavelengths.

Table 7-4. Summary of the intensity ratios, the PLQEs of total, prompt, and delayed emission, and the efficiency of R-DET in the MADN:TTM-TPA system.

Host	Dopant	r_1	r_2	Φ_{total}	Φ_{p}	Φ_{d}	$\Phi_{\text{R-DET}}$
MADN	TTM-TPA	0.69	0.31	0.27	0.186	0.084	0.31

Table 7-5. Summary of the decay lifetime and rate constants in the MADN:TTM-TPA system.

Host	Dopant	τ_{p} (10^{-9} s)	τ_{d} (10^{-9} s)	k_{p} (10^{7} /s)	k_{d} (10^{5} /s)	$k_{\text{r,D}}$ (10^{6} /s)	$k_{\text{nr,D}}$ (10^{6} /s)	$k_{\text{R-DET}}$ (10^{6} /s)	$k_{\text{F-DET}}$ (10^{5} /s)
MADN	TTM-TPA	7.27	160.1	2.56	6.03	4.77	12.91	7.94	8.74

From Equation 7-10~15, $k_{\text{R-DET}}$ and $k_{\text{F-DET}}$ are obtained by

$$k_{\text{R-DET}} = \frac{\Phi_{\text{d}}}{\Phi_{\text{p}}+\Phi_{\text{d}}} k_{\text{p}} \tag{7-23}$$

$$k_{\text{F-DET}} = \frac{k_{\text{d}}\Phi_{\text{F-DET}}}{1-\Phi_{\text{R-DET}}\Phi_{\text{F-DET}}} = \frac{k_{\text{p}}k_{\text{d}}}{k_{\text{R-DET}}}\frac{\Phi_{\text{d}}}{\Phi_{\text{p}}} \tag{7-24}$$

Therefore, $k_{\text{R-DET}}$ and $k_{\text{F-DET}}$ are can be obtained from Equation 7-23 and 24 as 7.94×10^6 /s and 8.74×10^5 /s, respectively. The detailed rate constants are summarised in Table 7-5. In addition, Figure 7-13 shows the comparison of the normalised integrated PL intensity for the TTM-TPA 3% doped in CBP and MADN films supporting the different exciton decay kinetics between them.

7.8 Summary

In summary, highly efficient NIR organic radical LEDs with low efficiency roll-off and high radiance were demonstrated based on intermolecular intersystem dual energy transfer. As singlet and triplet excitons generated by electrical excitation can be effectively transferred from MADN to TTM-TPA via FRET and DET, respectively, a maximum EQE of 9.6% was achieved, much higher than the control device using a CBP host, 6.1%. Also, a very high maximum radiance of 68,000 $mW \cdot sr^{-1} \cdot m^{-2}$ was attained with highly improved device lifetime. From the investigation of charge transport in the full and single-carrier devices, it was shown that charge transport, as well as charge balance, was substantially enhanced. Furthermore, the triplet-to-doublet DET in devices was demonstrated by analysing transient EL and MEL. The distinct delayed EL and positive MEL characteristics of the MADN-based device prove that the intersystem dual energy transfer between MADN and TTM-TPA contributes to the substantial enhancement of device performance. Exciton decay kinetics and energy transfer pathways were studied based on transient photophysical studies. Transient absorption data show highly effective and rapid FRET between MADN and TTM-TPA with the rise of doublet signal in several picoseconds. Moreover, the distinct delayed emission in the transient PL of the MADN:TTM-TPA blend in accordance with the slow EL decay recorded in the transient EL of the MADN-based device supports the mutual energy transfer between MADN T_1 and TTM-TPA D_1.

In conclusion, the intersystem dual energy transfer in the doublet EL emissive system was clearly demonstrated with the exceptionally high device performance. Therefore, this novel emission mechanism could shed light on a pathway to infrared light-emitting technologies based on doublet fluorescence.

Chapter 8 Summary and outlook

8.1 Matrix-free hyperfluorescent deep blue OLEDs

Hyperfluorescent OLEDs have been of much interest due to their great potential of simultaneously realising high efficiency and stability with good colour purity. However, to optimise their device performance, a wide gap host matrix is necessary to minimise aggregation and triplet DET from TADF donors to fluorescence acceptors, but it generally increases the driving voltage and complexity of devices.

In this thesis, MFHF OLEDs were explored based on the study of device characterisation and exciton dynamics in the MFHF emissive system. It was demonstrated that higher than 15% EQE could be achieved in MFHF devices employing the novel organometallic TADF materials, CMAs. Furthermore, to suppress the typical energy loss mechanisms, aggregation and triplet-DET, more effectively, encapsulated fluorophores were investigated in deep blue OLEDs. The newly designed MR emitters are encapsulated by alkyl straps to ensure high device performance in MFHF devices. It was demonstrated that higher than 20% EQE with close to 100% IQE can be achieved from MFHF devices with ultra-narrowband emission of 11~12 nm FWHM at ~450 nm peak wavelength. In addition, the MR emitter is well incorporated in fluorescent OLEDs with higher than 8% EQE and CIE_y ~0.05, realising pure blue emission.

To further improve the device performance of MFHF OLEDs, it is necessary to develop novel deep blue TADF donors that can show high efficiency without a wide gap host to optimise the combination of TADF donor and MR acceptor. Several recent reports show the great potential of nondoped deep blue TADF OLEDs with higher than 20% EQE.[235–237] Accordingly, much higher device performance could be demonstrated

by exploring novel deep blue TADF donors as future work. Also, there is a possibility to modify the En-DBPICz for better performance. For example, if the spectrum of En-DBPICz is slightly red-shifted, better PL-absorption overlap is attained, leading to more effective FRET for better device performance. Also, adding new moieties to the core structure of the emitter to increase steric hindrance could further suppress the energy loss channels.

Therefore, the more optimised combination of TADF donor and MR emitter would result in the substantial enhancement of device performance, and MFHF exploiting MR emitters could be a solution for realising highly efficient and stable pure blue OLEDs in the near future.

8.2 NIR organic radical LEDs based on doublet fluorescence

Organic radical LEDs show a unique emission mechanism based on doublet spin configurations, which is different from the typical organic emitters controlled by the management of singlet and triplet states. Moreover, they can show theoretically 100% IQE as the radiative doublet decay ($D_1 \rightarrow D_0$) is a spin-allowed process so that all of the electrically generated doublet excitons are capable of contributing to the emission process with nanosecond decay lifetime.

In this thesis, NIR emissive organic radicals were explored. Firstly, a novel NIR emissive organic radical, TPA-PyBTM', was applied in a mixed host system to improve charge balance and transport in an EML. Due to the intrinsically deep energy level of TPA-PyBTM', severe electron trapping in an EML was observed, resulting in large efficiency roll-off, low radiance and device stability. However, as electron transport

materials (B3PYMPM and B4PYMPM) are mixed with hole transport materials (CBP and TCTA), device performance was substantially improved in terms of efficiency roll-off, radiance, and lifetime. Secondly, intersystem dual energy transfer was demonstrated. As one of the anthracene derivatives, MADN, and an efficient NIR emissive organic radical, TTM-TPA, were combined, the substantially enhanced device performance of organic radical LEDs was achieved. A maximum EQE of almost 10% was attained with the NIR emission with 800 nm peak wavelength, overcoming the energy gap law found in typical nonradical-based OLEDs.

For achieving more enhanced device performance from doublet emitters, it is vital to research new designs of organic radicals with more optimised host-dopant combinations and novel device architectures. Severe electron trapping would be improved if the SOMO and LUMO energy levels of organic radicals could be shallower. Also, the enhancement of the intrinsic PLQE could lead to better EQE in devices. Moreover, the further optimisation of intersystem dual energy transfer could contribute to much better device performance in doublet EL devices. In terms of device physics, as organic radicals have deeper energy levels than nonradical emitters, the more appropriate charge transporting layers for the radical emitters should be investigated. In conclusion, with future work, doublet fluorescence could illuminate a new route to achieve highly efficient NIR OLEDs with the novel design of organic radicals and effective energy transfer processes.

References

1. Tang, C. W. & Vanslyke, S. A. Cite as. *Appl Phys Lett* **51**, 913–915 (2019).

2. Baldo, M. A. *et al.* Highly efficient phosphorescent emission from organic electroluminescent devices. *Nature* **395**, 151–154 (1998).

3. Baldo, M. A., Lamansky, S., Burrows, P. E., Thompson, M. E. & Forrest, S. R. Very high-efficiency green organic light-emitting devices based on electrophosphorescence. *Appl Phys Lett* **75**, 4–6 (1999).

4. Yersin, H. (Hartmut). *Highly efficient OLEDs with phosphorescent materials*. (Wiley-VCH, 2007).

5. Kim, J. *et al.* A Compensation Algorithm for Degradation in AMOLED Displays. *Society for Information Display* **49**, 445–448 (2018).

6. Holmes, R. J. *et al.* Efficient, deep-blue organic electrophosphorescence by guest charge trapping. *Appl Phys Lett* **83**, 3818–3820 (2003).

7. Giebink, N. C. *et al.* Intrinsic luminance loss in phosphorescent small-molecule organic light emitting devices due to bimolecular annihilation reactions. *J Appl Phys* **103**, 1–9 (2008).

8. Chopra, N. *et al.* High efficiency blue phosphorescent organic light-emitting device. *Appl Phys Lett* **93**, 1–4 (2008).

9. Lin, T. A. *et al.* Sky-Blue Organic Light Emitting Diode with 37% External Quantum Efficiency Using Thermally Activated Delayed Fluorescence from Spiroacridine-Triazine Hybrid. *Advanced Materials* **28**, 6976–6983 (2016).

10. Lee, J. *et al.* Deep blue phosphorescent organic light-emitting diodes with very high brightness and efficiency. *Nat Mater* **15**, 92–98 (2016).

11. Shin, H. *et al.* Sky-Blue Phosphorescent OLEDs with 34.1% External Quantum Efficiency Using a Low Refractive Index Electron Transporting Layer. *Advanced Materials* **28**, 4920–4925 (2016).

12. Zhang, Y., Lee, J. & Forrest, S. R. Tenfold increase in the lifetime of blue phosphorescent organic light-emitting diodes. *Nat Commun* **5**, 1–7 (2014).

13. Li, X. *et al.* Deep Blue Phosphorescent Organic Light-Emitting Diodes with CIEy Value of 0.11 and External Quantum Efficiency up to 22.5%. *Advanced Materials* **30**, 1–8 (2018).

14. Klimes, K., Zhu, Z. Q. & Li, J. Efficient Blue Phosphorescent OLEDs with Improved Stability and Color Purity through Judicious Triplet Exciton Management. *Adv Funct Mater* **29**, 1–8 (2019).

15. Endo, A. *et al.* Efficient up-conversion of triplet excitons into a singlet state and its application for organic light emitting diodes. *Appl Phys Lett* **98**, 1–3 (2011).

16. Uoyama, H., Goushi, K., Shizu, K., Nomura, H. & Adachi, C. Highly efficient organic light-emitting diodes from delayed fluorescence. *Nature* **492**, 234–238 (2012).

17. Hatakeyama, T. *et al.* Ultrapure Blue Thermally Activated Delayed Fluorescence Molecules: Efficient HOMO-LUMO Separation by the Multiple Resonance Effect. *Advanced Materials* **28**, 2777–2781 (2016).

18. Kondo, Y. *et al.* Narrowband deep-blue organic light-emitting diode featuring an organoboron-based emitter. *Nat Photonics* **13**, 678–682 (2019).

19. Nakanotani, H. *et al.* High-efficiency organic light-emitting diodes with fluorescent emitters. *Nat Commun* **5**, 1–7 (2014).

20. Adachi, J., Kakizoe, H., Kuen, P., Tsang, D. & Endo, A. Hyperfluorescence^{TM}; a Game Changing Technology of OLED Display. *Soc. Inf. Disp. Int.* **50**, 95–98 (2019).

21. Chan, C. Y. *et al.* Stable pure-blue hyperfluorescence organic light-emitting diodes with high-efficiency and narrow emission. *Nat Photonics* **15**, 203–207 (2021).

22. Jeon, S. O. *et al.* High-efficiency, long-lifetime deep-blue organic light-emitting diodes. *Nat Photonics* **15**, 208–215 (2021).

23. Zampetti, A., Minotto, A. & Cacialli, F. Near-Infrared (NIR) Organic Light-Emitting Diodes (OLEDs): Challenges and Opportunities. *Adv Funct Mater* **29**, 1–22 (2019).

24. Spano, F. C. & Silva, C. H- and J-aggregate behavior in polymeric semiconductors. *Annu Rev Phys Chem* **65**, 477–500 (2014).

25. Englman, R. & Jortner, J. The energy gap law for radiationless transitions in large molecules. *Mol Phys* **18**, 285–287 (1970).

26. Baigenta, D. R., Hamera, P. J., Frienda, R. H., Morattib, S. C. & Holmesb Abstract, A. B. Polymer electroluminescence in the near i&a-red. *Synth Met* **71**, 2175–2176 (1995).

27. Minotto, A. *et al.* Efficient near-infrared electroluminescence at 840 nm with “Metal-free” small-molecule:Polymer blends. *Advanced Materials* **30**, 1–9 (2018).

28. Murto, P. *et al.* Triazolobenzothiadiazole-Based Copolymers for Polymer Light-Emitting Diodes: Pure Near-Infrared Emission via Optimized Energy and Charge Transfer. *Adv Opt Mater* **4**, 2068–2076 (2016).

29. Wei, Y. C. *et al.* Overcoming the energy gap law in near-infrared OLEDs by exciton–vibration decoupling. *Nat Photonics* **14**, 570–577 (2020).

30. Xue, J. *et al.* Homoleptic Facial Ir(III) Complexes via Facile Synthesis for High-Efficiency and Low-Roll-Off Near-Infrared Organic Light-Emitting Diodes over 750 nm. *Chemistry of Materials* **29**, 4775–4782 (2017).

31. Graham, K. R. *et al.* Extended conjugation platinum(II) porphyrins for use in near-infrared emitting organic light emitting diodes. *Chemistry of Materials* **23**, 5305–5312 (2011).

32. Sommer, J. R. *et al.* Efficient near-infrared polymer and organic light-emitting diodes based on electrophosphorescence from (tetraphenyltetranaphtho[2,3]porphyrin)platinum(II). *ACS Appl Mater Interfaces* **1**, 274–278 (2009).

33. Kim, D. H. *et al.* High-efficiency electroluminescence and amplified spontaneous emission from a thermally activated delayed fluorescent near-infrared emitter. *Nat Photonics* **12**, 98–104 (2018).

34. Wang, S. *et al.* Highly Efficient Near-Infrared Delayed Fluorescence Organic Light Emitting Diodes Using a Phenanthrene-Based Charge-Transfer Compound. *Angewandte Chemie* **127**, 13260–13264 (2015).

35. Yuan, Y. *et al.* Over 10% EQE Near-Infrared Electroluminescence Based on a Thermally Activated Delayed Fluorescence Emitter. *Adv Funct Mater* **27**, 1–5 (2017).

36. Liu, T., Xie, G., Zhong, C., Gong, S. & Yang, C. Boosting the Efficiency of Near-Infrared Fluorescent OLEDs with an Electroluminescent Peak of Nearly 800 nm by Sensitizer-Based Cascade Energy Transfer. *Adv Funct Mater* **28**, 1–8 (2018).

37. Brodeur, J. *et al.* Highly Efficient and Spectrally Narrow Near-Infrared Fluorescent OLEDs Using a TADF-Sensitized Cyanine Dye. *Adv Opt Mater* **7**, 1–7 (2019).

38. Shahalizad, A. *et al.* Efficient Solution-Processed Hyperfluorescent OLEDs with Spectrally Narrow Emission at 840 nm. *Adv Funct Mater* **31**, 1–8 (2021).

39. Abdurahman, A. *et al.* A pure red luminescent β-carboline-substituted biphenylmethyl radical: Photophysics, stability and OLEDs. *J Mater Chem C Mater* **6**, 11248–11254 (2018).

40. Dong, S. *et al.* Effects of substituents on luminescent efficiency of stable triaryl methyl radicals. *Physical Chemistry Chemical Physics* **20**, 18657–18662 (2018).

41. Hattori, Y., Kusamoto, T. & Nishihara, H. Luminescence, Stability, and Proton Response of an Open-Shell (3,5-Dichloro-4-pyridyl)bis(2,4,6-trichlorophenyl)methyl Radical. *Angewandte Chemie* **126**, 12039–12042 (2014).

42. Heckmann, A. *et al.* Highly fluorescent open-shell NIR dyes: The time-dependence of back electron transfer in triarylamine-perchlorotriphenylmethyl radicals. *Journal of Physical Chemistry C* **113**, 20958–20966 (2009).

43. Hattori, Y. *et al.* Luminescent Mono-, Di-, and Triradicals: Bridging Polychlorinated Triarylmethyl Radicals by Triarylamines and Triarylboranes. *Chemistry - A European Journal* **25**, 15463–15471 (2019).

44. Hattori, Y., Kusamoto, T. & Nishihara, H. Highly photostable luminescent open-shell (3,5-dihalo-4-pyridyl)bis(2,4,6-trichlorophenyl)methyl radicals: Significant effects of halogen atoms on their photophysical and photochemical properties. *RSC Adv* **5**, 64802–64805 (2015).

45. Tanushi, A. *et al.* Nir emission and acid-induced intramolecular electron transfer derived from a somo-homo converted non-Aufbau electronic structure. *Journal of Physical Chemistry C* **123**, 4417–4423 (2019).

46. Cui, Z. *et al.* Radical-Based Organic Light-Emitting Diodes with Maximum External Quantum Efficiency of 10.6%. *Journal of Physical Chemistry Letters* **9**, 6644–6648 (2018).

47. Velasco, D. *et al.* Red organic light-emitting radical adducts of carbazole and tris(2,4,6-trichlorotriphenyl)methyl radical that exhibit high thermal stability and electrochemical amphotericity. *Journal of Organic Chemistry* **72**, 7523–7532 (2007).

48. Peng, Q., Obolda, A., Zhang, M. & Li, F. Organic light-emitting diodes using a neutral π radical as emitter: The emission from a doublet. *Angewandte Chemie - International Edition* **54**, 7091–7095 (2015).

49. Castellanos, S., Velasco, D., López-Calahorra, F., Brillas, E. & Julia, L. Taking advantage of the radical character of tris(2,4,6-trichlorophenyl) methyl to synthesize new paramagnetic glassy molecular materials. *Journal of Organic Chemistry* **73**, 3759–3767 (2008).

50. Ai, X. *et al.* Efficient radical-based light-emitting diodes with doublet emission. *Nature* **563**, 536–540 (2018).

51. Abdurahman, A. *et al.* Understanding the luminescent nature of organic radicals for efficient doublet emitters and pure-red light-emitting diodes. *Nat Mater* **19**, 1224–1229 (2020).

52. Guo, H. *et al.* High stability and luminescence efficiency in donor–acceptor neutral radicals not following the Aufbau principle. *Nat Mater* **18**, 977–984 (2019).

53. P. B. Littlewood. *Excitons: Theory*. *Encyclopedia of Condensed Matter Physics* (Oxford University Press, 2005).

54. W.Y. Liang. Excitons. *Phys Educ* **5**, 226–228 (1970).

55. B.P. Zakharchenya & S.A. Permogorov. *Excitons in Crystals*. *Encyclopedia of Condensed Matter Physics* (North-Holland, 2005).

56. J. Frenkel. On the transformation of light into heat in solids. I. *Physical Review* **37**, 17–44 (1931).

57. J.D. Wright. *Molecular crystals*. (Cambridge University Press, 1995).

58. Kolobov, A. v & Tominaga, J. Excitons. in *Springer Series in Materials Science* 321–363 (2016).

59. Wannier, G. H. The Structure of Electronic Excitation Levels in Insulating Crystals. *Physical Review* **52**, 191–197 (1937).

60. Nicholas J. Turro. *Modern Molecular Photochemistry*. (University science books, 1991).

61. Valeur, B. *Molecular fluorescence : principles and applications*. (Wiley-VCH, 2001).

62. Wolfgang Paul. Exclusion principle and quantum mechanics. *Nobel Lecture* (1946).

63. Hudson, J. M., Hele, T. J. H. & Evans, E. W. Efficient light-emitting diodes from organic radicals with doublet emission. *J Appl Phys* **129**, 1–16 (2021).

64. Cui, Z., Abdurahman, A., Ai, X. & Li, F. Stable luminescent radicals and radical-based leds with doublet emission. *CCS Chemistry* **2**, 1129–1145 (2020).

65. Wang, F., Liu, X. K. & Gao, F. *Advanced Nanomaterials for Solar Cells and Light Emitting Diodes*. (Elsevier, 2019).

66. Kasha Michael. Characterization of electronic transitions in complex molecules. *Discuss Faraday Soc* **9**, 14–19 (1950).

67. Franck, J. Elementary processes of photochemical reactions. *Transactions of the Faraday Society* **21**, 536–542 (1925).

68. Condon Edward. A theory of intensity distribution in band systems. *Physical Review* **28**, 1182–1201 (1926).

69. Joseph Shinar. *Organic Light-Emitting Devices*. (Springer, 2004).

70. Park, S. M., Kim, Y. H., Yi, Y., Oh, H. Y. & Won Kim, J. Insertion of an organic interlayer for hole current enhancement in inverted organic light emitting devices. *Appl Phys Lett* **97**, 1–3 (2010).

71. Kim, Y. K., Won Kim, J. & Park, Y. Energy level alignment at a charge generation interface between 4, 4′ -bis(N -phenyl-1-naphthylamino)biphenyl and 1,4,5,8,9,11-hexaazatriphenylene- hexacarbonitrile. *Appl Phys Lett* **94**, 1–3 (2009).

72. Chiba, T. *et al.* Ultra-high efficiency by multiple emission from stacked organic light-emitting devices. *Org Electron* **12**, 710–715 (2011).

73. Liao, L. S. & Klubek, K. P. Power efficiency improvement in a tandem organic light-emitting diode. *Appl Phys Lett* **92**, 1–3 (2008).

74. Song, L. *et al.* Harvesting triplet excitons with exciplex thermally activated delayed fluorescence emitters toward high performance heterostructured organic light-emitting field effect transistors. *ACS Appl Mater Interfaces* **9**, 2711–2719 (2017).

75. Tsang, D. P. K. & Adachi, C. Operational stability enhancement in organic light-emitting diodes with ultrathin Liq interlayers. *Sci Rep* **6**, 1–9 (2016).

76. He, G. *et al.* Very high-efficiency and low voltage phosphorescent organic light-emitting diodes based on a p-i-n junction. *J Appl Phys* **95**, 5773–5777 (2004).

77. Volz, D. *et al.* From iridium and platinum to copper and carbon: New avenues for more sustainability in organic light-emitting diodes. *Green Chemistry* **17**, 1988–2011 (2015).

78. Murawski, C., Leo, K. & Gather, M. C. Efficiency roll-off in organic light-emitting diodes. *Advanced Materials* **25**, 6801–6827 (2013).

79. Scholz, S., Kondakov, D., Lüssem, B. & Leo, K. Degradation mechanisms and reactions in organic light-emitting devices. *Chem Rev* **115**, 8449–8503 (2015).

80. Sasabe, H. *et al.* Influence of substituted pyridine rings on physical properties and electron mobilities of 2-methylpyrimidine skeleton-based electron transporters. *Adv Funct Mater* **21**, 336–342 (2011).

81. Forster, T. Transfer mechanisms of electronic excitation. *Discuss. Faraday Soc.* **27**, (1959).

82. Adronov, A. & Frechet, J. M. J. Light-harvesting dendrimers. *Chemical Communications* 1701–1710 (2000).

83. Scholes, G. D. Long-Range Resonance Energy Transfer in Molecular Systems. *Annu Rev Phys Chem* **54**, 57–87 (2003).

84. Menke, S. M. & Holmes, R. J. Exciton diffusion in organic photovoltaic cells. *Energy Environ Sci* **7**, 499–512 (2014).

85. Dexter, D. L. A theory of sensitized luminescence in solids. *J Chem Phys* **21**, 836–850 (1953).

86. L. J. Rothberg & A. J. Lovinger. Status of and prospects for organic electroluminescence. *J. Mater. Res.* **11**, 3174–3187 (1996).

87. Brown, A. R. *et al.* Optical spectroscopy of triplet excitons and charged excitations in poly (pphenylenevinylene) light-emitting diodes. *Chem Phys Lett* **210**, 61–66 (1993).

88. Chiang, C. J. *et al.* Ultrahigh efficiency fluorescent single and bi-layer organic light emitting diodes: The key role of triplet fusion. *Adv Funct Mater* **23**, 739–746 (2013).

89. Kondakov, D. Y., Pawlik, T. D., Hatwar, T. K. & Spindler, J. P. Triplet annihilation exceeding spin statistical limit in highly efficient fluorescent organic light-emitting diodes. *J Appl Phys* **106**, (2009).

90. Luo, Y. J., Lu, Z. Y. & Huang, Y. Triplet fusion delayed fluorescence materials for OLEDs. *Chinese Chemical Letters* **27**, 1223–1230 (2016).

91. Cheng, Y. Y. *et al.* On the efficiency limit of triplet-triplet annihilation for photochemical upconversion. *Physical Chemistry Chemical Physics* **12**, 66–71 (2010).

92. Kondakov, D. Y. Characterization of triplet-triplet annihilation in organic light-emitting diodes based on anthracene derivatives. *J Appl Phys* **102**, 1–5 (2007).

93. Di, D. *et al.* Efficient Triplet Exciton Fusion in Molecularly Doped Polymer Light-Emitting Diodes. *Advanced Materials* **29**, 1–7 (2017).

94. Wallikewitz, B. H., Kabra, D., Gélinas, S. & Friend, R. H. Triplet dynamics in fluorescent polymer light-emitting diodes. *Phys Rev B Condens Matter Mater Phys* **85**, 1–15 (2012).

95. Lim, H., Woo, S. J., Ha, Y. H., Kim, Y. H. & Kim, J. J. Breaking the Efficiency Limit of Deep-Blue Fluorescent OLEDs Based on Anthracene Derivatives. *Advanced Materials* **34**, 1–8 (2022).

96. Joshua Jortner, Sang-il Choi, Joseph L. Katz & Stuart A. Rice. Triplet energy transfer and triplet - triplet interaction in aromatic crystals. *Phys Rev Lett* **11**, 323–326 (1963).

97. Jankus, V., Aydemir, M., Dias, F. B. & Monkman, A. P. Generating light from upper excited triplet states: A contribution to the indirect singlet yield of a polymer oled, helping to exceed the 25% singlet exciton limit. *Advanced Science* **3**, 1–6 (2015).

98. B. Dick & B. Nickel. Accessibility of the lowest quintet state of organic molecules through triplet-triplet annihilation; an indo ci study. *Chem Phys* **78**, 1–16 (1983).

99. Fong, H. H. *et al.* Effects of tertiary butyl substitution on the charge transporting properties of rubrene-based films. *Chem Phys* **298**, 119–123 (2004).

100. Kim, H. G., Kim, K. H., Moon, C. K. & Kim, J. J. Harnessing Triplet Excited States by Fluorescent Dopant Utilizing Codoped Phosphorescent Dopant in Exciplex Host for Efficient Fluorescent Organic Light Emitting Diodes. *Adv Opt Mater* **5**, 1–6 (2017).

101. Liu, Z., Helander, M. G., Wang, Z. & Lu, Z. Efficient single-layer organic light-emitting diodes based on C545T-Alq3 system. *Journal of Physical Chemistry C* **114**, 11931–11935 (2010).

102. Heimel, P. *et al.* Unicolored phosphor-sensitized fluorescence for efficient and stable blue OLEDs. *Nat Commun* **9**, 1–8 (2018).

103. Cebrián, C. & Mauro, M. Recent advances in phosphorescent platinum complexes for organic light-emitting diodes. *Beilstein Journal of Organic Chemistry* **14**, 1459–1481 (2018).

104. Haneder, S. *et al.* Controlling the radiative rate of deep-blue electrophosphorescent organometallic complexes by singlet-triplet gap engineering. *Advanced Materials* **20**, 3325–3330 (2008).

105. Cui, L. S. *et al.* Fast spin-flip enables efficient and stable organic electroluminescence from charge-transfer states. *Nat Photonics* **14**, 636–642 (2020).

106. Wada, Y., Nakagawa, H., Matsumoto, S., Wakisaka, Y. & Kaji, H. Organic light emitters exhibiting very fast reverse intersystem crossing. *Nat Photonics* **14**, 643–649 (2020).

107. Moon, C. K. *et al.* Combined Inter- and Intramolecular Charge-Transfer Processes for Highly Efficient Fluorescent Organic Light-Emitting Diodes with Reduced Triplet Exciton Quenching. *Advanced Materials* **29**, 1–5 (2017).

108. Zhang, D., Song, X., Cai, M., Kaji, H. & Duan, L. Versatile Indolocarbazole-Isomer Derivatives as Highly Emissive Emitters and Ideal Hosts for Thermally Activated Delayed Fluorescent OLEDs with Alleviated Efficiency Roll-Off. *Advanced Materials* **30**, 1–10 (2018).

109. Wu, T. L. *et al.* Diboron compound-based organic light-emitting diodes with high efficiency and reduced efficiency roll-off. *Nat Photonics* **12**, 235–240 (2018).

110. Ahn, D. H. *et al.* Highly efficient blue thermally activated delayed fluorescence emitters based on symmetrical and rigid oxygen-bridged boron acceptors. *Nat Photonics* **13**, 540–546 (2019).

111. Hirata, S. *et al.* Highly efficient blue electroluminescence based on thermally activated delayed fluorescence. *Nat Mater* **14**, 330–336 (2015).

112. Lee, D. R. *et al.* Design Strategy for 25% External Quantum Efficiency in Green and Blue Thermally Activated Delayed Fluorescent Devices. *Advanced Materials* **27**, 5861–5867 (2015).

113. Wang, H. *et al.* Novel thermally activated delayed fluorescence materials-thioxanthone derivatives and their applications for highly efficient OLEDs. *Advanced Materials* **26**, 5198–5204 (2014).

114. Chen, J. X. *et al.* Managing Locally Excited and Charge-Transfer Triplet States to Facilitate Up-Conversion in Red TADF Emitters That Are Available for Both Vacuum- and Solution-Processes. *Angewandte Chemie - International Edition* **60**, 2478–2484 (2021).

115. Zhang, Q. *et al.* Efficient blue organic light-emitting diodes employing thermally activated delayed fluorescence. *Nat Photonics* **8**, 326–332 (2014).

116. Tao, Y. *et al.* Thermally activated delayed fluorescence materials towards the breakthrough of organoelectronics. *Advanced Materials* **26**, 7931–7958 (2014).

117. Goushi, K., Yoshida, K., Sato, K. & Adachi, C. Organic light-emitting diodes employing efficient reverse intersystem crossing for triplet-to-singlet state conversion. *Nat Photonics* **6**, 253–258 (2012).

118. Baldo, M. A. & Forrest, S. R. Transient analysis of organic electrophosphorescence: I. Transient analysis of triplet energy transfer. *Phys Rev B* **62**, 10958–10966 (2000).

119. Nakagawa, T., Ku, S. Y., Wong, K. T. & Adachi, C. Electroluminescence based on thermally activated delayed fluorescence generated by a spirobifluorene donor–acceptor structure. *Chemical Communications* **48**, 9580–9582 (2012).

120. Baldo M.A. Thompson M. E. Forrest S. R. High-efficiency fluorescent organic light-emitting devices using a phosphorescent sensitizer. *Nature* **403**, 750–753 (2000).

121. Kim, H. G., Kim, K. H. & Kim, J. J. Highly Efficient, Conventional, Fluorescent Organic Light-Emitting Diodes with Extended Lifetime. *Advanced Materials* **29**, 1–6 (2017).

122. Kim, H. G. *et al.* Triplet Harvesting by a Fluorescent Emitter Using a Phosphorescent Sensitizer for Blue Organic-Light-Emitting Diodes. *ACS Appl Mater Interfaces* **11**, 26–30 (2019).

123. Li, D., Hu, Y. & Liao, L. S. Triplet exciton harvesting by multi-process energy transfer in fluorescent organic light-emitting diodes. *J Mater Chem C Mater* **7**, 977–985 (2019).

124. C. de Mello, J., H. Felix, W. & H. Friend, R. An Improved Experimental Determination of External Photoluminescence Quantum Efficiency. *Advanced Materials* **9**, 230–232 (1997).

125. Greenham, N. C. *et al.* Measurement of absolute photoluminescence quantum efficiencies in conjugated polymers. *Chem Phys Lett* **241**, 89–96 (1995).

126. Samuela, I. D. W. *et al.* Picosecond Time-Resolved Photoluminescence of PPV Derivatives. *Synth Met* **84**, 497–500 (1997).

127. Samuel, I. D. W. *et al.* Time-resolved luminescence measurements in poly(p-phenylenevinylene). *Synth Met* **54**, 288 (1993).

128. Joseph R. Lakowicz. *Principles of Fluorescence Spectroscopy*. (Springe, 2006).

129. Dussault, D. & Hoess, P. Noise performance comparison of ICCD with CCD and EMCCD cameras. *Infrared Systems and Photoelectronic Technology* **5563**, 195–204 (2004).

130. An Introduction to ICCD cameras. https://andor.oxinst.com/learning/view/article/intensified-ccd-cameras.

131. Panesi, M., Miki, K., Prudhomme, S. & Brandis, A. On the assessment of a Bayesian validation methodology for data reduction models relevant to shock tube experiments. *Comput Methods Appl Mech Eng* **213–216**, 383–398 (2012).

132. Kawamura, Y., Brooks, J., Brown, J. J., Sasabe, H. & Adachi, C. Intermolecular interaction and a concentration-Quenching mechanism of phosphorescent Ir(III) complexes in a solid film. *Phys Rev Lett* **96**, 1–4 (2006).

133. Park, Y. S. *et al.* Exciplex-forming Co-host for organic light-emitting diodes with ultimate efficiency. *Adv Funct Mater* **23**, 4914–4920 (2013).

134. Park, Y. S., Kim, K. H. & Kim, J. J. Efficient triplet harvesting by fluorescent molecules through exciplexes for high efficiency organic light-emitting diodes. *Appl Phys Lett* **102**, 1–5 (2013).

135. Berera, R., van Grondelle, R. & Kennis, J. T. M. Ultrafast transient absorption spectroscopy: Principles and application to photosynthetic systems. *Photosynth Res* **101**, 105–118 (2009).

136. Park, J., Deria, P. & Therien, M. J. Dynamics and transient absorption spectral signatures of the single-wall carbon nanotube electronically excited triplet state. *J Am Chem Soc* **133**, 17156–17159 (2011).

137. Xu, Y. *et al.* Highly Efficient Blue Fluorescent OLEDs Based on Upper Level Triplet–Singlet Intersystem Crossing. *Advanced Materials* **31**, 1–8 (2019).

138. Manzoni, C., Polli, D. & Cerullo, G. Two-color pump-probe system broadly tunable over the visible and the near infrared with sub-30 fs temporal resolution. *Review of Scientific Instruments* **77**, 1–9 (2006).

139. G. Porter. Flash photolysis and spectroscopy. A new method for the study of free radical reactions. *Proceedings of the Royal Society of London. Series A* **200**, 284–300 (1950).

140. Zewail, A. H. Laser Femtochemistry. *Science (1979)* **242**, 1645–1653 (1987).

141. Zewail, A. H. Femtochemistry: Atomic-scale dynamics of the chemical bond. *Journal of Physical Chemistry A* **104**, 5660–5694 (2000).

142. J.S.Setchell Jr. Chapter 8. Colour description and communication. in *Colour Design* 219–253 (Woodhead Publishing, 2012).

143. T. SMITH & J. GUILD. The C.I.E. colorimetric standards and their use. *Trans. Opt. Soc.* **33**, 73–134 (1931).

144. Süsstrunk, S., Buckley, R. & Swen, S. Standard RGB Color Spaces. in *7th color imaging conference on fnal progress proceedings on society for imaging science and technology* 127–134 (1999).

145. Abhay Sharma. Understanding RGB Color Spaces for Monitors, Projectors, and Televisions. *Inf Disp (1975)* **35**, 17–43 (2019).

146. Soneira, R. M. Display color gamuts: NTSC to Rec.2020. *Inf Disp (1975)* **32**, 26–31 (2016).

147. Gill, W. D. Drift mobilities in amorphous charge-transfer complexes of trinitrofluorenone and poly-n-vinylcarbazole. *J Appl Phys* **43**, 5033–5040 (1972).

148. Murgatroyd, P. N. & Wills, H. H. Theory of space-charge-limited current enhanced by Frenkel effect. *J Phys D Appl Phys* **3**, 151–156 (1970).

149. Blom, P. W. M., de Jong, M. J. M. & Vleggaar, J. J. M. Electron and hole transport in poly(p-phenylene vinylene) devices. *Appl Phys Lett* **68**, 3308–3310 (1996).

150. Zhang, P. *et al.* Space-charge limited current in nanodiodes: Ballistic, collisional, and dynamical effects. *J Appl Phys* **129**, 1–32 (2021).

151. Faris Yılmaz. *Conducting polymers*. (IntecOpen, 2016).

152. Cai, C. *et al.* High-efficiency red, green and blue phosphorescent homojunction organic light-emitting diodes based on bipolar host materials. *Org Electron* **12**, 843–850 (2011).

153. Bozano, L., Carter, S. A., Scott, J. C., Malliaras, G. G. & Brock, P. J. Temperature- and field-dependent electron and hole mobilities in polymer light-emitting diodes. *Appl Phys Lett* **74**, 1132–1134 (1999).

154. Yasuda, T., Yamaguchi, Y., Zou, D. C. & Tsutsui, T. Carrier mobilities in organic electron transport materials determined from space charge limited current. *Japanese Journal of Applied Physics, Part 1: Regular Papers and Short Notes and Review Papers* **41**, 5626–5629 (2002).

155. Chu, T. Y. & Song, O. K. Hole mobility of N, N′ -bis(naphthalen-1-yl)- N, N′ -bis(phenyl) benzidine investigated by using space-charge-limited currents. *Appl Phys Lett* **90**, 1–3 (2007).

156. Khan, M. A. *et al.* Electron mobility of 4,7-diphyenyl-1,10-phenanthroline estimated by using space-charge-limited currents. *J Appl Phys* **103**, 1–4 (2008).

157. Malliaras, G. G., Salem, J. R., Brock, P. J. & Scott, C. Electrical characteristics and efficiency of single-layer organic light-emitting diodes. *Phys Rev B* **58**, R411–R414 (1998).

158. Dunlap, D. H., Parris, P. E. & Kenkre, V. M. Charge-Dipole Model for the Universal Field Dependence of Mobilities in Molecularly Doped Polymers. *Phys Rev Lett* **77**, 542–545 (1996).

159. Blom, P. W. M., de Jong, M. J. M. & van Munster, M. G. Electric-field and temperature dependence of the hole mobility in poly(p-phenylene vinylene). *Phys Rev B* **55**, R656–R659 (1997).

160. Weichsel, C. *et al.* Storage of charge carriers on emitter molecules in organic light-emitting diodes. *Phys Rev B* **86**, 1–9 (2012).

161. Baldo, M. A., Adachi, C. & Forrest, S. R. Transient analysis of organic electrophosphorescence. II. Transient analysis of triplet-triplet annihilation. *Phys Rev B* **62**, 10967–10977 (1999).

162. Wong, T. C., Kovac, J., Lee, C. S., Hung, L. S. & Lee, S. T. Transient electroluminescence measurements on electron-mobility of N-arylbenzimidazoles. *Chem Phys Lett* **334**, 61–64 (2001).

163. Vicki Cleave, B., Yahioglu, G., le Barny, P., Friend, R. H. & Tessler, N. Harvesting Singlet and Triplet Energy in Polymer LEDs. *Advanced Materials* **11**, 285–288 (1999).

164. Nikitenko, V. R. *et al.* The overshoot effect in transient electroluminescence from organic bilayer light emitting diodes: Experiment and theory. *J Appl Phys* **81**, 7514–7525 (1997).

165. Lee, J. H., Lee, S., Yoo, S. J., Kim, K. H. & Kim, J. J. Langevin and trap-assisted recombination in phosphorescent organic light emitting diodes. *Adv Funct Mater* **24**, 4681–4688 (2014).

166. Lin, M. te, Li, M., Chen, W. H., Omary, M. A. & Shepherd, N. D. Transient electroluminescence determination of carrier mobility and charge trapping effects in

heavily doped phosphorescent organic light-emitting diodes. *Solid State Electron* **56**, 196–200 (2011).

167. Ruslan P. Ozerov & Anatoli A. Vorobyev. *Physics for Chemists*. (Elsevier, 2007).

168. Guo, X. *et al.* Magneto-Electroluminescence Studies on the Role of Intermolecular Spin–Orbital Coupling Processes for the Transition between Singlet and Triplet Excitons in Exciplex-Based Phosphorescent Organic Light-Emitting Diodes. *Adv Opt Mater* **8**, 1–9 (2020).

169. Ding, B. & Alameh, K. Simultaneous monitoring of singlet and triplet exciton variations in solid organic semiconductors driven by an external static magnetic field. *Appl Phys Lett* **105**, 1–5 (2014).

170. Yuan, P., Qiao, X., Yan, D. & Ma, D. An inversion of magnetic field effects in electromer-based organic light-emitting diodes. *J Mater Chem C Mater* **7**, 1035–1041 (2019).

171. Wang, F. J., Bässler, H. & Vardeny, Z. V. Magnetic field effects in π-conjugated polymer-fullerene blends: Evidence for multiple components. *Phys Rev Lett* **101**, 1–4 (2008).

172. Ding, B. *et al.* Magnetic field modulated exciton generation in organic semiconductors: An intermolecular quantum correlated effect. *Phys Rev B* **82**, 1–4 (2010).

173. Sheng, Y. *et al.* Hyperfine interaction and magnetoresistance in organic semiconductors. *Phys Rev B* **74**, 1–9 (2006).

174. Jia, W. *et al.* Spin-orbital coupling induced high-field decay of magneto-electroluminescence in pristine Alq3-based organic light-emitting diodes. *Org Electron* **22**, 210–215 (2015).

175. Lei, Y. L. *et al.* Driving current and temperature dependent magnetic-field modulated electroluminescence in Alq3-based organic light emitting diode. *Org Electron* **10**, 889–894 (2009).

176. Mermer, Ö. *et al.* Large magnetoresistance in nonmagnetic π-conjugated semiconductor thin film devices. *Phys Rev B* **72**, 1–12 (2005).

177. Hu, B., Yan, L. & Shao, M. Magnetic-field effects in organic semiconducting materials and devices. *Advanced Materials* **21**, 1500–1516 (2009).

178. Pu, Y. J. *et al.* Absence of delayed fluorescence and triplet-triplet annihilation in organic light emitting diodes with spatially orthogonal bianthracenes. *J Mater Chem C Mater* **7**, 2541–2547 (2019).

179. Yuan, P., Qiao, X., Yan, D. & Ma, D. Magnetic field effects on the quenching of triplet excitons in exciplex-based organic light emitting diodes. *J Mater Chem C Mater* **6**, 5721–5726 (2018).

180. Merrifield, R. E. Theory of magnetic field effects on the mutual annihilation of triplet excitons. *J Chem Phys* **48**, 4319–4320 (1968).

181. McCamey, D. R. *et al.* Spin Rabi flopping in the photocurrent of a polymer light-emitting diode. *Nat Mater* **7**, 723–728 (2008).

182. Lupton, J. M., McCamey, D. R. & Boehme, C. Coherent spin manipulation in molecular semiconductors: Getting a handle on organic spintronics. *ChemPhysChem* **11**, 3040–3058 (2010).

183. Ehrenfreund, E. & Vardeny, Z. V. Effects of magnetic field on conductance and electroluminescence in organic devices. *Isr J Chem* **52**, 552–562 (2012).

184. Lawrence, J. E., Lewis, A. M., Manolopoulos, D. E. & Hore, P. J. Magnetoelectroluminescence in organic light-emitting diodes. *Journal of Chemical Physics* **144**, 1–10 (2016).

185. *Evaluation of measurement data — Guide to the expression of uncertainty in measurement*. (JCGM, 2008).

186. Bell, S. *Measurement Good Practice Guide No. 11 The Beginner's Guide to Uncertainty of Measurement*. (National Physical Laboratory, 1999).

187. Cox, M. & O'Hagan, A. Meaningful expression of uncertainty in measurement. *Accreditation and Quality Assurance* **27**, 19–37 (2022).

188. Kim, J. H., Lee, K. H. & Lee, J. Y. Design of thermally activated delayed fluorescent sensitizers for high efficiency over 20% and long lifetime in yellow fluorescent organic light-emitting diodes. *J Mater Chem C Mater* **8**, 5265–5272 (2020).

189. Jeon, S. K., Park, H. J. & Lee, J. Y. Highly Efficient Soluble Blue Delayed Fluorescent and Hyperfluorescent Organic Light-Emitting Diodes by Host Engineering. *ACS Appl Mater Interfaces* **10**, 5700–5705 (2018).

190. Zhang, D., Song, X., Cai, M. & Duan, L. Blocking Energy-Loss Pathways for Ideal Fluorescent Organic Light-Emitting Diodes with Thermally Activated Delayed Fluorescent Sensitizers. *Advanced Materials* **30**, 1–10 (2018).

191. Zhang, D. *et al.* Efficient and Stable Deep-Blue Fluorescent Organic Light-Emitting Diodes Employing a Sensitizer with Fast Triplet Upconversion. *Advanced Materials* **32**, 1–9 (2020).

192. Braveenth, R. *et al.* Achieving Narrow FWHM and High EQE Over 38% in Blue OLEDs Using Rigid Heteroatom-Based Deep Blue TADF Sensitized Host. *Adv Funct Mater* **31**, 1–9 (2021).

193. Ahn, D. H., Jeong, J. H., Song, J., Lee, J. Y. & Kwon, J. H. Highly Efficient Deep Blue Fluorescent Organic Light-Emitting Diodes Boosted by Thermally Activated Delayed Fluorescence Sensitization. *ACS Appl Mater Interfaces* **10**, 10246–10253 (2018).

194. Furukawa, T., Nakanotani, H., Inoue, M. & Adachi, C. Dual enhancement of electroluminescence efficiency and operational stability by rapid upconversion of triplet excitons in OLEDs. *Sci Rep* **5**, 1–8 (2015).

195. Di, D. *et al.* High-performance light-emitting diodes based on carbene-metal-amides. *Science (1979)* **359**, 159–163 (2017).

196. Feng, J. *et al.* Carbene-Metal-Amide Polycrystalline Materials Feature Blue Shifted Energy yet Unchanged Kinetics of Emission. *Chemistry of Materials* **32**, 4743–4753 (2020).

197. Conaghan, P. J. *et al.* Efficient Vacuum-Processed Light-Emitting Diodes Based on Carbene–Metal–Amides. *Advanced Materials* **30**, 1–5 (2018).

198. Y. Sato, T. Ogata, S. Ichinosawa & Y. Murata. Characteristics of organic electroluminescent devices with new dopants. *Synth Met* **91**, 103–107 (1997).

199. Wu, Y. S., Liu, T. H., Chen, H. H. & Chen, C. H. A new yellow fluorescent dopant for high-efficiency organic light-emitting devices. *Thin Solid Films* **496**, 626–630 (2006).

200. Feng, J. *et al.* Environmental Control of Triplet Emission in Donor–Bridge–Acceptor Organometallics. *Adv Funct Mater* **30**, 1–11 (2020).

201. Baumann, J. & Fayer, M. D. Excitation transfer in disordered two-dimensional and anisotropic three-dimensional systems: Effects of spatial geometry on time-resolved observables. *J Chem Phys* **85**, 4087–4107 (1986).

202. Peumans, P., Yakimov, A. & Forrest, S. R. Small molecular weight organic thin-film photodetectors and solar cells. *J Appl Phys* **93**, 3693–3723 (2003).

203. Scully, S. R. & McGehee, M. D. Effects of optical interference and energy transfer on exciton diffusion length measurements in organic semiconductors. *J Appl Phys* **100**, 1–5 (2006).

204. Nagata, R., Nakanotani, H., Potscavage, W. J. & Adachi, C. Exploiting Singlet Fission in Organic Light-Emitting Diodes. *Advanced Materials* **30**, 1–6 (2018).

205. Jakoby, M., Richards, B. S., Lemmer, U. & Howard, I. A. Investigations of singlet and triplet diffusion in thermally activated delayed-fluorescence emitters: Implications for hyperfluorescence. *Phys Rev B* **100**, 1–9 (2019).

206. Leventis, A. *et al.* Highly Luminescent Encapsulated Narrow Bandgap Polymers Based on Diketopyrrolopyrrole. *J Am Chem Soc* **140**, 1622–1626 (2018).

207. Fujiwara, Y. *et al.* Double alkylene-strapped diphenylanthracene as a photostable and intense solid-state blue-emitting material. *Journal of Organic Chemistry* **78**, 2206–2212 (2013).

208. Zhang, Q. *et al.* Design of efficient thermally activated delayed fluorescence materials for pure blue organic light emitting diodes. *J Am Chem Soc* **134**, 14706–14709 (2012).

209. Zhang, Y. *et al.* Sterically Wrapped Multiple Resonance Fluorophors for Suppression of Concentration Quenching and Spectrum Broadening. *Angewandte Chemie - International Edition* **61**, 1–6 (2022).

210. Patil, V. V. *et al.* Purely Spin-Vibronic Coupling Assisted Triplet to Singlet Up-Conversion for Real Deep Blue Organic Light-Emitting Diodes with Over 20% Efficiency and y Color Coordinate of 0.05. *Advanced Science* **8**, 1–8 (2021).

211. Wei, J. *et al.* Indolo[3,2,1-jk]carbazole Embedded Multiple-Resonance Fluorophors for Narrowband Deep-blue Electroluminescence with EQE≈34.7 % and CIEy≈0.085. *Angewandte Chemie - International Edition* **60**, 12269–12273 (2021).

212. Lee, H. L., Chung, W. J. & Lee, J. Y. Narrowband and Pure Violet Organic Emitter with a Full Width at Half Maximum of 14 nm and y Color Coordinate of Below 0.02. *Small* **16**, 1–5 (2020).

213. Niebel, C. *et al.* Dibenzo[2,3:5,6]pyrrolizino[1,7-bc]indolo[1,2,3-lm]carbazole: A new electron donor. *New Journal of Chemistry* **34**, 1243–1246 (2010).

214. Rivoal, M. *et al.* Substituted dibenzo[2,3:5,6]-pyrrolizino[1,7-bc]indolo[1,2,3-lm]carbazoles: A series of new electron donors. *Tetrahedron* **69**, 3302–3307 (2013).

215. Arnault, E. *et al.* Phototoxic Action Spectrum on a Retinal Pigment Epithelium Model of Age-Related Macular Degeneration Exposed to Sunlight Normalized Conditions. *PLoS One* **8**, 1–12 (2013).

216. Zhao, Z. C., Zhou, Y., Tan, G. & Li, J. Research progress about the effect and prevention of blue light on eyes. *Int J Ophthalmol* **11**, 1999–2003 (2018).

217. Lu, T. & Chen, F. Quantitative analysis of molecular surface based on improved Marching Tetrahedra algorithm. *J Mol Graph Model* **38**, 314–323 (2012).

218. Zhang, Q. *et al.* Nearly 100% internal quantum efficiency in undoped electroluminescent devices employing pure organic emitters. *Advanced Materials* **27**, 2096–2100 (2015).

219. Green, A. P. & Buckley, A. R. Solid state concentration quenching of organic fluorophores in PMMA. *Physical Chemistry Chemical Physics* **17**, 1435–1440 (2015).

220. Aziz, H., Popovic, Z. D., Hu, N.-X., Hor, A.-M. & Xu, G. Physics and Chemistry of III-V Compound Semiconductor Interfaces. *Science (1979)* **283**, 1900–1902 (1999).

221. Lee, J. H., Wu, C. I., Liu, S. W., Huang, C. A. & Chang, Y. Mixed host organic light-emitting devices with low driving voltage and long lifetime. *Appl Phys Lett* **86**, 1–3 (2005).

222. Chwang, A. B., Kwong, R. C. & Brown, J. J. Graded mixed-layer organic light-emitting devices. *Appl Phys Lett* **80**, 725–727 (2002).

223. Liu, S. W. *et al.* Blue mixed host organic light emitting devices. *Thin Solid Films* **453–454**, 312–315 (2004).

224. Kondakova, M. E. *et al.* High-efficiency, low-voltage phosphorescent organic light-emitting diode devices with mixed host. *J Appl Phys* **104**, 1–17 (2008).

225. Lee, J., Lee, J. I., Lee, J. Y. & Chu, H. Y. Enhanced efficiency and reduced roll-off in blue and white phosphorescent organic light-emitting diodes with a mixed host structure. *Appl Phys Lett* **94**, (2009).

226. Chopra, N. *et al.* High efficiency and low roll-off blue phosphorescent organic light-emitting devices using mixed host architecture. *Appl Phys Lett* **97**, (2010).

227. Li, D., Hu, Y. & Liao, L. S. Triplet exciton harvesting by multi-process energy transfer in fluorescent organic light-emitting diodes. *J Mater Chem C Mater* **7**, 977–985 (2019).

228. Zhang, X. *et al.* Highly efficient red phosphorescent organic light-emitting devices based on solution-processed small molecular mixed-host. *J Lumin* **161**, 300–305 (2015).

229. Hsiao, C. H., Chen, Y. H., Lin, T. C., Hsiao, C. C. & Lee, J. H. Recombination zone in mixed-host organic light-emitting devices. *Appl Phys Lett* **89**, (2006).

230. Kim, K. H., Yoo, S. J. & Kim, J. J. Boosting Triplet Harvest by Reducing Nonradiative Transition of Exciplex toward Fluorescent Organic Light-Emitting

Diodes with 100% Internal Quantum Efficiency. *Chemistry of Materials* **28**, 1936–1941 (2016).

231. Méhes, G., Goushi, K., Potscavage, W. J. & Adachi, C. Influence of host matrix on thermally-activated delayed fluorescence: Effects on emission lifetime, photoluminescence quantum yield, and device performance. *Org Electron* **15**, 2027–2037 (2014).

232. Steiner', U. E. & Ulrich', T. Magnetic Field Effects in Chemical Kinetics and Related Phenomena. *Chem Rev* **89**, 51–147 (1989).

233. Ern, V. & Merrifield, R. E. Magnetic field effect on triplet exciton quenching in organic crystals. *Phys Rev Lett* **21**, 609–611 (1968).

234. Serevičius, T. *et al.* Triplet-Triplet Annihilation in 9,10-Diphenylanthracene Derivatives: The Role of Intersystem Crossing and Exciton Diffusion. *Journal of Physical Chemistry C* **121**, 8515–8524 (2017).

235. Zou, S. J. *et al.* High-Performance Nondoped Blue Delayed Fluorescence Organic Light-Emitting Diodes Featuring Low Driving Voltage and High Brightness. *Advanced Science* **7**, 1–9 (2020).

236. Han, J. *et al.* Narrowband blue emission with insensitivity to the doping concentration from an oxygen-bridged triarylboron-based TADF emitter: nondoped OLEDs with a high external quantum efficiency up to 21.4%. *Chem Sci* **13**, 3402–3408 (2022).

237. Xia, G. *et al.* A TADF Emitter Featuring Linearly Arranged Spiro-Donor and Spiro-Acceptor Groups: Efficient Nondoped and Doped Deep-Blue OLEDs with CIEy <0.1. *Angewandte Chemie - International Edition* **60**, 9598–9603 (2021).

List of Publications

- **Hwan-Hee Cho**, Alexander S. Romanov, M Bochmann, Neil. C. Greenham, Dan Credgington, 'Matrix-free Hyperfluorescent Organic Light-Emitting Diodes Based on Carbene-Metal-Amides' *Adv. Opt. Mater*. 2021, 9, 2001965.

- **Hwan-Hee Cho,** Shun Kimura, Neil C. Greenham, Yuki Tani, Ryota Matsuoka, Hiroshi Nishihara, Richard H. Friend, Tetsuro Kusamoto, Emrys W. Evans, 'Near-infrared Light-Emitting Diodes from Organic Radicals with Charge Control' *Adv. Opt. Mater.* 2022, 2200628.

- **Hwan-Hee Cho,** Dan G. Congrave, Hugo Bronstein, Neil. C. Greenham, 'Deep Blue Fluorescent Organic Light-Emitting Diodes Exploiting an Encapsulated Diphenyl Anthracene' in preparation.

- Dan G. Congrave,* **Hwan-Hee Cho,*** Hugo Bronstein, Neil. C. Greenham, 'Covalently Encapsulated Ultra-Narrowband Emitters Enable True Blue Matrix-Free Hyperfluorescence' in preparation. *contribution equally

- **Hwan-Hee Cho,** Sebastian Gorgon, Feng Li, Changsoon Cho, Neil C. Greenham, Richard H. Friend, Emrys W. Evans, 'Highly efficient Near-Infrared Organic Radical Light-Emitting Diodes with Intersystem Dual Energy Transfer' in preparation.